Universität
Zürich UZH

Physik-Institut
Wissenschaftlicher Jahresbericht

April 2010 - März 2011

Winterthurerstrasse 190, CH-8057 Zürich/Schweiz

The picture on the front shows Saskia Bosma and Stephen Weyeneth of the *Superconductivity and Magnetism* group setting up the liquid Helium coolant flow for the torque magnetometer (see Sec. 12). Hugo Keller is watching them. On the back a miniaturized magnetic torque sensor is shown used to study even the tiniest superconducting samples.

Sekretariat	044 635 5721	secret@physik.uzh.ch
Prof. C. Amsler	044 635 5784 022 767 2914	amsler@cern.ch
Prof. L. Baudis	044 635 5777	lbaudis@physik.uzh.ch
Prof. H.-W. Fink	044 635 5801	hwfink@physik.uzh.ch
Prof. H. Keller	044 635 5748	keller@physik.uzh.ch
Prof. J. Osterwalder	044 635 5827	osterwal@physik.uzh.ch
Prof. A. Schilling	044 635 5791	schilling@physik.uzh.ch
Prof. U.D. Straumann	044 635 5768	strauman@physik.uzh.ch

The annual reports are available on the internet: http://www.physik.uzh.ch/reports.html.

Begleitwort

Am Physik-Institut verfolgen die neun Forschungsgruppen eine Reihe von aktuellen Forschungsprojekten aus der modernen Experimentalphysik. Das breite Spektrum der Forschungsthemen reicht von der Untersuchung biologischer Systeme, über die Oberflächenphysik und die Physik magnetischer und supraleitender Materialien, bis hin zu fundamentalen Wechselwirkungen und Systemen in der Elementarteilchen- und Astroteilchenphysik. Alle Projekte wurden in enger Zusammenarbeit mit nationalen und internationalen Forschungsstätten, wie beispielsweise dem Paul Scherrer Institut, dem CERN in Genf, sowie mit in- und ausländischen Universitäten durchgeführt. Diese Forschungsarbeiten wurden neben der Universität Zürich auch vom Schweizerischen Nationalfonds, mit Drittmittelbeiträgen von nationalen und internationalen Forschungsinstituten, im Rahmen von EU-Projekten, sowie von in- und ausländischen Stiftungen unterstützt.

Dieser Jahresbericht dokumentiert die zwischen April 2010 und März 2011 erzielten Fortschritte der Forschungsgruppen des Physik-Instituts. Er ist relativ kurz gefasst und es werden nur die *Highlights* der Forschungsarbeiten der einzelnen Gruppen präsentiert, wovon ich einige Beispiele kurz erwähnen möchte.

In der Gruppe um Prof. H.-W. Fink ist es erstmals gelungen mit Hilfe einer miniaturisierten Elektronenlinse kohärente Beugungsbilder eines C-Nanotubes und eines Tabak-Mosaik Viruses aufzunehmen. In diesem Zusammenhang konnte auch gezeigt werden, dass es eine bijektive Beziehung zwischen einem Beugungsbild und einem Hologramm gibt. Dieser Isomorphismus zwischen Holografie und kohärenter Beugung erlaubt es, die Kenntnis der Streuphase aus dem Hologramm mit der hohen Auflösung des Beugungsbilds zu kombinieren. Experimente mit kohärentem Licht haben diese Beziehung bereits erfolgreich ausnutzen können. Erste Experimente mit kohärenten Elektronen und einem einzelnen Protein (Ferritin) erscheinen vielversprechend.

Neue Ergebnisse des XENON100 Experiments, an welchem die Gruppe von Prof. L. Baudis beteiligt ist, engten den erlaubten Bereich für Dunkle Materie ein. Die mit dem XENON100-Detektor im italienischen Gran-Sasso-Untergrundlabor aus hundert Tagen Messdauer mit bisher unerreichter Empfindlichkeit gewonnenen Daten lieferten keine Hinweise für die Existenz von sogenannten WIMPs (Weakly Interacting Massive Particles), den führenden Kandidaten für Dunkle Materie. Jedoch folgten aus den neuen Daten die bislang besten Grenzen in der Suche nach Dunkler Materie und die stärksten Einschränkungen für Modelle der Teilchenphysik hierzu.

Die an zwei Experimenten am Large Hardon Collider des CERN beteiligten Gruppen des Physik-Instituts (Gruppe C. Amsler am CMS und Gruppe U. Straumann am LHCb) können auf ein äusserst erfolgreiches erstes Jahr zurückblicken. Der LHC nahm im März 2010 seinen Betrieb bei vorher unerreichter Kollisionsenergie von 7 TeV auf und die Experimente haben mit den im Laufe des Jahres gesammelten Daten eine Fülle interessanter Analysen ausführen können. Das LHCb Experiment, an dem die Gruppe Straumann einen wesentlichen Beitrag leistet, hat in mehreren Analysen bereits nach den ersten Monaten eine mit den weltbesten Resultaten vergleichbare Präzision erreichen können. Für 2011 wird vom LHC eine um Grössenordnungen höhere Datenmenge erwartet, die es den beiden Experimenten ermöglichen wird, bei der Suche nach neuen Phänomenen der Elementarteilchenphysik in bislang unerforschte Regionen vorzustossen.

Besonderen Dank möchte ich dem technischen und administrativen Personal des Physik-Instituts aussprechen, welches entscheidend zum Gelingen der im Berichtsjahr ausgeführten Forschungsarbeiten beigetragen hat. Nur Dank der grosszügigen finanziellen Unterstützung von verschiedenen forschungsfördernden Institutionen konnten diese Projekte erfolgreich realisiert werden.

Der vollständige Jahresbericht wie auch die Jahresberichte früherer Jahre können auf der Website des Physik-Instituts eingesehen werden (http://www.physik.uzh.ch/reports.html). Die Forschungsprojekte des Physik-Instituts findet man auf den Websites der Forschungsdatenbank der Universität Zürich (http://www.research-projects.uzh.ch/u110.htm).

Zürich, im Mai
Prof. Dr. Hugo Keller

Mitarbeiter

Wissenschaftliches Personal

Prof. Christof	Aegerter	Phys. Systembiologie
Adrian	Aeschbacher	PTM
Dr. Ernest	Aguiló	CMS
Dr. Yves	Allkofer	AEgIS, DARWIN
Prof. Claude	Amsler	AEgIS, DARWIN, DIRAC, CMS
Dr. Jonathan	Anderson	LHCb
Sebastian	Arrenberg	CDMS
Dr. Ali	Askin	XENON
Daniel	Assmann	Phys. Systembiologie
Dr. Holger	Bartolf	PTM
Prof. Laura	Baudis	CDMS, DARWIN, GERDA, XENON
Annika	Behrens	DARWIN, XENON
Markus	Bendele	Supraleitung & Magnetismus
Dr. Roland	Bernet	LHCb
Dr. Vittorio	Boccone	ArDM
Saskia	Bosma	Supraleitung & Magnetismus
Olaf	Bossen	PTM
Dr. Tobias	Bruch	CDMS, DARWIN, GERDA, XENON
Angela	Büchler	LHCb
Albert	Bursche	LHCb
Dr. Luca	Castiglioni	Oberflächenphysik
Nicola	Chiapolini	LHCb
Prof. Vincenzo	Chiochia	CMS
William	Creus	DARWIN
Huanyao	Cun	Oberflächenphysik
Michel	De Cian	LHCb
Dr. Simon Marie	de Visscher	CMS
Dr. Jan-Hugo	Dil	Oberflächenphysik
Patrik	Donà	Oberflächenphysik
Christian	Elsasser	LHCb
Dr. Andreas	Engel	PTM
Dr. Conrad	Escher	Bio-Physik
Carlotta	Favaro	CMS
Dr. Alfredo	Ferella	DARWIN, GERDA, XENON
Prof. Hans-Werner	Fink	Bio-Physik
Francis	Froborg	GERDA
Arno	Gadola	CTA
Christopher	Geis	XENON
Giulia	Ghielmetti	Phys. Systembiologie
Prof. Thomas	Greber	Oberflächenphysik
Roman	Gredig	CTA
Michael	Greif	Oberflächenphysik
Dr. Dominik	Grögler	Bio-Physik
Henrik	Grundmann	PTM
Zurab	Guguchia	Supraleitung & Magnetismus

Wissenschaftliches Personal (cont)

Patrick	Helfenstein	Bio-Physik
Adrian	Hemmi	Oberflächenphysik
Dr. Matthias	Hengsberger	Oberflächenphysik
Ben	Huber	CTA
Kevin	Inderbitzin	PTM
Andreas	Jaeger	CMS
Colette	Janssen	Oberflächenphysik
Prof. Hugo	Keller	Supraleitung & Magnetismus
Alexander	Kish	DARWIN, XENON
Gabriel	Landolt	Oberflächenphysik
Dr. Tatiana	Latychevskaia	Bio-Physik
Dominik	Leuenberger	Oberflächenphysik
Dr. Jean-Nicolas	Longchamp	Bio-Physik
Dr. Haifeng	Ma	Oberflächenphysik
Dr. Alexander	Maisuradze	Supraleitung & Magnetismus
Dr. Aaron	Manalaysay	CTA, DARWIN, XENON
Dr. Teresa	Marrodan-Undagoitia	DARWIN, XENON
Dr. Fabian	Meier	Oberflächenphysik
Barbara	Millan Mejias	CMS
Dr. Martin	Morscher	Oberflächenphysik
Stefan	Muff	Oberflächenphysik
Dr. Katharina	Müller	H1, LHCb
Dr. Ferenc	Muranyi	Supraleitung & Magnetismus
Ulrike	Nienhaus	Phys. Systembiologie
Prof. Jürg	Osterwalder	Oberflächenphysik
Dr. Polina	Otyugova	CMS
Dr. Juan Pablo	Palacios	CMS
Dr. Christian	Regenfus	AEgIS, DARWIN
Dr. Mark	Reibelt	PTM
Mirena Ivova	Rikova	CMS
Dr. Peter	Robmann	CMS, H1, $\pi \to e\nu$
Dr. Tanja	Rommerskirchen	CMS
Dr. Josef	Roos	Supraleitung & Magnetismus
Silvan	Roth	Oberflächenphysik
Christophe	Salzmann	LHCb
Mirna	Saliba	Bio-Physik
Prof. Andreas	Schilling	PTM
Michael	Schindlberger	Phys. Systembiologie
Thomas	Schluck	Phys. Systembiologie
Dr. Alexander	Schmidt	CMS
Dr. Marc	Schumann	DARWIN, XENON
Dr. Luca	Scotto Lavina	ArDM
Dr. Nicola	Serra	LHCb
Bartosz	Slomski	Oberflächenphysik
Dr. Hella	Snoek	CMS
Dr. Olaf	Steinkamp	LHCb

Wissenschaftliches Personal (cont)

Dr. Elvira	Steinwand	Bio-Physik
Evelyn	Stilp	Supraleitung & Magnetismus
Dr. James	Storey	AEgIS, CMS
Dr. Simon	Strässle	Supraleitung & Magnetismus
Prof. Ulrich	Straumann	H1, LHCb, CTA
Michal	Tarka	GERDA
Dr. Mark	Tobin	LHCb
Dr. Andries	van der Schaaf	$\pi \to e\nu$
Dr. Jeroen	van Tilburg	LHCb
Mauro	Verzetti	CMS
Dr. Achim	Vollhardt	Elektronik, LHCb, CTA
Fabian	von Rohr	PTM
Manuel	Walter	DARWIN
Dr. Rasmus	Westerstrøm	Oberflächenphysik
Dr. Stephen	Weyeneth	Supraleitung & Magnetismus
Bastian M.	Wojek	Supraleitung & Magnetismus
Dr. Hirofumi	Yanagisawa	Oberflächenphysik

Technisches und administratives Personal

Eva	Baby	Sekretariat
Renata	Bernasconi	Sekretariat
Kurt	Bösiger	Werkstatt
Tiziano	Crudeli	Zeichnen
Denis	Dürst	Werkstatt
Daniel	Florin	Elektronik
Carmelina	Genovese	Sekretariat
Ruth	Halter	Sekretariat
Alina	Horwege	Bio-Physik
Martin	Klöckner	Oberflächenphysik
Hanspeter	Koch	Vorlesungsbetrieb
Bruno	Lussi	Werkstatt
Reto	Maier	Werkstatt
Tizian	Naterop	Werkstatt
Lucien	Pauli	Vorlesungsbetrieb
Luc	Pazeller	Oberflächenphysik
Jacky	Rochet	AEgIS, CMS, DARWIN
Monika	Röllin	Sekretariat
Dr. Jean-Pierre	Ruder	CHIPP
Sandra	Saornil Gamarra	LHCb
Marcel	Schaffner	Werkstatt
Jacqueline	Schenk	Sekretariat
Silvio	Scherr	Werkstatt
Stefan	Siegrist	PTM, Supraleitung & Magnetismus
Peter	Soland	Elektronik
Stefan	Steiner	CAD, LHCb, CTA
Michael	Weber	Vorlesungsbetrieb

Contents

Physics of Fundamental Interactions and Particles 1

1 Towards a dark matter experiment 1

2 Search for Cold Dark Matter Particles with CDMS-II 6

3 GERDA: Neutrinoless Double Beta Decay in Germanium 8

4 Cold Dark Matter Search with XENON 10

5 DARWIN: dark matter WIMP search with noble liquids 13

6 Very High Energy Gamma Ray Astronomy with CTA 16

6.1 Mirror tracking 16

6.2 Light concentrators for the FACT camera 17

6.3 FlashCam preamplifiers 18

6.4 FlashCam trigger 19

7 Testing lepton universality: the $\pi \rightarrow e\overline{\nu}$ / $\pi \rightarrow \mu\overline{\nu}$ branching ratio 21

8 Study of Coulomb-bound $\boldsymbol{\pi K}$-pairs 23

9 Particle Physics at DESY/HERA (H1) 27

9.1 D^* tagged photo- and electroproduction of charm 28

10 Particle Physics with LHCb 34

10.1 The LHCb detector 34

10.2 Detector performance and first running experience 34

10.3 Physics results 36

10.4 Summary and outlook 41

11 Particle physics with CMS 44

11.1 Commissioning of the silicon pixel detector 45

11.2 Improvements to hit and track reconstruction 45

11.3 Searches for the Higgs boson decaying into $\tau^+\tau^-$ 46
11.4 $B_s \to J/\psi\ \phi$ 47
11.5 Study of b–baryons 49
11.6 b-jet tagging 50
11.7 Preparations for the pixel detector upgrade 52

Condensed Matter Physics 54

12 Superconductivity and Magnetism 54
12.1 Search for orbital currents in superconducting $YBa_2Cu_4O_8$ 54
12.2 Iron isotope effects in the iron-based superconductor $FeSe_{1-x}$ 55
12.3 NMR study of the iron-pnictide system $EuFe_{1.9}Co_{0.1}As_2$ 57
12.4 Pressure effect on superconducting properties of $YBa_2Cu_3O_x$ 58

13 Phase transitions and superconducting photon detectors 60
13.1 Physics of superconducting thin-film nanostructures 60
13.2 First-order phase transition deep in the vortex state of $YBa_2Cu_3O_7$ 62
13.3 A.c.-calorimetry set up for vortex-shaking experiments 63
13.4 Bose-Einstein condensation of magnetic bosonic quasiparticles 64

14 Surface Physics 66
14.1 Resonant photoelectron diffraction (RXPD) 68
14.2 Symmetry protected spin structures in topological insulators 69
14.3 Ultrafast dynamics in photo-induced field emission 71

15 Physics of Biological Systems 73
15.1 Diffraction microscopy and the Oversampling Method 74
15.2 Schematic of the Coherent Electron Diffraction Microscope and experimental realization . 75
15.3 Conditions for non-destructive imaging of a single biomolecule 76
15.4 Recent achievements in coherent diffraction microscopy 76
15.5 Novel Fourier-domain constraint for Fast Phase Retrieval 77
15.6 Summary of recent achievements in Coherent Diffraction Microscopy 79
15.7 Electron column 80

16 Physical Systems Biology and non-equilibrium Soft Matter 82
16.1 Photoelastic properties of Drosophila wing imaginal discs 82
16.2 Velocity distributions in levitated granular media 85

Infrastructure and Publications 88

17 Mechanical Workshop 88

18 Electronics Workshop 92

19 Publications 95
19.1 Elementary particles and their interactions 95
19.2 Condensed matter 108

1 Towards a dark matter experiment

Y. Allkofer, C. Amsler, V. Boccone, W. Creus, A. Ferella, P. Otyugova, C. Regenfus, L. Scotto Lavina, J. Rochet

(ArDM and DARWIN Collaborations)

The interaction of Weak Interacting Massive Particles (WIMPs) with nuclei in a dark matter detector generates recoil energies below typically 100 keV. The differential cross section decreases exponentially with increasing recoil energy. This makes WIMP detection difficult due to the low energy background. Hence massive detectors with low detection thresholds are needed, among them cryogenic ones using noble liquids such as liquid argon (LAr). The Zurich group has designed and built the light readout system for the 1 ton LAr detector ArDM which is being developed at CERN. Details on the detector can be found in previous annual reports and in recent publications [1–4].

The ArDM detector was filled for the first time with 1 ton of LAr in 2009. Several important parameters such as stable cryogenic operation in high LAr purity, high scintillation light yield, and detection of events down to energies of tens of keV's could be verified. The test was performed with a partial light readout assembly consisting of half of the PMT's[1], no electric field and no charge readout. The LAr purity was found to be constant over the measurement time of three weeks by monitoring the decay time of the slow component of the light signal [3].

The measurements were done with external sources such as ^{22}Na, delivering positrons (annihilating into two 511 keV γ's) and monochromatic 1275 keV γ's. The light yield produced by one of the 511 keV γ's, following (multiple) Compton scattering, was measured by triggering with a 4" Na(Tl) crystal on the second 511 keV emitted in the opposite direction, and on the 1275 keV γ. Figure 1.1 shows the light yield distributions for the source located at two different vertical distances to the photomultiplier array [3]. The simulated distribution is shown for comparison. Good agreement is found with an average light yield of typically 0.4 p.e./keV, which is roughly half of the yield that would be obtained with a completed detector (14 PMT's)[2]. We are therefore confident to be able to reach our goal of 30 keV threshold in ArDM for WIMP detection.

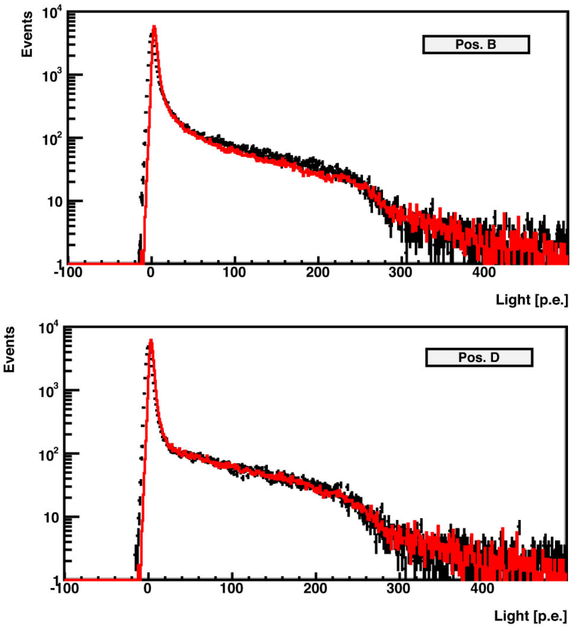

Fig. 1.1 – Light yield in the 1-ton LAr detector for 511 keV γ's (in photoelectrons, p.e.) at two positions of the ^{22}Na- source. The measurements are in black, the simulated data in red.

The light yields of nuclear recoils in LAr are poorly known, especially below 50 keV (see e.g. ref. [5]). A suitable way to produce nuclear recoils of known energies in the lab is n-Ar elastic scattering with monoenergetic neutrons, detecting the neutron as a function of scattering angle. We have therefore

---

[1] 7 Hamamatsu R5912-MOD 8" PMT's with Pt-underlay

[2] Due to quenching the light yield for nuclear recoils in the few 10 keV range is ≈30% lower than for electrons (Fig. 1.9).

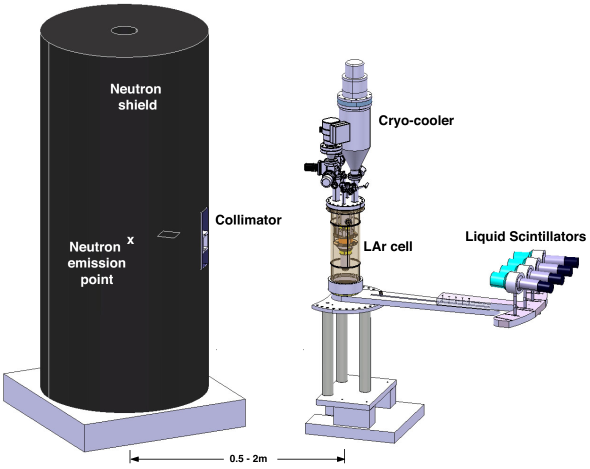

Fig. 1.2 – The neutron generator with polyester shielding, the LAr cell, the cryocooler and the four liquid scintillators detecting the scattered neutrons.

set up a scattering experiment with collimated 2.45 MeV neutrons from our $dd \rightarrow {}^3\mathrm{He}\, n$ source [6]. The target is a small ($<1\ell$) test cell (77 mm high and 74 mm in diameter) and liquid scintillation counters (LSC, EJ301 from SCIONIX) detect the scattered neutrons in coincidence as a function of scattering angle (Fig. 1.2). To reduce the measurement time we use four LSC's to cover various angles in parallel.

The fusion chamber is surrounded by a 90 cm diameter shield of borated polyester and the experiment confined within a radiation controlled fence in our laboratory at CERN. Residual radiation (mainly from scattered neutrons and X-rays) is well below the authorized limit of 2.5 μSv/h. The neutrons are collimated through a polyethylene orifice within roughly 1% × 4π sr. The neutron flux (up to 5×10^6 n/s in 4π according to specifications) is controlled through the applied high voltage and discharge current.

The neutron flux was measured with a 5" LSC located at the collimator exit. The polyethy lene collimator was surrounded by a 2 mm thick lead box against X-rays inserted into the polyester shielding. According to NSD-Fusion, the highest possible voltage and current are 100 kV, resp. 15 mA, corresponding to a flux of 10^7n/s into 4π. The flux increases proportionally to the current and to the voltage $\mathrm{V}^{2.8}$.

Measurements were made with and without polyethylene collimator and the rates corrected for the solid angle, assuming a detection efficiency of the LSC of 80%. A NIM MPD-4 module was used to discriminate between neutrons and X-rays. Figure 1.3 shows the measured neutron intensity (blue, red and orange points) compared with the values specified by NSD-Fusion (green crosses for 10mA and orange crosses for 15mA [6]). Insufficient lead shielding leads to a strong X-ray contamination. The measured flux was roughly one order magni-

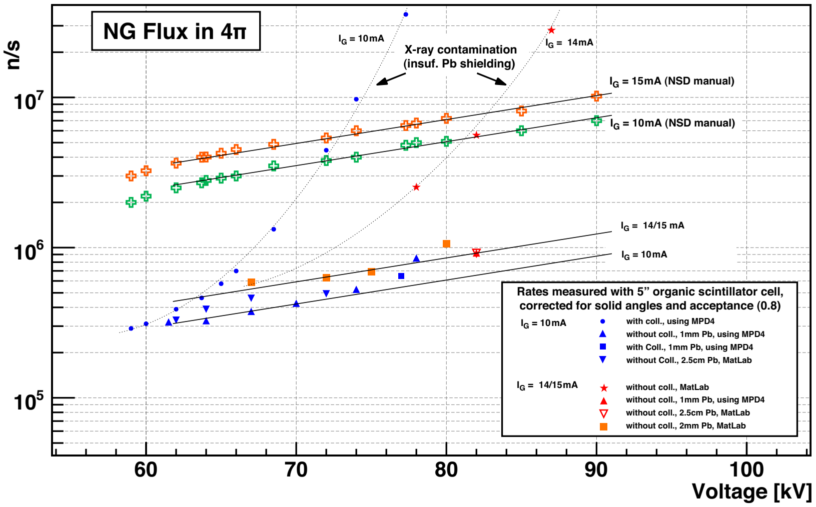

Fig. 1.3 – Neutron generator flux into 4π (see text). Lines are drawn to guide the eye.

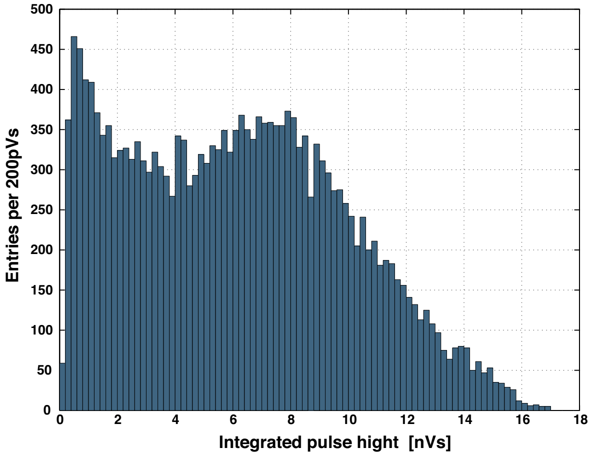

Fig. 1.4 – Raw neutron spectrum.

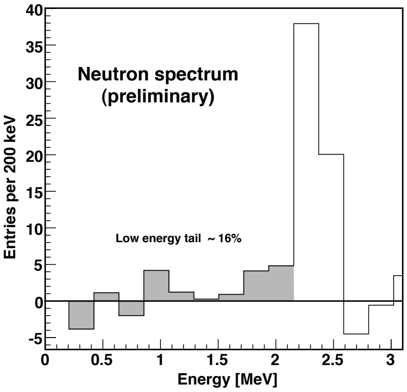

Fig. 1.5 – Neutron energy spectrum obtained by unfolding the response of the LSC.

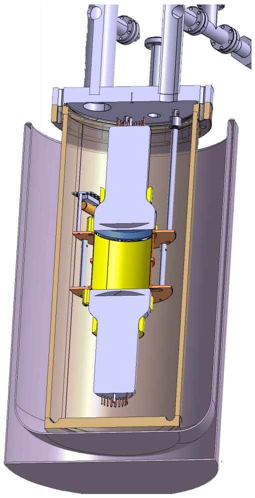

Fig. 1.6 – LAr cell with its 2 PMT's on top and bottom of the LAr volume.

tude smaller than anticipated, with a maximum of 10^6 n/s. However, the generator was upgraded recently by NSD-fusion, leading to a factor $2-3$ improvement in neutron flux.

The neutron energy distribution (smeared by collimator scattering) must be known to measure the light yield from LAr accurately. Figure 1.4 shows the neutron energy distribution measured by a 5" LSC placed at the exit of the collimator. Ideally the spectrum should be flat without collimator scattering, infinite resolution and single n-scattering. The spectrum of Fig. 1.5 was obtained by unfolding the response of the LSC. The latter was obtained with an AmBe-source, by measuring the neutron energy through the time-of-flight between the source and the neutron counter over a distance of 1 m. The start time was determined from the 4.4 MeV γ detected in a BGO crystal located close to the AmBe-source.

We have started to measure the scintillation response of LAr to nuclear recoils with the LAr cell shown in Fig. 1.6. Wavelength shifting reflectors (Tetraphenyl-Butadiene, TPB, on Tyvek foils) were mounted on the inner walls of the cell to convert the 128 nm light into 400 nm. The cell was read out by two Hamamatsu R6091-01MOD PMT's with platinum underlay for cryogenic operation. An internal ^{210}Pb-source emitted 5.3 MeV α's and up to 1.2 MeV electrons. The component ratio CR is defined as the ratio of integrated light yield during the first 50 ns to the total light yield. Thus a high CR corresponds to the emission of light with mainly the fast component. Heavily ionizing particles such as α's or nuclear recoils lead to a large CR value [7]. Figure 1.7 shows the component ratio CR from one of our first measurements of argon luminescence with the fusion generator. A clear contribution from neutron induced nuclear recoils is observed at $CR \sim 0.8$.

A first measurement of the scintillation efficiency for nuclear recoils relative to electrons was performed with a 5" LSC at 65° from the incident beam direction, at a distance of 50 cm from the LAr cell. The time-of-flight between the LAr cell and the LSC's could be determined off-line and used to remove background, e.g. from multiple neutron

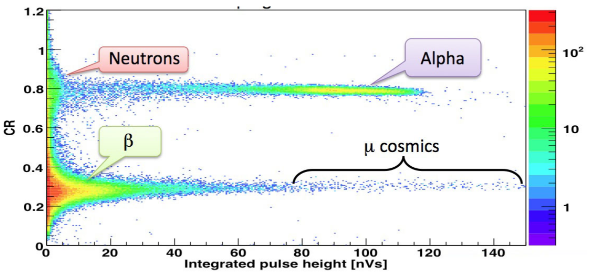

Fig. 1.7 – Component ratio CR in LAr for 2.45 MeV neutrons, 5.3 MeV α's and 1.3 MeV electrons and cosmic muons.

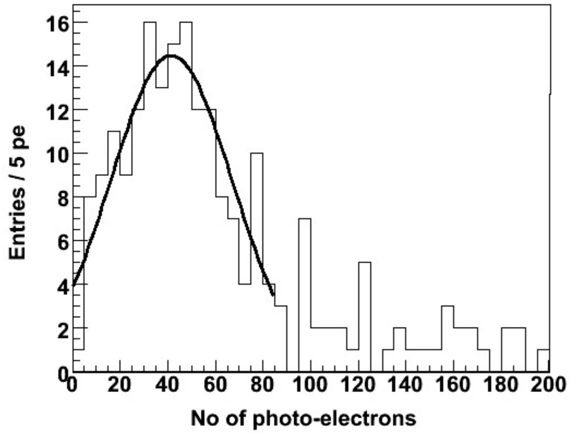

Fig. 1.8 – Integrated pulse height distribution in the LAr cell for neutron scattering at 65°.

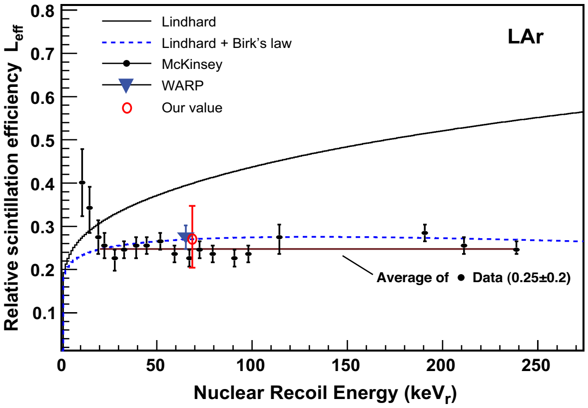

Fig. 1.9 – Relative scintillation efficiency in LAr as a function of recoil energy (from ref. [5]). Our preliminary result is shown by the red data point.

scattering in the cell. The reference time was determined with a Na-source located at equal distance from the LAr-cell and the LSC, and using the two back-to-back 511 keV γ's. At 65° the argon recoil energy is 69 keV with 2.45 MeV incident neutrons. This corresponds to a time-of-flight of 23 ns for 2.4 MeV neutrons flying to the LSC. Good pulse shape separation between proton and background (γ-induced electron recoils) could be achieved with the LSC by analogue pulse shape discrimination.

Several cuts were applied in the offline analysis. For example, we required the component ratio CR to be larger than 0.6 (see Fig. 1.7). We also rejected events close to the PMT windows by comparing the signals from the two PMT's. A time-of-flight window between 18 and 31 ns was selected. Figure 1.8 shows the pulse height distribution in LAr for 69 keV recoils. We obtained a scintillation efficiency of 0.27 (with about 25% error) in this first attempt. Figure 1.9 shows our data point compared with data from ref. [5].

Light yields of nuclear recoils are usually determined relative to electronic recoils. The electronic light yield is determined with various external γ-sources and also with a ^{83}Kr^{m} source which can be connected directly to the gaseous phase in our setup. We use a linear dependence on energy between 60 and 1062 keV, but are working on a calibration at the 122 keV line from ^{57}Co, as is the standard in the field. To improve the light yield and the measurements with radioactive sources we upgraded our LAr cell to reduce the thickness of the stainless steel vessel and the LAr volume. Tetratex foils[3] were used instead of the Tyvek reflectors, and TPB-Paraloid coating was replaced by 0.08 mg·cm^{-2} of evaporated TPB. Figure 1.10 shows the spectrum of the 60 keV line from Am-decay. During data taking the mean life of the the slow component was much lower than the established value of 1.6 μs, due to the impurity of the LAr (see e.g. ref. [3]). By extrapolating the light yield to maximum purity we could set a lower limit of 3.2 p.e./keV.

Most of the mechanical components for the final measurements are now installed in our laboratory. During the next months we will commission the gas handling system and the cryocooler (Gifford-McMahon-type) mounted on top of the LAr cell. A cooling serpentine is bonded to the temperature regulated cold head and provides the liquefaction of the recirculated gas. Gas purification is achieved by two cleaning cartridges. They reduce the O_2 and H_2O contamination in the gas below 20 ppm. A second air blower has been installed for the neutron generator to operate at maximum power. The completed system will be operational by summer 2011, ready for data taking during several weeks to accumulate enough statistics at various scattering angles. A further upgrade of the LAr cell with a smaller active volume (and less surrounding material) to reduce multiple scattering and enhance the light yield is also foreseen.

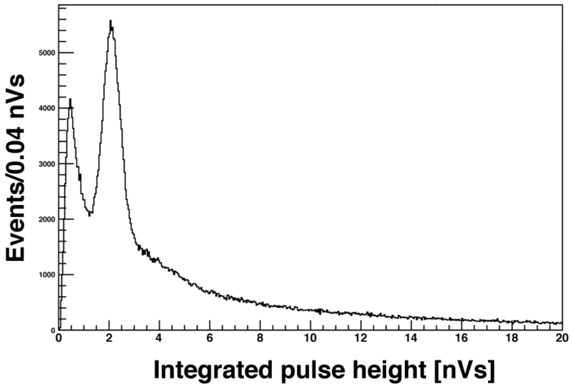

Fig. 1.10 – Energy spectrum from Am-decay measured with the refurbished LAr cell, showing the 60 keV line.

[1] C. Amsler *et al.*,
Journal of Instrumentation **3** (2008) P02001.

[2] V. Boccone *et al.*,
Journal of Instrumentation **4** (2009) P06001.

[3] C. Amsler *et al.*,
Journal of Instrumentation **5** (2010) P11003.

[4] V. Boccone,
PhD-Thesis, Universität Zürich, 2010.

[5] D. Gastler *et al.*,
arXiv:1004.0373v1 [physics.ins-det].

[6] NSD-Fusion: http://www.nsd-fusion.com.

[7] A. Hitachi *et al.*, Phys. Rev. **B 27** (1983) 5279.

2 Search for Cold Dark Matter Particles with CDMS-II

S. Arrenberg, L. Baudis, T. Bruch

in collaboration with:
Department of Physics, California Institute of Technology, Department of Physics, Case Western Reserve University, Fermi National Accelerator Laboratory, Lawrence Berkeley National Laboratory, Department of Physics, Massachusetts Institute of Technology, Department of Physics, Queen's University, SLAC National Accelerator Laboratory/KIPAC, Department of Physics, Santa Clara University, Department of Physics, Southern Methodist University, Department of Physics, Stanford University, Department of Physics, Syracuse University, Department of Physics, Texas A & M University, Department of Physics, University of California, Berkeley, Department of Physics, University of California, Santa Barbara, Departments of Physics & Elec. Engr., University of Colorado Denver, Department of Physics, University of Florida, Gainesville, School of Physics & Astronomy, University of Minnesota, Minneapolis.

(CDMS-II Collaboration)

The Cryogenic Dark Matter Search (CDMS-II) experiment operated in the Soudan Underground Laboratory a total of 19 Ge ($\sim$230 g each) and 11 Si ($\sim$105 g each) detectors at a temperature of $\sim$40 mK to search for signals from Weakly Interacting Massive Particles (WIMPs) scattering off the target nuclei. They were designed to detect the phonons and ionization from an interaction within the crystal. The ionization was lower for nuclear recoils, produced by WIMP candidates, than for electron recoils, caused mostly by background photons. Fewer than 10^{-4} of the electron recoils in the bulk of the detector were misidentified as nuclear recoils. The main source of misidentified electron recoils were events with interactions in the first few μm of the detector surfaces, which also constituted the dominant background for the CDMS-II experiment. Due to incomplete charge collection these surface events had reduced ionization. Hence, they could mimic a WIMP-nucleus interaction. Neutron background from cosmogenics and radioactive processes was much less significant.

In December 2009 the CDMS-II collaboration published the results from a WIMP search analysis that yielded the world's most stringent constraints on the spin-independent WIMP-nucleon cross section at that time [1]. Since then the collaboration has focussed on developing improved detector technologies and reanalyzing the available data with regard to WIMP models that require a refined approach in order to increase the sensitivity. We participated in the reanalysis efforts. In particular our group performed an improved search for inelastic dark matter (iDM) [2].

Inelastic dark matter scattering has been proposed as a way to resolve the tension between the DAMA claim, the observation of an annual modulation due to the movement of the Earth around the Sun [3], and results from other WIMP-search experiments [1; 4]. The inelastic scenario assumes that WIMPs can only scatter off baryonic matter by transition into an excited state at a certain energy above the ground state. The WIMP-mass splitting between the WIMP and its excited state enters the iDM scenario as an additional free parameter.

Initial constraints from CDMS on the iDM model interpretation of the DAMA claim were set using a recoil-energy range of 10–100 keV [1]. Last year we reanalysed the entire data set taken at Soudan for two main reasons: within the allowed parameter space of the iDM model the energy spectrum may reach significantly beyond the 100 keV upper threshold used in the analysis, hence an extension to 150 keV increases the sensitivity. Moreover, the expected rate drops to zero for low recoil energies, in contrast to the elastic-scattering case. Since most of the dominant surface-event background occurred at energies just above our

10 keV threshold [5], where no iDM signal is expected, the sensitivity could be further enhanced by defining a looser surface-event rejection cut based upon the estimated background with recoil energy between 25 keV and 150 keV. The final surface-event background was calculated to be $0.8^{+0.5}_{-0.3}$(stat.)$^{+0.3}_{-0.2}$(syst.) given the exposure of 969 kg·days.

After fixing all event selection criteria, the signal region was "unblinded". We observed three WIMP candidates between 25 keV and 150 keV, at 37.3 keV, 73.3 keV and 129.5 keV, the latter occurring above the analysis range from previous analyses. The probability to observe three or more background events in this energy range including the surface-event background and the much lower neutron background is 11%, which is low but not negligible. Thus, this analysis does not constitute a significant detection of WIMP scattering.

Constraints emerging from this analysis are shown in Fig. 2.1. The only remaining parameter space allowed by CDMS data is within a narrow region at WIMP masses of $\sim$100 GeV/c^2 and WIMP-mass splittings between 85 keV and 135 keV. Due to the occurrence of the three candidate events between 25 keV and 150 keV the constraints on the iDM parameter space are slightly weaker than from our previous analysis for which no events were observed at intermediate energies where the rate is expected to peak. Though this analysis was performed with regard to the iDM scenario, the expansion of the analysis range to 150 keV could be useful to test other models predicting a signal at tens of keV recoil energy. A preprint discussing this analysis [6] was submitted to PRD.

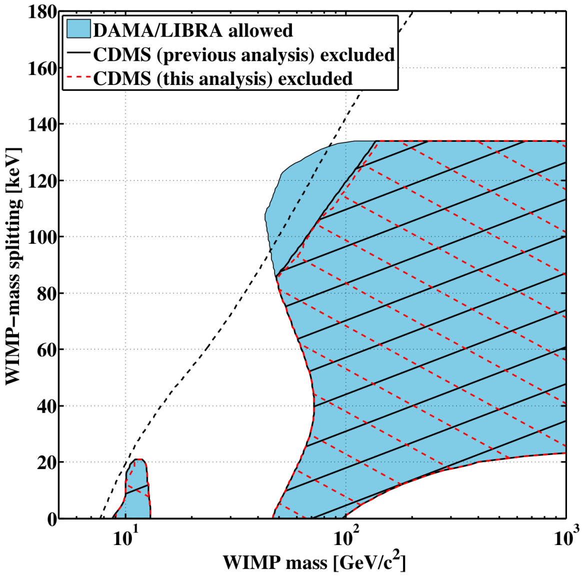

Fig. 2.1 – The blue/shaded regions represent WIMP masses and WIMP-mass splittings for which cross sections exist that are compatible with the modulation spectrum observed by DAMA/LIBRA at 90% C.L. The hatched regions show constraints on these parameters from the reanalysis (red/dashed) and from our previous analysis (black/solid) [1]. The black/dashed line represents the maximum reach of the CDMS-II experiment.

[1] Z. Ahmed *et al.* (CDMS II), Science **327**, 1619 (2010).

[2] D. Smith and N. Weiner, Phys. Rev. D **64**, 043502 (2001).

[3] R. Bernabei *et al.* (DAMA), Eur. Phys. J. C **67**, 39 (2010).

[4] E. Aprile *et al.* (XENON100), arXiv:1104.2549 [astro-ph.CO].

[5] Z. Ahmed *et al.* (CDMS II), Phys. Rev. Lett. **102**, 011301 (2009).

[6] Z. Ahmed *et al.* (CDMS II), arXiv:1012.5078 [astro-ph.CO].

3 GERDA: Neutrinoless Double Beta Decay in Germanium

L. Baudis, T. Bruch, A. Ferella, F. Froborg, M. Tarka

in collaboration with:
INFN Laboratori Nazionali del Gran Sasso LNGS, Institute of Physics, Jagellonian University Cracow, Institut für Kern- und Teilchenphysik Technische Universität Dresden, Joint Institute for Nuclear Research Dubna, Institute for Reference Materials and Measurements Geel, Max Planck Institut für Kernphysik Heidelberg, Universitá di Milano Bicocca e INFN Milano, Institute for Nuclear Research of the Russian Academy of Sciences, Institute for Theoretical and Experimental Physics Moscow, Russian Research Center Kurchatov Institute, Max-Planck-Institut für Physik München, Dipartimento di Fisica dell Universitá di Padova e INFN, Physikalisches Institut Eberhard Karls Universität Tübingen

(Gerda Collaboration)

During the past decades, neutrino oscillation experiments have established that neutrinos can change their flavor eigentstate while propagating over macroscopic distances. The interpretation of these observations is that neutrinos have mass and that, like in the quark sector, the mass eigenstates are different from the weak eigenstates, i.e. neutrinos mix. The aim of ongoing research is to determine the full mixing matrix of neutrinos, including CP violating phases, to clarify the Dirac or Majorana nature of neutrinos, and to fix their absolute mass scale. The observation of the neutrinoless double beta ($0\nu\beta\beta$) decay would prove that the neutrino is a Majorana fermion and that lepton number is violated. The measurement of its rate would provide information on the effective Majorana neutrino mass.

Fig. 3.1 – Mock-up of the GERDA setup situated underground at LNGS. Currently, a string with three natural Ge-detectors is inside the cryostat. Enriched ^{76}Ge detectors are installed this year.

GERDA is an experiment to search for the $0\nu\beta\beta$ decay in enriched ^{76}Ge detectors (Q-value $Q = (2039.006 \pm 0.050)$ keV), using a novel shielding concept. Bare germanium diodes are operated in a 65 m^3 cryostat filled with liquid argon and surrounded by a 3 m water Cerenkov shield. The aim of GERDA is to scrutinize the claim of a discovery of neutrinoless double beta decay [1] and to reach a sensitivity of 270 meV for the effective Majorana mass. In a second phase, a background index of 10^{-3} events/(keV kg y) shall be reached, which is two orders of magnitude lower than achieved so far. This will allow to probe half-lifes of about $T_{1/2} = 1.4 \times 10^{26}$ y at 90% CL with an exposure of 100 kg·y, and to reach a sensitivity of 110 meV for the effective Majorana mass.

The construction phase of GERDA at the Gran Sasso Underground Laboratory (LNGS) has been completed (see Fig. 3.1) and the commissioning with a first string of three natural Ge detectors started in summer 2010. Data taking with existing enriched ^{76}Ge detectors will start in mid 2011.

Our group is responsible for the full calibration system of the experiment. For energy as well as pulse shape calibration of the enriched Ge detectors, three ^{228}Th sources are to be used. During a calibration run, the sources are lowered by several meters from their parking position on top of the cryostat down to the detectors. Since the sources stay inside the cryostat to prevent radon entering the system, they are placed on tantalum cylinders to properly shield the detectors from their radiation during physics runs. The sources have been custom made by our group, with the assistance of PSI, in order to suppress potential (α, n) reactions in the source materials, which might contribute to the GERDA background.

For the current commissioning phase, a manual calibration system, partly designed and built at UZH, is used. A new, automated system for three sources and with two redundant positioning methods is currently being built in Zurich.

Weekly runs with the sources in position ensure the frequent monitoring of the energy calibration and resolution of the individual germanium diodes which is necessary when combining the data from several diodes over long measuring periods. An iterative automated calibration routine has been developed by us. It uses three alternative energy reconstruction algorithms and is now accepted as standard by the collaboration.

Figure 3.2 shows the variations in the observed position of the single escape peak of the ^{208}Tl line at 2103.5 keV over a period of several months. This energy is close to the $0\nu\beta\beta$ transition energy of (2039.006 ± 0.050) keV [2]. All three diodes currently mounted in the cryostat show excellent stability with deviations from the nominal value below ±0.5 keV.

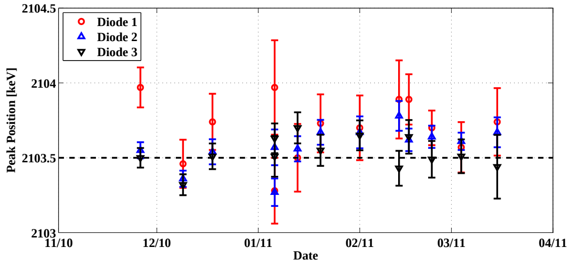

Fig. 3.2 – Long term fluctuations of the energy calibration of three natural Ge detectors currently operated in GERDA using the single-escape peak of the 2614.5 keV ^{208}Tl transition at 2103.5 keV. The observed variations are within 0.5 keV.

A general-purpose MySQL relational database has been developed in order to collect the calibration information and the analysis routine will be part of the GERDA analysis framework.

In summer 2010 the GERDA collaboration has decided to deploy Broad Energy Germanium (BEGe) detectors for the second phase of GERDA. Initial studies had shown that the pulse shape discrimination capabilities of these detectors allow to suppress a high fraction of the expected background in the region of interest for $0\nu\beta\beta$ [3]. To demonstrate that working detectors can be produced from enriched Ge, a full production-chain validation has been performed [4] and five detectors were manufactured. Our group was involved in this process, along with a few other GERDA institutions.

A test campaign with these depleted BEGe detectors is ongoing at LNGS in order to characterize the crystals in terms of their active volume, charge collection and pulse shape discrimination performance. The dead layer of a detector confines its active volume and suppresses external backgrounds. Hence a precise knowledge of the crystal dead layers is essential before they will be operated in GERDA. We are involved in these tests, which scans the detector surface with collimated low-energy γ-rays to determine the dead layer, and use the 1.33 MeV line of ^{60}Co to determine the active volume. The Monte Carlo simulations, required for the data analysis, are currently ongoing at UZH. Our group will be further involved in the production and testing of the enriched BEGe diodes, in collaboration with the other GERDA institutions, and negotiations for the production of 20 kg of enriched Ge detectors have started.

[1] H.V. Klapdor-Kleingrothaus *et al.*,
Phys. Lett. B 586, 198-212 (2004).

[2] G. Douysset *et al.*,
Phys. Rev. Lett. 86, 4259 (2001).

[3] D. Budjas *et al.*, JINST 4, P10007 (2009).

[4] M. Agostini *et al.*,
Nucl. Phys. B Proc. Suppl. (2010).

4 Cold Dark Matter Search with XENON

A. Askin, L. Baudis, A. Behrens, T. Bruch, A. Ferella, C. Geis, A. Kish, A. Manalaysay, T. Marrodan Undagoitia, M. Schumann

in collaboration with:
Columbia, UCLA, INFN, University of Münster, University of Coimbra, Subatech, Weizmann Institute, University of Mainz, SJTU, MPIK Heidelberg, Rice University, University of Bologna, Nikhef

(XENON Collaboration)

The XENON program is focussed on the direct detection of Weakly Interacting Massive Particles (WIMPs) [1], which are candidates for the dark matter in the Milky Way. XENON employs time projection chambers (TPCs) which are filled with cryogenic liquid xenon (at about $-90°$C) as target material. Operated in two-phase (liquid/gas) mode, simultaneously reading light and charge signals from scintillation and ionization, respectively, the TPC provides 3-dimensional interaction vertex reconstruction on an even-by-event basis and efficient discrimination against background signals from γ or β decays in the detector materials or the experiment's surroundings.

The XENON100 detector is taking data at the Gran Sasso Underground Laboratory (LNGS) since 2009. First results from data recorded during an early 11.2 days commissioning run have revealed that XENON100 suffers hundred times less background than any other direct dark matter detection experiment [4]. No event candidates were observed in the WIMP region and the derived upper limits on spin-independent WIMP-nucleon cross sections were the lowest obtained so far [3]. Figure 4.1 compares the measured background spectrum with a simulated spectrum accounting for the known intrinsic radioactive contaminations of all materials used for the detector. Most background measurements have been performed with the low background germanium spectrometer (HPGe) Gator [4], which is operated at LNGS by our group.

The background of this instrument, shown in Fig. 4.2, is very low and comparable to the best HPGe detectors available. Gator, however, provides a larger sample cavity, a necessary requirement to measure tiny radioactive contamination in raw materials for detector construction, such as copper, titanium, stainless steel, and PTFE (Teflon). In the bottom part, Fig. 4.2 shows the deconvolution of the background spectrum into the contribution from different materials, derived by a best fit method from the measured data [4].

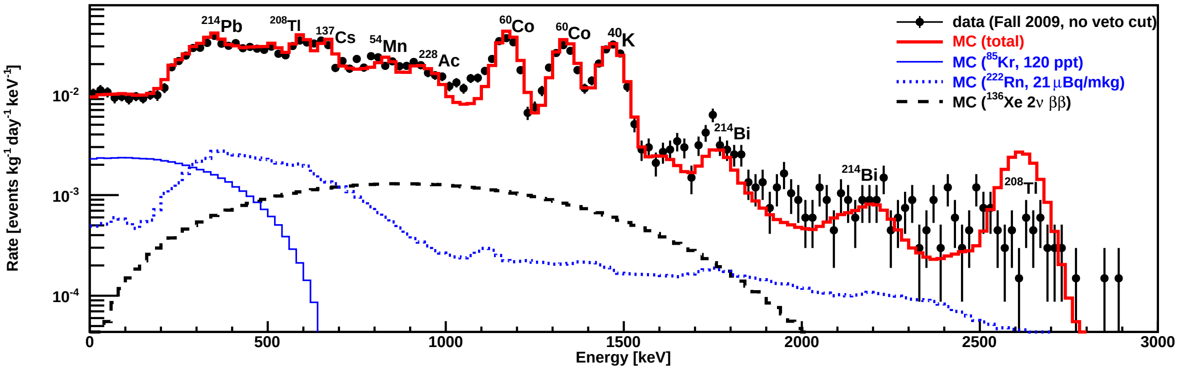

Fig. 4.1 – Measured background spectrum of XENON100 during the comissioning run [3] nicely reproduced by a detailed Monte Carlo study of the detector and shield.

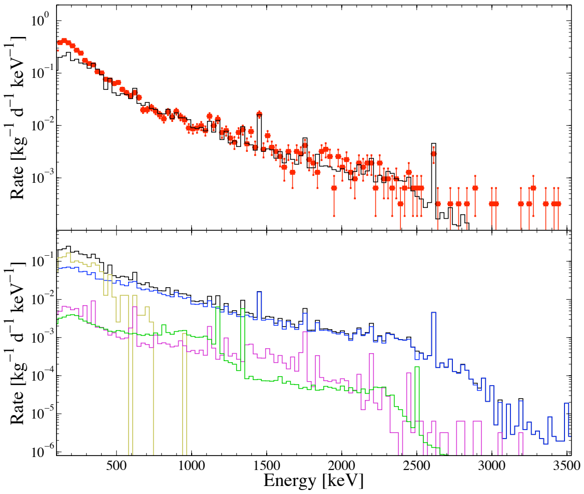

Fig. 4.2 – Top: background spectrum of the low background germanium spectrometer Gator, together with a best fit from a Monte Carlo study. Bottom: Decomposition into the contributions from various materials: natural radioactivity in Cu (blue), cosmogenic radio-nuclides in Ge and Cu (green), ^{222}Rn decays inside the shield (magenta), and ^{210}Pb in the Pb shield (yellow).

The increased sensitivity of XENON100 and all future detectors requires improved analysis techniques. For the first time in dark matter searches, the Profile Likelihood method, commonly used in high energy physics, has been applied [5]. The method properly accounts for known systematic uncertainties and makes a quantitative statement about the likelihood of the observation to be just background or to include a signal.

The results of a much larger data set of 100.9 life days, taken in the first half of 2010, have been published recently [3]. Three events were observed in the pre-defined WIMP search region between 8.4 keV and 44.6 keV for the nuclear recoil energy with an expected background of (1.8 ± 0.6) events. The resulting upper limit on the spin-independent WIMP-nucleon scattering cross section is well below all previous results which severely constrains the interpretation of the DAMA and CoGeNT results [7] as being due to light mass WIMPs (Fig. 4.3). Moreover, it enters the sensitivity region for supersymmetric WIMP dark matter accessible at the LHC [8].

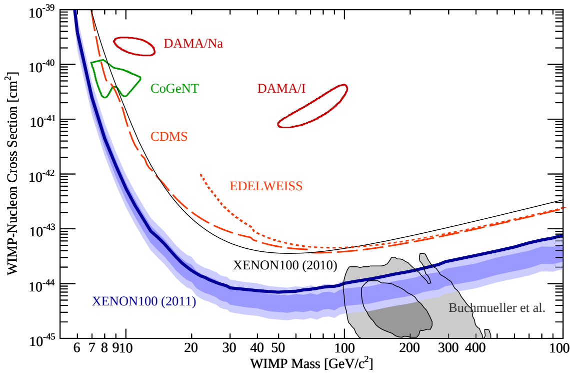

Fig. 4.3 – Thick blue line: 90% CL upper limit on the spin-independent WIMP-nucleon scattering cross section from 100.9 days of XENON100 data [3]. Blue shaded region: expected sensitivity for the exposure in absence of a WIMP signal. Thin black curve: XENON100 limit from the comissioning run [3].

XENON100 is in continuous operation at LNGS with a new dark matter run that started in March 2011. The next phase, XENON1T, is expected to enter its construction phase in Fall 2011. Our group is responsible for data acquisition and electronics and for the design and manufacturing of the inner detector structure. We also test new low-radioactive light sensors.

Besides the R&D activities for XENON1T and within the DARWIN project [9], the research performed in our laboratory is focused on understanding the properties of liquid xenon as dark matter target, in particular at lowest energies. The neutral WIMPs would interact with the xenon nuclei, resulting in nuclear recoils. The dominant γ and β backgrounds involve electromagnetic interactions with the atomic electrons, generating electron recoils. The energy range for all these processes will be extended towards lower energies in the XÜRICH detector [10] which is filled with about 3 kg of xenon. The measurement of the electronic recoil scale, which is completely unknown below 9.4 keV, is ongoing. The study of the nuclear recoil scale will follow as soon as the new neutron facility at UZH becomes available.

[1] B.W. Lee and S. Weinberg, Phys. Rev. Lett. 39, 165 (1977).

[4] E. Aprile *et al.* (XENON100), Phys. Rev. D 83, 082001 (2011).

[3] E. Aprile *et al.* (XENON100), Phys. Rev. Lett. 105, 131302 (2010).

[4] L. Baudis *et al.*, submitted to JINST, arXiv:1103.2125 (2011).

[5] E. Aprile *et al.* (XENON100), submitted to Phys. Rev. D, arXiv:1103.0303 (2011).

[3] E. Aprile *et al.* (XENON100), submitted to Phys. Rev. Lett., arXiv:1104.2549 (2011).

[7] C.E. Aalseth *et al.* (CoGeNT), Phys. Rev. Lett. 106, 131301 (2011); C. Savage *et al.*, JCAP 0904, 010 (2009).

[8] O. Buchmueller *et al.*, arxiv:1102.4585 (2011).

[9] L. Baudis (DARWIN), arXiv:1012.4764 (2010) http://darwin.physik.uzh.ch ./

[10] A. Manalaysay *et al.*, Rev. Sci. Instrum. 81, 073303 (2010).

5 DARWIN: dark matter WIMP search with noble liquids

Y. Allkofer, C. Amsler, L. Baudis, A. Behrens, T. Bruch, W. Creus, A. Ferella, A. Kish, A. Manalaysay, T. Marrodán Undagoitia, C. Regenfus, M. Schumann, M. Walter

in collaboration with:
ETHZ, INFN, University of Münster, Subatech, Weizmann Institute, University of Mainz, MPIK Heidelberg, Rice University, University of Bologna, Nikhef, Karlsruhe University, Columbia, UCLA, Princeton (DARWIN Consortium)

DARWIN [1] is an R&D and design study for a facility to detect dark matter induced signals by observing the charge and light produced in multi-ton scale liquid noble gas targets, using techniques which have already been successful in 10 kg-100 kg detectors [2–4], and which soon will be studied at the ton-scale. The goal is to probe the spin-independent WIMP-nucleon cross section well below 10^{-47}cm^2 (10^{-11}pb), which is three orders of magnitude beyond the current best limits. In conjunction with other WIMP targets, with indirect searches and with the LHC, DARWIN should allow us to learn not only about the WIMP properties, but also about their density and velocity distribution in our local vicinity in the Milky Way.

Approved by ASPERA [5] in late 2009, the DARWIN study has officially started in April 2010, and a Technical Design Study is expected to become available by early 2013. The letter of intent and the proposal for the construction of the facility would be submitted by mid and late 2013, respectively, with the construction and commission phases scheduled for 2014-2015. The period of operation and physics data taking is foreseen for 2016-2020.

Recent results from noble liquid detectors have shown that these offer a promising technology to push the sensitivity of direct WIMP searches far beyond existing limits into the regime of favored theoretical predictions. To support the dark matter interpretation, measurements of the interaction cross section for different targets are mandatory [6]. Liquid argon (LAr) and xenon (LXe), having high charge and light yields for nuclear recoils expected from WIMP-nucleus scattering, are excellent WIMP targets. A noble liquid Time Projection Chamber (TPC) is a scalable, large, self-shielding, homogeneous and position sensitive WIMP detector. The relative size of the charge and light signals, as well as their timing allows efficient discrimination against electron recoil events, while good spatial resolution helps to identify the neutron background.

Operating a LAr and a LXe target under similar experimental conditions would allow to better constrain the WIMPs mass (see Fig. 5.1), and to distinguish between spin-independent and spin-dependent couplings (^{40}Ar has no spin, while natural xenon contains 26.4% ^{129}Xe and 21.2% ^{131}Xe with $1/2^+$ and $3/2^+$ ground states, respectively). From a technical point of view, there are many

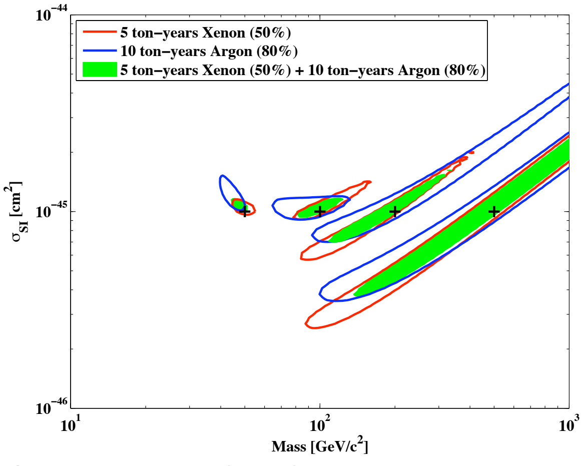

Fig. 5.1 – Spin-independent WIMP-nucleon cross section versus WIMP mass for benchmark scenarios of 10^{-45}cm^2 (10^{-9}pb) and four WIMP masses (+ symbols). Also shown are the 1-σ constraints for exposures of 5 t year in LXe (assuming 50% acceptance of nuclear recoils) and 10 t year in LAr (assuming 80% acceptance of nuclear recoils), as well as the combined result.

common aspects to LAr and LXe dark matter TPCs, such as cryostat design, charge and light readout, purification of noble liquids, HV system for the drift field, field uniformity and charge extraction, use of ultra-low radioactivity materials and shields as well as the underground infrastructure and safety aspects.

DARWIN unites the ample expertise in Europe on liquid noble gas detectors, low-background techniques, cryogenic infrastructures, underground infrastructures and shields as well as on the physics related to the direct detection of WIMPs. Connections among the participating institutions are established through several work packages, such as:

- design of cryostat, inner TPC, high-voltage and cryogenic systems based on the experience gained by existing LAr and LXe experiments,
- study of novel, high quantum-efficiency and low-radioactivity light sensors and UV light collection schemes,
- study of the light and charge yields of electronic and nuclear recoils at low energies,
- study of new concepts to read out the ionization signal, such as large-area thick gas electron multipliers (GEMs), large-area gaseous photomultipliers (GPM) and CMOS pixel detectors coupled to electron multipliers,
- study of low-noise, low-power and cost-effective electronics for light and charge read-out, as well as new DAQ and data processing schemes,
- optimization of noble gas purification procedures concerning water and electronegative impurities and radioactive isotopes such as ^{39}Ar, ^{85}Kr and ^{222}Rn; studies of material outgassing, liquid handling and purity monitoring procedures,
- material selection and process control needed for ultra-low background operation; exploration of optimal underground locations and cost-effective shielding.
- study of the scientific impact and establishment of a framework in which results from indirect dark matter searches, cosmology and the LHC can be combined with direct dark matter searches; asses the impact of potential results on astrophysics.

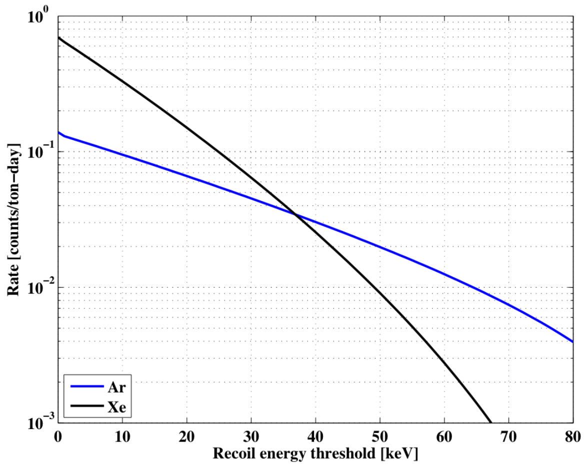

Fig. 5.2 – Event rates in LAr and LXe as a function of energy threshold for a WIMP-nucleon cross section of 10^{-45}cm^2 and a WIMP mass of 100 GeV/c^2.

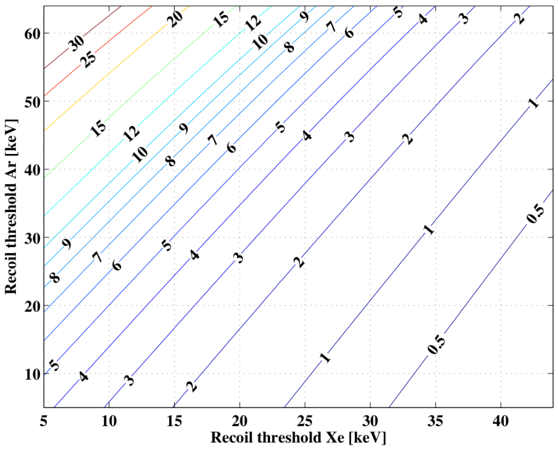

Fig. 5.3 – The detector mass scaling factor between argon and xenon for achieving a similar sensitivity to a standard WIMP as a function of the thresholds on the nuclear recoil energy.

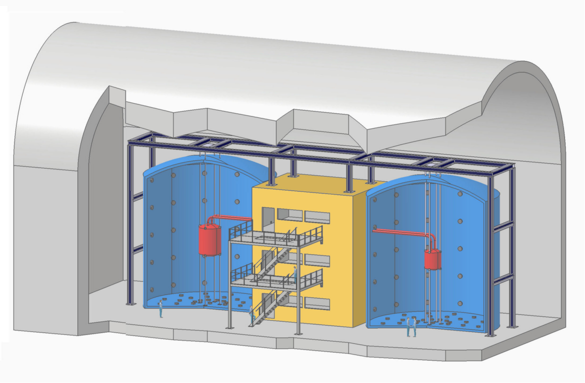

Fig. 5.4 – A preliminary sketch of the DARWIN facility, which would operate 20 t (10 t) and 8 t (5 t) of total (fiducial) argon and xenon mass in double-walled cryostats immersed in large water Cerenkov shields.

The final configuration and the size of DARWIN are under study. The optimal choice of the fiducial mass for the two target materials is a function of detector-dependent quantities such as energy thresholds and WIMP parameters like mass and interaction cross section. Figure 5.2 shows the event rates in LAr and LXe as a function of energy threshold for a WIMP-nucleon cross section of 10^{-45}cm^2 and a WIMP mass of 100 GeV/c^2. Figure 5.3 shows the detector mass scaling factor between the two targets for achieving a similar sensitivity to a standard WIMP that interacts predominantly via coherent scattering on nuclei, as a function of energy thresholds.

To study the physics reach of the facility, we assume as benchmark scenarios fiducial masses of 10 t and 5 t for the LAr and LXe components, respectively, corresponding to roughly 20 t and 8 t of total argon and xenon mass (a preliminary sketch of DARWIN is shown in Fig. 5.4). Figure 5.5 shows the sensitivity to the spin-independent WIMP-nucleon cross section as a function of exposure for a WIMP mass of 100 GeV/c^2 and a nuclear recoil energy window of 30-100 keV and 10-100 keV in LAr and LXe, respectively. It also displays the number of events that would be detected for a WIMP-nucleon cross section of 10^{-44}cm^2 (10^{-8}pb) in the same energy windows. The assumptions for LXe are the following: a raw background of 10^{-4} events kg^{-1}day^{-1} keV^{-1}, which is a factor of 100 below the current XENON100 background [4], a 99.9% rejection of electronic recoils based on the ratio of the charge and light signals, and a 50% acceptance for nuclear recoils. For LAr, the assumptions are: a raw background of 0.45 events kg^{-1}day^{-1} keV^{-1}, with a factor of 10^8 rejection of electronic recoils based on pulse shape analysis and the charge-to-light ratio, a reduction of the ^{39}Ar rate by a factor of 25 relative to atmospheric argon (corresponding to an activity of 40 mBq/kg for ^{39}Ar) and a 80% acceptance for nuclear recoils.

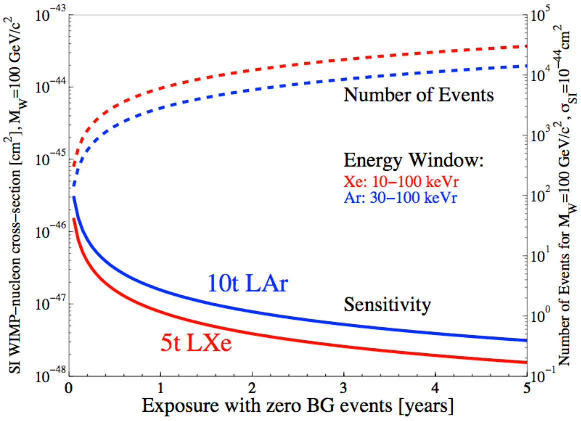

Fig. 5.5 – The sensitivity to the spin-independent WIMP-nucleon cross section as a function of exposure for 10 t LAr and 5 t LXe, for a WIMP mass of 100 GeV/c^2 and zero background events for a given exposure (left y-axis). The dashed lines show the number of events that would be detected for a WIMP-nucleon cross section of 10^{-44}cm^2 (right y-axis).

[1] L. Baudis (DARWIN), Proceedings of Science, PoS(IDM2010)122 (2010), arXiv:1012.4764 (2010), http://darwin.physik.uzh.ch/

[2] E. Aprile *et al.* (XENON100 Collaboration), Phys. Rev. Lett. **105**, 131302 (2010).

[3] E. Aprile *et al.* (XENON100), submitted to Phys. Rev. Lett., arXiv:1104.2549 (2011).

[4] E. Aprile *et al.* (XENON100), Phys. Rev. D **83**, 082001 (2011).

[5] http://www.aspera-eu.org/

[6] M. Pato, L. Baudis, G. Bertone, R. R. de Austri, L. E. Strigari and R. Trotta, Phys. Rev. D **83**, 083505 (2011).

6 Very High Energy Gamma Ray Astronomy with CTA

D. Florin, A. Gadola, R. Gredig, B. Huber, A. Manalaysay, S. Steiner, U. Straumann, A. Vollhardt

in collaboration with: University of Geneva, EPFL Lausanne, ETH Zürich, Jagiellonian University Cracow, MPI für Kernphysik Heidelberg, University of Leeds, Universität Tübingen.

The full CTA collaboration consists of 115 institutes from 23 countries.

(CTA)

The Cherenkov Telescope Array (CTA) is a planned next generation array of Imaging Atmospheric Cherenkov Telescopes (IACTs), and is the successor to the current generation of IACTs including MAGIC [1], H.E.S.S [2], and VERITAS [3]. These telescopes are used to detect Very High Energy (VHE) gamma ray photons, in the range of tens of GeV to tens of TeV, emitted from exotic (i.e. non-thermal) astrophysical sources such as quasars, supernovae and their remnants, gamma-ray bursts, and dark matter annihilations. When these gamma rays enter the Earth's upper atmosphere, they are converted to an electron-positron pair, with the two particles together sharing the energy of the parent gamma ray. The electron and positron trigger an electromagnetic shower containing many highly-energetic charged particles. Many of these particles travel at speeds exceeding the speed of light in the atmosphere, and as a result produce Cherenkov photons that travel in a cone to the ground. The IACTs detect these Cherenkov photons and can reconstruct the structure of the electromagnetic shower by viewing the shower from multiple telescopes, and by analyzing the time structure of the photon arrival times. The reconstructed electromagnetic shower can then be used to determine the direction and energy of the initial gamma ray that was incident upon the upper atmosphere.

CTA is currently in a phase of heavy research and development. The goal is not to build larger versions of the current IACTs arrays listed above, but to build *improved* versions based upon lessons learned from current experience, and also by exploiting new technologies that have arisen in the years since the current IACTs were designed. Efforts at UZH towards this goal include modular and distributed clock generation techniques (see Sec. 18), primary mirror alignment,optical components of the first Geiger-mode Avalanche Photodiode IACT camera, and a first fully-digital IACT camera.

6.1 Mirror tracking

The primary mirror of these telescopes is made up of many individual mirror segments. Our group is designing a fast and reliable tracking system that orients the individual mirror segments with an accuracy that fits the severe optical quality requirements.

The system makes use of a standard digital (CMOS) camera situated in the focal plain of the telescope. While the telescope is pointing to a bright light source (e. g. a star) the orientation of each mirror segment is optimised by maximizing apparent brightness of the mirror image.

To analyze the optical behavior and determine the prerequisites to align an entire telescope, a simulation-tool has been developed that is able to control parameters like the mirror PSF, mirror orientation, lens orientation/position and light source intensity. The resulting camera view can also be simulated (Fig. 6.1). With the help of this simulation the response can be estimated when a certain parameter is changed.

A test setup has been built at the UZH to optimize the alignment algorithm and test the camera usage.

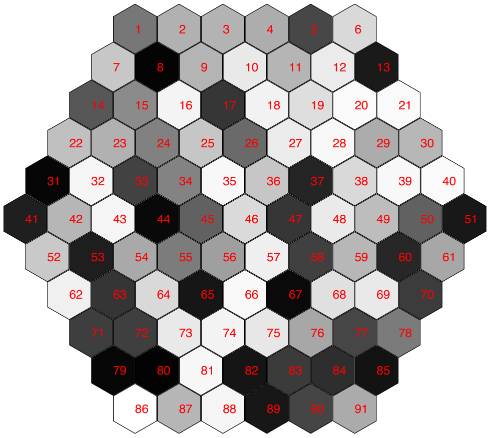

Fig. 6.1 – Example of a CTA-like telescope simulation with a camera in the focal plain and randomly aligned mirrors. Each hexagon represents an individual mirror segment.

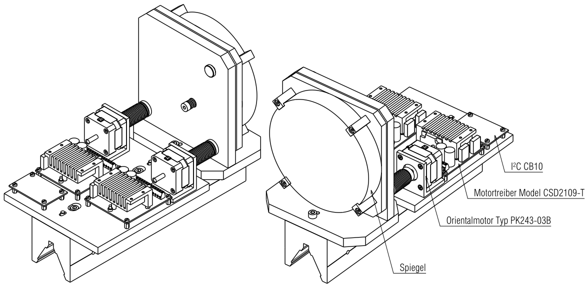

Fig. 6.2 – Schematics of the mirror mount.

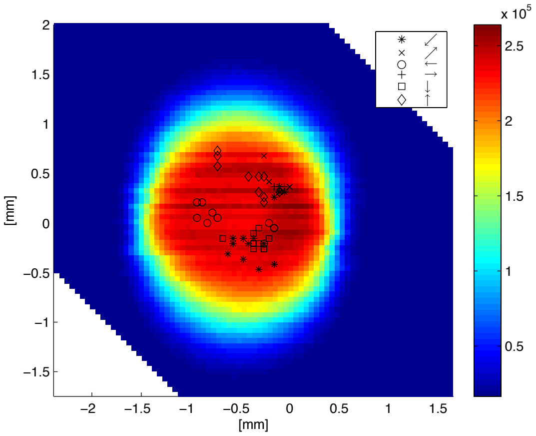

Fig. 6.3 – Results of a simulation cycle showing the illumination intensity of the camera depending on the mirror orientation (a. u.). The black symbols show the position found by the algorithm after displacing the mirror in the direction indicated by the arrows.

A spherical mirror of 6 inch diameter with a focal length of 1.5 m is installed on a mount where the tilt can be adjusted with the help of three positioning screws. Two of these screws are connected to stepping motors (Fig. 6.2) controlled by a complete embedded computer connected through a I^2C bus to the camera and capable of executing the scan algorithm. The system has been successfully tested and can deal with a noisy source or with a temporary blackout. For this test the light from an antenna-tower at about 2 km distance has been used as a light source. Figure 6.3 shows an example of the camera's response to different mirror positions. The optimal positions found by the algorithm while realigning the mirror are also shown.

6.2 Light concentrators for the FACT camera

Light incident on the telescope's primary mirror is reflected towards the mirror's focal plane where the pixelized camera is located. The desired field of view of the telescope which extends typically 1.5 to 2 m sets the scale of the camera. It is not practical to completely cover this area with photosensors. Instead, the single pixels are equipped with light concentrators which results in an almost full coverage. Current imaging air Cherenkov telescopes, like HESS and MAGIC, use compound parabolic concentrators, so-called Winston cones. They have a hollow body covered with reflective foils at the inner walls and are combined with photomultiplier tubes as photosensors. The CTA Group at UZH, in close cooperation with ETH Zurich, has contributed extensively to the development of parabolic solid light concentrators which make use of total internal reflection. These are made of injection-moulded polymethyl methacrylate and interface a hexagonal entrance to a square exit area tailored to the sensitive area of novel commercial 3x3 mm^2 Geiger-mode avalanche photodiodes (GAPD) (see. Fig. 6.4) which so far have not been used in IACTs. The increased areal

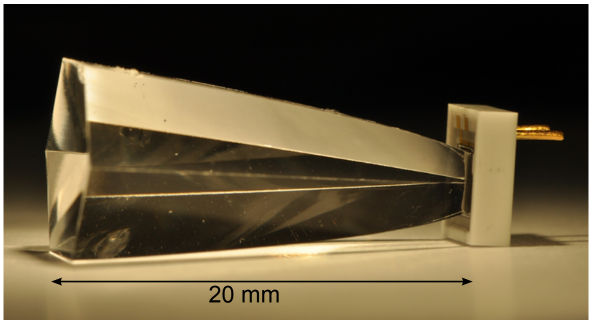

Fig. 6.4 – A light concentrator optically glued to a GAPD. The length of the concentrator is 20 mm. The 2.8x2.8 mm^2 exit area matches the GAPD's sensitive area of 3x3 mm^2.

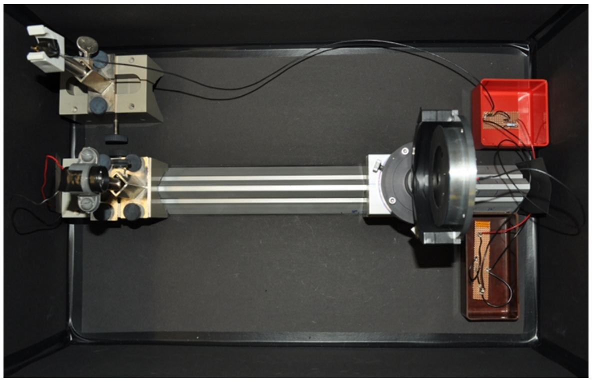

Fig. 6.5 – Top view of the goniometer test setup built to quantify the performance of the light concentrators.

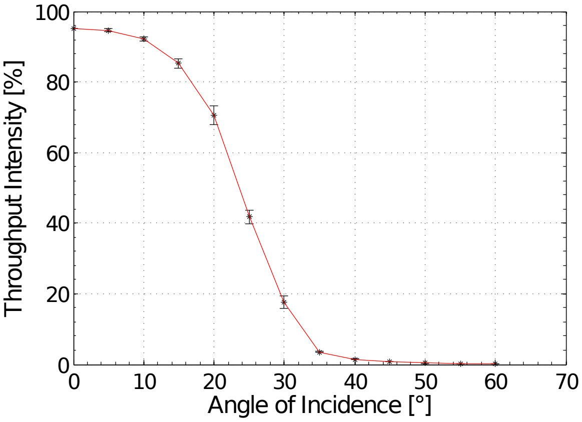

Fig. 6.6 – The light transmission of the light concentrator as a function of the zenith angle of incident photons. The shaded area indicates the angles subtended by the primary mirror.

acceptance can only be achieved at the cost of a reduced angular acceptance (see Fig. 6.6) which, in fact, is an advantage since which is effectively cut at $\sim 20°$ with the advantage of drastically reducing the sensitivity to stray photons from the night sky.

A test setup has been built at UZH (Fig. 6.5) which includes a light source providing almost parallel light and a goniometer in which a set of five light concentrators can be placed. The setup offers the possibility to measure light transmission through the concentrator at a fixed wavelength and vertical incidence, to characterize the angular response and to study optical cross talk between neighboring devices. In Fig. 6.6, the light throughput as a function of the zenith angle of incident rays is plotted as measured by this test setup.

6.3 FlashCam preamplifiers

FlashCam aims at building the first fully-digital IACT camera. Our efforts are two-fold: development of a non-linear preamplifier designed for increased dynamic range of the photomultiplier tubes, and design of the camera triggering system.

Photomultiplier tubes (PMT) are used in the telescope's camera to detect Cherenkov light. A low PMT gain of about 40'000 is required to slow down aging and increase the lifetime beyond ten years. The resulting very small output signals for single photoelectrons (phe) need to be amplified. Such amplification stage must have an excellent signal to noise ratio and a good amplitude resolution over a large dynamic range of up to 3'000 phe. The large dynamic range is normally covered by two parallel signal channels with different amplifications. Alternatively, a non-linear amplifier could be used connected to a single readout channel only. A non-linear amplification can be achieved, for example, by driving an operational amplifier (opamp) into saturation, but maintaining the charge (so increasing the signal width). The design shown in Fig. 6.7 with the current feedback opamp AD8001 satis-

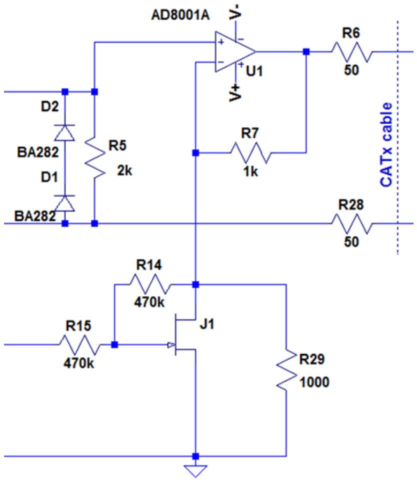

Fig. 6.7 – Amplfier circuitry using the AD8001 opamp. Input is on the upper left. The pseudo-differential output is transmitted through a CAT 5 cable to the FADC. The lower part of the circuit with the J-FET is used to set the gain.

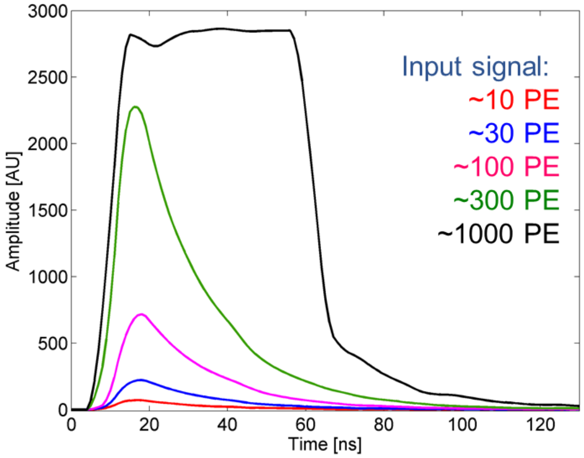

Fig. 6.8 – Digitized signals of different amplitudes. The saturation of the opamp is clearly visible for the 1000 phe pulse. The 300 phe pulse shows as well some saturation which is hardly recognizable for the untrained eye.

fies our requirements. The opamp has two distinct saturation modes: saturation caused by a large input signal, and saturation caused by driving the opamp's output signal beyond its output range. The first saturation mode causes ringing and is therefore not desired. A simple diode in the input circuit limits the input signal and prevents the opamp to saturate. The second mode can be achieved by the selected gain. This allows also setting the point between the linear and non-linear region. A set point of about 200 phe is chosen for our purpose.

Figure 6.8 shows digitized PMT pulses in the linear and in the saturation region. The original amplitude is determined by summing the signal over time window of 200 ns. This scheme can cope with high background levels (several incident photons during 10 ns) of low amplitude signals (< 10 phe).

Further studies with the amplifier will be performed and a first prototype board for the FlashCam with twelve PMTs and amplifiers will be built. Studies on the signal reconstruction are planned as well.

6.4 FlashCam trigger

The FADC outputs are passed to a Field-programmable Gate Array (FPGA). The FPGA stores the data in a digital ring buffer and performs a preliminary data reduction combining the signals from groups of three or seven neighbours to be presented to the trigger logic that initiates the readout of the associated FPGA information over Ethernet to a central server. FPGA-based triggering schemes offer much greater flexibility compared to the present analog systems. A good trigger algorithm must distinguish shower events from diffuse night sky background with high sensitivity over a wide range of energies and with good uniformity across the camera area.

The performance of trigger algorithms is assessed by Monte Carlo simulations which provide the "effective area" of the telescope. A *digital majority* requires a minimal number of signals above a certain amplitude threshold. This basic algorithm is used as a benchmark. *Digital sum* algorithms utilize the total amplitude of groups of pixels which improves the trigger uniformity. The effective areas, as a function of gamma ray energy, of these two triggering algorithms are shown in Fig. 6.9.

The performance of various triggering algorithms is assessed by Monte Carlo simulations. These simulations can be used to determine many properties of the triggering algorithm, the most important being the “effective area” of the telescope which measures the area of the Earth’s atmosphere from which gamma ray Cherenkov showers can be detected in a single telescope. The *digital majority* algorithm requires a minimal number of pixels having signals above a variable threshold. This basic algorithm is used as a benchmark. *Digital sums* form an alternative class of trigger algorithms which use the combined amplitude information over groupings of pixels to distinguish real showers from night sky background photons. The effective area, as a function of gamma ray energy, of one type of digital sum trigger is shown in Fig. 6.9. It would be very hard to implement such complex algorithm in the hardware-based triggers that are commonly used at present.

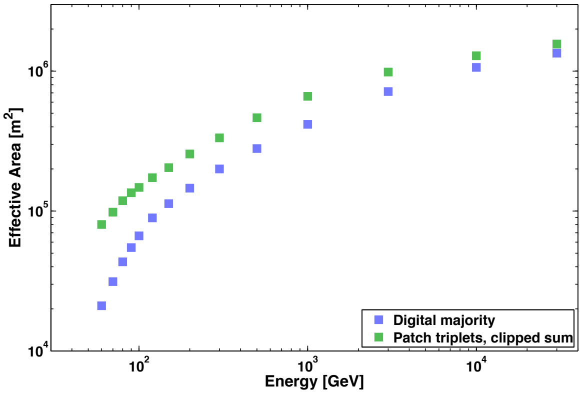

Fig. 6.9 – The effective collection area of a single telescope as a function of gamma ray energy, for two trigger algorithms (see text).

[1] J. A. Coarasa *et al.* (MAGIC Collaboration), J. Phys. Soc. Jap. Suppl **77B**, 49 (2008).

[2] B. Opitz *et al.* (HESS Collaboration), AIP Conf. Proc. **1223** 140 (2010).

[3] D. Hanna *et al.* (VERITAS Collaboration), J. Phys. Conf. Ser. **203** 012118 (2010).

7 Testing lepton universality: the $\pi \to e\overline{\nu}$ / $\pi \to \mu\overline{\nu}$ branching ratio

P. Robmann, A. van der Schaaf, P. Truöl and A. Palladino (guest from PSI/Virginia)

in collaboration with: University of Virginia, Charlottesville, USA; Institute for Nuclear Studies, Swierk, Poland; JINR, Dubna, Russia; PSI, Villigen, Switzerland and Rudjer Bošković Intitute, Zagreb, Croatia

(PEN Collaboration)

PEN [1] measures the branching ratio $B \equiv \Gamma_{\pi\to e\overline{\nu}(\gamma)}/\Gamma_{\pi\to\mu\overline{\nu}(\gamma)}$ with an accuracy $<0.05\%$. The present world average is $B{=}1.230(4){\cdot}10^{-4}$ [2]. In the Standard Model charged pion decays are mediated at tree level by (virtual) W exchange $\pi \to W \to \ell\overline{\nu}_\ell$. By measuring a ratio potentially large hadronic uncertainties in the initial pion state cancel resulting in a theoretical uncertainty $<0.01\%$. The theoretical prediction is based on the universality (flavour independence) of the $W \to \ell\overline{\nu}_\ell$ coupling strength and the notion that W couples to lefthanded fermions only which leads to "helicity suppression" (Γ vanishes in the limit $m_\ell \to 0$) and the present experimental result for B is the best of all available tests of these two concepts.

PEN uses a CsI crystal ball as main detector. Positron tracking is achieved with cylindrical MWPC's. Beam counters include a mini-TPC and an active scintillating target which is also used to record the decay signals [3].

The twobody decay $\pi \to e\overline{\nu}$ results in a monoenergetic positron (E $\sim \frac{1}{2}m_\pi c^2$) with an exponential decaytime distribution ($\tau_\pi \sim 26$ ns). The decay chain $\pi \to \mu\overline{\nu}$ followed by the threebody decay $\mu \to e\nu\overline{\nu}$ results in a continuous positron energy distribution (E $< \frac{1}{2}m_\mu c^2$) with a decay time first rising with τ_π and then falling with $\tau_\mu \sim 2197$ ns. For the two signal processes these energy and time probability density functions (pdf's) are uncorrelated and thus enter as onedimensional components in the total pdf. The main complication in separating these two contributions always was and still is the radiative tail of the positron energy in $\pi \to e\overline{\nu}$ decay which results in a $\sim 2\%$ overlap of the two processes. Figure 7.1 shows a cartoon of the situation.

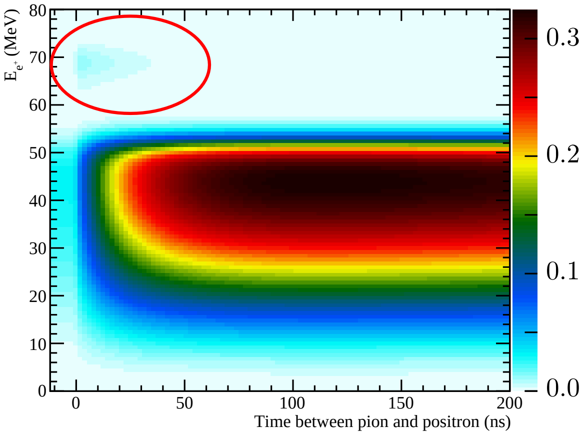

Fig. 7.1 – Distribution of the main observables distinguishing the decay modes $\pi \to eX$ and $\pi \to \mu X$. About 2% of the $\pi \to eX$ events are located in the region below 50 MeV dominated by $\pi \to \mu X$. The red contour indicates the main $\pi \to eX$ region.

If one wishes to keep the systematic uncertainty associated with this overlap below the envisaged few 10^{-4} level one has to know the yield of the lowenergy tail with a *relative* uncertainty better than 1%. At this level simulation can not be trusted so the distribution had to be measured in parallel.

Data taking

Data taking finished in 2010. Table 7.1 lists the vital information during the three years of data taking and the resulting statistical error in the branching ratio. Various readout triggers were implemented based primarily on the energy observed in the electromagnetic calorimeter. All but the main trigger (with energy threshold around 48 MeV) were prescaled.

Tab. 7.1 – PEN vital statistics during three years of data taking. The total *statistical* error in the branching ratio $\Delta B/B^{\mathrm{stat.}}$ is well below the goal accuracy. Footnotes indicate the main trigger conditions.

	2008	2009	2010	total	
measuring period	111	98	68	277	days
π stops	0.746	1.33	1.64	3.7	10^{11}
$\pi \to e\nu$ decays[a]	4.1	7.8	10.1	22.0	10^{6}
$\pi \to e\nu$ decays[b]	–	0.48	0.86	1.34	10^{6}
$\pi \to \mu \to e$ decays[c]	50	86	71	207	10^{6}
$\Delta B/B^{\mathrm{stat.}}$	0.07	0.04	0.03	0.02	%

[a] e^+ energy above 48 MeV

[b] full energy distribution, needed for low-energy tail, 1:10 - 1:16 prescaled

[c] $\Delta t(\pi - e^+) < 200$ ns, 1:64 prescaled

Data analysis

The analysis of a precision measurement such as PEN requires painstaking care and will take many (wo)man years. To remove any bias caused by theoretical prejudice a blind analysis is performed by training the reconstruction algorithms on small subsets of the data. To keep systematic errors under control the multidimensional maximum likelihood analysis uses pdf's straight from the measurement wherever possible. Only in regions where processes overlap GEANT4 simulations will take over from the observed pdf's.

Pushing systematic errors to the 10^{-4} region opens a can of worms (others would call the task challenging). Pions can scatter into the acceptance of the decay detectors, react with the target nuclei (producing energetic protons), decay during the $\sim$0.1 ns of travel inside the target, to name a few sources of background. Half a dozen processes will be included in the likelihood analysis and to cope with these event types a variety of additional observables will enter the pdf's: target waveform variables, preceding beam signals (affecting accidental coincidences), dE/dx information (to discriminate against protons), vertex location (to identify pion decays in flight) and probably more.

It is our intention to not only find the location of maximum likelihood in the multidimensional parameter space but to determine the full likelihood distribution for the branching ratio which has the advantage that the error distribution comes out for free. An unbinned likelihood analysis over 10^8 events in a parameter space with six or more dimensions is indeed "challenging" at least. A smart scan should avoid regions with low likelihood and will have to keep the required CPU power under control.

In the spirit of a blind analysis we are not able to show any results at this instant. Next year's report should show more!

[1] PEN Collaboration, PSI experiment R-05-01, D. Pocanic and A. van der Schaaf, spokespersons.

[2] G. Czapek *et al.*, Phys. Rev. Lett. **70** (1993) 17; D. I. Britton *et al.*, Phys. Rev. Lett. **68** (1992) 3000.

[3] see previous annual reports for details: `http://www.physik.unizh.ch/reports.html`

8 Study of Coulomb-bound πK-pairs

C. Amsler, A. Benelli[4], C. Regenfus, and J. Rochet

in collaboration with:
CERN, Czech Technical University, Institute of Physics and Nuclear Physics Institute ASCR (Czech Republic), Laboratori Nazionali di Frascati, Messina University, Trieste University, KEK, Kyoto Sangyo University, Tokyo Metropolitan University, IFIN-HH (Bucharest), JINR (Dubna), Skobeltsin Institute for Nuclear Physics (Moscow), IHEP (Protvino), Santiago de Compostela University, Bern University.

(DIRAC Collaboration)

The DIRAC experiment at CERN (PS212) is measuring the lifetime of electromagnetically bound $\pi^+\pi^-$- or $\pi^\mp K^\pm$-pairs ($\pi\pi$-atoms or pionium, and πK-atoms). Results for $\pi\pi$-atoms have been published earlier by the DIRAC-I collaboration [1]. The final result for the mean life [2] is 3.15 ± 0.20 (stat) ± 0.19 (syst) fs which leads to the determination of the difference in the isospin 0 and 2 $\pi\pi$-scattering lengths with a precision of 4%, namely $|a_0 - a_2| = 0.2533 \pm 0.0079$ (stat) ± 0.0075 (syst) m_π^{-1}, in agreement with results obtained from K-decay into 3π [3] and K-decay into $2\pi e\nu$ [4].

We are mainly involved in the study of πK-atoms (DIRAC-II experiment) for which we developed and built the aerogel Čerenkov counters to distinguish pions from kaons. The mean life of the πK-atom is related to the isospin 1/2 and 3/2 πK scattering lengths ($a_{1/2}$ and $a_{3/2}$) or, more precisely, to the absolute value of the difference between the two scattering lengths, a quantity that was calculated within 5% from Roy-Steiner dispersion-relations [5]. A measurement of the mean life will test low-energy QCD concepts involving the u- and d-quarks for $\pi\pi$, and extending to the s-quark sector for πK. The expected mean life of πK-atoms is 3.7 fs with large uncertainty [6].

Details on the apparatus can be found in Ref. [7] and in previous annual reports. We use the 24 GeV/c proton beam from the PS which traverses a thin Pt- (or Ni-) target. The secondary particles emerging from the target in the forward direction are analyzed in a double-arm magnetic spectro-meter. Electrons and positrons are vetoed by N_2-Čerenkov detectors and muons by scintillation counters behind thick absorbers. Kaons are separated from pions and protons by heavy gas (C_4F_{10}) Čerenkov counters (which fire on pions) and by an aerogel Čerenkov counters (which fires on both pions and kaons, but not not on the more numerous protons). Our group has developed and built the 37ℓ aerogel Čerenkov counter [8] and the gas system for the C_4F_{10} counters [9]. The aerogel detector consists of three independent modules. Two of them have refractive index $n = 1.015$ and are used for kaons between 4 and 5.5 GeV/c. At small angles with respect to the primary beam axis the momenta increases up to 8 GeV/c and hence an aerogel counter with lower refractive index ($n = 1.008$) is used to suppress fast protons.

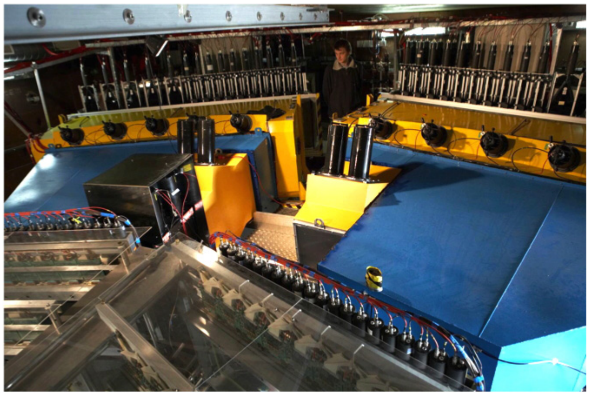

Fig. 8.1 – The DIRAC experiment. The black box on the left houses the aerogel counters. The yellow boxes are the heavy gas counters. The blue boxes contain the N_2 counters. The photomultipliers in the back belong to the detectors rejecting muons.

---

[4] Visitor from JINR, Dubna

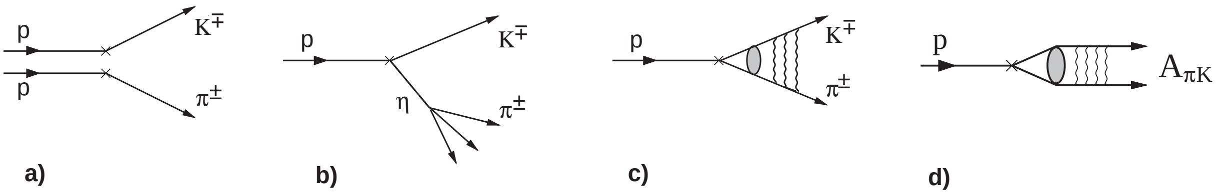

Fig. 8.2 – Production mechanisms of πK-pairs: a) accidental-pairs from two protons; b) non-Coulomb-pairs from long-lived intermediate states such as the η-meson; c) Coulomb-pairs from direct production or from short-lived intermediate states; d) πK-atoms.

A photograph of the equipment downstream of the dipole magnet is shown in Fig. 8.1.

Figure 8.2 shows the four mechanisms which contribute to the production of $\pi^{\pm}K^{\mp}$-pairs. Briefly, πK- (or $\pi\pi$-) atoms produced by incident protons fly in the forward direction and are ionized while crossing the target, leading to a peak from "atomic" pairs at very small relative momenta between the two particles (typically < 3 MeV/c in the c.m.s system). Since ionization competes with other processes such as annihilation, the number of atomic pairs grows with increasing lifetime. Unbound πK-pairs ("Coulomb-pairs") which interact electromagnetically are also produced and their numbers are related to the number of atoms [10]. The background stems from non-Coulomb pairs due to K and π mesons from long-lived resonances (which therefore do not interact), and from accidentals (pairs produced by two different proton interactions).

The DIRAC collaboration observed πK-atoms for the first time with the data collected in 2007 [11]. This result led to a lower limit for the mean life of πK-atoms of 0.8 fs in the 1s-state, which could be translated into an upper limit of $|a_{1/2} - a_{3/2}| < 0.58\ m_{\pi}^{-1}$. Details can be found in Ref. [11–13].

For the 2007 data we had used only the detectors downstream of the magnet. Three main improvements were implemented for the 2008 – 2010 runs. A scintillation fibre detector (SFD, described below) and microdrift chambers are now available to determine the interaction point in the production target with better precision. The SFD measures tracks with good resolution ($\sigma = 60\ \mu$m), high efficiency (98%) and improves the resolution on the transverse momentum Q_T from 3 MeV/c to 1 MeV/c, which reduces the background by typically a factor of four. ADC's for the aerogel detectors were also not available in the 2007 runs while this information is now recorded and, accordingly, the detection efficiency for kaons with the aerogel and the contamination from protons can be calculated reliably. The detection efficiency for kaons is typically 95% above 5 GeV/c and the contamination from protons around 5%, except for high energy protons close to the beam axis for which the proton contamination rises significantly. However, simulation shows that even a contamination of 100% is not problematic since no enhancement is observed for protons at small relative longitudinal momenta.

Finally, in 2007 the main goal was the observation of πK-atoms and hence a platinum target was chosen for which the production cross section was high. However, for platinum the breakup probability as a function of mean life (53% for 3.7 fs) is flattening off above ~ 4 fs and hence we could only give a lower limit for the mean life. We now use a nickel target for which the dependence between breakup probability and mean life is described by a steeper function, although atoms are produced with a lower cross section.

During 2010 we tuned the Monte Carlo simulation of the scintillation fibre detector (SFD). A sketch of the detector is shown in Fig. 8.3. The detector consists of 3 planes (x, y, and w) of scintillating fibres (diameter 205 μm). The x- and y-planes are made of 8 layers each with 480 fibres while the w-planes contain 3

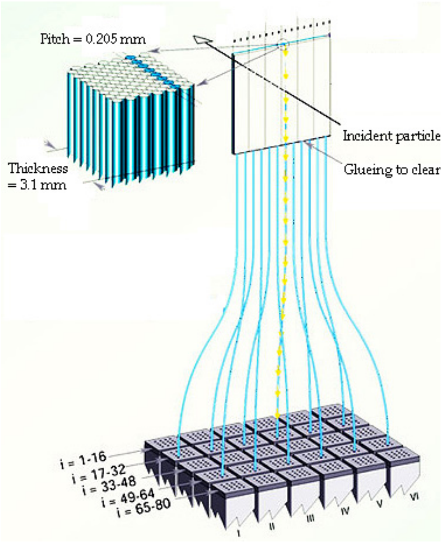

Fig. 8.3 – Layout of the scintillating fibre detector.

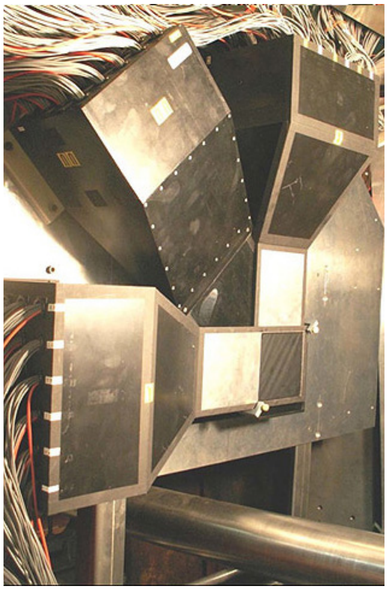

Fig. 8.4 – The scintillating fibre detector.

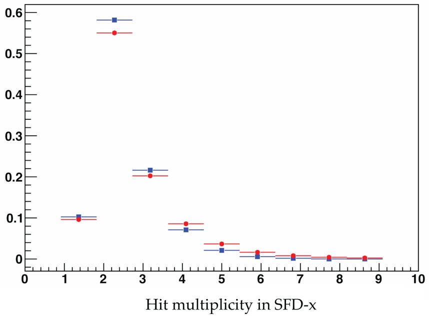

Fig. 8.5 – Hit multiplicity in the SFD x plane.

layers of 320 fibres. The fibres are read out in columns of 8, respectively 3 fibres by 30 × 16 Hamamatsu H6568 photomultipliers. The area covered by each plane is about 10 × 10 cm^2 and contributes only 1% radiation length. The timing resolution is 460 ps. A photograph of the detector is shown in Fig. 8.4.

We now illustrate the performance of the SFD using $\pi^+\pi^-$ data which are more abundant than πK data. The x-plane of the SFD detector was equipped with new readout electronics featuring both TDC's and ADC's. An important software tool was developed using the ADC information, the peak sensing algorithm, which compares the signal amplitudes for neighbouring hits to reduce background. Figure 8.5 compares the measured hit multiplicity with simulation after having applied the peak sensing algorithm. Figure 8.6 shows the distribution of the distance between two tracks measured by the SFD x-plane. In both plots good agreement between data and simulation is observed.

In 2010 we also proceeded with the analysis of the 2008 –2009 data with the upstream detectors, selecting πK events as cleanly as possible. The SFD detector and the nearby ionization hodoscope are used to resolve double tracks. Drift chamber (DC) tracking is performed and only upstream tracks that have hits in the SFD are kept. The distance between the DC extrapolation at the SFD plane and the actual SFD hit has to be smaller than 1 cm. Particle identification using the heavy gas Cerenkov and aereogel detectors is then performed and a precise timing between the two tracks is required. The relative transverse momentum is required to be smaller than $Q_T = 4$ MeV/c, the relative longitudinal momentum less than $|Q_L| = 20$ MeV/c. Figure 8.7 shows the experimental π^+K^- and π^-K^+ distributions with fit results superimposed. The fit includes atomic pairs (red), Coulomb pairs (blue) and non-Coulomb pairs (magenta). The sum of Coulomb and non-Coulomb pairs is shown in black.

A method to measure the energy difference ΔE_ninside between the pionium np- and ns-states was proposed as follows [14]. When moving inside

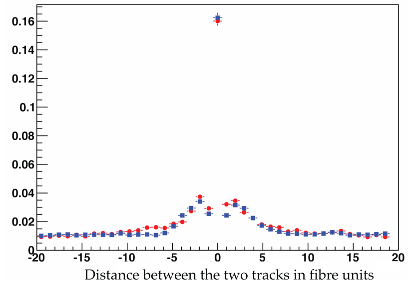

Fig. 8.6 – Distribution of the distance between the π^+ and π^- tracks in the x-plane of the SFD. The measured data are shown in red, the simulation in blue.

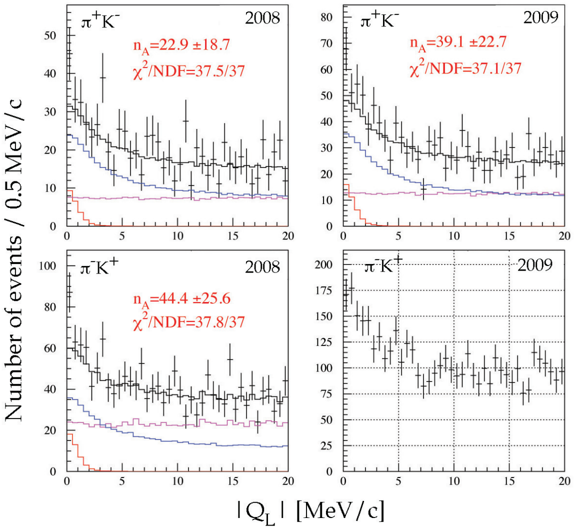

Fig. 8.7 – Distributions of longitudinal relative momentum Q_L for the 2008 and 2009 data. Top: π^+K^-; bottom: π^-K^+. The measured data are shown by the histograms with error bars; the other histograms are described in the text. The analysis of the π^-K^+ data from 2009 is in progress.

the target, the atoms interact with an applied electric field. Some of them leave the target in the $2p$-state. The decay into $\pi^0\pi^0$ being forbidden from p-states the main decay process is $2p - 1s$ radiative transition with subsequent annihilation from $1s$ into $\pi^0\pi^0$. Thus, the mean life of the atom in the $2p$-state is determined by radiative transition, $\tau(2p) \simeq 12$ ps [10], which is much slower than annihilation from ns-states. One can then measure the energy difference ΔE_n by observing the field dependence of the decay rate in the applied electric field. This determines the combination $2a_0 + a_2$ of the $\pi\pi$-scattering lengths. Combining with our measurement from the $1s$-state we will be able to derive a_0 and a_2 separately. This method can also be applied to the πK-system to obtain $a_{1/2}$ and $a_{3/2}$ separately.

During summer 2010 DIRAC took data with excellent detector performance and stable beam from the PS accelerator. DIRAC has been approved to run at least until the end of 2011. More data on πK-atoms will be collected in 2011 together with measurements of the energy difference between the ns and np states of pionium.

[1] B. Adeva *et al.* (DIRAC Collaboration), Phys. Lett. **B 619** (2005) 50.

[2] B. Adeva *et al.* (DIRAC Collaboration), submitted to Phys. Rev. Lett.

[3] J. R. Bately *et al.*, Eur. Phys. J. **C 64** (2009) 589.

[4] J. R. Bately *et al.*, Eur. Phys. J. **C 70** (2010) 635.

[5] P. Büttiker, S. Descotes-Genon, B. Moussallam, Eur. Phys. J. **C 33** (2004) 409.

[6] J. Schweizer, Phys. Lett. **B 587** (2004) 33.

[7] B. Adeva *et al.* (DIRAC Collaboration), Nucl. Instrum. Methods in Phys. Res. **A 515** (2003) 467.

[8] Y. Allkofer *et al.*, Nucl. Instr. Meth. in Phys. Res. **A 582** (2007) 497;
Y. Allkofer *et al.*, Nucl. Instr. Meth. in Phys. Res. **A 595** (2008) 84.

[9] S. Horikawa *et al.*, Nucl. Instr. Meth. in Phys. Res. **A 595** (2008) 212.

[10] L. L. Nemenov, Sov. J. Nucl. Phys. **41** (1985) 629;
L. Afanasyev and O. Voskresenskaya, Phys. Lett. **B 453** (1999) 302.

[11] B. Adeva *et al.* (DIRAC Collaboration), Phys. Lett. **B 674** (2009) 11.

[12] Y. Allkofer, PhD Thesis, University of Zurich (2008).

[13] C. Amsler, Proc. of Science PoS EPS-HEP (2009) 078.

[14] Addendum to PS212 (09/02/11): CERN-SPSC-2011-001 (SPSC-P-284 Add. 5).

9 Particle Physics at DESY/HERA (H1)

K. Müller, P. Robmann, U. Straumann, and P. Truöl

in collaboration with:
C. Grab, Institut für Teilchenphysik der ETH, Zürich; S. Egli, M. Hildebrandt, and R. Horisberger, Paul–Scherrer–Institut, Villigen, and 39 institutes outside Switzerland

(H1 - Collaboration)

While now almost four years have passed since the H1-experiment at the electron-proton collider HERA at DESY in Hamburg has finished taking data, the analysis of these data continues. Eight papers have been published ([1]-[8]) and further results, some of them still preliminary, have been presented at the "XVIII. International Workshop on Deep-Inelastic Scattering and Related Subjects (DIS 2010)" in Florence [9] in April 2010 and at the "35th International Conference on High Energy Physics (ICHEP 2010)" in Paris [10] in July 2010, or will be communicated at the "XIX. International Workshop on Deep-Inelastic Scattering and Related Subjects (DIS 2011)" in Newport News, Virginia [11] in April 2011 ([12]-[28]).

The central aim of these analyses remains the exploration of proton structure and tests of quantum chromodynamics (QCD) predictions. This program entails e.g. the precise determination of the neutral and charged electroweak current cross sections at high momentum transfer leading to parton density functions (PDF) in pre-HERA inaccessible domains of Bjorken x and momentum transfer Q^2, now combining H1-data with those of the neighbouring ZEUS-collaboration, the precise measurement of the running coupling constant α_s through a variety of channels, diffractively produced final states, hidden and open charm and beauty production as well as a few remaining searches for states outside the Standard Model.

These topics have been addressed last year:

- Extension of the structure function measurements to high inelasticity and direct assessment of the longitudinal component using also data from the runs with lower energy proton beams [7] (see also last years annual report for details [29]).
- Using neutral and charged current data with polarized beams for a combined electroweak and QCD fit [15], combining H1 and ZEUS structure function data for improved next-to-next-to-leading order (NNLO) PDF fits (HERAPDF1.5 NNLO) [12; 13], extending the combination procedure to the charm contribution $F_2^{c\bar{c}}$ [14].
- Search for contact interactions [28], squarks [6], and lepton flavor violation [8].
- Improved determination of the strong coupling α_s through combination of the H1 and ZEUS inclusive and jet production cross sections [16], as well as through a refined analysis of H1 data on multijet production at high Q^2 [17].
- Various aspects of charm and beauty production through D^*-tagging (see below for details) or lifetime-tagging [4; 25–27].
- Analysis of different exclusive channels [2; 18; 23; 24], e.g. by using the very forward proton and neutron spectrometers [1; 5; 19], as well as the isolation of the diffractive contributions to different channels [3; 20–22].

With the advent of the LHC graduate students from the Swiss institutions no longer contribute to the analyses. We continue, however, to serve as referees in the diffraction (Katharina Müller) and the heavy flavour (Christoh Grab and Peter Truöl) working groups.

9.1 D^* tagged photo- and electroproduction of charm

Charm and beauty production have been addressed by both HERA collaborations since 1996 with increasing statistics and detail. These measurements have confirmed the notion that heavy quarks are predominantly produced via boson-gluon fusion, $\gamma g \rightarrow c\bar{c}$ or ÃŁ$\gamma g \rightarrow b\bar{b}$, which is sensitive to the gluon density in the proton and allows its universality to be tested. The photon is radiated from the incoming lepton and the gluon from the proton. The cross section is largest for photoproduction, i.e. for photons with virtuality $Q^2 \approx 0$ GeV^2, but the production of charm quarks contributes up to 20 % to the inclusive ep scattering cross section for higher momentum transfer. Therefore, the correct treatment of the effects related to the charm quark contribution, in particular the mass effects, in perturbative QCD calculations is important for the determination of parton distribution functions, where different schemes to incorporate these effects are available. In addition to the case where the photon enters the hard process directly, one has also to consider the case where the partonic structure of the photon is resolved.

One of the pioneering articles in this area was based on the theses of two UZH graduate students, David Müller and Martin zur Nedden. It presented the first analysis where photo- and electroproduction of charmed quarks was directly linked to the gluon density [30]. $D^{*\pm}$ based charm tagging was applied, too, as in part of the later work [31; 32]. This technique makes use of the fact, that the decay chain:

$$D^{*\pm}(2010) \rightarrow D^0(1865)\pi^{\pm}_{\text{slow}} \rightarrow K^{\mp}\pi^{\pm}\pi^{\pm}_{\text{slow}}$$

distinguishes itself by a clear peak at 145 MeV in the distribution of the invariant mass difference ΔM:

$$\Delta M = M(K^{\mp}\pi^{\pm}\pi^{\pm}_{\text{slow}}) - M(K^{\mp}\pi^{\pm})$$

This is demonstrated in Figs. 9.1 and 9.2, which compare the early results [30] with those from the most recent analyses to be discussed here [33; 34].

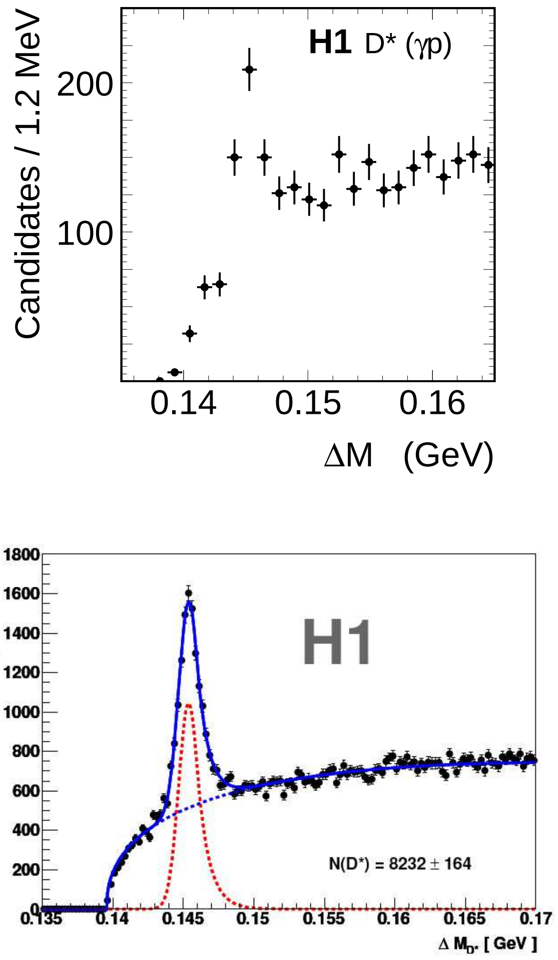

Fig. 9.1 – Distribution of ΔM for D^* candidates in photoproduction. Top: first H1-data from 1999 [30] (489±92 events, 60 % of total sample). Bottom: new data including the fit function [33].

The latter are based on an integrated luminosity of 93 and 348 pb^{-1}, for photoproduction and deep-inelastic scattering (DIS), respectively, compared to 10 and 21 pb^{-1} in the old analysis, with apparent improvement in the number of events observed. The momenta of the charged decay products were measured in the central tracking detectors. In the DIS case the events were triggered by an electromagnetic cluster in the backward electromagnetic calorimeter SPACAL. In the photoproduction case the new data had to rely on the fast-track-trigger (FTT) based on information from the central jet chamber, while in the old data photo-

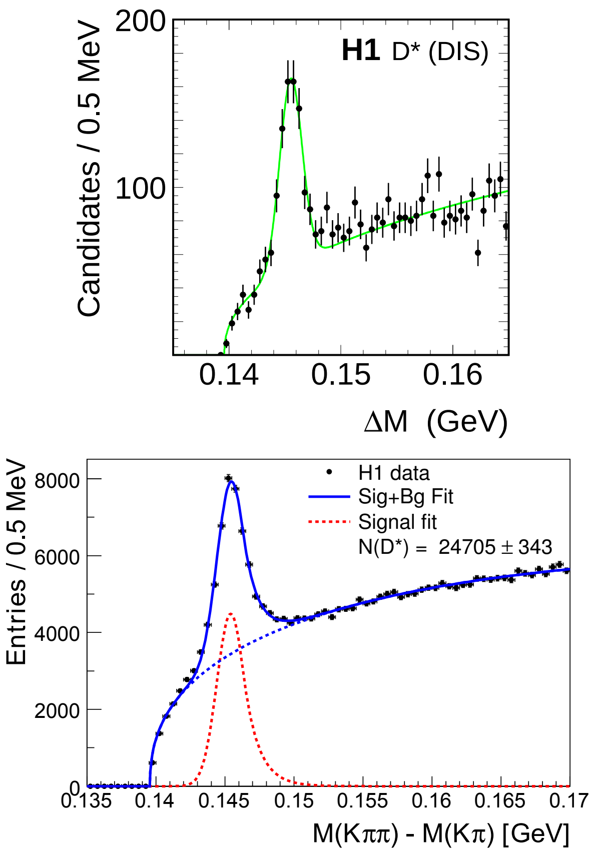

Fig. 9.2 – Distribution of ΔM for D^* candidates in deep inelastic scattering. Top: first H1-data from 1999 [30] (583±35 events). Bottom: new data including the fit function [34].

produced events could be triggered by signals in the low scattering angle electron taggers at 33 and 44 m downstream of the electron beam (ETAG33 and ETAG44). Skipping details of the analyses, of the normalisation procedures and of the evaluation of the systematic errors, selected results are displayed in Figs. 9.3 – 9.6.

Figure 9.3 shows the differential cross section for photoproduction as function of the invariant mass of the photon-proton system and of the transverse momentum p_T of the D^*. The data are compared to two theoretical calculations. In one of them, labeled FMNR [35] the production of heavy quarks is calculated in the so called massive scheme, where heavy quarks are produced only perturbatively via boson gluon fusion. In the alternative massless scheme the heavy quarks are treated as massless partons. These two schemes should be appropriate in different regions of phase space, the massive scheme should be reliable when the transverse momentum p_T of the heavy quarks is of similar size compared to the charm mass m_c ($\approx$ 1.5 GeV) , whereas the massless scheme is expected to be valid for $p_T > m_c$. Calculations in the general-mass variable-flavour-number scheme (GMVFNS) [36] combine the massless with the massive scheme. In the FMNR program a NLO calculation in the collinear approach is implemented, i.e. transverse momenta are generated in the hard scattering process and effects from the finite transverse momenta of the gluons enter only at NLO. The resolved and direct processes are calculated separately providing weighted parton level events with two or three outgoing partons, i.e. a charm quark pair and pos-

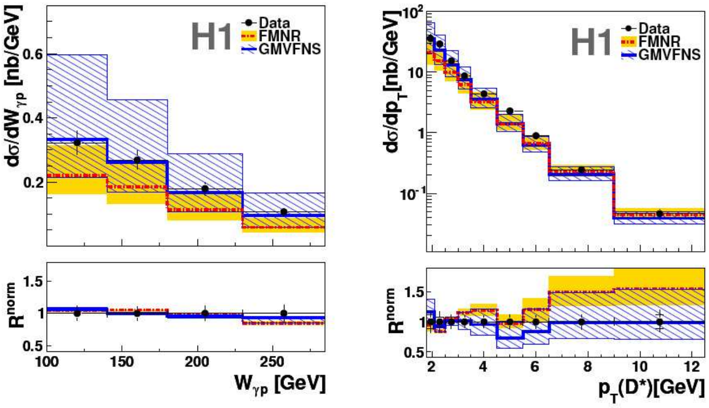

Fig. 9.3 – Differential D^* cross section as a function of the invariant mass of photon-proton system $W_{\gamma p}$ and of the D^* transverse momentum $p_T(D^*)$ compared to the next-to-leading order calculations FMNR [35] and GMVFNS [36]. The normalized ratio theory/experiment R^{norm} is also shown, which allows comparison of the shape independent of the normalisation.

sibly one additional light parton. In the adaptation to the HERA data both calculations use the HERAPDF1.0-set for the proton [38] but slightly different PDF's for the photon and also slightly different fragmentation functions for the charmed quarks. The influence of these choices as well that of m_c and of the renormalisation and factorisation scales is reflected in the uncertainty bands of the models. The precision of the measurements is much higher than the accuracy of the NLO calculations. The uncertainty of the NLO predictions is dominated by the variation of the renormalisation scale, which leads to a large change in the normalisation, but only small differences in the shapes of some distributions. Within these large uncertainties, both NLO predictions agree with the cross section as a function of $p_T(D^*)$ and $W_{\gamma p}$.

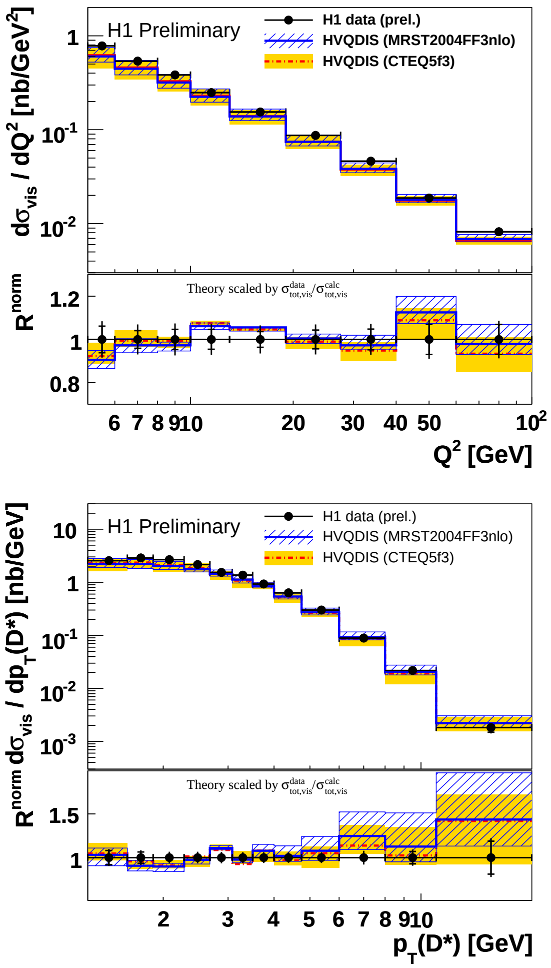

Fig. 9.4 – Differential D^* cross section as a function of the photon virtuality Q^2 (top) and the transverse momentum $p_T(D^*)$ (bottom) in the visible kinematical range of $5 < Q^2 < 100$ GeV^2, inelasticity $0.02 < y < 0.7$, pseudorapidity $|\eta(D^*)| < 1.8$ and $p_T(D^*) > 1.25$ GeV/c. The inner error bars show the statistical error, the outer error bars include the systematic errors. The measured data are compared to predictions by the next-to-leading order calculation HVQDIS [37] with two different proton parton densities. The bands indicate the theoretical uncertainties.

A selection of the deep inelastic scattering data is shown in Figs. 9.4 – 9.6. The dependence of the cross section on Q^2 and $p_T(D^*)$ is again compared to a fixed order NLO calculation (HVQDIS) [37] based on collinear factorisation and the DGLAP evolution equations. This calculation assumes three active flavours (u, d, s) in the proton (fixed-flavour number scheme: FFNS) and massive charm quarks are produced dynamically, predominantly via boson gluon fusion. The total visible cross section has been measured to be $\sigma_{\text{vis,tot}}(e^{\pm}p \rightarrow e^{\pm}D^{*\pm}X) = 6.44 \pm 0.09\,(\text{stat.}) \pm 0.49\,(\text{syst.})$ nb, while HVQDIS predicts typically 5.7 ± 1.3 nb. The visible region is defined in Fig. 9.4. For the comparison to an alternative NLO calculation based on the zero-mass variable flavour-number scheme (ZM-VFNS) [39], where the charm quark is considered as a massless constituent of the proton we must refer to the H1-publication [34]. Within the uncertainties introduced by the choice of the model parameters HVQDIS seems to describe the data well, while ZM-VFNS is less successful.

The charm contribution $F_2^{c\bar{c}}(x, Q^2)$ to the proton structure function is obtained via the expression for the one photon exchange cross section for charm production

$$\frac{d^2\sigma^{c\bar{c}}}{dx dQ^2} = \frac{2\pi\alpha_{em}^2}{Q^4 x} \times \left(\left[1 + (1-y)^2\right] F_2^{c\bar{c}}(x, Q^2) - y^2 F_L^{c\bar{c}}(x, Q^2)\right) ,$$

where α_{em} is the electromagnetic coupling constant. The contribution from $F_L^{c\bar{c}}$ is small in the present phase space. The visible inclusive $D^{*\pm}$ cross sections in bins of inelasticity y and

Q^2 can be converted to a bin centre corrected $F_2^{c\bar{c}\,exp}(\langle x\rangle, \langle Q^2\rangle)$ by extrapolating the visible cross sections to the full phase space using input from HVQDIS. The small beauty contribution is subtracted, too. The uncertainty of this extrapolation procedure is included in the systematic error [34].

Figures 9.5 and 9.6 show results for $F_2^{c\bar{c}}$. They agree very well with the independent H1-measurement using the lifetime charm tag obtained from the central silicon vertex detector CST built by the Swiss groups [40]. The FFNS NLO calculation gives a good description of the data with either choice of two recently published proton PDFs (see [34] for references). Equally well does HERAPDF1.0, which has been extracted from the combined inclusive proton structure function data of the H1 and ZEUS detectors in a general-mass variable-flavour-number scheme, interpolating between FFNS and the ZM-VFNS [38].

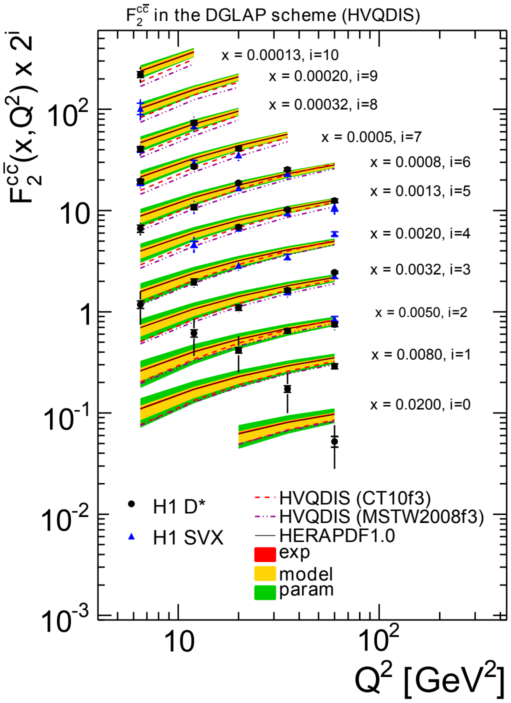

Fig. 9.5 – $F_2^{c\bar{c}}$ as a function of Q^2 for different x, as derived in the framework of NLO DGLAP. The inner error bars show the statistical, the outer error bar the total uncertainty which includes statistical, experimental systematic, extrapolation and model uncertainty added in quadrature. Also shown are the results using the H1 vertex detector (H1 SVX) [40], NLO DGLAP predictions from HVQDIS [37] with two different proton PDFs, and HERAPDF1.0 predictions [38].

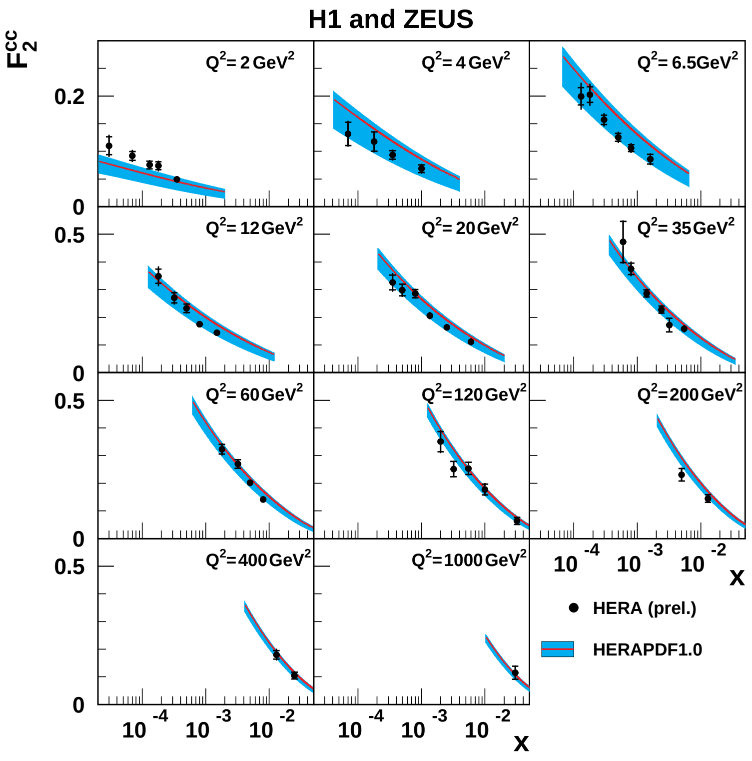

Fig. 9.6 – Combined results for $F_2^{c\bar{c}}$ from H1 and ZEUS using different charm tagging methods. Uncertainties of 5-10 % are achieved in the explored region $2 < Q^2 < 1000$ GeV^2 and $10^{-5} < x < 10^{-1}$ [14]. The spread in the HERAPDF1.0 prediction reflects the uncertainty in the charm quark mass 1.354$< m_c <$1.65 GeV.

The uncertainty on $F_2^{c\bar{c}}$ for the HERAPDF1.0 prediction is dominated by the variation of the charm mass in the PDF fit. The agreement attests to the fact that the gluon density determined from the scaling violations of the inclusive proton structure function is consistent with the one needed in charm production. A recent analysis of the combined $F_2^{c\bar{c}}$ data from H1 and ZEUS [14] has demonstrated that the inclusion of the charm data can restrict the allowed range of m_c considerably. This then has consequences for the accuracy of the predictions for e.g. W-boson production at LHC energies.

[1] F.D. Aaron *et al.* [H1], Eur. Phys. J. C **68** (2010) 381.

[2] F.D. Aaron *et al.* [H1], Eur. Phys. J. C **68** (2010) 401.

[3] F.D. Aaron *et al.* [H1], Eur. Phys. J. C **70** (2010) 15.

[4] F.D. Aaron *et al.* [H1], Eur. Phys. J. C **71** (2011) 1509.

[5] F.D. Aaron *et al.* [H1], Eur. Phys. J. C **71** (2011) 1578.

[6] F.D. Aaron *et al.* [H1], Eur. Phys. J. C **71** (2011) 1572.

[7] F.D. Aaron *et al.* [H1], Eur. Phys. J. C (2011), in print.

[8] F.D. Aaron *et al.* [H1], Phys. Lett. B (2011), in print.

[9] Contributions to XVIII. International Workshop on Deep-Inelastic Scattering and Related Subjects (DIS 2010), Florence, Italy, April 19-23, 2011[5].

[10] Contributions to 35th International Conference on High Energy Physics, Paris, France, July 21-28, 2010 [5].

[11] Contributions to XIX. International Workshop on Deep-Inelastic Scattering and Related Subjects (DIS 2011), Newport News, April 11-16, 2011[5].

[12] *H1 and ZEUS combined measurement of neutral and charged current cross sections at HERA* [10]

[13] *H1 + ZEUS pdf fits including HERA-II high Q^2 data (HERAPDF1.5 NNLO)* [10; 11]

[14] *QCD analysis of combined H1 and ZEUS $F_2^{c\bar{c}}$ data* [11]

[15] *Combined electroweak and QCD fit of inclusive neutral and charged current data with polarized lepton beams at HERA* [11]

[16] *QCD analysis with determination of α_s based on HERA inclusive and jet data (H1+ZEUS)* [11]

[17] *Measurement of multijet production and α_s in deep-inelastic ep-scattering at high Q^2* [11]

[18] *Measurement of the azimuthal correlation between the scattered electron and the most forward jet in deep-inelastic scattering at HERA* [10; 11]

[19] *Very forward photon spectrum and neutron P_T distribution measured with the forward neutron calorimeter (FNC)* [10; 11]

[20] *Measurement of the diffractive structure function F_2^{D3} with the very forward proton spectrometer (VFPS)* [9]

[21] *Exclusive diffractive J/ψ production at low $W_{\gamma p}$* [11]

[22] *Dijet production in diffractive deep inelastic scattering using the very forward proton spectrometer (VFPS)* [11]

[23] *Transverse momentum of charged particles in an extended pseudorapidity range* [9; 11]

[24] *K_s^0 production at high Q^2 at HERA II* [9]

[25] *D^* production at low Q^2 in an extended phase space* [10]

[26] *D^* with jets in photoproduction* [9]

[27] *Measurement of the photoproduction of b-quarks at threshold at HERA* [11]

[28] *Search for contact interactions at HERA* [10]

---

[5] www-h1.desy.de/publications/H1preliminary.short.list.html

[29] Physik-Institut, University of Zürich, Annual Reports 1996/7 ff.; available at *http://www.physik.uzh.ch/reports.html*

[30] C. Adloff *et al.* [H1], Nucl. Phys. B **545** (1999) 21.

[31] A. Aktas *et al.* [H1], Eur. Phys. J. C **50** (2007) 251.

[32] F. D. Aaron *et al.* [H1], Phys. Lett. B **686** (2010) 91; A. Aktas *et al.* [H1], Eur. Phys. J. C **51** (2007) 271; C. Adloff *et al.* [H1], Phys. Lett. B **528** (2002) 199; C. Adloff *et al.* [H1], Z. Phys. C **72** (1996) 593.

[33] *Measurement of inclusive D^* meson cross sections in photoproduction at HERA*^{5}.

[34] *Measurement of inclusive $D^{\pm}$ meson production and determination of $F_2^{c\bar{c}}$ at low Q^2 in deep-inelastic scattering at HERA*, F.D. Aaron *et al.* [H1], submitted to Eur. J. Phys. C; see also [25].

[35] S. Frixione *et al.*, Phys. Lett. B **308** (1993) 137; S. Frixione, P. Nason and G. Ridolfi, Nucl. Phys. B **454** (1995) 3.

[36] G. Kramer and H. Spiesberger, Eur. Phys. J. C **38** (2004) 309; B. A. Kniehl *et al.*, Eur. Phys. J. C **62** (2009) 365.

[37] B.W. Harris and J. Smith, Phys. Rev. D **57** (1998) 2806; idem Nucl. Phys. B **452** (1995) 109.

[38] F.D. Aaron *et al.* [H1/ZEUS], JHEP **1001** (2010) 109.

[39] G. Heinrich and B. A. Kniehl, Phys. Rev. D **70** (2004) 094035; C. Sandoval, *Inclusive production of hadrons in neutral and charged current ceep inelastic scattering*, DESY-THESIS-2009-044, Ph.D. Thesis Univ. Hamburg (2009).

[40] F. D. Aaron *et al.* [H1], Eur. Phys. J. C **65** (2010) 89.

10 Particle Physics with LHCb

J. Anderson, R. Bernet, A. Bursche, A. Büchler, N. Chiapolini, M. De Cian, Ch. Elsasser, K. Müller, J. Palacios (until January 11), Ch. Salzmann, S. Saornil, N. Serra, St. Steiner, O. Steinkamp, U. Straumann, J. van Tilburg (until March 11), M. Tobin, A. Vollhardt

The full LHCb collaboration consists of 54 institutes from Brazil, China, France, Germany, Ireland, Italy, The Netherlands, Poland, Romania, Russia, Spain, Switzerland, Ukraine, the United Kingdom and the United States of America.

(LHCb - Collaboration)

The LHCb [1] experiment is the smallest of the four large experiments at the Large Hadron Collider (LHC) and is dedicated to b-physics. The main goal of the experiment is the indirect search for New Physics (NP) through precision measurements of CP violating phases and rare heavy-quark decays. Of particular interest are processes that are strongly suppressed in the Standard Model (SM), such as flavour-changing neutral current $b \to s$ transitions. In these loop mediated processes, NP can lead to significant deviations from SM predictions through additional amplitudes involving new heavy particles. These indirect searches extend the discovery potential for new particles to a mass range far beyond that accessible in direct searches. Moreover, observing the pattern of deviations from SM predictions will give insights into the underlying dynamics of the NP and will permit the parameters of New Physics models to be constrained.

The analysis strategies for six selected key measurements have been described in detail in the LHCb “roadmap” document [2]. They comprise measurements of the CKM angle γ from $B \to DK$ tree decays and from penguin-mediated charmless charged two-body B decays, the measurement of the $B_s^0\bar{B}_s^0$ mixing phase ϕ_s, the determination of the branching fraction of the very rare decay $B_s^0 \to \mu^+\mu^-$, measurements of angular distributions in the rare decay $B^0 \to K^\star\mu^+\mu^-$, and measurements of radiative $b \to s\gamma$ decays.

10.1 The LHCb detector

To exploit best the strongly forward peaked $b\bar{b}$ production cross section at the LHC, the LHCb detector is laid out as a single-arm forward spectrometer. Its acceptance covers polar angles from 15 mrad to 300 mrad in the bending plane of the spectrometer magnet and 250 mrad in the non-bending plane. This corresponds to a pseudo-rapidity coverage of about $1.9 < \eta < 4.9$. LHCb captures almost 40% of the $b\bar{b}$ production cross section at the LHC while covering only about 4% of the solid angle. An additional benefit of measuring at small polar angles is the possibility to trigger on low-p_T particles down to transverse momenta p_T of only a few GeV. The detector has been described in previous annual reports [3] and in [1].

10.2 Detector performance and first running experience

The LHCb experiment was fully operational from the first day of LHC collisions at a centre of mass energy of 0.9 TeV end of autumn 2009, except for the computing farm for the higher-level triggers (HLT), which was only partially installed. About 37 pb^{-1} of pp collisions at 7 TeV were collected during the 2010 LHC run, with a data taking efficiency of more than 90%. The polarity of the LHCb spectrometer magnet was reversed several times to minimise possible systematics due to detector asymmetries.

LHC running conditions and the instantaneous luminosity provided by the accelerator evolved rapidly throughout the 2010 run. As the LHC luminosity increased, trigger conditions were gradually tightened such that the available readout bandwidth and CPU in the HLT farm were fully exploited. Data were taken at the highest luminosity available from LHC at all times, although during the later part of the run this meant operating the experiment at significantly higher numbers of *pp* interactions per bunch crossing than foreseen under nominal conditions. Peak instantaneous luminosities close to the LHCb nominal luminosity were achieved towards the end of the 2010 run, but with only 344 instead of 2622 colliding bunches. These running conditions corresponded to an average number of visible interactions per bunch crossing, μ, of up to 2.4, where nominal LHCb operating conditions correspond to $\mu = 0.4$. The HLT farm has been completed over the 2010/2011 Christmas break.

The instantaneous luminosity will gradually increase in in 2011 running period and about 1 fb^{-1} are expected to be delivered until the end of 2011. For many of the key physics channels at LHCb, significant measurements can already be expected from the 2010/2011 LHC run. The collaboration has already published three papers [4–6] and presented many new results at conferences [8–28].

An excellent vertex resolution is essential for the high-level trigger and for many physics analyses. To minimise extrapolation errors from the first measurement points to the vertex position, the LHCb vertex detector is installed inside the LHC vacuum vessel. The sensitive area of the detector starts at a distance of only 8 mm from the beam axis during data taking. The detectors have to be retracted by 3 cm during beam injection. An internal alignment of better than 5 μm of the vertex detector has been obtained. Fill-to-fill variations in the position of the detectors are also as small as 5 μm. A single-hit resolution of 4 μm has been measured for the innermost readout strips. The measured track impact parameter resolution is slightly worse than expected from simulation, possible reasons for this are being investigated.

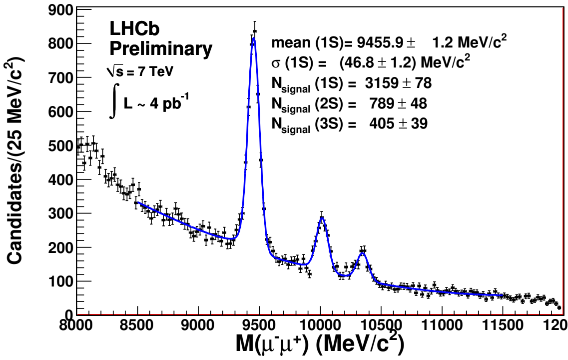

Fig. 10.1 – $\mu^+\mu^-$ invariant mass distribution showing the $\Upsilon(1s)$, $\Upsilon(2s)$ and $\Upsilon(3s)$ resonances.

Good momentum and invariant mass resolutions are crucial for the rejection of combinatorial backgrounds. Measured spatial resolutions in the tracking system are approaching those expected from test beams and simulation. Small differences are remaining from residual misalignments. Since the acceptance of the LHCb tracking system for cosmics is negligibly small, its spatial alignment relies entirely on beam data. The good progress in the understanding of the alignment is demonstrated by the invariant mass resolution obtained for $J/\Psi \rightarrow \mu^+\mu^-$ decays, which was 17.1 MeV in May 2010 and had reached 13.3 MeV in December 2010. From simulation, an invariant mass resolution of 12.1 MeV is expected. Figure 10.1 shows a $\mu^+\mu^-$ invariant mass distribution in the mass range of the $\Upsilon(1s)$, $\Upsilon(2s)$ and $\Upsilon(3s)$ resonances. An invariant mass resolution of 47 MeV is obtained, here, and the three resonances are clearly resolved.

An excellent kaon/pion separation over a wide momentum range is another important ingredient for many analyses. Two RICH detectors with three different radiators cover momenta down to about 2 GeV, needed to identify kaons for B flavour tagging, and up to 100 GeV, required for a clean separation of two-body hadronic B decays.

The particle-identification performance has been studied with data using tag-and-probe methods on $\phi \rightarrow K^+K^-$, $K_s^0 \rightarrow \pi^+\pi^-$ and $\Lambda \rightarrow p\pi$ decays and is found to be close to expectations from simulation over the full momentum range. The importance of kaon/pion separation for two-body hadronic B decays is illustrated in Fig. 10.2. The

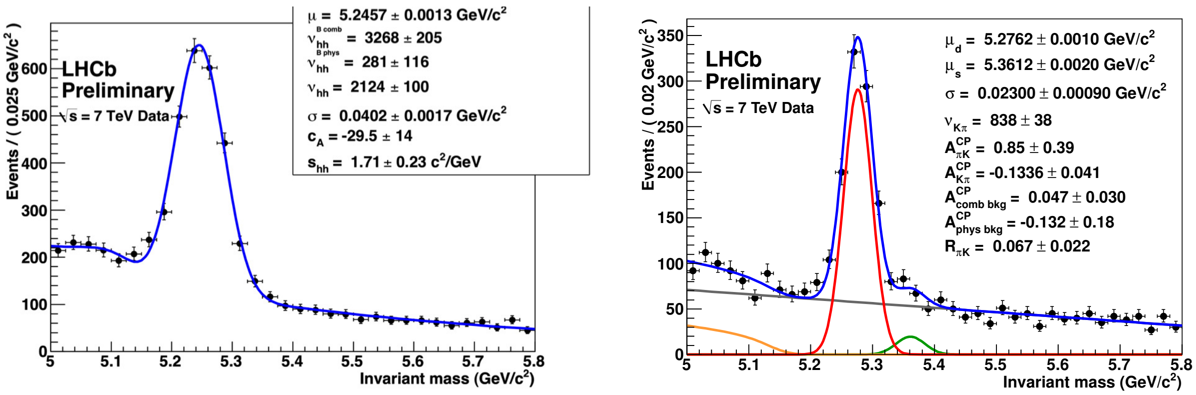

Fig. 10.2 – Left: $B \to h^+h^-$ invariant mass distribution where the pion mass hypothesis was applied for both final-state particles. Right: $B^0_{d,s} \to K^\pm\pi^\mp$ using only loose kaon and pion identification criteria.

left plot shows a $B \to h^+h'^-$ invariant mass spectrum before particle-identification cuts, where the pion mass hypothesis was applied for both final-state particles. Despite the good invariant mass resolution, the contributions from $B^0 \to \pi^+\pi^-$, $B \to K^\pm\pi^\mp$ and $B^0_s \to K^+K^-$ cannot be separated kinematically. The right plot shows the invariant mass spectra for $B^0_s \to K^+K^-$ after particle-identification cuts have been applied. A clean signal with excellent invariant-mass resolution of 23 MeV is observed here as well as for the other two decay modes.

Finally, the performance of the electromagnetic calorimeter in electron and photon reconstruction is illustrated in Fig. 10.3, which shows an e^+e^- invariant mass distribution with a clear $\chi_{c1,2} \to J/\psi\gamma$ signal.

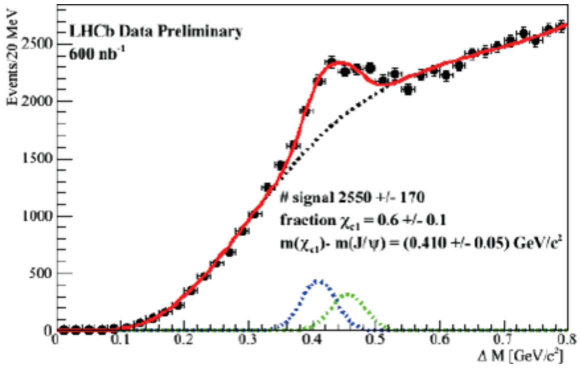

Fig. 10.3 – e^+e^- invariant mass distribution showing a $\chi_{c1,2} \to J/\psi(\mu^+\mu^-)\gamma$ signal.

10.2.1 Tracker Turicensis: operation and performance

The Tracker Turicensis (TT) was constructed at the Physics Institute and has been described in previous annual reports [3]. After its installation in LHCb the detector was operated with high efficiency during the entire data taking period. By the time of the LHC turn on in October 2009 more than 99% of the 144'000 detector channels were fully operational. The average hit detection efficiency was found to exceed 99%. During 2010 some of the readout channels were lost due to broken bond wires. All affected modules have been repaired in Zurich during the Christmas shutdown. S. Saornil and M. Tobin are in charge of maintaining a stable and efficient operation of the TT and monitoring its performance while N. Chiapolini is responsible for its alignment.

10.3 Physics results

10.3.1 J/ψ production and $b\bar{b}$ cross section

Measurements of differential cross sections for prompt J/ψ and $b \to J/\psi X$ production have been performed using 5.2 pb^{-1} of data [29]. The measurement was performed in two-dimensional bins of pseudo-rapidity from $2 < \eta < 4.5$ and transverse momentum from $0 < p_T < 14$ GeV. To separate prompt J/ψ and J/ψ from b decays, the pseudo proper time $t_z = \Delta z \cdot M_{J/\psi}/p_z$ was used, where

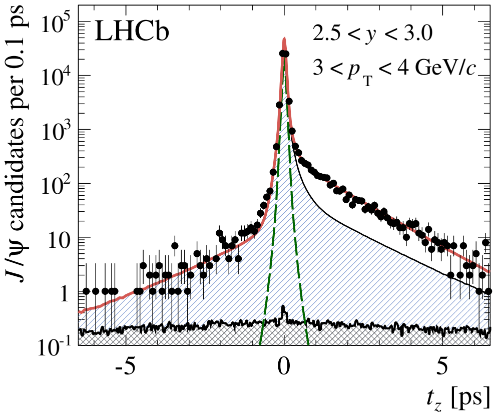

Fig. 10.4 – Distribution of the J/ψ "pseudo proper time" t_z in one of the (p_T, η) bins used in the measurement of differential J/ψ cross sections.

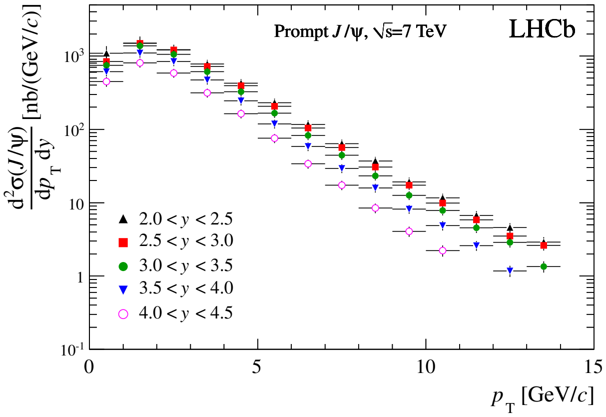

Fig. 10.5 – Prompt J/Ψ production cross-section as a function of p_T in bins of y, assuming no polarisation of the prompt J/ψ.

Δz is the displacement of the J/ψ vertex from the primary vertex along the beam axis, $M_{J/\psi}$ is the J/ψ mass and p_z is the component of the J/ψ momentum along the beam axis. The distribution of t_z in one of the (p_T, η) bins used in the analysis is shown in Fig. 10.4. Combinatorial backgrounds in the t_Z distribution were estimated by combining J/ψ vertices from one event with primary vertices from a different event. The dominating uncertainty on the prompt J/ψ cross section is due to the still unknown J/ψ polarisation in prompt production. Its measurement in LHCb requires a larger data sample. The differential cross section assuming unpolarised J/ψ production is shown in Fig. 10.5. The results are in good general agreement with recent theoretical calculations at high p_T, although the uncertainties on these predictions are still rather large.

The LHCb Monte Carlo simulation, based on PYTHIA 6.4 [30] and EvtGen [31], was used to extrapolate the measured $b \to J/\psi X$ cross section from the LHCb acceptance to the full polar angle range. Using the average $b \to J/\psi X$ branching fraction for inclusive b-hadron decays to J/ψ measured at LEP [32], a $b\bar{b}$ production cross section of $\sigma(pp \to b\bar{b}X) = 288 \pm 4 \pm 48$ μb is calculated. This result is in excellent agreement with an earlier LHCb measurement of the $b\bar{b}$ production cross section that was based on 15 nb^{-1} of data and used $B^0 \to D^0\mu^- X^+$ decays [5]. In this analysis, the impact parameter of the reconstructed D^0 momentum with respect to the primary vertex was used to identify D mesons from b decays and wrong-sign $D^0\mu^+$ combinations were used to estimate backgrounds. Here, a $b\bar{b}$ production cross section of $\sigma(pp \to b\bar{b}X) = 284 \pm 20 \pm 49$ μb was calculated for the full polar angle range, in good agreement with the newer and more precise measurement. Prior to these measurements, simulation studies assessing the LHCb physics reach had assumed a $b\bar{b}$ production cross section of 250 μb at $\sqrt{s} = 7$ TeV.

10.3.2 Direct CP violation in charged charmless B decays

A measurement of direct CP violation in charged charmless hadronic two-body decays is ongoing [13]. Competitive results with previous measurements from the B factories and the Tevatron can be expected from the 2011 data sample. An invariant mass distribution for $B^0_{d,s} \to K^\pm\pi^\mp$ decays was already shown in Fig. 10.2 above. Separating the event sample further into $B^0_d, \bar{B}^0_s \to K^+\pi^-$ and $\bar{B}^0_d, B^0_s \to K^-\pi^+$, a clear difference in event yields is visible in the invariant mass spectra shown in Fig. 10.6. The raw asymmetry between the B^0 and $\bar{B}^0$ yields deviates from zero at the level of three standard deviations and is compatible with the known world average CP asymmetry. An asymmetry is also visible in the B_s^0 vs. $\bar{B}_s^0$ event yields although the effect is not yet statistically significant, here. The distributions are not corrected for production and detection asymmetries. These corrections, however, are expected to be small.

10.3.3 $B_s^0\,\bar{B}_s^0$ flavour oscillations

The ability to resolve the fast $B_s^0\bar{B}_s^0$ flavour oscillations is an important ingredient for several LHCb key measurements. A measurement of the $B_s^0\bar{B}_s^0$ oscillation frequency in $B_s^0 \to D_s^-(3)\pi$ decay modes has been presented. Despite the still limited statistics, a competitive measurement with existing results from the Tevatron is obtained due to the excellent proper-time resolution of the experiment. Another important ingredient for oscillation measurements is the ability to tag the initial flavour of the B meson at production. Opposite-side lepton, kaon and vertex-charge tags make use of distinctive signatures from the decay of the accompanying b hadron in the event to imply the flavour of the B meson under study. Same-side tags directly determine the flavour of the B meson under study, using the charge of a pion, in the B^0 case, or a kaon, in that of the B_s^0, from the b quark fragmentation chain or from the decay of excited B states. Flavour-specific decay channels such as $B^+ \to J/\psi K^+$, $B^0 \to J/\psi K^\star(K^+\pi^-)$ and $B^0 \to D^0\mu^+\nu_\mu$ are employed to optimise and calibrate the flavour-tagging algorithms. As an example of the tagging performance, Fig. 10.7 shows the observed flavour asymmetry as a function of the B meson proper time for decays $B^0 \to D^0\mu^+\nu_\mu$. The initial flavour at production was determined using opposite side lepton and kaon tags, the flavour at decay is given by the charge of the final state muon. The flavour oscillation is clearly visible and in good agreement with the known $B^0\bar{B}^0$ oscillation frequency Δm_d.

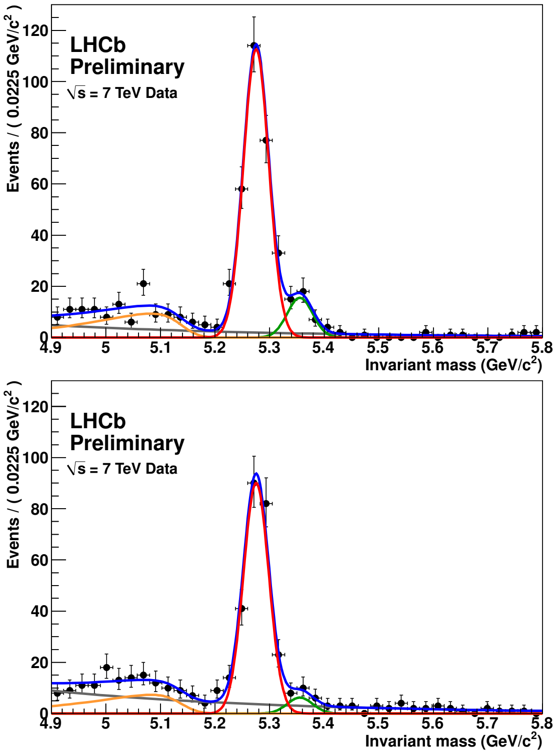

Fig. 10.6 – Invariant mass distributions for $B_d^0\,,\bar{B}_s^0 \to K^+\pi^-$ (top) and $\bar{B}_d^0\,,B_s^0 \to K^-\pi^+$ (bottom). Red: fitted signals from B_d^0 and $\bar{B}_d^0$ decays; green: B_s^0 and $\bar{B}_s^0$ decays; yellow: background from mis-identified three-body decays; grey: combinatorial background. No corrections were made for production- and detector asymmetries.

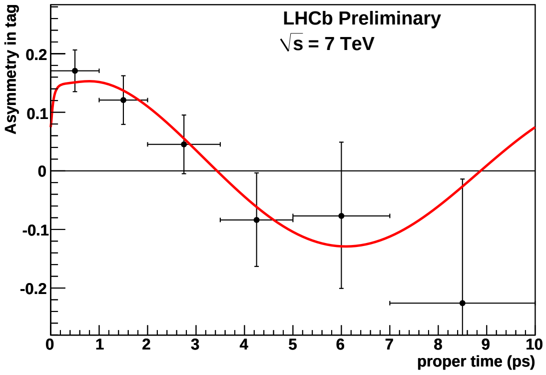

Fig. 10.7 – Flavour asymmetry as a function of the B proper time in $B \to D\mu\nu_\mu$ decays. Opposite-side lepton and kaon taggers were used to tag the initial flavour of the B meson. The overlayed fit function was obtained fixing Δm_d to its PDG value [38].

10.3.4 The rare decay $B_s \to \mu\mu$

A. Büchler, Ch. Elsasser, J. van Tilburg, N. Serra and O. Steinkamp are deeply involved in this key LHCb measurement. The present best upper limits on the branching fraction, reported by the Tevatron experiments [34; 35], are still an order of magnitude above the SM prediction $(3.35 \pm 0.32) \times 10^{-9}$ [33] leaving room for a clear NP signal. On the other hand, reducing the current limits would severely constrain the parameter space for NP models [36]. An upper limit close to the best limits reported by the Tevatron experiments is obtained already from the relatively small data set. This first LHCb result has been shown at conferences and is accepted for publication [37]. For 1 fb^{-1} collected in 2011, a 90% exclusion limit approaching the SM branching fraction is expected if no signal is observed. A 5σ observation of the SM value will require 6-10 fb^{-1}. The analysis strategy is described in detail in Ref. [2]. An important feature is the extensive use of control channels in order to reduce the dependency on simulation. Here, the analysis profits from the large samples of hadronic two-body B decays that LHCb collects.

One of the fields of activity of our group is the calibration of the invariant mass likelihood. The $\mu^+\mu^-$ invariant mass is the main variable distinguishing signal from background. The invariant mass resolution for B_s was studied by Ch. Elsasser by interpolating the resolution for the resonances J/Ψ, $\Psi(2S)$, $\Upsilon(1S)$, $\Upsilon(2S)$ and $\Upsilon(3S)$. The result was found in good agreement with the invariant mass resolution extracted from $B \to hh$ decays.

An alternative method which is expected to reduce the background is studied by A. Büchler. In her thesis she determines an event-by-event invariant mass error for each $\mu^+\mu^-$ candidate by propagating the errors on the muon momenta and the opening angle between the two muons obtained from the track and vertex fit. The method corrects for biases in the errors given by the track and the vertex. It is calibrated and tested using other two-body decays such as $J/\Psi \to \mu^+\mu^-$, $J/\Psi \to \mu^+\mu^-$ and $B \to hh$. At hadron colliders the luminosity and the production cross section are generally poorly known so it is more convenient to do relative measurements. There are several well known $B_{d,u}$ branching ratios measured by B-factories which can be used. In particular the $B^+ \to J/\Psi K^+$ branching ratio is known at 3% level. This mode has a similar trigger and the same particle identification as the $B_s \to \mu^+\mu^-$ decay. The dominant uncertainty with this strategy will be the ratio of fragmentation fractions $f_s/f_{d,u}$, which was measured to about 12% precision at LEP [39].

A method for determining f_s/f_d in a model independent way using the relative yields of $B^0_{d,s} \to D^-_{d,s}\pi^+$ and $B^0_{d,s} \to D^-_{d,s}K^+$ measured by LHCb has been proposed [40]. A precision of 6-9% on f_s/f_d from this analysis is expected by summer 2011. Preliminary results with a precision close to the world best were presented at winter conferences [12].

10.3.5 Lepton Flavour Violating B-decays

Given the large number of B-mesons, the high momentum resolution and efficient particle identification, LHCb has the potential to greatly improve the sensitivity to Lepton Flavour Violating B-meson decays, e.g. $B_s \to e^\pm\mu^\mp$ and $B_s \to \mu^\pm\tau^\mp$. These decays are forbidden in the SM but they are allowed in several of its extensions, the simplest of these being the Pati-Salam model [41], where a leptoquark exchange can mediate these decays at tree level.

Here we can profit of our groups experience in rare decays, in particular $B_s \to \mu^+\mu^-$. Ch. Elsasser, collaborating with N. Serra and O. Steinkamp, will focus on the study of these decay channels using 2011-2012 data.

10.3.6 $B^0 \to K^\star\mu^+\mu^-$

Angular distributions in the rare decay $B^0 \to K^\star\mu^+\mu^-$ give rise to several observables that are sensitive to NP contributions [42]. Very promising is the forward-backward asymmetry A_{FB}, defined by the angle between the μ^- direction and the direction of the B^0 measured in the rest frame of the $\mu^+\mu^-$ system. First measurements of A_{FB} as a

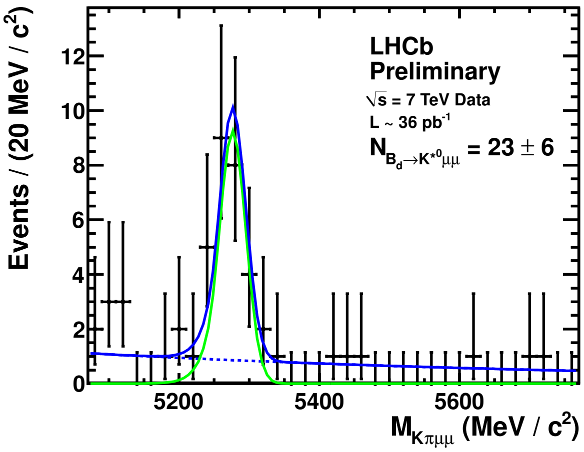

Fig. 10.8 – $K\pi\mu\mu$ invariant mass distribution showing a clear $B^0 \to K^\star\mu^+\mu^-$ signal.

function of the dilepton invariant mass squared q^2 have been published by the BaBar [43], Belle [44] and CDF [45] collaborations. All three experiments observed a flipped sign of A_{FB} in the low q^2 region, larger than predicted by the SM although the statistical precision is still too low for definitive conclusions.

Already with the 37 pb^{-1} of data accumulated in 2010, LHCb observes a clear $B^0 \to K^\star\mu^+\mu^-$ signal, as shown in Fig 10.8. With only 100 pb^{-1} of data, LHCb will reach a sensitivity to A_{FB} that is similar to the current measurements from the B factories and CDF. Assuming the same central value as measured by Belle, a 5 σ deviation from the SM could be measured by LHCb with about 1 fb^{-1} of data.

One of the most critical aspects of the analysis are possible biases on the angular distributions due to detector acceptance and selection cuts. J. Anderson, M. De Cian, Ch. Salzmann and N. Serra play a key role in this aspect of the analysis. Given the good agreement between measurement and simulation demonstrated with 2010 data we intend to make event-by-event corrections based on the simulation. The procedure will be validated on the control channel $B^0 \to J/\Psi(\mu^+\mu^-)K^\star$ which has the same final state as the $B^0 \to K^\star\mu^+\mu^-$ but about 50 times more statistics. A similar strategy will be used to evaluate systematics uncertainties. Ch. Salzmann has shown how this validation can be performed using $B^0 \to J/\Psi K^*$ data collected in 2010. The correction uses several inputs such as the particle identification efficiencies. M. De Cian is studying how to extract these efficiencies from the measurement using a tag and probe method.

10.3.7 Forward electroweak physics

J. Anderson, A. Bursche, N. Chiapolini, and K. Müller are involved in measurements of W, Z and Drell-Yan production in the forward region which provide an important test of the SM. Theoretical predictions are known to next-to-next-to leading order in perturbative QCD [46] and the uncertainties vary between 3% and 10% depending on rapidity, where the dominant uncertainty is due to the knowledge of the parton distribution functions (PDFs) of the proton. Measurements of the differential cross sections for electroweak bosons decaying into muon final states and the ratios of these cross sections can probe the parton density functions at low x where the PDFs are hardly constrained by previous measurements and also test the QCD predictions in a previously unexplored region. Preliminary results on differential cross section measurements and ratios of W and Z production based on 16.5 pb^{-1} have been presented at several conferences [19].

The results are summarised in Fig. 10.9 for final state muons having transverse momenta larger

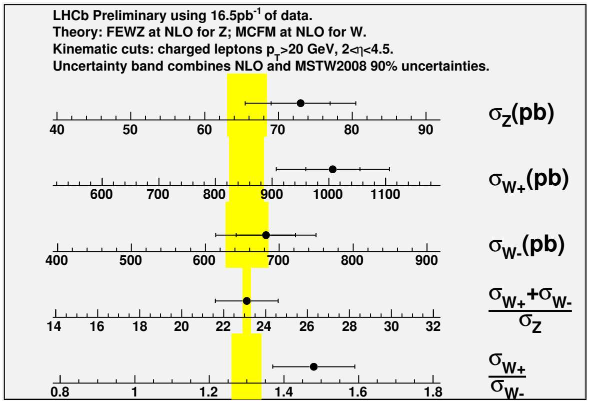

Fig. 10.9 – Summary of W and Z production cross sections and cross section ratios with muons in the pseudo-rapidity range $2 < \eta_\mu < 4.5$ and transverse momentum larger than 20 GeV. The vertical band indicates the theory prediction with its error.

than 20 GeV and lying within pseudorapidities $2 < \eta_\mu < 4.5$. In addition, the invariant mass of the two muons from the Z boson decay must be between $81 < m_Z < 101$ GeV. All cross sections and ratios are in good agreement with next-to-leading order predictions [47]. The precision will significantly improve with a more precise determination of the luminosity. The cross section ratios which are independent of the luminosity and where some of the systematic errors cancel will constitute a very precise test of the SM with increased statistics. Already by the end of 2011 all these measurements will be limited by systematics.

A key ingredient is the determination of various efficiencies from the measured data. Here, our group is making significant contributions. A. Bursche has developed techniques to monitor the trigger efficiency for W and Z which both require one muon with high transverse momentum in the trigger and also for Drell-Yan events which are triggered by the di-muon trigger. The offline tracking efficiency was determined by M. De Cian using a tag and probe method. The same method is used to measure the tracking efficiency in J/Ψ or Υ decays. A tag and probe method is also used by J. Anderson to determine the muon reconstruction efficiency.

In future it is planned to study in more detail the backgrounds for the W analysis and to extend the measurements to events with jets accompanying the electroweak boson (A. Bursche). A detailed understanding of the dominant background (kaons or pions and muons from semileptonic decays) is crucial for the reduction of the systematic error. A measurement of the cross section for jets plus an electroweak boson will be sensitive to the gluon content in the proton. Low mass Drell-Yan will allow to probe PDFs down to Bjorken-x values as low as 10^{-5}. Here, the PDFs are basically not constrained by previous experiments. N. Chiapolini will study Drell-Yan production.

10.4 Summary and outlook

The LHCb experiment has performed very well throughout the 2010 LHC run. About 37 pb^{-1} of data have been recorded, with a data taking efficiency exceeding 90%. A number of early analyses have demonstrated the ability of the LHCb detector to produce high quality results under harsher conditions than the experiment was designed for. Key performance parameters match or are close to expectations from simulation studies. Further improvements are still expected from better calibration and alignment. In addition to what has been discussed in this report, LHCb has already made some world best and world first measurements of B-hadron branching ratios. In several key analyses, sensitivities approaching those of existing measurements can already be expected from the 2010 data sample. With the much larger data sample expected for 2011, LHCb will be able to probe for New Physics signatures.

[1] A.A. Alves Jr. *et al.* [LHCb collaboration], JINST 3 S08005 (2008).

[2] B. Adeva *et al.* [LHCb Collaboration], *Roadmap for selected key measurements of LHCb*, arxiv:0912.4179v2 [hep-ex].

[3] Physik-Institut, University of Zürich, Annual Reports 1996/7 ff.; available at *http://www.physik.unizh.ch/reports.html.*

[4] R. Aaij *et al.* [LHCb Collaboration], Phys. Lett. B**698** (2011) 14-20.

[5] R. Aaij *et al.* [LHCb Collaboration], Phys. Lett. B**694** (2010) 209-216.

[6] Raij *et al.* [LHCb Collaboration], Phys. Lett. B**693** (2010) 69-80.

[7] Preliminary LHCb results presented at 46th Rencontres de Moriond on Electroweak Interactions and Unified Theories, 13 - 20 Mar 2011, La Thuile, Italy, Les Rencontres de Physique de la Vallée d'Aoste, 27 Feb - 5 Mar 2011, La Thuile, Italy, Workshop on Discovery Physics at the LHC, 5 - 10 Dec 2010, Mpumalanga, South Africa, 35th Inter-

national Conference on High Energy Physics, 22 - 28 Jul 2010, Paris, France.

[8] *First observation of the decay* $B_s^0 \rightarrow K^{\star 0}\bar{K}^{\star 0}$
CERN-LHCb-CONF-2011-019.

[9] *A measurement of the relative cross-section* $\sigma(X_{c2})/\sigma(X_{c1})$ *prompt* X_c *production at* $\sqrt{s}$ *= 7 TeV in LHCb*
CERN-LHCb-CONF-2011-020.

[10] *Measurement of the* B_c^+ *to* B^+ *production cross-section ratios at* $\sqrt{s} = 7$ *TeV in LHCb*
CERN-LHCb-CONF-2011-017.

[11] *Inclusive jets and dijets in LHCb*
CERN-LHCb-CONF-2011-015.

[12] *Measurement of the relative yields of the decay modes* $B^0 \rightarrow D\pi^+, B^0 \rightarrow DK^+, B_s^0 \rightarrow D_s^-\pi^+$*, and determination of* fs/fd *for 7 TeV pp collisions*
CERN-LHCb-CONF-2011-013.

[13] *Measurement of direct CP violation in charmless charged two-body B decays at LHCb*
CERN-LHCb-CONF-2011-011.

[14] *Measurement of* Δm_d *in* $B^0 \rightarrow D\pi^+$
CERN-LHCb-CONF-2011-010.

[15] *Observation of double* J/Ψ *production in proton-proton collisions at a centre-of-mass energy of* $\sqrt{s} = 7$ *TeV*
CERN-LHCb-CONF-2011-009.

[16] *First observation of the decay* $\overline{B}_s^0 \rightarrow D^0 K^{\star 0}$ *and measurement of the ratio of branching fractions* $\frac{B(\overline{B}\rightarrow D^0 K^{\star 0})}{B(\overline{B}_d^0\rightarrow D^0 \rho^0)}$
CERN-LHCb-CONF-2011-008.

[17] *Improved Measurements of the Cabibbo Favored Decays* $B_{(s)} \rightarrow D_{(s)}\pi\pi\pi$ *and* $\Lambda_b \rightarrow \Lambda_c\pi\pi\pi$ *Branching Fractions*
CERN-LHCb-CONF-2011-007.

[18] *Measurement of* Δm_s *in the decay* $B_s^0 \rightarrow D_s(K^+K\pi)(3)\pi$
CERN-LHCb-CONF-2011-005.

[19] *W and Z production at* $\sqrt{s}$*= 7 TeV with the LHCb experiment*
CERN-LHCb-CONF-2011-012.

[20] *Optimization and calibration of the LHCb flavour tagging performance using 2010 data*
CERN-LHCb-CONF-2011-003.

[21] *b-hadron lifetime measurements with exclusive* $b \rightarrow J/\Psi X$ *decays reconstructed in the 2010 data*
CERN-LHCb-CONF-2011-001.

[22] *Measurement of the inclusive* Φ *cross-section in pp collisions at* $\sqrt{s}$*=7TeV with the LHCb experiment*
CERN-LHCb-CONF-2010-014.

[23] *Prompt charm production in pp collisions at s = 7 TeV*
CERN-LHCb-CONF-2010-013.

[24] *Measurements of* B^0 *mesons production cross-section in pp collisions at* $\sqrt{s} = 7$ *TeV using* $B^0 \rightarrow D^{\star -}\mu^+\nu_\mu X$ *decays*
CERN-LHCb-CONF-2010-012.

[25] *Measurement of prompt* $\overline{\Lambda}/\Lambda$ *and* $\overline{\Lambda}/K_S^0$ *production ratios in inelastic non-diffractive pp collisions at s = 0.9 and 7 TeV*
CERN-LHCb-CONF-2010-011.

[26] *Measurement of the* J/Ψ *production cross-section at* $\sqrt{s}$ *= 7 TeV in LHCb*
CERN-LHCb-CONF-2010-010.

[27] *Measurement of the* $\overline{p}/p$ *ratio in LHCb at* $\sqrt{s}$ *= 900 GeV and 7 TeV*
CERN-LHCb-CONF-2010-009.

[28] *Prompt* K_S^0 *production in pp collisions at* $\sqrt{s}$ *= 900 GeV*
CERN-LHCb-CONF-2010-008.

[29] R. Aaij *et al.* [LHCb Collaboration], *Measurement of* J/Ψ *production in pp collisions at* $\sqrt{s}$ *= 7 TeV*, submitted to Eur. Phys. J. C, arXiv:1103.0423 [hep-ex].

[30] T. Sjöstrand, S. Mrenna and P.Z. Skands,
J. High Energy Phys.**0605** (2006) 026.

[31] D.J. Lange,
Nucl. Instrum. and Meth. A**462** (2001) 152.

[32] P. Abreu *et al.* [DELPHI Collaboration],
Phys. Lett. B**341** (1994) 109;
O. Adriani *et al.* [L3 Collaboration],
Phys. Lett. B**317** (1993) 467;
D. Buskulic *et al.* [ALEPH Collaboration],
Phys. Lett. B**295** (1992) 396.

[33] M. Blanke, A. Buras, D. Guadagnoli and C. Tarantino, JHEP 0610:003 (2006).

[34] V. Abazov *et al.* [D0 Collaboration],
Phys. Lett. B**693** (2010) 539.

[35] CDF preliminary, *Search for* $B_s^0 \to \mu^+\mu^-$ *and* $B_d^0 \to \mu^+\mu^-$ *Decays in 3.7* fb^{-1} *of* $p\overline{p}$ *Collisions with CDFII*, CDF Public Note 9892.

[36] O. Buchmüller *et al.*, Eur. Phys. J. C**64** (2009) 391.

[37] R. Aaij *et al.* [LHCb Collaboration], *Search for the rare decays* $B_s^0 \to \mu^+\mu^-$ *and* $B^0 \to \mu^+\mu^-$, accepted by Phys. Lett. B, arxiv:1103.2465v1 [hep-ex].

[38] K. Nakamura *et al.* [Particle Data Group], J. Phys. G **37** (2010) 075021.

[39] D. Asner *et al.*, *Averages of b-hadron, c-hadron, and tau-lepton Properties*, arXiv:1010.1589,

[40] R. Fleischer, N. Serra and N. Tuning, Phys. Rev. D**82** (2010) 034038.

[41] J. Pati and A. Salam, Phys. Rev. D**10** (1974), 275.

[42] J. Altmannshofer *et al.*,
JHEP **0901** (2009) 019;
F. Kruger and J. Matias,
Phys. Rev. D**71** (2005) 094009;
U. Egede *et al.*, JHEP**032** (2008) 0811.

[43] B. Aubert *et al.*, Phys. Rev. D**79** (2009) 031102.

[44] J.T. Wei *et al.*, Phys. Rev. Lett.**103** (2009) 171801.

[45] T. Aaltonen *et al.*, Phys. Rev. D **79** (2009) 011104.

[46] R. Gavin *et al.*, arXiv:1011.3540 [hep-ph].

[47] J. M. Campbell, R. K. Ellis, Phys. Rev. D**62** (2000) 114012.

11 Particle physics with CMS

E. Aguiló, C. Amsler, S. de Visscher, M. Ivova, B. Millán Mejías, P. Otyugova, C. Regenfus, P. Robmann, J. Rochet, T. Rommerskirchen, A. Schmidt, and J. Storey

V. Chiochia, C. Favaro, A. Jaeger, H. Snoek, and M. Verzetti

in collaboration with: Paul Scherrer Institut (PSI) and the CMS Collaboration

After commissioning with cosmic rays the CMS experiment [1] at the LHC recorded proton collisions in December 2009 at the center of mass energy of 900 GeV. The detector performances had to be verified first by comparing with our current knowledge of the standard model. The mass distributions in Fig. 11.2, obtained after various selection cuts, illustrate some of the known particles "rediscovered" by CMS. A run at the unprecedented energy of 7 TeV took place in March – December 2010, collecting about 40 pb^{-1} (see Fig. 11.1). The data analysis of the 2010 dataset is now well advanced. When writing this report, 41 journal articles by the CMS collaboration had been published or were in print. One of us (V.C.) was Deputy Project Manager of the silicon tracker in 2010 and now chairs the *B*-physics analysis group, that has so far released six journal articles on quarkonium, *B* mesons and inclusive *b*-quark production measurements. One of us (H.S.) convenes the pixel calibration and reconstruction group. The silicon pixel detector is the innermost component of the CMS experiment. It allows a precise reconstruction of charged particles and the identification of secondary vertices from long-lived particles. The 53 cm long barrel pixel section, with about 48 million channels, consists of three cylindrical layers at radii between 4.4 cm and

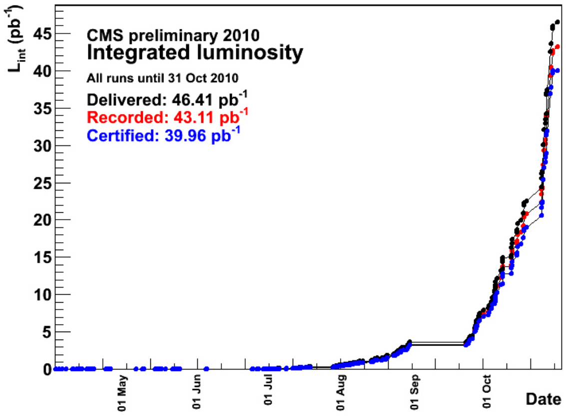

Fig. 11.1 – Integrated luminosity in the 2010 run at $\sqrt{s} = 7$ TeV.

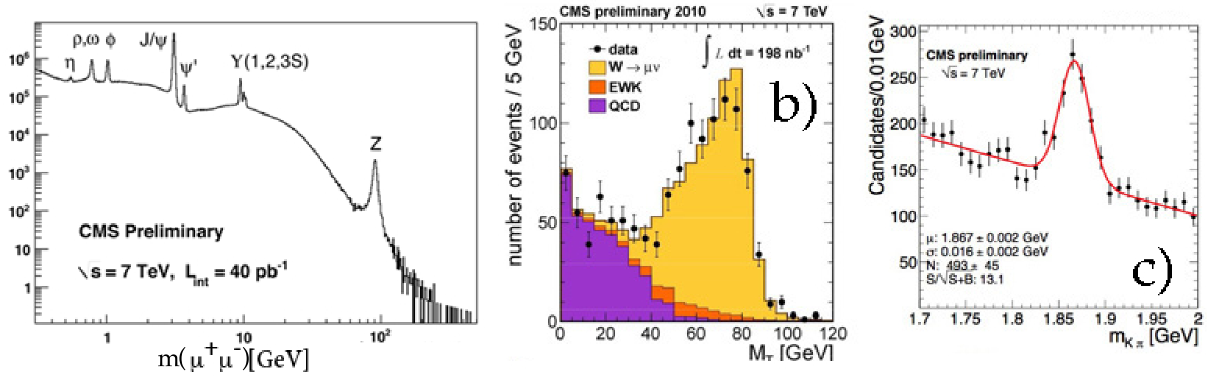

Fig. 11.2 – Some preliminary results obtained during summer 2010: a) $\mu^+\mu^-$ mass distribution showing the vector mesons and the Z^0 peak; b) transverse mass distribution of muons showing the (Jacobian) peak from $W \to \mu\nu$ decay; c) $K^-\pi^+$ mass distribution showing the D^0.

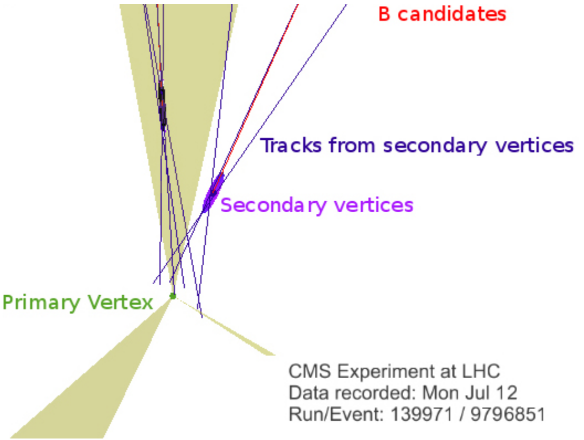

Fig. 11.3 – CMS event showing two displaced vertices from B hadron decays [5].

10.2 cm. Two endcap disks at each side of the barrel section provide coverage up to large rapidities. Details can be found in various publications such as [2–4]. Figure 11.3 shows an event with two displaced vertices from b hadron decays.

11.1 Commissioning of the silicon pixel detector

Our first priority was to measure the pixel detector performance with LHC collisions and to compare with expectations. We performed several important measurements and calibrations, ranging from the detector occupancy to position resolution [6]. The position resolution was improved with the larger data samples collected at $\sqrt{s}$ =7 TeV. The technique was based on pairs of consecutive hits along a trajectory in the overlap region between two adjacent modules within a layer (see last year's annual report). The data were compared to predictions from the detailed PIXELAV simulation [7]. The transverse and longitudinal resolutions are shown in Fig. 11.4 as a function of cluster length. The agreement between data and prediction is remarkable, demonstrating the excellent understanding of the detector response already in the early phase of its operation.

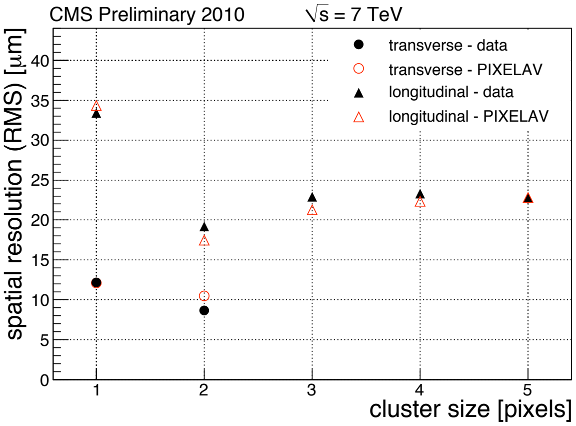

Fig. 11.4 – Transverse and longitudinal hit position resolution of the pixel barrel detector compared to the predictions from PIXELAV simulations.

11.2 Improvements to hit and track reconstruction

Searches for the Higgs boson and Supersymmetry depend heavily on the identification of τ leptons and b-quarks. Since the transverse momentum of the τ jet is large compared to the τ mass, the decay pions emerge as collimated jets in which individual tracks become inseparable with increasing momentum. Hits in the pixel sensors merge forming broad clusters (in the inner-most pixel layer when the opening angle between two trajectories is below 5 mrad). For a typical 3-prong τ decay this angle corresponds to a transverse momentum of 150 GeV/c. Hit merging deteriorates the reconstruction of the τ mass, thus excellent spatial resolution is needed for τ reconstruction.

Merged clusters generate peaks in the cluster charge distribution at integer multiples of the minimum ionizing energy deposit. We have therefore developed an algorithm to split the merged cluster. The track impact angle on the sensor is used to compare the observed cluster shapes from the expected ones which were simulated with very high-p_t jets. Figure 11.5 shows the track reconstruction efficiency as a function of transverse momentum and opening angle with the closest neighboring track. The cluster splitting technique (red triangles) recovers 20% of the tracking efficiency at large transverse momenta for which the tracks have neighbors with opening angles below 5 mrad.

We also performed a study to determine the effects that possible misalignments of the tracker detectors would have on the J/ψ lifetime fits (which determine the fraction of J/ψ mesons coming from B decays). The effect of the various misalignments led to a relative error in the B-fraction ranging from 0.5 to 9% [8].

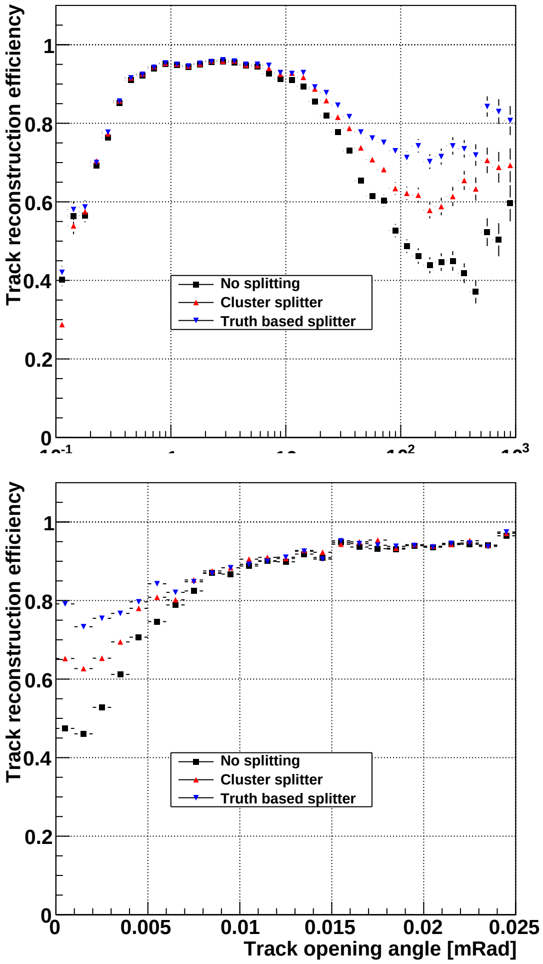

Fig. 11.5 – Track reconstruction efficiency versus transverse momentum for high-p_t jets (top) and of opening angle with the nearest track. The current reconstruction is represented by the black squares; ideal cluster splitting is given by blue triangles while the performance of our splitting algorithm is represented by red triangles.

11.3 Searches for the Higgs boson decaying into $\tau^+\tau^-$

CMS has searched for the neutral Higgs boson[5] decaying into $\tau^+\tau^-$ at $\sqrt{s}$ = 7 TeV using 36 pb^{-1} [9]. The reconstructed $\tau^+\tau^-$ mass distribution for leptonic τ decays is shown in Fig. 11.6. There is no evidence for a Higgs boson signal and we set 95% CL upper bounds on the Higgs boson cross section times the τ pair branching fraction. Furthermore, we can interpret the upper limit in the MSSM parameter space given by the mass of the pseudoscalar state, m_A and the ratio of the vacuum expectation values of the two Higgs doublets, $\tan\beta$, for the benchmark scenario m_h^{max} (Fig. 11.7). The present results exclude a region in $\tan\beta$ down to values smaller than those excluded by the Tevatron for m_A < 140 GeV/c^2, and significantly extend the excluded region of

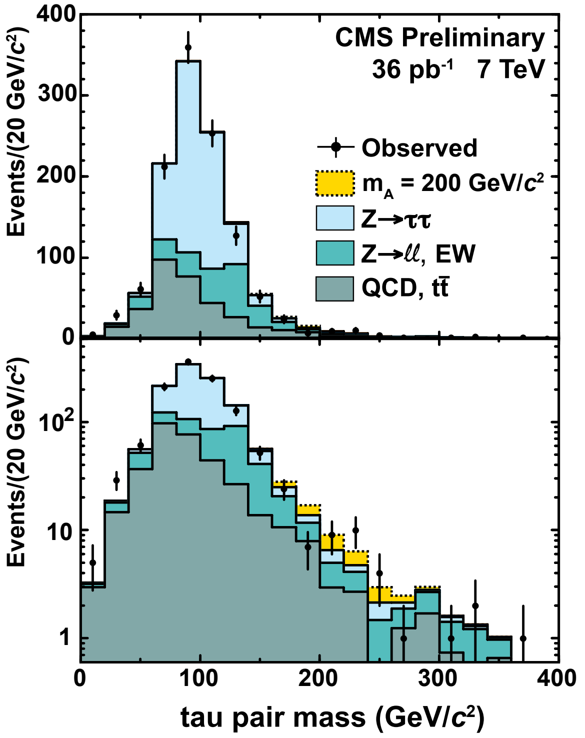

Fig. 11.6 – Reconstructed τ pair invariant mass distribution (linear and logarithmic scales) with the expected backgrounds. The possible contribution from a Higgs boson (m_A =200 GeV/c^2) is shown in yellow.

---

[5] Minimum Supersymmetric Standard Model (MSSM) Higgs.

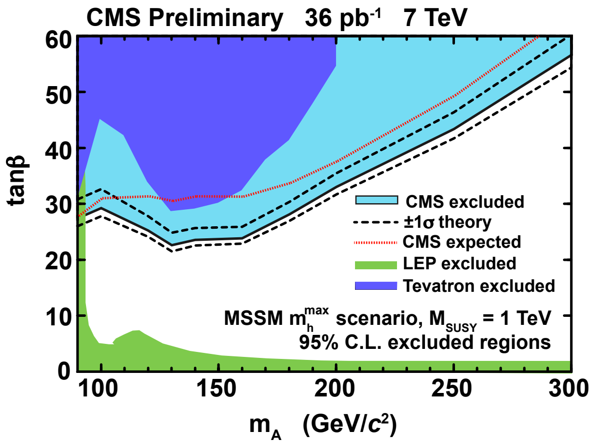

Fig. 11.7 – Regions in parameter space of $\tan\beta$ vs. m_A excluded at 95% CL by CMS, Tevatron and LEP.

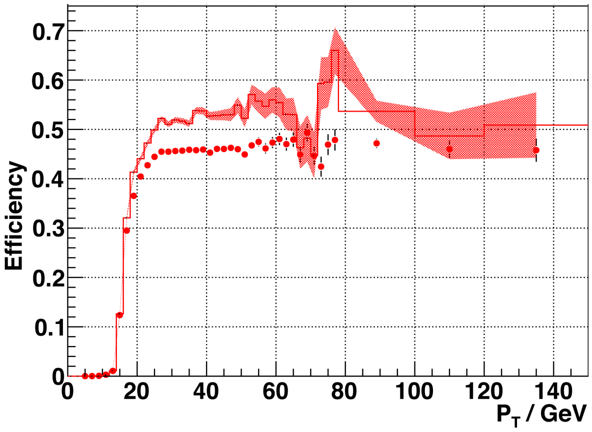

Fig. 11.8 – τ reconstruction efficiency as a function of transverse momentum for two scenarios, corresponding to the 2010 (solid histogram) and 2011 (circles) running conditions.

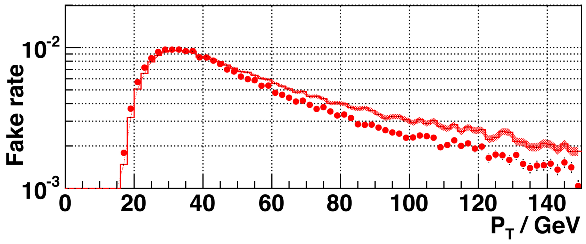

Fig. 11.9 – Fake rate as a function of the τ transverse momentum for 2010 (solid histogram) and 2011 (circles) running conditions.

MSSM parameter space at larger values of m_A.

We are preparing data driven measurements of the τ identification efficiency and studying τ tagging performance using different collision pile-up scenarios. Hadronic τ decays mainly lead to one or three charged pions, with or without neutral pions. The identification algorithm starts with a charged hadron at high transverse momentum, combining with other nearby reconstructed charged hadrons and neutral pions, retaining the combinations consistent with τ decay kinematics. The most isolated one is then selected. Figures 11.8 and 11.9 show the identification efficiency and background contamination from Monte Carlo simulation in two luminosity scenarios for the 2010 and 2011 data taking. A loss of efficiency is observed in 2011 due to the increase in pile-up events. We are optimizing the algorithm to cope with the new running conditions and will soon release an updated Higgs exclusion limit for this channel.

11.4 $B_s \to J/\psi\ \phi$

The decay $B_s \to J/\psi(\to \mu^+\mu^-)\phi(\to K^+K^-)$ is a benchmark channel for CMS for which we have prepared the corresponding software. We are studying this channel to determine the B_s mass and average lifetime of the B_s^H and B_s^L eigenstates. An analysis of the angular correlations can be performed to extract $\Delta\Gamma_s$. Since the expected value for $\Delta\Gamma_s/\Gamma_s$ is small (around 0.2) the mean lives of the two eigenstates are difficult to measure directly from the decay length distribution. However, the two states contribute differently to the angular correlations between the decay particles. We expect to achieve an r.m.s uncertainty of 0.04 on $\Delta\Gamma_s/\Gamma_s$ for an integrated luminosity of about 1 fb^{-1} [10] which should easily be reachable in 2011.

The B_s candidates are selected first with the two-muon trigger, requiring opposite sign muons and reconstructing the J/ψ with a transverse momentum larger than 0.5 GeV/c. The two hadrons (transverse momentum above 0.7 GeV/c) are assumed to be kaons. Their invariant mass is required to be within 10 MeV/c^2 of the known ϕ mass. A

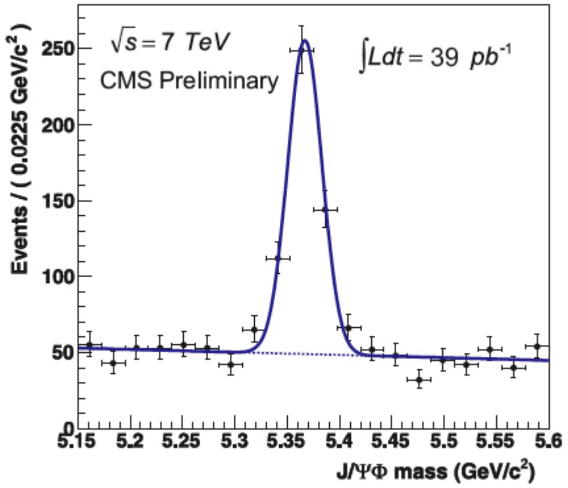

Fig. 11.10 – $(\mu^+\mu^)K^+K^-$ invariant mass distribution at $\sqrt{s} = 7$ TeV and $\mathcal{L} = 39$ pb^{-1} showing 377 ± 26 B_s decays.

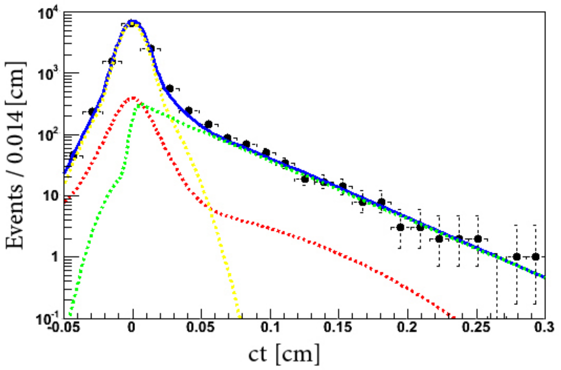

Fig. 11.11 – Decay length distribution with likelihood fit. Red: background; yellow: prompt background; green: signal; blue: total.

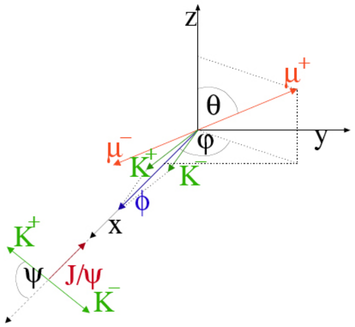

Fig. 11.12 – Definition of the angles θ, ϕ and ψ that describe $B_s \to J/\psi\ \phi$ decay.

kinematic fit constraining the J/ψ mass and a cut on the B_s decay length ($c\tau/\sigma > 3$) are then applied. Figure 11.10 shows the B_s with an integrated luminosity of 39 pb^{-1}, obtained by CMS at 7 TeV. The fitted mass is 5367.0 ± 1.2 MeV (compared to the PDG value of 5366.3 ± 0.6 MeV [11]). Figure 11.11 shows the decay length distribution for the B_s. A two-dimensional likelihood fit was applied. The result from the fit is $c\tau = 454.6 \pm 15.8\ \mu$m (compared to the PDG value of 425.0 ± 12.6 μm).

Figure 11.13 shows our preliminary distributions for the angles θ, ϕ and ψ (defined in Fig. 11.12) for the data collected so far in 2010 and 2011. The similarities with Monte Carlo simulation using the decay parameters from ref. [10] are quite encouraging.

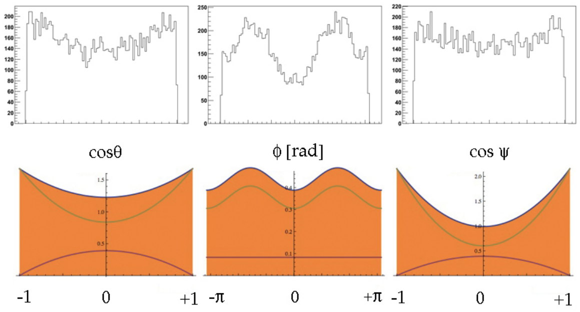

Fig. 11.13 – Top: Measured distributions of $\cos\theta$, ϕ and $\cos\psi$ obtained with 46 pb^{-1} at 7 TeV. Bottom: Predictions for CP-odd (pink) and CP-even (green) B_s-states [10].

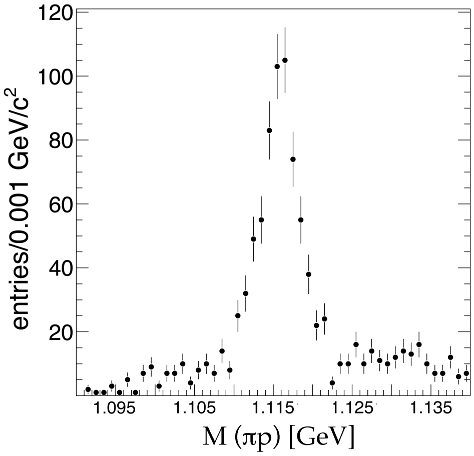

Fig. 11.14 – πp invariant mass distribution showing the Λ ($\bar{\Lambda}$).

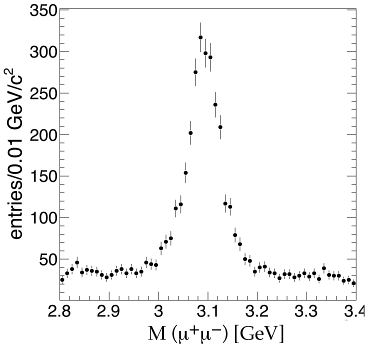

Fig. 11.15 – $\mu^+\mu^-$ invariant mass distribution showing the J/ψ.

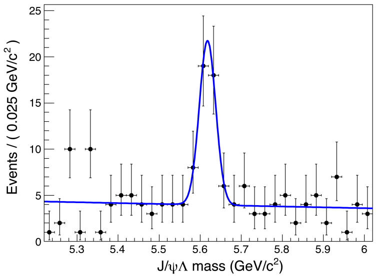

Fig. 11.16 – $J/\psi\Lambda$ invariant mass distribution with 40 pb^{-1} of data (36 ± 9 events) with Λ_b fit (blue line).

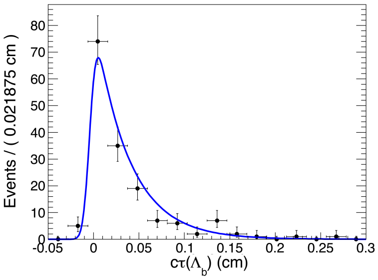

Fig. 11.17 – Λ_b proper decay length distribution.

11.5 Study of b–baryons

The spectroscopy of heavy baryons is of interest to QCD and to models of the strong interaction [12]. The quark model predicts 56 heavy ground state baryons (with at least one c or b-quark). So far only 8 b-baryons have been observed, but the evidence often rests on a handful to a few dozen events.

The study of heavy baryons by our group was launched with a study of the neutral Λ_b (udb). The decay channel $\Lambda_b \to J/\psi\ \Lambda$ with $J/\psi \to \mu^+\mu^-$ and $\Lambda \to \pi^- p$ can be studied at CMS. Both Λ_b and Λ are long-lived particles, traveling up to several centimeters before decaying (leading to displaced vertices), and muons in the final state which can be triggered on. The Λ (Fig. 11.14) is combined with the $J/\psi \to \mu^+\mu^-$ (Fig. 11.15) to form Λ_b candidates. Distributions of invariant mass and proper decay length of the Λ_b are shown in Figs. 11.16 and 11.17, respectively.

These data were collected in 2010 with an integrated luminosity of 40 pb^{-1}. A clear Λ_b mass peak is observed after applying a series of cuts (e.g. reasonably large transverse momenta and proper decay length $c\tau(\Lambda) > 1$ cm, $c\tau(\Lambda_b) > 50$ μm). A maximum likelihood fit was performed with a single Gaussian plus a linear background for the mass distribution, and a Gaussian plus exponential function for the proper decay length. We obtain $M(\Lambda_b) = 5618 \pm 5$ MeV and $c\tau(\Lambda_b) = 379 \pm 33$ μm (statistical errors only) in agreement with the known values (5620.2 ± 1.6 MeV, resp. 417 ± 11 μm [11]).

The reconstructed Λ_b candidates are a starting point to search for further heavy baryons, the $\Sigma_b^{(*)+}$ (uub) and $\Sigma_b^{(*)-}$ (ddb). The dominant decay mode is $\Sigma_b \to \Lambda_b\pi$, a strong decay that takes place at the primary vertex. The selection of the soft pion coming from Σ_b is not easy in the dense environment around the primary vertex. Apply-

Fig. 11.18 – Q-value distribution for $\Sigma_b \to \Lambda_b\pi$ for positive (left) and negative (right) charges from the first 40 pb^{-1} of data. The blue line shows a simultaneous maximum likelihood fit.

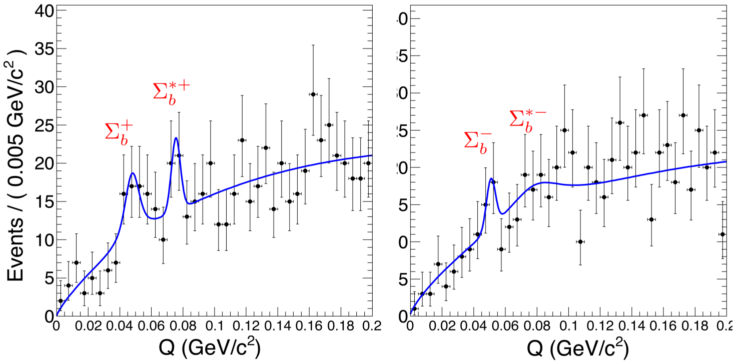

ing loose cuts in view of the still limited statistics, and combining each Λ_b candidate with an extra track, leads to four potential peaks from Σ_b states. Figure 11.18 shows the reconstructed Q-value distribution of the decay $\Sigma_b \to \Lambda_b\pi$ where $Q = M(\Lambda_b\pi) - M(\Lambda_b) - M(\pi)$. The theoretically predicted Q-values lie in the range 0.03 – 0.1 GeV [13]. A simultaneous maximum likelihood fit was applied with a smooth function to parameterize the background and a Breit-Wigner distribution convoluted with a Gaussian for each mass peak. Equidistance between the peak mean values were required. Our preliminary measurements are in agreement with theoretical expectations and the measurements by CDF [14]. These early indications of signals from the very first and limited LHC data make the study of b-baryons very promising.

Triggers specific to particular processes will be needed as the luminosity increases. CMS reconstructs b-hadrons through their decay into a $J/\psi \to \mu^+\mu^-$. Triggering on J/ψ is achieved with the high level trigger on $\mu^+\mu^-$ and the additional requirement that the J/ψ should be emitted from a secondary vertex. However, many channels such as $\Lambda_b \to J/\psi(\to \mu^+\mu-)\Lambda(\to p^+\pi^-)$, $\Xi_b^- \to J/\psi(\to \mu^+\mu-)\Xi^-(\to \Lambda\pi^-)$, $\Omega_b^- \to J/\psi(\to \mu^+\mu-)\Omega^-(\to \Lambda K^-)$ have long-lived particles leading to tertiary vertices far away from the J/ψ vertex, often beyond the pixel detector. The straightforward approach is to select high transverse momentum tracks (proton from Λ decay) with large impact parameter with respect to the secondary and primary vertices. A second lower transverse momentum track (e.g. pion from Λ decay) is then required. This work is in progress.

11.6 b-jet tagging

Identifying jets containing b-decays ("b-tagging") is an essential tool for a wide range of topics in and beyond the Standard Model [15]. In CMS b-tagging tools have been applied in e.g. measurements of the inclusive b- and t-quark production cross-sections.

We have been involved in b-tagging since many years with one of us (A.S.) coordinating the commissioning of b-jet identification with 7 TeV collision data [16]. The crucial device for good b-tagging performance is the pixel detector which reconstructs charged tracks close to the proton-proton interaction point. One of the most important quantities is the impact parameter (IP),

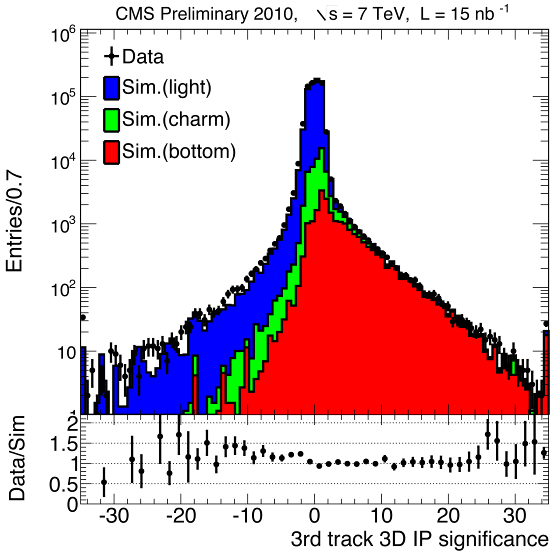

Fig. 11.19 – Impact parameter (IP) significance of the third track in a jet (ordered by IP significance) compared to simulation results for light, charm and jets.

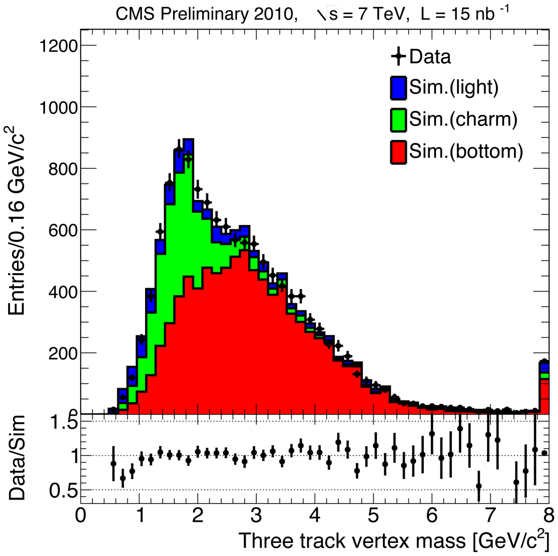

Fig. 11.20 – Invariant mass of secondary vertices with at least three tracks compared to simulation results.

the distance of closest approach of a trajectory to the proton-proton interaction vertex. The IP significance of the third track in a jet is shown in Fig. 11.19. The tail in this distribution is quite sensitive to b-quarks, and is therefore used as discriminator in a high purity b-tagging algorithm. The secondary vertex from B decays can be reconstructed using the so-called adaptive vertex fitting technique [17]. A secondary vertex with three or more tracks has a high probability of being a B decay vertex. The flight distance which is defined as the separation between the primary and secondary vertices is used in the b-tagging algorithm.

Another important quantity is the invariant mass of the secondary vertex, assuming pions. This quantity is shown in Fig. 11.20 for vertices with three or more tracks. With the vertex mass one can distinguish between light flavours, charm and beauty. This was used in the measurement of the inclusive b production cross-section [18], the first precision measurement using b-tagging in CMS. First results on performance in b-tagging have been published [16] but systematic errors are still large. Our group continues to play a leading role in the b-tagging group in 2011.

In parallel with CMS studies of the inclusive cross-section for $pp \rightarrow b + X$ we contributed to the study of the angular correlation between pairs of B mesons. We have enhanced the performance of the b-tagging algorithm to reconstruct two b-jets with close spacial separation. We select events with one secondary vertex each which have similar spatial coordinates (distance smaller than typically 20μm), mix them pairwise and reconstruct them. Events for which both initial secondary vertices are reconstructed in the mixed events are then counted. The efficiency of the vertex finder is calculated as the fraction of the number of secondary vertices in the mixed sample to the corresponding number in both event samples before mixing. The efficiency was studied as a function of vertex separation ΔR, defined as $\sqrt{\Delta\eta^2 + \Delta\phi^2}$, where η is the pseudorapidity and ϕ the azimuthal angle.

On the other hand, we have predicted the fraction of b-quarks produced collinearly or not, that is via gluon-splitting or through flavor creation/excitation, respectively. This study, made with `Pythia` and `Madgraph`, led to a first estimate of the relative importance of the "gluon splitting" peak compared to the back-to-back region mainly due to flavor creation or excitation. This was calculated for different p_T ranges of the leading jet (Fig. 11.21. The ΔR dependence of the double vertex reconstruction efficiency (Fig. 11.22) shows very good agreement for the shape between data and simulation, with discrepancies below 2% [19]. Efficiencies of typically 90% for the double vertex reconstruction can be reached.

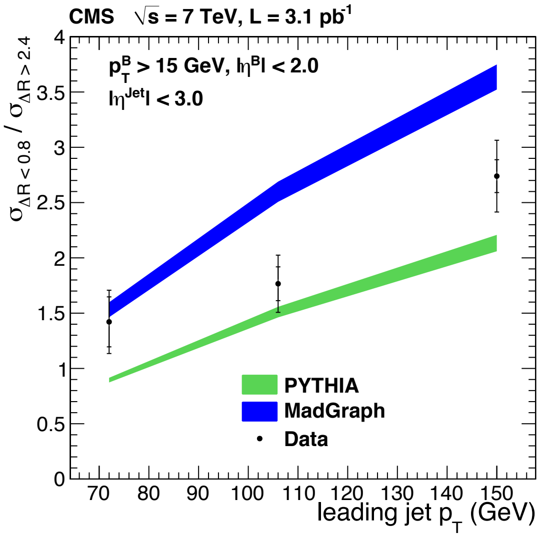

Fig. 11.21 – Ratio between the gluon splitting region (ΔR <0.8) and the back-to-back region (ΔR >2.4) for three values of the p_T cut.

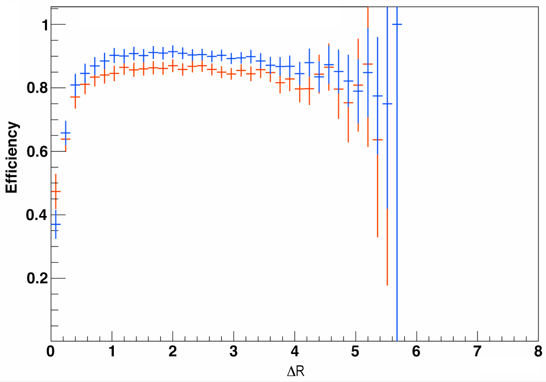

Fig. 11.22 – Double vertex reconstruction efficiency as a function of ΔR for a vertex separation of 20 μm. The data are shown in red, the simulation in blue.

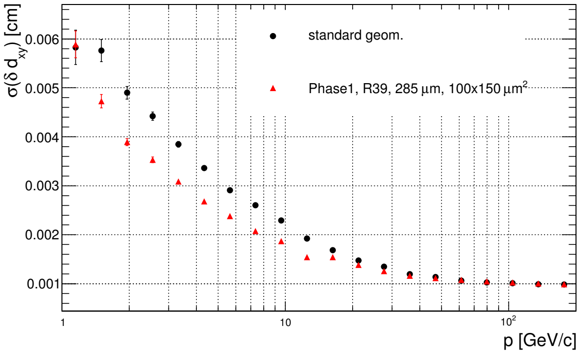

Fig. 11.23 – Transverse impact parameter resolution versus number of tracks at a luminosity of 10^{34} cm^{-2}s^{-1}, before and after the upgrade.

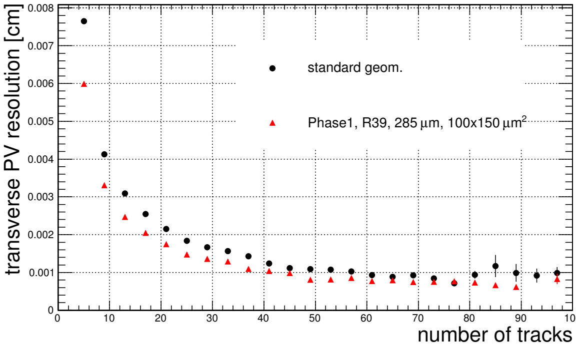

Fig. 11.24 – Transverse primary vertex position resolution as a function of the number of tracks.

11.7 Preparations for the pixel detector upgrade

The pixel system will be replaced in 2016 – 2017 during the "Phase 1" luminosity upgrade. Major modifications to the detector layout and to the readout electronics will be needed to prevent data losses and to provide sufficiently good performance in hit and track reconstruction. The new detector will include an additional fourth barrel layer and one disk in each endcap section. The passive material will be reduced by up to a factor of two in the central tracking region, thanks to the new readout electronics and evaporative cooling technique. Adopting the 0.13 μm CMOS technology for the front-end chip in the innermost layers is currently under evaluation.

We have assessed the performance of the upgraded detector [20]. For the transverse impact parameter resolution the expected enhancement is about 25% in the barrel (Fig. 11.23) and up to 40% in the endcaps. The transverse primary vertex resolution will improve by about 20% (Fig. 11.24). A 20% improvement is expected on decay vertices from b-hadrons. A replacement of the innermost sensors will be required after the high luminosity run. Up to 50% improvement in spatial resolution and reconstruction performance was estimated with thinner sensors with smaller pixel cells (75×100 μm^2). Data taking with CMS resumed in March 2011 and will continue during 2012, with a short break during the winter holidays. The LHC luminosity in 2011 already exceeded 3.5×10^{32} cm^{-2}s^{-1}, surpassing the values from 2010. The expected integrated luminosity 2011/12 is several fb^{-1}. The machine should be able to reach the design center-of-mass energy of $\sqrt{s} = 14$ TeV after the 2013 – 2014 shutdown.

[1] S. Chatrchyan *et al.* [CMS Collaboration], Journal of Instrumentation **3** (2008) S08004.

[2] Y. Allkofer *et al.*, Nucl. Instr. Meth. in Phys. Research **A 584** (2008) 2.

[3] V. Chiochia *et al.*, Nucl. Instr. Meth. in Phys. Research **A 568** (2006) 51.

[4] A. Schmidt *et al.*, Journal of Instrumentation **4** (2009) P05003.

[5] V. Khachatryan *et al.* [CMS Collaboration], JHEP **1103** (2011) 136.

[6] V. Khachatryan *et al.* [CMS Collaboration], Eur. Phys. J. C **70** (2010) 1165.

[7] M. Swartz, Nucl. Instrum. Meth. **A 511** (2003) 88.

[8] V. Khachatryan *et al.* [CMS Collaboration], Eur. Phys. J. **C 71** (2011) 1575.

[9] V. Khachatryan *et al.* [CMS Collaboration], CMS-PAS-HIG-10-002.

[10] L. Wilke, PhD-Thesis, University of Zurich (2009).

[11] K. Nakamura *et al.* (Particle Data Group) J. Phys. G: Nucl. Part. Phys. **37** (2010) 075021.

[12] E. Klempt and J.-M. Richard, Rev. Mod. Phys. **82** (2010) 1095.

[13] W.Y.P. Hwang and D.B. Lichtenberg, Phys. Rev. **D 35** (1987) 3526.

[14] T. Aaltonen *et al.*, Phys. Rev. Lett. **99** (2007) 202001.

[15] A. Schmidt, Proceedings of Science (EPS-HEP 2009) 439.

[16] The CMS Collaboration, CMS Physics Analysis Summary BTV-10-001 (2010).

[17] R. Fruewirth, W. Waltenberger, and P. Vanlaer, CMS Note 2007/008 (2007).

[18] The CMS Collaboration, CMS Physics Analysis Summary BPH-10-009 (2010).

[19] CMS collaboration, submitted to J. of High Energy Phys.

[20] C. Favaro, Nucl. Instrum. Meth in Phys. Research **A** (in print).

12 Superconductivity and Magnetism

M. Bendele, S. Bosma, Z. Guguchia, A. Ichsanov (till September 2010), H. Keller, A. Maisuradze (since April 2010), F. Murányi (till September 2010), J. Roos (till April 2010), S. Siegrist (since January 2010), E. Stilp (since December 2010), S. Strässle (till August 2010), S. Weyeneth, B. M. Wojek (till January 2011)

Visiting scientists: D. Di Castro, M.V. Eremin, B. Graneli, B.I. Kochelaev, R. Puzniak, A. Shengelaya

Emeritus members: K.A. Müller (Honorarprofessor), T. Schneider (Titularprofessor), M. Mali, J. Roos

in collaboration with:
ETH Zürich (J. Karpinski), Paul Scherrer Institute (K. Conder, R. Khasanov, E. Morenzoni), Max-Planck-Institute for Solid State Research Stuttgart (A. Bussmann-Holder), University of Geneva (Ø. Fischer, J. M. Triscone), University of Rome (D. Di Castro), Kazan State University (A. Dooglav, M. V. Eremin, B. I. Kochelaev), Polish Academy of Sciences (R. Puzniak), Tbilisi State University (A. Shengelaya).

We report on research projects in the field of high-temperature superconductors (HTS's) and materials with novel electronic properties. Our studies involve various complementary techniques, such as muon-spin rotation (μSR), electron paramagnetic resonance (EPR), nuclear magnetic resonance (NMR), nuclear quadrupole resonance (NQR), and SQUID and torque magnetometry. Besides focusing on cuprates and conventional superconductors, the investigations have been extended to the recently discovered iron-based superconductors.

12.1 Search for orbital currents in superconducting $YBa_2Cu_4O_8$

The concept of orbital currents (OC's) was proposed to explain the pseudogap of the cuprate superconductors [1]. However, the present state of knowledge about OC's is contradictory both in theory and experiment. No evidence for local fields was found i.e. in a yttrium nuclear magnetic resonance (NMR) investigation by our group [2].

Recently, Zeeman perturbed nuclear quadrupole resonance was applied to evaluate weak magnetic fields in the context of OC's in cuprate superconductors [3]. The magnetic environment of the barium atom in *c*-axis oriented powder samples of $YBa_2Cu_4O_8$ was investigated in the pseudogap phase at 90 K. The Ba atom is of particular interest since it is situated outside, but close to the copper oxide bilayer, at a position where the combined fields from the two neighboring layers would be enhanced because of the suggested ferromagnetic order within the bilayer. Zeeman perturbed nuclear resonance makes use of the fact that the Ba atom has both a quadrupolar and a nuclear magnetic moment. This technique is a rarely implemented variant of nuclear quadrupole resonance (NQR), which utilizes the local electric field gradient to lift the nuclear spin degeneracy. The Zeeman perturbation is introduced by means of an external coil as a weak static magnetic field (of order mT). For a typical ^{137}Ba NQR resonance line of a few hundred kHz width (see inset of Fig. 12.1), the resonance line split caused by a field of the order of mT would not be directly observable. The principle of the measurement is to detect a weak local magnetic field through a beat oscillation superposed on the Gaussian shaped decay of the spin echo intensity, caused by homonuclear dipolar fields (Fig. 12.1). In order to demonstrate the sensitivity of the technique for weak local magnetic fields, the Ba nucleus was studied at 300 K, where no OC's are expected. The result of this measurement is presented in Fig. 12.1, revealing the expected dominating Gaussian decay of the spin echo intensity with pulse separation time τ. This curve is our zero-field reference. The measurement procedure was calibrated using applied Zeeman fields of known strength. Fields calculated from the response were found to deviate less than 0.07 mT from the Zeeman fields actually applied with the calibrated external coil. In all experiments, background contributions, including Earth's magnetic field, were shielded.

In conclusion, the results, as evident from Fig. 12.2 do not indicate the presence of local fields at the Ba site in the pseudogap phase of c-axis oriented $YBa_2Cu_4O_8$. The detection limit of our method excludes static or dynamic field larger than 0.07 mT and 0.7 mT, respectively [3].

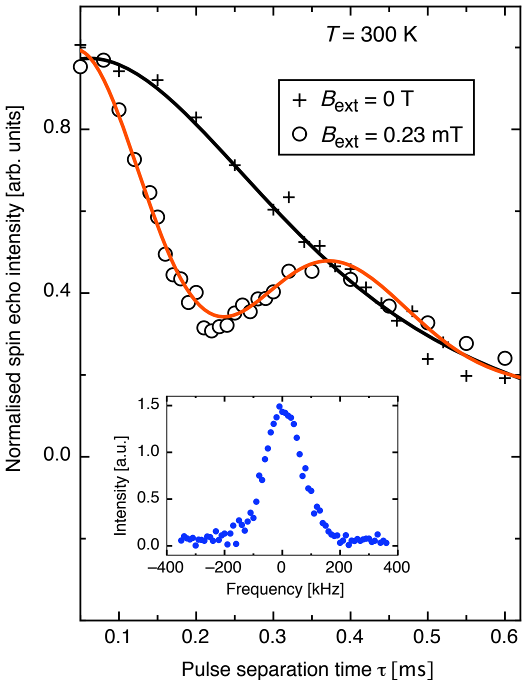

Fig. 12.1 – Dependence of the normalized ^{137}Ba spin-echo intensity as a function of the pulse separation time τ at 300 K for B_{ext} parallel to the c-axis of $YBa_2Cu_4O_8$. Results are shown for B_{ext} =0 T and B_{ext} =0.23 mT. The inset shows the ^{137}Ba resonance line at 300 K in zero external field.

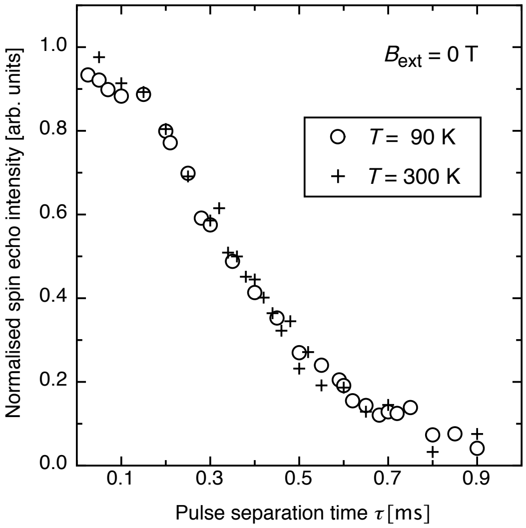

Fig. 12.2 – Spin echo intensity decay with pulse separation time τ in c-axis oriented $YBa_2Cu_4O_8$ for no applied field at 300 K and 90 K. No distinguishable difference in the normalized intensity was detected in the pseudogap phase.

[1] S. Chakravarty *et al.*,
Phys. Rev. B **63**, 094503 (2001).

[2] S. Strässle *et al.*,
Phys. Rev. Lett. **101**, 237001 (2008).

[3] S. Strässle *et al.*,
Phys. Rev. Lett. **106**, 097003 (2011).

12.2 Iron isotope effects in the iron-based superconductor $FeSe_{1-x}$

In 1990 we started a project on isotope effects in cuprate HTS's at the University of Zurich. Since then we performed a number of isotope effect studies. As a result, we observed several novel oxygen isotope ($^{16}O/^{18}O$) effects (OIE's) on different quantities in cuprate HTS's, including i.e. the transition temperature T_{c}, the in-plane magnetic penetration depth $\lambda_{ab}(0)$, the pseudogap temperature T^{*}, the superconducting energy gap Δ_0, the Néel temperature T_{N}, and the spin-glass freezing temperature T_g [1; 2]. All these unconventional OIE's clearly indicate that lattice effects are effective in all phases of cuprate HTS's imposing serious constraints on theoretical models [3].

Recently, we started an investigation of the Fe iso-

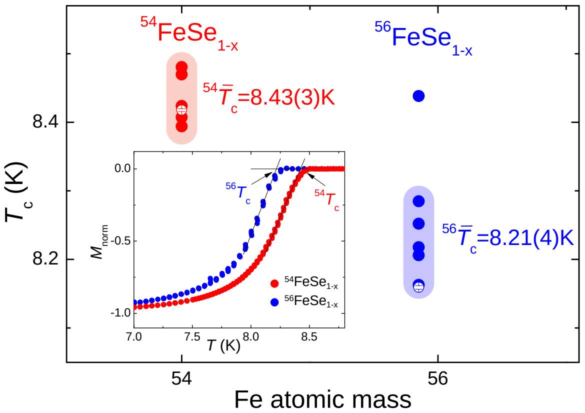

Fig. 12.3 – The superconducting transition temperature of $FeSe_{1-x}$ as a function of Fe atomic mass. The open symbols correspond to the samples studied by neutron powder diffraction. The inset shows the normalized magnetization curves for a pair of $^{54}FeSe_{1-x}$ and $^{56}FeSe_{1-x}$ samples.

tope effect (FeIE) on T_c in the iron-based superconductor $FeSe_{1-x}$ belonging to the "11" family [4]. The substitution of natural Fe (containing ≃ 92% of ^{56}Fe) by its lighter isotope ^{54}Fe in $FeSe_{0.975}$ ($T_c \simeq 8.2$ K) leads an isotope shift of the transition temperature of $\Delta T_c = 0.22(5)$ K, corresponding to an FeIE exponent $\alpha_{Fe} = 0.81(15)$ (see Fig. 12.3) [4].

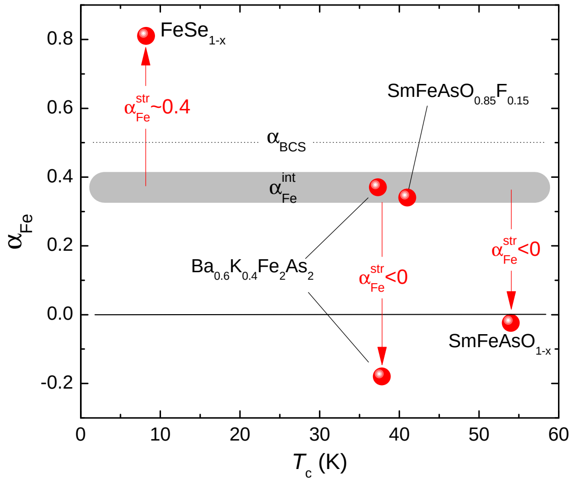

Fig. 12.4 – Fe isotope exponent α_{Fe} versus superconducting transition temperature ($FeSe_{1-x}$ [4], $Ba_{0.6}K_{0.4}Fe_2As_2$ and $SmFeAsO_{0.85}F_{0.15}$ [6], $Ba_{0.6}K_{0.4}Fe_2As_2$ [7], and $SmFeAsO_{1-x}$ [8]). The arrows indicate the direction of the shift from the intrinsic FeIE exponent $\alpha^{int}_{Fe} \simeq 0.35$ to 0.4 caused by structural effects.

This value is positive and considerably larger than the BCS value $\alpha_{BCS} = 0.5$.

In addition, the lattice parameters of the ^{54}Fe /^{56}Fe exchanged $FeSe_{1-x}$ samples were investigated carefully by neutron powder diffraction. It turned out that the *a*- and *b*-axes are slightly larger for $^{54}FeSe_{1-x}$ than those for $^{56}FeSe_{1-x}$, while the *c*-axis is marginally smaller for $^{54}FeSe_{1-x}$ than for $^{56}FeSe_{1-x}$. However, the volume of the unit cell remains unchanged. These slight differences in the lattice constants in the Fe isotope exchanged samples give rise to a slight change of the shape of the Fe_4Se pyramid and anion height which is known to affect T_c in Fe-based HTS's [5], and in turn may contribute to the total Fe isotope shift of T_c [4].

The currently reported results of the FeIE on T_c in Fe-based HTS's are highly controversial. The values of the FeIE exponent α_{Fe} for various families of Fe-based HTS were found to be as well positive ($\alpha_{Fe} \simeq 0.3$ to 0.4) [6], as negative ($\alpha_{Fe} \simeq$ -0.18 to -0.02)) [7; 8], or even to be exceedingly larger than the BCS value $\alpha_{BCS} = 0.5$ as found for $FeSe_{1-x}$ ($\alpha_{Fe} \simeq 0.8$) [4]. Recently, we have shown [9] that the Fe isotope substitution causes small structural modifications which, in turn, affect T_c. Upon correcting the isotope effect exponent for these structural effects, an almost unique value of $\alpha_{Fe} \simeq 0.35$ to 0.4 is found for at least three different families of Fe-based HTS (see Fig. 12.4).

[1] G. M. Zhao *et al.*,
J. Phys.: Condens. Matter **13**, R569 (2001).

[2] H. Keller, in *Superconductivity in Complex Systems*, edited by K. A. Müller and A. Bussmann-Holder, Structure and Bonding 114, Springer-Verlag, Berlin, Heidelberg, New York (2005) pp. 114-143.

[3] H. Keller, A. Bussmann-Holder, and K. A. Müller,
Materials Today **11**, 38 (2008).

[4] R. Khasanov *et al.*,
New J. Phys., **12**, 073024 (2010).

[5] Y. Mizuguchi *et al.*,
Supercond. Sci. Technol. **23**, 054013 (2010).

[6] R. H. Liu *et al.*,
Nature (London) **459**, 64 (2009).

[7] P. M. Shirage *et al.*,
Phys. Rev. Lett. **103**, 257003 (2009).

[8] P. M. Shirage *et al.*,
Phys. Rev. Lett. **105**, 037004 (2010).

[9] R. Khasanov *et al.*,
Phys. Rev. B **82**, 212505 (2010).

12.3 NMR study of the iron-pnictide system $EuFe_{1.9}Co_{0.1}As_2$

Among the iron-based pnictide HTS's, the family $EuFe_{2-x}Co_xAs_2$ is particularly interesting since Eu^{2+} is a rare-earth ion with a $4f^7$ electronic configuration and a total electron spin S=7/2. This compound is built up by $[FeAs]^{2-}$ layers, separated by layers of magnetic Eu^{2+} ions [1]. $EuFe_2As_2$ exhibits both a spin density wave (SDW) ordering of the Fe moments and an antiferromagnetic ordering of the localized Eu^{2+} moments below 190 K and 19 K, respectively [1; 2]. In contrast to the other '122' systems, where the substitution of Fe by Co leads to superconductivity [3], the compounds containing Eu^{2+} exhibit the onset of a superconducting transition but seem to be hindered to reach zero resistivity at ambient pressure [4]. The study of the interaction between the localized Eu^{2+} moments and the conducting Fe_2As_2 layer is important for the understanding of superconductivity. The conduction electrons essentially determine the unusual superconducting properties and the high T_c's.

In order to investigate the coupling between the Eu and $Fe_{1.9}Co_{0.1}As_2$ layers as well as to study the magnetic transitions in $EuFe_{1.9}Co_{0.1}As_2$, a combination of X-ray diffraction, magnetization, and ^{75}As nuclear magnetic resonance (NMR) experiments were performed on single crystals [5]. Magnetic susceptibility as well as ^{75}As-NMR measurements reveal a decrease of the SDW transition temperature to T_{SDW}=120 K for $EuFe_{1.9}Co_{0.1}As_2$.

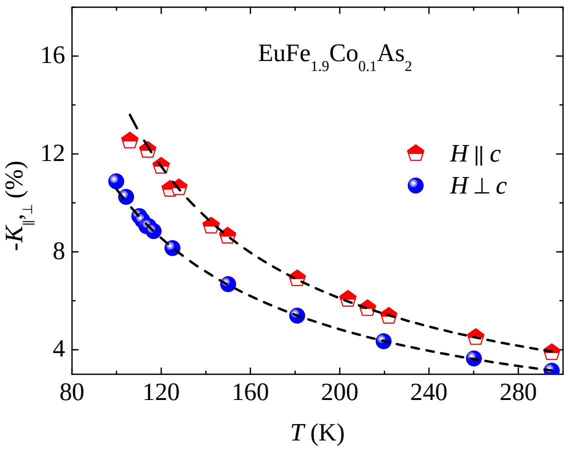

Fig. 12.5 – Temperature dependence of the ^{75}As magnetic shift in a single crystal $EuFe_{1.9}Co_{0.1}As_2$ for $H \parallel c$ and $H \perp c$. The dashed lines represent the Curie-Weiss behavior.

It was found that the ^{75}As NMR spectra are characterized by a large negative frequency shift with respect to the ^{75}As NMR Larmor frequency for all orientations of the magnetic field with respect to the crystallographic c-axis. The temperature dependence of the ^{75}As magnetic shift K above T_{SDW}=120 K is well described by a Curie-Weiss-like behavior $K(T)=K_0+C_K/(T+\Theta)$ for both $H \parallel c$ ($K_\parallel$) and $H \perp c$ ($K_\perp$) (see Fig. 12.5). This suggests that the temperature dependent part $K_{Eu}(T)$ of the shift arises from the hyperfine coupling between the ^{75}As nuclei and the Eu^{2+} $4f$ moments. A linear relation between K_{Eu} and the susceptibility χ_{Eu} of the localized Eu^{2+} $4f$ moments was observed, from which the hyperfine coupling constant A_{Eu} = -1.9×10^7 A/m per μ_B was estimated. This value of A_{Eu} is almost 60 times larger than the one reported for the '1111' system [6]. Such a large A_{Eu} indicates a strong coupling between the Eu^{2+} localized moments and the $Fe_{1.9}Co_{0.1}As_2$ layers, suggesting that the magnetic exchange interaction between the localized Eu $4f$ moments is mediated by the itinerant Fe $3d$ electrons. The strong interaction between the localized Eu^{2+} moments and the charge carriers in the $Fe_{2-x}Co_xAs_2$ layers may cause pair breaking [7], which may be the reason why it is difficult to reach superconductivity in $EuFe_{2-x}Co_xAs_2$.

[1] H. Raffius *et al.*, J. Phys. Chem. Solids **54**, 135 (1993).

[2] Y. Xiao *et al.*, Phys. Rev. B **80**, 174424 (2009).

[3] A. S. Sefat *et al.*, Phys. Rev. Lett. **101**, 117004 (2008).

[4] Y. He *et al.*, J. Phys.: Condens. Matter **22**, 235701 (2010).

[5] Z. Guguchia *et al.*, Phys. Rev. B, **83**, 144516 (2011).

[6] P. Jeglič *et al.*, Phys. Rev. B **79**, 094515 (2009).

[7] A. A. Abrikosov *et al.*, Zh. Eksp. Teor. Fiz. **39**, 1781 (1960).

12.4 Pressure effect on superconducting properties of YBa$_2$Cu$_3$O$_x$

YBa$_2$Cu$_3$O$_x$ was the first high temperature superconductor with a superconducting transition temperature T_c above the boiling point of nitrogen. However, the microscopic pairing mechanism leading to high-temperature superconductivity is still not resolved and is subject of intense debates. Hydrostatic pressure is a useful tool to tune the interatomic distances in the lattice which in turn modifies both the lattice dynamics [1] and the exchange coupling between Cu-spins in cuprates [2; 3]. Therefore, a detailed study of the pressure effect on superconducting properties, e.g. the superfluid density $\rho_s \propto 1/\lambda^2$, the gap magnitude Δ_0, and the BCS ratio, may provide important information to clarify the mechanism of superconductivity in the cuprates.

Recently, we performed muon-spin rotation (μSR) studies of the pressure effect on the magnetic penetration depth λ in YBa$_2$Cu$_3$O$_x$ at various oxygen concentrations (6.45$\leqslant x \leqslant$6.98). It is known that there are two contributions determining the pressure effect on T_c: (i) the charge transfer from the chain oxygen sites to the CuO$_2$ planes, and (ii) the pressure effect on the pairing interaction strength [4].

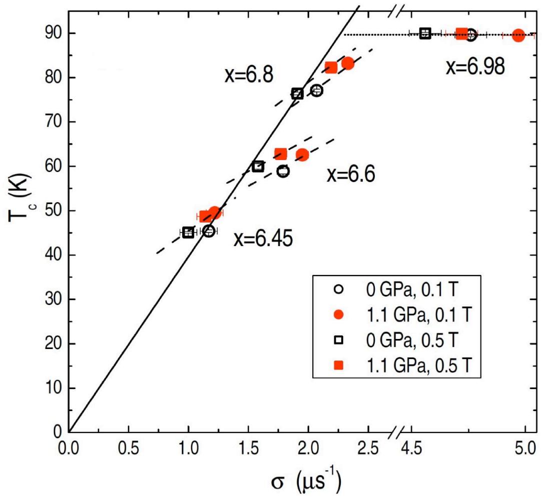

Fig. 12.6 – Uemura plot (T_c vs. σ) at zero and applied pressure $P = 1.1$ GPa for YBa$_2$Cu$_3$O$_x$ at various dopings x. The solid line is the Uemura line while the other lines are guides to the eye. The dashed lines show the pressure effect on the slope $\gamma = \partial\sigma/\partial T_c$ (see text).

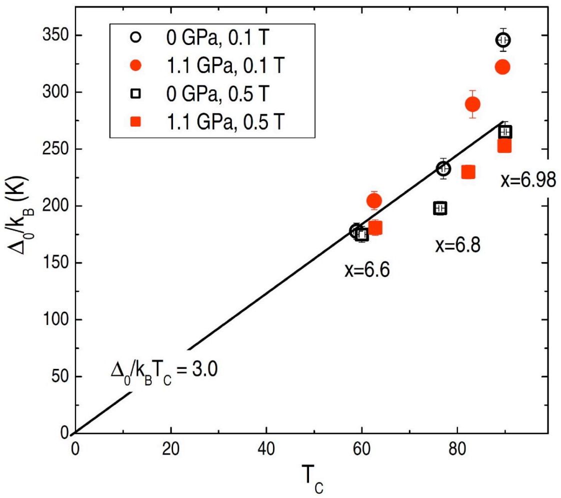

Fig. 12.7 – Relation of the zero-temperature gap Δ_0 and T$_c$ in YBa$_2$Cu$_3$O$_x$ at different dopings, fields, and pressures. The solid line corresponds to $\Delta_0/k_B T_c = 3$.

While the first contribution at ambient pressure follows the Uemura relation [5], the second one, usually determined by the temperature dependence of thermodynamic properties under pressure, is not well studied so far. The μSR technique is a powerful tool to investigate the temperature dependence of the superfluid density $\rho_s \propto \sigma \propto 1/\lambda^2$ at various pressures and fields. From the temperature dependence of the muon depolarization rate σ the value of $\sigma(T{=}0)$ and the gap-to-T_c (Δ_0/T_c) ratio were extracted (Figs. 12.6 and 12.7). Both quantities $\sigma(T{=}0)$ and Δ_0/T_c increase with increasing pressure P, implying that the coupling strength also increases with pressure. Interestingly, the Uemura relation [5] does not hold under pressure. The slope $\gamma = \partial T_c/\partial\sigma \simeq 20$ K$/\mu$s^{-1} is a factor of two smaller than that of the Uemura relation $\gamma_U = 40$ K$/\mu$s^{-1}. Note that the same slope was previously observed for the OIE on the magnetic penetration depth [6]. The parameter γ was found to be independent of the oxygen content for underdoped $YBa_2Cu_3O_x$ with an average value of $\gamma = 20(3)$ K$/\mu$s^{-1}. Taking into account the two mechanisms which increase T_c under pressure mentioned above, the two mechanisms also give rise to an increase of $\sigma = \sigma_U + \sigma_V$. While the first term accounts for the increase of the carrier concentration in the CuO_2 plane according to the Uemura relation, the second term is related to the modified pairing intercation V due to pressure.

Taking $\gamma = 20$ K$/\mu$s^{-1} for underdoped $YBa_2Cu_3O_x$ and using the previously reported value $\partial T_c/\partial P = 4$ K/GPa for underdoped $YBa_2Cu_3O_x$ [7], one may express the pressure effect on σ_V as follows: $\beta_P = \partial \ln\sigma_V/\partial P \equiv (\Delta\sigma_V/\sigma)/\Delta P \simeq 4\ /T_c$ GPa^{-1}. In this form the doping (or T_c) dependence of the pressure effect on σ_V resembles that of the OIE on σ: $\beta_M = \partial\ln\sigma/\partial\ln M$, where $\partial\ln M$ is the relative change of oxygen mass and $\partial P \propto \partial\ln M$. This implies that β_P is finite at optimal doping and increases with decreasing doping (or decreasing T_c). Additional studies should better clarify the relation between β_P and β_M.

In conclusion, both our studies of isotope effects in cuprates and iron-based superconductors and the recent studies on pressure effects on the magnetic penetration depth in doped $YBa_2Cu_3O_x$ strongly suggest that lattice effects are essential for the appearance of superconductivity in these systems.

[1] M. Calamiotou *et al.*, Phys. Rev. B **80**, 214517 (2009).
[2] W. A. Harrison, *Electronic Structure and the Properties of Solids* (Freeman, San Francisco, 1980).
[3] R. Ofer *et al.*, Phys. Rev. B **78**, 140508(R) (2008).
[4] X. J. Chen *et al.*, Phys. Rev. Lett. **85**, 2180 (2000).
[5] Y. J. Uemura *et al.*, Phys. Rev. Lett. **62**, 2317 (1989).
[6] H. Keller in *Superconductivity in complex systems*, ed. K. A. Müller and A. Bussmann-Holder, p. 114, Springer-Verlag Berlin, Heidelberg, New York (2005).
[7] C. C. Almasan *et al.* Phys. Rev. Lett. **69**, 680 (1992).

13 Phase transitions and superconducting photon detectors

A. Aeschbacher, F. von Rohr, H. Grundmann, O. Bossen, K. Inderbitzin, H. Bartolf, M. Reibelt, S. Siegrist, A. Engel and A. Schilling

in collaboration with: University of Bern (K. Krämer), Tohoku University (N. Toyota), Karlsruhe Institut für Technologie (K. Il'in), Deutsches Zentrum für Luft- und Raumfahrt (H.-W. Hübers, A. Semenov), FIRST Lab ETH Zürich, ESRF Grenoble (C. Mazzoli), PSI Villigen (M. Medarde).

13.1 Physics of superconducting thin-film nanostructures and fast single-photon detectors

Within our project on superconducting nanowire single-photon detectors (SNPD, for a description of the detectors and their detection mechanism, see one of the previous reports), we have mainly followed two directions in the past year.

One objective has been to explore alternatives to the NbN thin films that are almost exclusively used for such detectors. A good detector material for SNPD has to fulfill several requirements. An absorbed photon has to generate a large quantity of quasi-particles, *i.e.* broken Cooper-pairs, favoring materials with small superconducting energy gap. The quasi-particles should be concentrated around the absorption site, thus their diffusion coefficient D must be small. And last but not least, the minimum volume needed to become normal-conducting in order to generate a detectable voltage signal should be as small as possible, leading to the requirement of a short coherence length ξ for the dimension in the applied-current direction and a small cross-sectional area of the superconducting strip, *i.e.* ultra-thin films ($\sim$ nanometer) and the applicability of state-of-the-art nanostructuring techniques to achieve strip widths of 100 nm or less.

Although NbN does fulfill all of these requirements it has certain limitations. Besides difficulties in fabricating high-quality thin films—which can in principle be overcome—NbN has a relatively high critical temperature T_c (up to $\approx$ 17 K, depending on film thickness) and thus large energy gap, limiting the useful spectral range to near-infrared and higher-energy photons. In the search for alternatives we have focused on TaN, which is chemically and structurally very similar to NbN. We have started our investigations by preparing a series of TaN thin films in a multi-purpose DC-magnetron sputtering machine (FIRST Lab, ETH Zürich). The films were then dry-etched by reactive-ion etching to form standard 4-point bridges for resistivity measurements. By adjusting the sputtering conditions we could easily vary the nitrogen content in the resulting films and achieve critical temperatures of about $T_c \approx 8$ K for a ≈ 27 nm thick film. Further parameters obtained from an analysis of magneto-conductivity measurements are listed in Tab. 13.1 and are compared to those of NbN [1].

Tab. 13.1 – Some important material parameters of TaN thin films in comparison with NbN. λ is the magnetic penetration depth and N_0 is the electron density of states at the Fermi-energy. Other parameters are explained in the text.

	T_c (K)	$\xi(0)$ (nm)	$\lambda(0)$ (nm)	D (cm^2/s)	N_0 (10^{47} m^{-3}J^{-1})
TaN	8	5.0	700	0.5	2.0
NbN	16	4.5	400	0.5	3.5

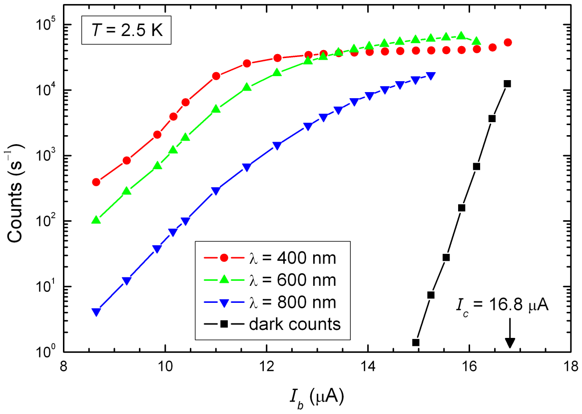

Fig. 13.1 – Count rates of a TaN SNPD measured at 2.5 K as a function of the applied bias current for three different photon wavelengths as indicated in the graph. The dark and background counts are also plotted for comparison. The appearance of a plateau of nearly constant count rates for 400 and 600 nm photons is indicative of absorption-limited detection efficiency.

Our collaborators at the Karlsruhe Institute of Technology were able to further improve the quality of TaN thin film structures in a dedicated sputtering setup. They have now reached critical temperatures up to $T_c \approx 10$ K for relatively thick films, which decreases to ≈ 8 K in films as thin as 3 nm. Very recently we were able to characterize a meander structure of dimensions typical for SNPD. A preliminary analysis of the results shows that it is possible to fabricate successfully operating detectors (see Fig. 13.1). They appear to be stable over extended periods of time with no degradation and can be easily operated over a large range of operating conditions. An extended analysis and comparison to NbN SNPD is under way.

Our interest in TaN as a detector material has been motivated also by a second focus. Although research in SNPD over roughly the last ten years has mainly been aimed at their performance as detectors for visible and near-infrared photons, essentially the same detection mechanism has already been proposed long before for higher energy keV X-ray photons [2] or even for detecting MeV alpha-particles [3]. To be able to test the detector properties for X-ray photons, we have designed and installed a setup with a *NEPTUNE* 50 kV X-ray source from *OXFORD Industries* (see Fig. 13.2), including adequate radiation shielding and, together with the Electronics Workshop, the necessary control electronics for safe operation.

The setup was tested at the end of 2010 with a conventional NbN SNPD that was optimized for optical photons. In Fig. 13.3 we show 20 traces of X-ray absorption events recorded with a digi-

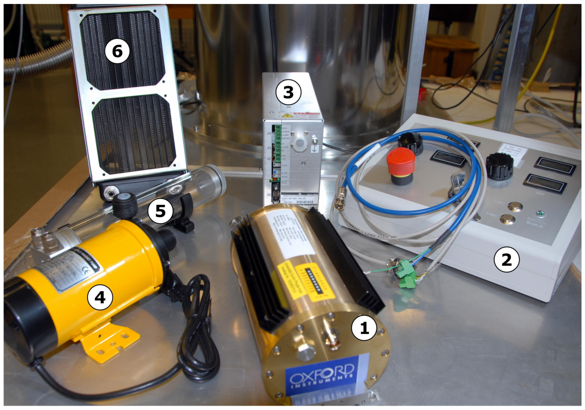

Fig. 13.2 – Parts of the X-ray source setup: 1 X-ray source, 2 control electronics (made in-house), 3 high-voltage supply, 4 water pump, 5 water reservoir, 6 radiator.

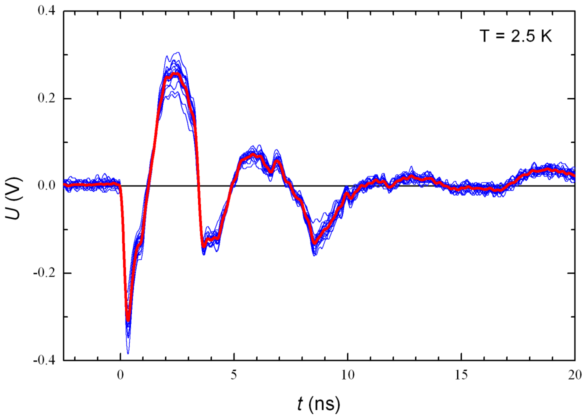

Fig. 13.3 – Traces of 20 recorded pulses after X-ray photon absorption (blue lines) and the average pulse shape (red line).

tal oscilloscope (blue lines) and the average pulse shape of these 20 pulses (red line) demonstrating its functionality. Based on the absorption probability for keV-X-ray photons in nanometer-thin NbN films we have to assume, however, that most of the photons were not absorbed in the superconducting structure, but rather in the sapphire substrate. The corresponding absorption events were thus probably triggered by secondary excitations, *e.g.* phonons or secondary electrons. This fact will have a detrimental effect on the very small jitter of the detector, one of the great advantages of SNPD compared to other single-photon detectors, because the timing of the detection event will depend on the absorption depth inside the substrate.

Therefore, TaN may be the detector material of choice since its absorption length for keV-photons is up to by a factor of 10 shorter than that of NbN. Already 100 nm thick TaN films should have an absorption probability of several percent, which might be sufficient for certain applications. On the other hand, such relatively thick films involve a number of new challenges, particularly for the nanofabrication process. We have adapted our process steps accordingly and we are now able to produce high-quality structures of the required dimensions. Our next goal will be to test X-ray SNPD based on $\sim$ 100 nm thick films.

13.2 First-order phase transition deep in the vortex state of $YBa_2Cu_3O_7$

Small-angle neutron-diffraction experiments (SANS) on the vortex lattice in clean, detwinned and fully oxygenated $YBa_2Cu_3O_7$ single crystals have recently revealed a previously unknown structural phase transitions within the vortex-solid phase . At $T = 2$ K and with the magnetic field directed parallel to the c-axis, its structure changes at $B \approx 2$ T from a low-field hexagonal to a distorted hexagonal phase, and at $B \approx 6.7$ T to a rhombic structure. Based on the observation of the abrupt and discontinuous changes in the lattice structure, these transitions have been suggested to be of first order [5].

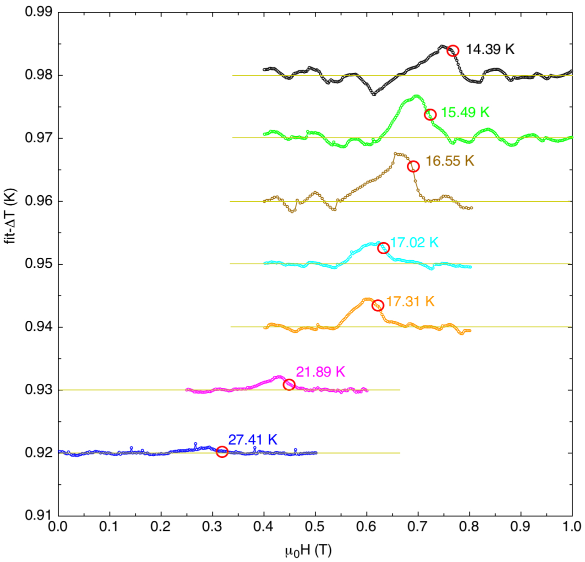

Fig. 13.4 – Magnetocaloric effect measured on a $YBa_2Cu_3O_7$ single crystal on ramping the field $\parallel c$ down. A polynomial background was subtracted and the curves are vertically shifted for clarity.

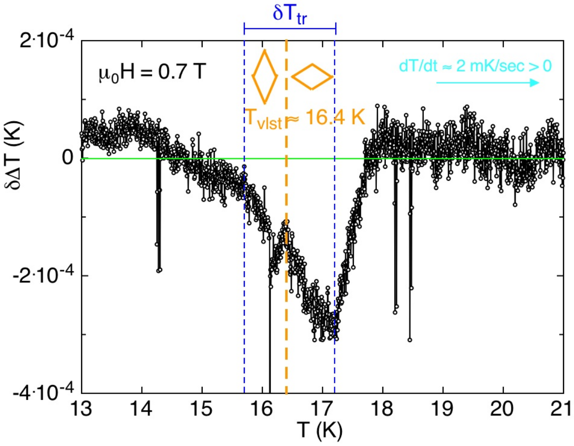

Fig. 13.5 – Temperature DTA scan showing the cooling effect due to the latent heat absorbed at the first-order phase transition.

We have investigated the magnetic phase diagram of one of the $YBa_2Cu_3O_7$ single crystals used in the above mentioned SANS study in our a home-built differential-calorimetry (DTA) setup and in a commercial SQUID magnetometer. In Fig. 13.4 we show the magnetocaloric effect, *i.e.*, the change of the sample temperature on varying the magnetic field, measured with a superimposed longitudinal a.c. magnetic field with an amplitude $\mu_0 h_{ac} \approx$

0.4 mT at a frequency $f = 11$ mHz. On entering the low-field phase from the high-field phase, the sample temperature rises by certain amount before relaxing again to the base temperature of the experiment. In a related experiment in a constant magnetic field but with increasing temperature we observed a corresponding cooling-effect when crossing the phase-transition line from below (Fig. 13.5). The measured variations in sample temperature are therefore indeed related to abrupt changes in entropy of the sample and cannot simply caused by dissipative thermal effects induced by a possible vortex motion that would lead to a heating effect in all cases. Knowing the thermal constants of the experiment, these variations in temperature can be converted to changes in entropy ΔS that we show in an inset of Fig. 13.6 [6].

A further very strong evidence that the observed thermal effects are stemming from a true thermodynamic first-order phase transition comes from corresponding magnetization M measurements, in which we observed step-like features ΔM (not shown here) than can be related to ΔS using the Clausius-Clapeyron relation. The resulting estimated changes in entropy agree reasonably well with the corresponding thermal data (see inset of Fig. 13.6), and we therefore conclude that we have found a thermodynamic evidence for a true first-order phase transition in the vortex state of $YBa_2Cu_3O_7$.

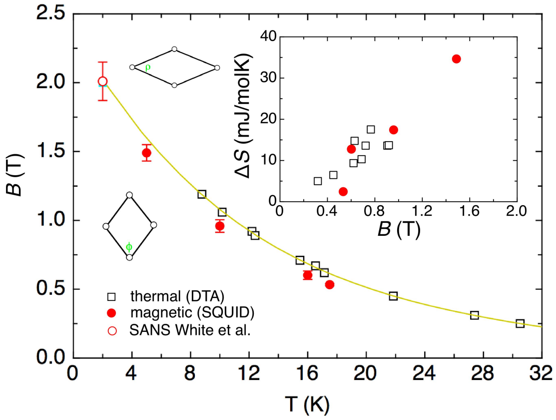

Fig. 13.6 – Phase diagram and entropy difference of a detwinned $YBa_2Cu_3O_7$ single crystal between the high-field and the low-field phase as derived from thermal DTA and SQUID magnetometry data.

13.3 A.c.-calorimetry set up for vortex-shaking experiments

In the last annual report we have announced an a.c. calorimetry set up with a resistive thermometer. The main improvements in the thermal design as compared to our previous set up are a significant reduction of the heat capacity of the sample platform and a replacement of the heat link by an adjustable link consisting of a thin copper wire. This approach has the advantage that the same sample platform can be used over a wide range of temperatures with an appropriate choice of the heat link. The sample temperature is now measured with a resistive thermometer (bare Cernox 1050 chip) in a Wheatstone-bridge configuration. The measuring frequencies in typical a.c.-calorimetry experiments are of the order of 1 Hz or below and are dictated by the sample heat capacity and the thermal conductivity of the used heat link [7]. To reduce both electrical interference and the $1/f$ noise in the fairly noisy environment of the PPMS (*Physical Property Measurement System, Quantum Design Inc.*), the small amplitude of the low-frequency temperature oscillations is measured as follows: we excite the sample thermometer with a carrier frequency of 45 kHz that is modulated with the low-frequency measuring signal. The reference resistor in the Wheatstone bridge is computer controlled and can be automatically adjusted to minimize the measured voltage difference and therefore also to maximize the measuring range of the used lock-in amplifier. The amplitude of the low-frequency component of the signal (typically measured during ≈ 100 sec) is finally obtained by fast-Fourier transformation of the output signal of the lock-in amplifier. In this way, both the $1/f$ noise and other sources of electrical noise are dramatically reduced [8]. With the result of this procedure and the known values for excitation current, frequency and reference resistors we can calculate the resulting amplitude of the low-frequency oscillation in the temperature of the sample platform. This can finally be used to obtain the heat capacity of the sample platform carrying the sample of interest.

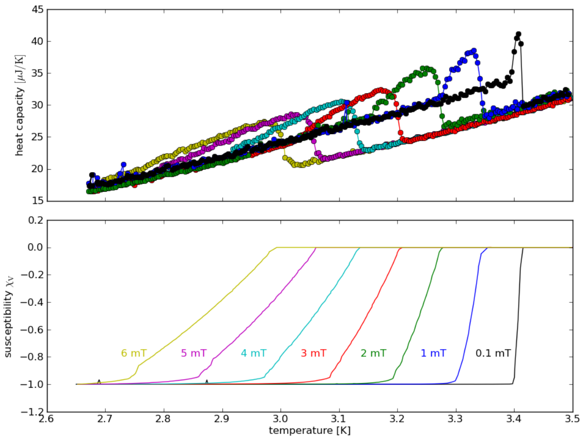

Fig. 13.7 – Upper part: Test measurement of the specific heat of a 37 mg In sample on a sample platform in an external magnetic field, measured with the here described home built a.c. calorimetry experiment. Lower part: Real part of the a.c. susceptibility of the same sample (see text).

In Fig. 13.7 we show the result of a corresponding test measurement, taken at the transition form the normal to the superconducting state of an indium sample (37 mg) in various magnetic fields and with an amplitude ≈ 1 mK of the temperature oscillation. As indium is a type-I superconductor, the transition to superconductivity in a finite magnetic field is of first order (see related peaks in the heat capacity in Fig. 13.7). Moreover, depending on the sample geometry, the sample enters an inhomogeneous intermediate state upon cooling below the transition temperature, which results in a broadening of the transition as measured both by a.c. susceptibility and specific heat (upper and lower part of Fig. 13.7).

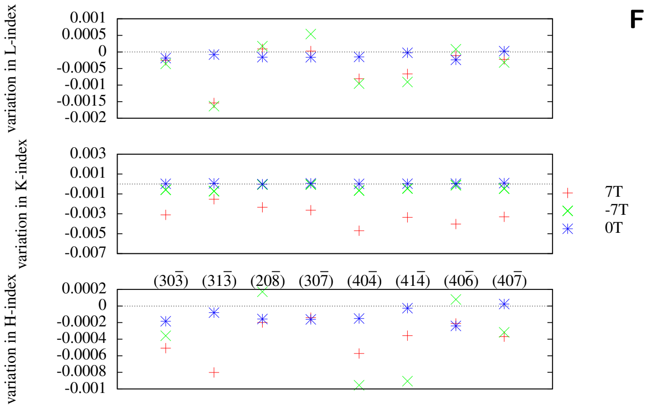

This kind of test measurement confirms that we have achieved a sufficient accuracy for our purpose (detecting first order and continuous phase transitions) with a very low instrumental broadening on the temperature scale (≈ 1 mK). It is worth mentioning that the present design also allows for measurements of the magnetocaloric effect or for conventional continuous-heating and relaxation experiments to measure heat capacities, respectively, with or without the application of an external "shaking" a.c. magnetic field.

13.4 Possible lattice distortion at the Bose-Einstein condensation of magnetic bosonic quasiparticles in TlCuCl$_3$

We have suggested that the positions of the spin-carrying atoms in certain magnetic insulators might discontinuously change at the critical field H_c (*i.e.*, at the onset of antiferromagnetic ordering), in some resemblance to a Spin-Peierls instability in one dimensional magnetic chains [9]. We stated that a thorough structural analysis around this magnetic phase transition of any magnetic insulator is indispensable. We have therefore done corresponding experiments on single crystals of TlCuCl$_3$ (provided by Dr. Karl Krämer, University of Bern), using neutron diffraction and X-ray diffraction methods in order to increase the significance of our experiments.

Fig. 13.8 – Variation of selected X-ray peak positions in applied magnetic fields of $\mu_0 H = 0$ T, 7 T and -7 T, as compared to a first measurement without magnetic field. The shown variation of the peak indices (HKL) is measured with respect to the reciprocal lattice units of the original zero-field measurement based on the unit cell given in [10]. The peaks are labeled in the lower panel and ordered according to their scattering angle. The equal spacing on the x-axis was chosen to increase clarity of the plot and does not reflect the value of the scattering angle.

The X-ray measurements were performed at the ID20-beamline of the ESRF in Grenoble. In order to detect a change in crystal symmetry, eleven peaks were selected, including peaks forbidden by the P 21/c symmetry of $\mathrm{TlCuCl_3}$ in the normal (*i.e.*, unmagnetic) phase. The chosen peaks were studied using a wavelength of $\lambda = 1.4$ Å ($E = 8.9$ keV), near the copper K-edge) at $T = 2.5$ K and applied fields of $\mu_0 H = 0$ T, 7 T and -7 T to eliminate possible magneto-elastic effects of the experimental offset.

We observed apparently field-induced shifts of certain peak positions (see Fig. 13.8). However, we were not yet able to develop a scenario that consistently reproduces all the measured data. Therefore we cannot draw a final conclusion about a possible structural change at the transition to the antiferromagnetic state based on these data alone.

The neutron-diffraction experiments were performed at the RITA-II spectrometer at the PSI in Villigen. The peaks were investigated at $T = 2$ K with several different magnetic fields in a range between $\mu_0 H = 0$ to 13.5 T since it was not possible to identify a clear trend in peak position and intensity based on only two magnetic fields used in the X-ray experiments.

The relative development of the position, height and width of the peaks does not show a common trend nor any abrupt change of relevant magnitude at the critical field $\mu_0 H \approx 6$ T. In Fig. 13.9 we plotted the variation of the corresponding intensities as a function of magnetic field. The change of the lattice parameters was estimated from the change of the peak positions, and the resulting changes in the peak intensity were simulated based on this result. This simulated variation of the peak intensity was by almost one order of magnitude larger than the experimental variation of the peak height, however, which clearly shows that the true change of the peak position must be much smaller than the experimental resolution achieved in this experiment.

To conclude, the proposed sizeable distortion of the crystal symmetry could not be confirmed for $\mathrm{TlCuCl_3}$ up to now.

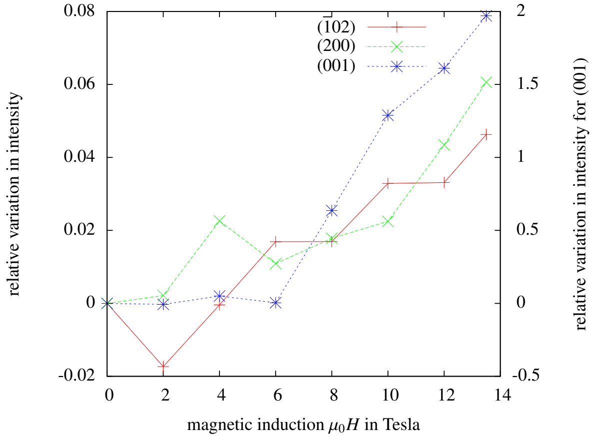

Fig. 13.9 – Relative variation of the neutron peak intensity I. Plotted is the relative difference $(I(0) - I(H))/I(0)$ where $I(0)$ is the measurement for $H = 0$. Note that for the (001)-Peak the right scale applies. The lines are guides to the eye.

[1] H. Bartolf, doctoral thesis,
University of Zürich, 2009.

[2] A. Gabutti *et al.*,
Nucl. Instrum. Methods A, **278**, (1989) 425.

[3] D. E. Spiel *et al.*,
Appl. Phys. Lett., **7**, (1965) 292.

[4] A. J. Kerman *et al.*,
Phys. Rev. B, **79**, (2009) 100 509(R).

[5] J. S. White *et al.*,
Phys. Rev. Lett., **102**, (2009) 097001.

[6] A. Schilling and M. Reibelt,
Rev. Sci. Instrum., **78**, (2007) 033904.

[7] O. M. Corbino, Phys. Zeits., **11**, (1910) 413.

[8] J. H. Scofield, Am. J. Phys., **62**, (1994) 129.

[9] R. Dell'Amore *et al.*,
Phys. Rev. B, **79** (2009) 014438.

[10] H. Tanaka *et al.*,
J. Phys. Soc. Jpn., **70**, (2001) 939.

14 Surface Physics

T. Greber, M. Hengsberger, J. H. Dil, H. Yanagisawa, H. Ma, R. Westerstrøm, L. Castiglioni,
M. Morscher, F. Meier, D. Leuenberger, B. Slomski, S. Roth, H. Cun, A. Hemmi, G. Landolt, M. Greif,
C. Janssen, P. Donà, S. Muff, L. Pazeller, M. Klöckner, J. Osterwalder

The group investigates surface and interface phenomena at the atomic level. For this purpose the surface physics laboratory is well equipped for the preparation and characterization of clean single-crystalline surfaces, metal and molecular monolayer films, as well as covalently bonded single layers, using a wide variety of experimental techniques. In addition, we currently operate two photoemission spectrometers at the nearby Swiss Light Source (SLS), one for spin- and angle-resolved photoemission spectroscopy (SARPES) and one for photoelectron diffraction and holography. Moreover, the group is participating actively in the buildup of the new beamline PEARL (PhotoEmission and Atomic Resolution Laboratory) at the SLS.

The research carried out during the report period can be grouped into four topics:

- **Monolayer films of hexagonal boron nitride (*h*-BN) and graphene on metal surfaces**
  Due to their strong intra-layer sp^2 bonds, these two materials form robust and chemically inert single honeycomb layers that couple weakly to the third dimension. The mechanical stiffness of these bonds leads to the formation of strongly corrugated superstructures with interesting functionalities when grown on top of transition metal surfaces with different lattice constants [1–3]. A prominent example is the boron nitride nanomesh that forms upon high-temperature chemical vapor deposition of borazine on Rh(111) [4]. Graphene forms corresponding structures on Rh(111) and Ru(0001) but with inverted corrugations [5]. These systems are studied in our group within two different contexts. The first one is the synthesis of heteroepitaxial layers of graphene and *h*-BN with a view on future electronic devices based on graphene. Due to its insulating properties and similar crystal structure and lattice constant, *h*-BN appears to be the ideal "gate oxide" [6]. The second context is the exploitation of these corrugated functional layers as templates for the growth of molecular adlayers with defined periodicities. Due to the inertness of these films, they can be brought into water or organic solvents, and we currently explore whether well-organized molecular layers can be deposited directly and much cheaper from solutions. This activity is supported by a Sinergia project of the Swiss National Science Foundation, funding a consortium of four different groups. Because these studies require a large supply of samples, a growth chamber has been built in which *h*-BN or graphene films can be grown on four-inch Si(111) wafers covered with monocrystalline Rh(111) films. The chamber is placed in a dedicated clean-room, which enables us to process these samples in a dust-free environment.

- **Molecular adsorbates and molecular monolayers**
  During this year we have continued to study the assembly of water molecules to small clusters when adsorbed at low temperature on the *h*-BN nanomesh. While coverages near one monolayer lead to the formation of nanoice clusters of typically 40 atoms [7], water hexamers are the most frequent species at much lower coverages. These clusters are trapped by the ring dipoles surrounding the 2 nm wide pores of the nanomesh [3]. Exploratory studies of the adsorption of tetrafluoro-tetracyanoquinodimethane (TCNQF4), a molecule with a high electron affinity, on the nanomesh were carried out with the goal to observe the behaviour of a negatively charged species within the electrostatic landscape of the nanomesh. In a multilayer of

Ar@C$_{60}$ endofullerenes, the hybridization of the Ar 3p electronic level with molecular orbitals of the fullerene cage could be observed for the first time [8]. Finally, resonant x-ray photoelectron diffraction (RXPD) experiments have been performed with circularly polarized light of the SLS in order to combine structural information with sensitivity to magnetism. While this method will in the future be applied to magnetic molecules in order to study their magnetic coupling to a ferromagnetic substrate, a first proof-of-principle experiment has been carried out on a clean Ni(111) sample (see Sec. 14.1).

- **Ultrafast processes at surfaces**
  This past year marks the start of the new NCCR 'Molecular Ultrafast Science and Technology' (MUST) in which our group participates with an activity aimed at femto- and attosecond studies of molecular processes at surfaces. In the first project year a compact angle-resolved photoemission chamber was designed and ordered, which will be moved to various ultrashort pulsed light sources available within the consortium. Concurrently, the existing photoemission chamber equipped with an elliptical display analyzer (EDA) was used to study Bi(114), a stepped surface where strong spin-orbit splitting leads to a spin-split one-dimensional surface state [9]. In a parallel activity, the photo-induced field emission spectra resulting from focussing a pulsed laser beam tightly onto a sharp tungsten tip could be understood quantitatively (see Sec. 14.3).

- **Spin-resolved photoemission and momentum mapping**
  Our spin-resolved photoemission chamber (COPHEE) at the SLS has continued to be in high demand as a general user instrument due to its unique performance. Spectacular results were obtained in collaboration with a group from Princeton University on a novel class of materials, so-called *topological insulators*. Spin-resolved ARPES data measured at the COPHEE end station have helped to demonstrate the spin texture inversion below and above the Dirac point in BiTlSe$_2$ [10] (see Sec. 14.2). In the meantime the group has started its own, independent activity on topological insulators, focusing on the growth of ultrathin films and on new compounds. Moreover, the studies of the Rashba effect in ultrathin Pb films on Si(111) were continued with the goal to influence the spin splitting of the quantum well states by interface engineering. A strong dependence of the electron effective mass of these states on the character of the interface could be explained [11]. Finally, spin state interference was observed in the surface alloy of Sb/Ag(111), a system where the Rashba-type spin splitting of the surface states is smaller than the intrinsic linewidth of their photoemission peaks. As a consequence, the spin polarization vector rotates into the plane perpendicular to the quantization axis of the Rashba system [12].

In the following, three highlights of last year's research are presented in more detail.

[1] T. Greber, e-J. Surf. Sci. Nanotechnol. 8, 62 (2010).

[2] S. Berner *et al.*, Angew. Chem. Int. Ed. 46, 5115 (2007).

[3] J. H. Dil *et al.*, Science 319, 1824 (2008).

[4] M. Corso *et al.*, Science 303, 217 (2004).

[5] T. Brugger *et al.*, Phys. Rev. B 79, 045407 (2009).

[6] C. R. Dean *et al.*, Nature Nanotech. 5, 722 (2010).

[7] H. Ma *et al.*, Chem. Phys. Chem. 11, 399-403 (2010).

[8] M. Morscher *et al.*, Phys. Rev. A 82, 051201(R) (2010).

[9] J. W. Wells *et al.*, Phys. Rev. Lett. 102, 096802 (2009).

[10] Su-Yang Xu *et al.*, ScienceExpress, DOI: 10.1126/science.1201607.

[11] B. Slomski *et al.*, Phys. Rev. B 83, 035409 (2011).

[12] F. Meier *et al.*, J. Phys: Condens. Matter 23, 072207 (2011).

14.1 Resonant photoelectron diffraction (RXPD) for the determination of magnetic and atomic structure

in collaboration with: Frithjof Nolting, Swiss Light Source, PSI, CH-5232 Villigen, Switzerland.

X-ray photoelectron spectroscopy (XPS) with angular resolution (XPD) allows structure determination paired with chemical and magnetic sensitivity [1]. At x-ray absorption resonance the signal is maximal for a given chemical species [2; 3]. If resonant angle scanned photoelectron diffraction (RXPD) is applied to a magnetic system the magnetization direction can be extracted from the dichroic signature in the x-ray absorption coefficient, which depends on the orientation of the angular momenta of the exciting photons with respect to the magnetisation. For magnetized Ni(111) the XPD patterns excited with circularly polarized light at the L_2 resonance yield the precise structure and magnetization direction [4].

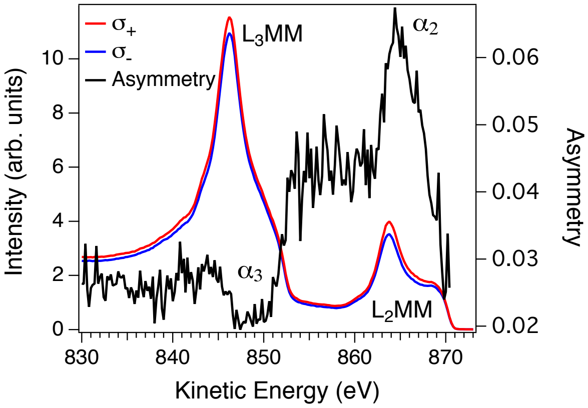

Fig. 14.1 – Near normal photoemission spectra from magnetized Ni(111) excited with left and right circularly polarized light (σ^+ and σ^-). The photon energy was set to the L$_2$-resonance at $\hbar\omega = 870.5$ eV. The spectra have been normalized with the photon flux. The L_2MM and the L_3MM Auger deexcitation peaks are indicated. The asymmetry between right and left circularly polarized light exhibits two distinct extrema α_2 and α_3, on which we performed XPD measurements.

Figure 14.1 shows the circular dichroism in the photoemission spectra which are excited at the L_2 ($2p_{\frac{1}{2}} \rightarrow 3d$) x-ray absorption resonance ($\hbar\omega = 870.5$ eV) with right (σ^+) and left (σ^-) circularly polarized photons. In ferromagnetic nickel the 3d valence shell is spin polarized, which produces a pronounced dichroism. Figure 14.2 displays XPD patterns of Ni(111). The XPD map in (a) is dominated by the information on the atomic structure which corresponds to that of a face centered cubic (fcc) crystal that is cut along the (111) plane [5]. In order to visualize the dichroic information, we form the asymmetry between the α_2^+ and the α_2^-

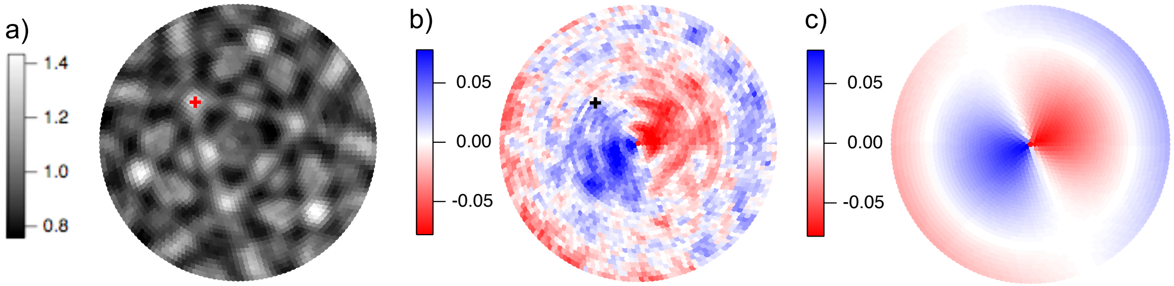

Fig. 14.2 – (a) Resonant x-ray photoelectron diffraction (RXPD) data of Ni(111). The 3500 stereographically projected data points for polar angles $0 \leq \theta \leq 70°$ of the intensity at α_2 (E_{kin}=863.8 eV, $\hbar\omega = 870.5$ eV, σ^+) in Fig. 14.1. The data are normalized with the average polar intensity. The [011]-direction is marked with a red cross. (b) Asymmetry of two XPD data sets at α_2 measured with right and left circularly polarized light. The twofold i.e. dipolar pattern reveals the direction of the magnetization. (c) Fit of the dichroic dipole (D-function) to the asymmetry in (b).

XPD scans (see Fig. 14.2b). These data contain information on the dipolar (magnetic) nature of dichroism and higher order multipoles, which are related to differences in the diffraction patterns due to different source waves [6; 7]. The dipolar part has the symmetry expected for in plane magnetisation. Figure 14.2c shows the fit of a dipolar function D, which determines the direction of the average magnetisation $\mathbf{m}'$. The rotation of the sample and the incidence of the light impose on D *two* nodal lines ($\mathbf{m}' \cdot \mathbf{L}_{ph} = 0$), where $\mathbf{L_{ph}}$ is the angular momentum vector of the photons.

These experiments show that resonant photoelectron diffraction may be exploited in the study of the geometric structure around a photoemitter and its magnetic momentum orientation [4]. We expect the method to be useful for the investigation of the spin structure in magnetic molecules.

[1] C. S. Fadley, J. Electron Spectrosc. Relat.Phenom. 78, 2 (2010).

[2] P. Krüger *et al.*, Phys. Rev. Lett. 100, 055501 (2008).

[3] M. Treier *et al.*, Phys. Rev. B 80, 081403 (2009).

[4] M. Morscher *et al.*, arXiv:1103.4280.

[5] J. Wider *et al.*, Phys. Rev. Lett. 86, 2237 (2001).

[6] T. Greber *et al.*, Phys. Rev. B 45, 4540 (1992).

[7] H. Daimon *et al.*, Jap. J. Appl. Phys. 32, L1480 (1993).

14.2 Symmetry protected spin structures in topological insulators

in collaboration with: Zahid Hasan, Department of Physics, Princeton University, Princeton, New Jersey 08544, USA; and Luc Patthey, Swiss Light Source, Paul Scherrer Insititute, 5232 Villigen, Switzerland.

Topological insulators are a novel phase of condensed matter where strong spin-orbit interaction induces a band gap in the bulk but also the formation of topologically protected surface states [1]. This protection is caused by a peculiar spin structure of the surface states: for a given momentum direction there is only one (or in the extended case any other odd number) spin-polarized Fermi level crossing. Because time-reversal symmetry is not broken in these materials it follows that for opposite momenta the spin also has to be opposite. Therefore backscattering of non-magnetic defects is highly reduced as it would require a spin flip. A further concequence of the time-reversal symmetry is that the spin-polarized bands must cross at the centre of the Brillouin zone, where the momentum is zero, and at other specific high symmetry points linked by a reciprocal lattice vector. The odd number of spin-polarized bands and the forced crossing at given points in the Brillouin zone together guarantee that the surface states will always cross the Fermi level as long as time-reversal symmetry is not broken. This is in short what constitutes the topological protection of the surface metallicity.

The fact that the unusual properties of a topological insulator are determined by the spin structure of its surface states makes spin- and angle-resolved photoemission (SARPES) an central experimental probe for these systems [2]. In Fig. 14.3 the measured spin-polarization and resulting spin structures are shown for Bi_2Te_3. Through these measurements we could unambiguously verify that these systems are topological insulators with only a single Dirac cone at the surface [3]. However, it has been found that for Bi_2Te_3 the Dirac cone is not perfectly circular for energies away from the Dirac point, but becomes increasingly hexagonal and even snow-flake like [4]. As a concequence of this warping it is expected that the spin polarization vector obtains an out-of-plane component between the cusps of the constant energy surfaces [5]. As can be seen in the spin-structure summary in Fig. 14.3 this is exactly what we observe for Bi_2Te_3 in our spin-resolved photoemission experiments.

The three-fold symmetry of the out-of-plane polarization significantly enhances the phase-space for scattering events and thus reduces the conductivity. On the other hand, it also increases the possibility for spin injection into the system and gives an extra degree of freedom for any spin manipulation. By using ternary instead of binary compounds the number of possible topological insulators, with potentially different electronic and spin texture properties, is dramatically enhanced. This is exemplified by the results obtained for $TlBiSe_2$ shown in Fig. 14.4. For this system the Dirac point is well separated from the bulk valence band which allows us to measure the spin texture below this crossing point [6]. As can be seen in Fig. 14.4b) the momentum scan measured below the Dirac point shown an inverted spin-polarization signal compared to all measurements performed above this point. This means that when one places the chemical potential at the Dirac point only a very small voltage needs to be applied to switch between reversed spin textures. This could thus be an interesting material for realizing a low-power spin transistor.

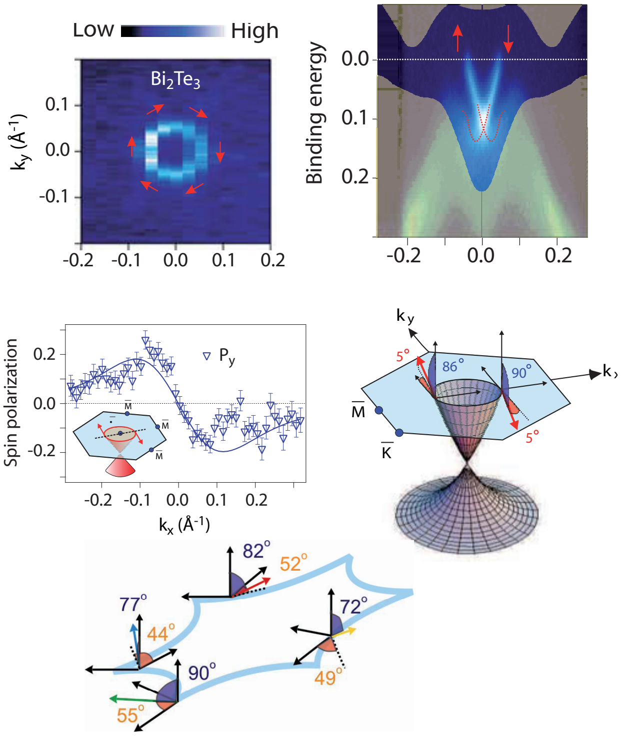

Fig. 14.3 – Experimental Fermi surface and band dispersion (top two panels), as well as spin texture (bottom three panels) of the single Dirac cone topological insulator Bi_2Te_3 (from Ref. [3]).

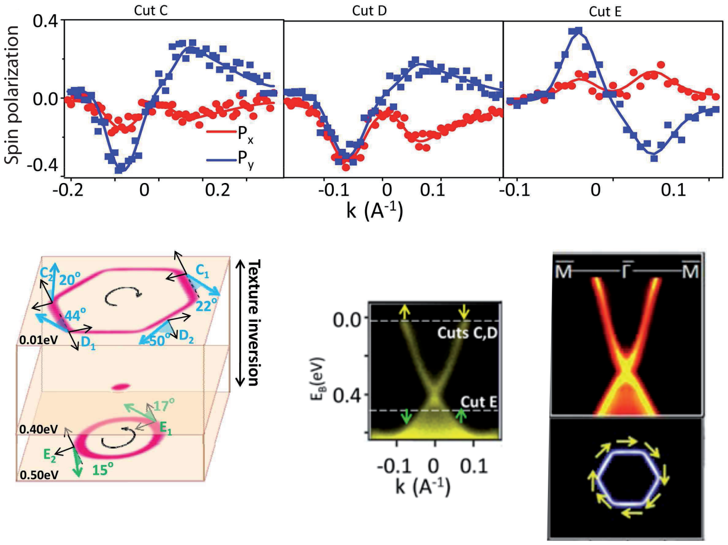

Fig. 14.4 – Dirac cone and spin structure of $TlBiSe_2$ showing the reversal of the spin texture above and below the Dirac point. Top panels: spin polarization curves along the cuts indicated in the center figure below. Bottom left: schematic illustration of constant energy surfaces observed at two energies, one above and one below the Dirac point. Spin polarization vectors measured at selected points are also plotted (from Ref. [6]).

[1] M. Z. Hasan and C. L. Kane, Rev. Mod. Phys. 82, 4 (2010).

[2] J. H. Dil, J. Phys.: Condens. Matter 21, 403001 (2009).

[3] D. Hsieh *et al.*, Nature 460, 1101 (2009).

[4] Z. Alpichshev *et al.*, Phys. Rev. Lett. 104, 016401 (2010).

[5] L. Fu, Phys. Rev. Lett. 103, 266801 (2009).

[6] Su-Yang Xu *et al.*, ScienceExpress, DOI: 10.1126/science.1201607.

14.3 Ultrafast dynamics in photo-induced field emission

in collaboration with: Christian Hafner, Laboratory for Electromagnetic Fields and Microwave Electronics, ETH Zürich.

When a focused laser pulse illuminates a metallic tip, optical electric fields are enhanced at the tip apex due to plasmonic effects, and the enhanced fields induce pulsed field emission in combination with a moderate DC voltage applied to the tip. Depending on the strength of the enhanced fields, different field emission mechanisms are considered to be dominant [1; 2]. For relatively weak fields, single-electron excitations by single- and multi-photon absorption are prevalent, and photo-excited electrons are tunneling through the surface potential barrier; this so called photo-field emission process is most interesting for applications and was studied in our lab in great detail.

Previously it was found that two-photon photoemission yields the best compromise between a high multi-photon excitation cross section and a thin tunneling barrier [3]; this finding was obtained by simulating the local field enhancement by solving the Maxwell equations using finite-elements methods [4], and by calculating the local emission currents within Fowler-Nordheim theory. In order to confirm experimentally the relative contributions for various parameter sets (bias voltage, laser focus and intensity) we upgraded our field emission setup by implementing an electron energy analyzer (see Fig. 14.5). In order to distinguish electrons emitted from different facets of the tungsten tip, a large plate with phosphor coating and pinhole in the center was installed as a counter electrode between the tip and the analyzer. The field emission pattern of the clean tungsten tip can be observed on the phosphor plate where the most intense electron emission is observed around the [310]-type facets. The pinhole is positioned at the edge of one of those regions (see Fig. 14.5).

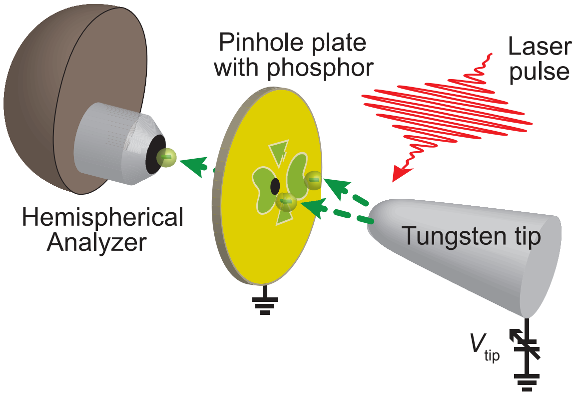

Fig. 14.5 – The experimental setup.

The field emission current is influenced by two factors: 1) the electron occupation number and 2) the transmission probability through the surface barrier [5; 6]. The occupation number is given by an electron distribution function $f(E)$, which is the Fermi-Dirac distribution function in the case of field emission, and the transmission probability depends exponentially on an area of the surface barrier indicated by the hatched area in Fig. 14.6a. Therefore, the positive energy side of the spectrum falls off due to a rapid decrease of the occupation number, while the negative energy side falls off because of the exponential decay of the transmission probability due to the increase of the surface barrier area. A typical field emission spectrum shows thus an asymmetric peak. An energy spread of 0.21 eV was observed, which is close to the value measured with 1 meV energy resolution in previous work (0.19 eV) [7], confirming our reasonable energy resolution.

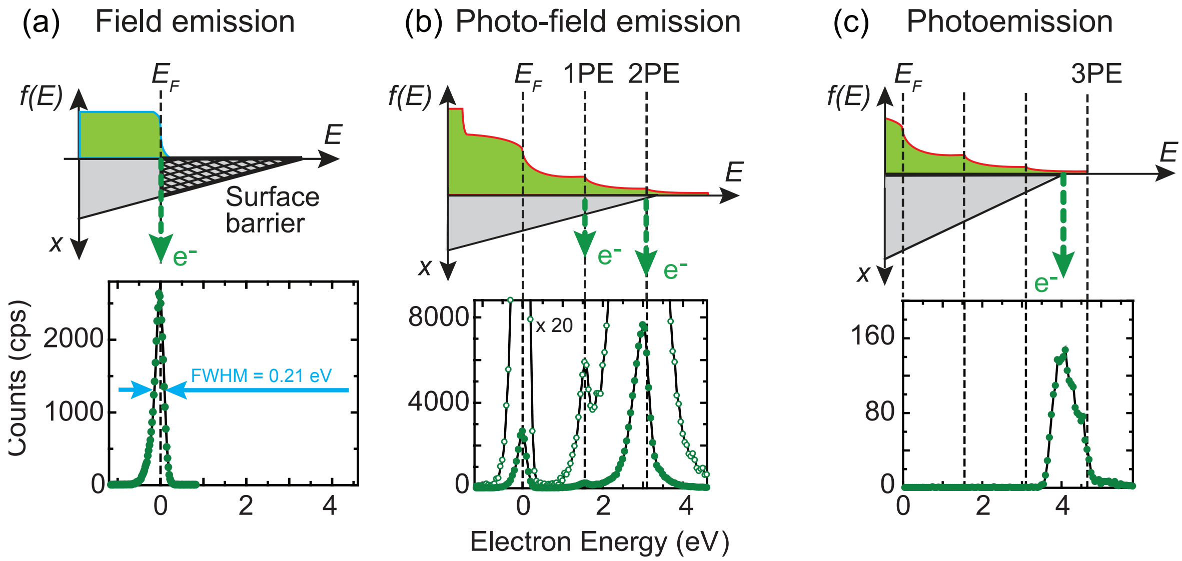

Fig. 14.6 – Top panels: schematic energy diagrams illustrating the different mechanisms that contribute to the electron yield. Bottom panels: measured energy distributions.
(a) Field emission from a Fermi-Dirac distribution. The tip voltage V_{tip} was -2300 V and no laser was used.
(b) Nonequiliburium electron distribution just after laser absorption including electron-electron scattering; V_{tip} = -2300 V and laser power P_L = 50 mW.
(c) At low bias voltage V_{tip} = -500 V and high laser power P_L = 50 mW 3-photon photoemission dominates.

When illuminated by a pulsed laser with moderate peak intensity, the current increases due to photoexcited carriers, which encounter a largely reduced tunneling barrier at higher energy. As conjectured in Ref. [3], the spectrum is dominated by electrons excited by two photons as shown in the spectrum in Fig. 14.6b. Eventually, as the bias voltage is reduced the tunneling barrier becomes too large and the emission spectrum is dominated by photoelectrons excited in a three-photon process as shown in spectrum (c). This is the first time that photon-field emission spectra were measured in such detail, and corroborated by full dynamical calculation including the electron-electron scattering dynamics and the transient heating of the electron gas. The results are published in a forthcoming paper [8].

At the end of 2010, H. Yanagisawa was awarded an *Ambizione* grant by the Swiss National Science Foundation. He has moved the setup to ETH Zürich, where he will continue this research using phase-controlled few-cycle laser pulses available in the laboratory of Prof. U. Keller.

[1] P. Hommelhoff *et al.*, Phys. Rev. Lett. 96, 077401 (2006).

[2] H. Yanagisawa *et al.*, Phys. Rev. Lett. 103, 257603 (2009).

[3] H. Yanagisawa *et al.*, Phys. Rev. B 81, 115429 (2010).

[4] For Max-1, see http://alphard.ethz.ch/.

[5] R. Gomer, "Field Emission and Field Ionization", (American Institute of Physics, New York, 1993).

[6] G. Fursey, "Field Emission in Vacuum Microelectronics", (Kluwer Academic / Plenum Publishers, New York, 2003).

[7] H. Ogawa *et al.*, Surf. Sci. 357-358, 371 (1996).

[8] H. Yanagisawa *et al.*, cond-mat: arXiv 1103.4310.

15 Physics of Biological Systems

Conrad Escher, Hans-Werner Fink, Dominik Grögler (until May 2010), Patrick Helfenstein, Alina Horwege (since May 2010), Tatiana Latychevskaia, Jean-Nicolas Longchamp, Mirna Saliba (since December 2010), Elvira Steinwand (until December 2010).

in collaboration with:
Dr. Ian Cox, Photek Ltd (Great Britain); Eugen Ermantraut, Clondiag Chip Technologies GmbH (Germany); Dr. Petr Formanek, University of Dresden (Germany); Prof. Bruno Klaholz, Universit of Strassbourg (France); Prof. John Miao, University of California at Los Angeles (USA); Prof. Jannik C. Meyer, University of Vienna (Austria); Dr. Soichiro Tsujino, PSI (Switzerland).

The structural investigation of individual biological objects by employing coherent low energy electrons is the primary goal of our research. It involves holography with low energy electrons as well as coherent diffraction and is assisted by microstructuring techniques using a focussed gallium ion beam device. Our current activities are divided in the following interconnected individual projects:

- **Electron Holography**
  The overall idea is to apply holography with low energy electrons to investigate the structure of individual biological molecules. Major experimental challenges are to improve the interference resolution in electron holograms, establish methods for creating free standing thin films of Graphene transparent for low energy electrons as well as appropriate techniques to present a single protein to the coherent electron wave front. Next to these experimental issues, a second, equally important aspect for achieving high resolution structural information is the reconstruction of the electron holograms. This is achieved by back-propagating the object wave information, recorded in the hologram plane, by employing a numerical algorithm to solve the integrals governing this coherent optics problem.

- **Electron and Ion Point Sources**
  Field Ion Microscopy and related techniques are employed for fabricating and applying novel electron and ion point sources. In collaboration with the PSI, field emitter arrays are characterized and specified for their use as bright electron sources for the XFEL (X-Ray Free Electron Laser) project.

- **Fluorescent Microscopy**
  The aim of this project is to directly observe the dynamics of single DNA molecules in liquids by video fluorescent microscopy. In combination with molecular anchoring techniques, adopted from Clondiag, we also address the energetics of a single DNA molecule. Appropriate DNA modifications for attaching fluorescent proteins to are designed by Clondiag Chip Technologies in Jena and shall serve us in our efforts to obtain structural information about proteins by electron holography.

- **Coherent Low-Energy Electron Diffraction Microscopy**
  This is our most recent approach of using coherent electron wave fronts for structural biology at the single molecule level. It is based on an iterative phase retrieval scheme pioneered by John Miao from the University of California at Los Angeles with whom we collaborate in this project. Below we shall discuss the recent achievements in this project in some more detail.

Most of the protein structural information available today has been obtained from crystallography experiments by means of averaging over many molecules assembled into a crystal. Nevertheless, a strong desire to gain structural data from just a single molecule is emerging. We are working towards the objective of deriving atomic structure information from experiments carried out on just one individual molecule subject to the interaction with a coherent low-energy electron wave. Meanwhile, it has been thoroughly established that electrons with kinetic energies below 200 eV are the only radiation known today where elastic scattering dominates. Radiation damage-free imaging of a single biological molecule is thus possible by recording its oversampled coherent low-energy electron diffraction pattern.

15.1 Diffraction microscopy and the Oversampling Method

X-ray and electron diffraction microscopy have traditionally been limited to crystalline samples. The repeating crystalline structure amplifies the signal in certain directions, so that the far-field diffraction pattern shows discrete Bragg peaks. Such an X-ray diffraction pattern lacks information on the phase of the object wave upon scattering which is needed to provide unambiguous information on the real space location of the atoms. The recovery of a single molecule structure from its diffraction pattern constitutes an inverse problem, which requires a solution to the phase problem. Historically, Gabor's invention of holography [1], dating back to 1948, was the first approach towards solving the phase problem by recording the interference of the object wave with a reference wave. In 1952, Sayre first proposed the possibility of recovery of phase information of non-crystalline samples by oversampling its diffraction pattern [2]. In 1972, Gerchberg and Saxton proposed the first iterative algorithm to recover the object structure from the amplitude of the scattered wave [3]. This algorithm was successfully applied to recover an object from its oversampled diffraction pattern by Miao et al. [4]. They demonstrated that the phase retrieval algorithm converges (after several 1000 iterations) if the initial conditions are such that the surrounding of the molecule is known. Given that the diffraction pattern is sampled above Nyquist frequency (oversampled), the uniquely-defined phase distribution can be recovered from the scattering record [5]. Thus, the experimental recording of a far-field diffraction pattern followed by numerical recovery of the object structure constitutes the novel class of high resolution coherent diffraction imaging techniques. In what follows, we summarize the state of the art as well as recent achievements in this fairly active field, which are to some extent also catalyzed by the emerging XFEL facilities around the world. CDI has successfully been applied to image nanocrystals [6], single cells [7] and individual bacteria [8] with X-rays. A carbon nanotube was imaged at atomic resolution with high energy electrons [9]; three-dimensional objects could be reconstructed from a single diffraction pattern [10]. Most applied phase retrieval methods are based on hybrid input-output and error reduction algorithms [11]. However, a number of problems associated with the reconstruction procedure remain: non-uniqueness of the solution due to unavoidable noise in experimental diffraction patterns, missing data in the overexposed central area of the diffraction pattern, complex-valued transmission functions likely to be exhibited by imaged objects, and finally, stagnation of the iterative process often at partial solutions. These shortcomings explain why there is still an ongoing search for better reconstruction methods and alternative experimental techniques. Modifications of the reconstruction methods with the goal to optimize the convergence of the iterative process, such as charge-flipping [12] and the so called shrink-wrap [13] algorithms have recently been suggested. Furthermore, novel experimental techniques to simplify the reconstruction process without sacrificing high resolution, such as Fresnel Diffraction Imaging [14] and Fourier Transform Holography [15] have recently been proposed. In the latter a small hole next to the sample provides the reference wavefront which in turn reduces the reconstruction process to a single Fourier transform while, at the same time, the achievable resolution remains as high as in conventional CDI.

15.2 Schematic of the Coherent Electron Diffraction Microscope and experimental realization

We have embarked onto using the damage-free radiation provided by coherent low-energy electrons to realize coherent diffraction imaging of single molecules. The overall setup of our coherent electron diffraction imaging microscope is sketched in Fig. 15.1. A sharp W-tip acts as an electron point source emitting a coherent spherical electron wave with kinetic energies between 50 and 300 eV. A micro-lens placed a few microns away from the electron emitter forms a coherent parallel wave (see Fig. 15.3) that impinges onto a molecule attached to a micro-structure some distance behind the lens in a field-free region. At a distant detector, the intensity of the diffraction pattern corresponding to the amplitude-square of the Fourier transform of the object is recorded with high spatial resolution. In order to sample this pattern with sufficiently high frequency to match the oversampling requirement, the object must be surrounded by a no-density region.

Our diffraction microscope has been designed and built featuring a dedicated detector system, available since March 1st 2011, for obtaining oversampled diffraction patterns. It comprises a microchannel plate, a small grain phosphor screen di-

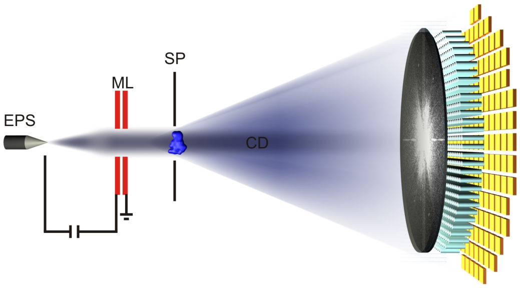

Fig. 15.1 – The coherent electron diffraction microscope for imaging individual biomolecules. (EPS): coherent electron point source, (ML): low aberration micro-lens to form a parallel electron wavefront, (SP): sample imbedded inside the coherent electron beam, (CD): coherent diffraction pattern, (DU): detector unit, featuring a high spatial resolution low-energy electron detector that fulfils the oversampling condition.

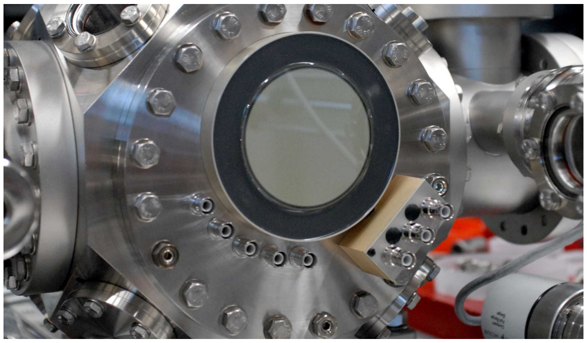

Fig. 15.2 – Ambient pressure side of the 75 mm diameter detector showing the fiber optic plate and connectors for the micro-channel-plate detector.

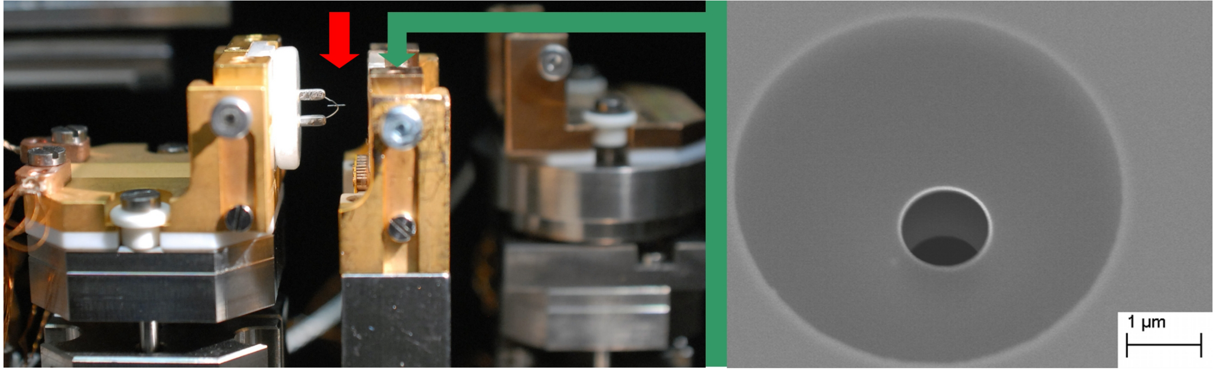

Fig. 15.3 – Formation of a low-energy coherent parallel electron wavefront. The electron point source (marked by the red arrow) is mounted onto a nanometer precision Piezo stage and positioned close to a micro machined lens (green arrow) exhibiting a 1micron bore. In this way a parallel beam of sub-micron width is formed beyond the lens. A SEM image of the lens is shown at the right.

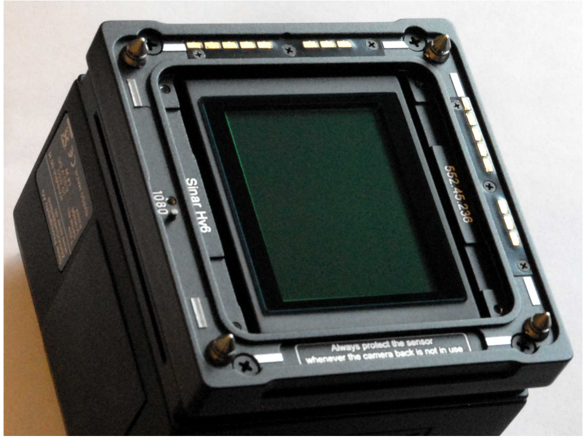

Fig. 15.4 – A high resolution CCD chip (Sinar AG, Zurich) featuring 8000x6000 pixels is optically coupled to the fiber optic plate for recording the diffraction pattern with high spatial resolution and a 16 bit dynamics.

rectly deposited onto a fibre optic plate (see Fig. 15.2) and a high resolution (8000x6000 pixels) CCD chip (Fig. 15.4). An electrochemically etched single W[111] crystal serves as the source of coherent low-energy electrons. It is mounted on a three-axis manipulator so that the tungsten tip can be positioned with sub-nanometer precision. The sample is mounted on a separate four-axis manipulator to enable centering it in the electron beam. An additional degree of freedom for rotating the sample has been included so that sets of diffraction patterns at various tilt angles can be acquired.

15.3 Conditions for non-destructive imaging of a single biomolecule

Radiation damage is the major problem that obstructs imaging an individual biological molecule for structural analysis. Due to the strong inelastic scattering of X-rays and high-energy electrons there is little hope for obtaining structural information from just one molecule. Even the expected results of the XFEL projects currently under development involve averaging. In fact, more than 10^5 diffraction patterns of identical molecules must be recorded in order to obtain structural detail at a resolution of 3 , even with a 10 fs X-ray pulse containing 10^{12} photons at 1.5 wavelength. This implies that currently there is still no tool or concept at hand based on X-rays or high-energy electrons that has a realistic chance of imaging just one single biological molecule at atomic resolution.

In contrast to the current state-of-the-art imaging methods as briefly sketched above, we could recently show that a molecule as fragile as DNA withstands irradiation by coherent low-energy electrons and remains unperturbed even after a total dose of at least 5 orders of magnitude larger than the permissible dose in X-ray or high-energy electron imaging [16]. These recent findings demonstrate that coherent low-energy electrons are the only non-damaging Angstrom wavelengths radiation known today. This is the pre-requisite for the current proposal: with coherent low-energy electrons it shall thus be possible to look at truly just one entity if it comes to high resolution diffraction microscopy of individual biomolecules.

15.4 Recent achievements in coherent diffraction microscopy

15.4.1 Published results

Apart from radiation damage, electron lens aberrations are a major barrier limiting the resolution of electron microscopy. By scaling down an electron lens by several orders of magnitude, we circumvented the problem of intrinsic lens aberrations and ended up with a conceptually simple one micron sized lens exhibiting aberrations comparable to those of magnetic objective lenses used in modern high end electron microscopes [18].

By using our coherent electron source in combination with such a micro-lens it has been possible to form a parallel beam and direct it towards a carbon nanotube bundle suspended over a micromachined slit in a silicon nitride membrane. In this way the first coherent electron diffraction pattern, albeit not yet fulfilling the oversampling condition needed for reconstruction, of a single nanometer-sized object using low-energy electrons has been obtained [19].

15.4.2 Imaging biological samples

While a dedicated UHV instrument is in operation and micro-lens fabrication is meanwhile also routinely possible, a major focus must now be directed towards appropriate preparation of single biomolecules, detecting their diffraction pattern with high spatial resolution at the detector level and retrieving the phase of the object-wave by a fast converging iterative numerical algorithm. It has turned out that it is feasible to obtain a hologram of a biological object prior to recording a diffraction pattern of the very same biological sample. This provides a great benefit, not available in any other diffraction setup. Usually, the central region of the diffraction pattern providing the low resolution information about the object is missing due to the overexposure of the zero and low order diffraction. In our setup, this usually missing information is provided by first gathering a hologram of the very same object just before the micro-lens is activated to form a parallel beam to obtain a diffraction pattern of the very same object. This is illustrated in Figs. 15.5 and 15.6 showing electron holograms and the corresponding diffraction patterns of a tobacco mosaic virus (TMV) (sample by courtesy of the University of Strasbourg) and an individual double wall carbon nanotube, stretched over a 200 nm wide opening in a silicon nitride membrane.

While both diffraction patterns have not yet been sampled at high rates, since the 8000x6000 pixel CCD chip has just been delivered (March 1st), the nanotube diffraction pattern displayed in Fig. 15.6 has been obtained already with the enlarged MCP detector of 75 mm in diameter. The orange circle in Fig. 15.6 indicates a k-vector that corresponds to a resolution of currently 3.9 . In future experiments this value shall be pushed into the 2 regime by detecting even higher orders of the diffraction pattern.

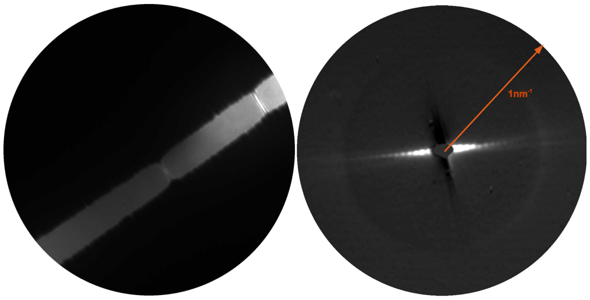

Fig. 15.5 – Left: Hologram of a TMV taken with 78 eV electrons. Right: Coherent diffraction pattern taken of the very same TMV with electrons of 137 eV kinetic energy. The modulations apparent in the diffraction pattern correspond to a length of 18 nm in real space - the width of an individual TMV.

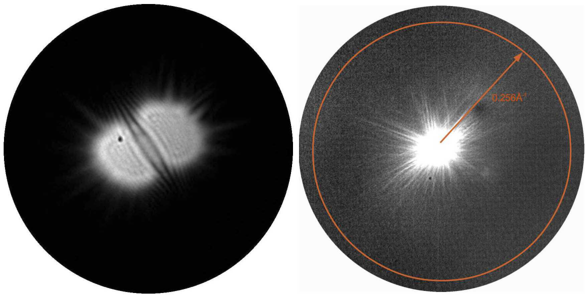

Fig. 15.6 – Left: Hologram of a double wall carbon nanotube (DWCNT) taken with 62 eV electrons. Right: Coherent diffraction pattern taken of the very same DWCNT with electrons of 127 eV kinetic energy.

15.5 Novel Fourier-domain constraint for Fast Phase Retrieval [17]

The distribution of the scattered object wave in the far-field $O_0(X,Y)$ is given by the Fourier transform of the object transmission function $o(x,y)$: $O_0(X,Y) = FT(o(x,y))$. Although the object shape cannot easily be recognized in its far-field image, it can be uncovered by an iterative reconstruction processes. While there is an intensive search for optimal constraints in the object plane to improve the reconstruction routines, possibilities to apply constraints in the Fourier domain have not yet been explored. Recently, we proposed a novel, simple and powerful Fourier-domain constraint providing fast and reliable reconstructions. In common phase retrieval methods, the phase of the iterated field O_i is adapted for the next iterative loop, while the amplitude is replaced by the square root of the measured intensity:

$$O_{i+1} = \frac{O'_i}{|O'_i|}\sqrt{I_0}, \tag{15.1}$$

where $I_0 = O_0 O_0^*$. We propose using the following constraint instead:

$$O_{i+1} = \frac{O'_i}{|O'_i|^2 + \epsilon} O_0 O_0^* = l O_0 O_0^*. \tag{15.2}$$

This formula is derived via a direct analogy to holography, where the transmission of a recorded hologram H is given by $H \sim R^* O + R O^*$. Here, R denotes the reference wave and O the object wave. In the reconstruction process, the hologram is multiplied with the reference wave resulting in the straightforward reconstructed object wave $RH/|R|^2 = O$. This approach can be applied for reconstructing a diffraction pattern if we formally treat the measured intensity of the diffraction pattern $O_0 O_0^*$ as a hologram H and O'_i as the reference wave R see Eq. 15.2. This novel constraint, unlike the one given by Eq. 15.1, does not only account for the phase of O'_i, but also for its amplitude. The latter must gradually approach the amplitude of O_0. In order to avoid division by zero, a constant ϵ is added in the denominator. Any additional constraint in the object plane can still be selected independently of the Fourier-domain constraint.

The performance of our novel constraint is demonstrated by the reconstruction of a simulated and experimental light optical diffraction pattern, the result of the latter is shown in Fig.15.7. We also compared the performance of our novel reconstruction algorithm to those of established reconstruction methods. Among these, the so called "shrink-wrap" algorithm [13] is considered to be the most effective. By using the "shrink-wrap" algorithm the simulated diffraction pattern was already reconstructed after about 70 iterations. However, the "shrink-wrap" algorithm failed when applied to our experimental diffraction pattern. The reason could be that the "shrink-wrap" algorithm relies on a continuously updated support mask, which could not be well defined for our experimental sample as there were some fine scratches around the object as verified by optical microscopy.

This novel algorithm has a number of advantages in comparison to other algorithms: any initial guess about the shape of the object is irrelevant for the convergence of our routine. This independence of the object topology shall be highly beneficial for the reconstruction of objects that cannot be confined within a certain area suitable for "masking", or for objects that are surrounded by some features which cause unwanted contribution to the diffraction pattern. A low-resolution reconstruction of the object is already achieved after a few iterations. This low-resolution reconstruction can then be either further refined by additional iterations or it can be used as an input for any other conventional phase retrieval method.

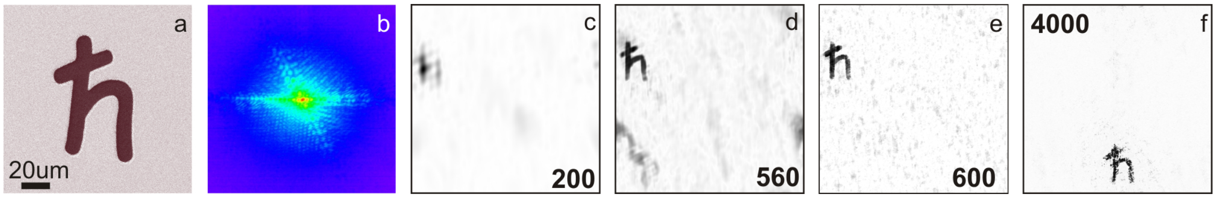

Fig. 15.7 – Recovery of the letter "h" from its experimental diffraction pattern. (a) SEM image of the object. (b) Recorded light optical diffraction pattern displayed in a logarithmic intensity scale. (c) Low-resolution image of the object recovered after 200 iterations. (d) Recovered amplitude of the object after 560 iterations, (e) after 600 iterations and (f) after 4000 iterations using a routine with a tight mask.

15.6 Summary of recent achievements in Coherent Diffraction Microscopy

The following achievements towards structural biology of single molecules have been established:

- Micro-lens design and routine fabrication
- Minimal spherical aberrations by a downscaling concept
- First coherent diffraction pattern with low-energy electrons of an inorganic sample
- First coherent diffraction pattern of a biological sample, a TM-virus
- Implementation of a new low-energy electron detector exhibiting 15 micron spatial resolution
- Implementation of a 8000x6000 pixel detector with 16bit dynamics
- A novel fast and reliable numerical method for the reconstruction of diffraction patterns
- Method for retrieving the 3-dimensional object distribution by 3-dimensional deconvolution
- The relation between a hologram and a coherent diffraction pattern of the same object
- Freeze drying biological sample preparation

15.6.1 Biological sample preparation

While we initially envisioned using tips, well defined by field ion microscopy prior to their use as a sample holder, we dropped this strategy in favour of planar samples for supporting a single biological molecule. The reason for this is the advantage of being able to post-accelerate the parallel beam emerging from the micro-lens towards the sample. By this means, the deBroglie wavelength can be adjusted in a simple manner, while a non-planar sample, such as a tip, would introduce unwanted electron optical aberrations. Figure 15.8 displays preliminary efforts in using graphene and double wall carbon nanotubes as sample holders. While it turns out that graphene is in fact sufficiently transparent even for our low-energy electrons, as evident from Fig. 15.8a and 15.8b, the cleanliness of graphene remains to be a serious problem. At present, the level of dirt on a free-standing graphene flake is just too high to allow its use as a reliable sample holder for proteins. However, efforts to obtain really clean graphene are underway worldwide and there is thus a fair chance that one of the pioneers of using graphene in TEM studies, namely Prof. Jannik Meyer from the Boltzmann Institute in Vienna, shall provide us with clean graphene samples in the near future.

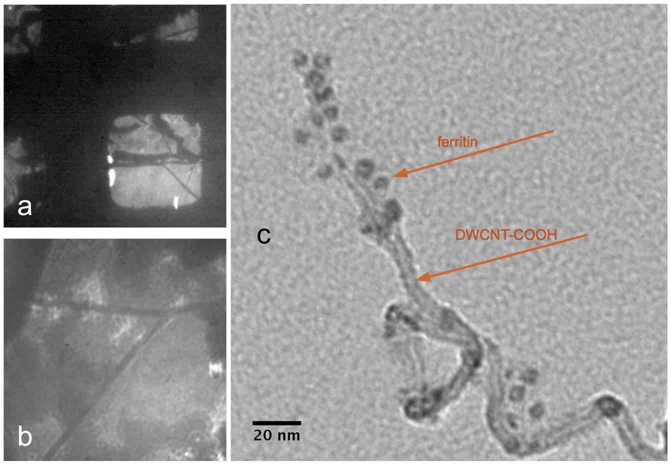

Fig. 15.8 – a) Graphene flakes deposited onto an 8 micron square copper grid show transmission for 450eV electrons. b) Even at just 65 eV kinetic energy, a significant transmission through graphene is observed; however it is apparent that the graphene sheet is highly contaminated. c) TEM image of ferritin molecules attached to a carbon nanotube.

In the meantime, we focussed on using functionalized carbon nanotubes or DNA molecules as templates for presenting the desired protein to the coherent planar electron wavefront. In both cases these elongated structures shall be placed over holes 200 nm in diameter milled in thin silicon nitride membranes by our focussed ion beam machine. An example of ferritin attached to the outer wall of a double wall carbon nanotube, taken with a standard TEM at our University, is shown in Fig. 15.8c. For modifying DNA molecules and attaching proteins to the double helix, we have enrolled the support of Clondiag Chip Technologies, a company based in Jena, Germany.

15.7 Electron column

Beyond the micro-lens, a second electron optical element, for instance an Einzel-lens exhibiting three apertures of one millimeter in diameter each shall be incorporated to bring the following important improvements to the coherent diffraction microscope: First, the divergence angle of the beam impinging onto the sample could be further reduced and consequently the spatial coherence of the parallel electron beam would increase. This shall ameliorate the quality of the reconstructions. Second, the diameter of the parallel electron beam at the sample shall effectively be reduced to 50nm without losing intensity. The oversampling criterion requires that the reconstructed region is at least twice as big as the illuminated region of the sample. Because the size of the reconstructed region is inversely proportional to the pixel size of the detector, a reduction of the beam diameter shall relax the strong requirement on the spatial resolution of the detector and facilitate the fulfillment of the oversampling criterion. Third, the addition of a millimeter-sized Einzel-lens would permit to build a complete electron column with an overall size of just a few millimeters. Simulations performed in the frame of the Master thesis of Flavio Wicki have shown that the size of the focus which could be obtained with such an electron column shall be as small as 5nm. The size of the electron column in combination with our low-energy electron point source shall permit us to build a SEM with a significantly reduced size compared to conventional SEMs. Furthermore, kinetic electron energies below 100 eV shall provide high surface sensitivity while ultra high vacuum compatibility is ensured. Such a machine shall be a worldwide novelty in the field of scanning electron microscopy.

We have dedicated a system, formerly used for electron holography, to the task of implementing such a mini electron-column. It is displayed in Fig. 15.9 together with the first design of such mini-lens which is readily being built in our machine shop and shall be subject to a first test in the frame of an ongoing Master thesis. We envision that the implementation of such an electron column shall be combined with a secondary-electron detector and a scanning system. Once such a mini SEM is working, it shall also be employed for coherent diffraction imaging experiments on single biomolecules. It will just be a matter of adjusting the voltage on the lenses to go from a focused beam to parallel one.

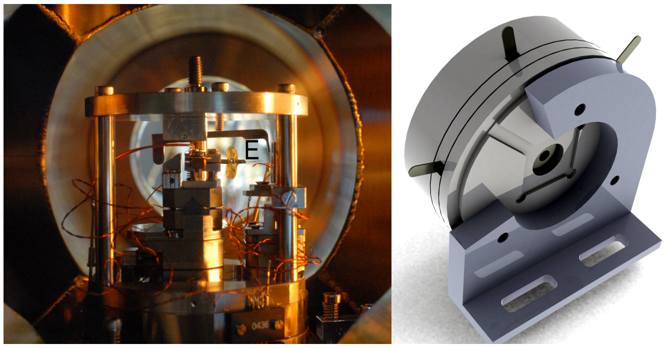

Fig. 15.9 – At left, inside view of a modified electron holography system which shall incorporate an electron column of some millimeters in size. The electron emitter is marked with the letter E. At right, a design for a miniature electron column is shown which combines a micro-lens with an Einzel-lens in one column.

[1] Dennis Gabor, Nature **161**, 777-778 (1948).

[2] D. Sayre, Acta Cryst. **5**, 843 (1952).

[3] R. W. Gerchberg and W. O. Saxton, Optik **35** 237-246 (1972).

[4] J. Miao *et al.*, Nature **400**, 342-344 (1999).

[5] J. Miao *et al.*, Phys. Rev. B **67** 174104 (2003).

[6] I. K. Robinson *et al.*, Phys. Rev. Lett. **87** 1955051 (2001).

[7] D. Shapiro *et al.*, Proc. Natl. Acad. Sci. U.S.A. **102** 15343 (2005).

[8] J. Miao *et al.*, Proc. Natl. Acad. Sci. U.S.A. **100** 110 (2003).

[9] J. M. Zuo *et al.*, Science **300** 1419 (2003).

[10] K. S. Raines *et al.*, Nature **463** 214 (2010).

[11] J. R. Fienup, Appl. Optics **21** 2758 (1982).

[12] G. Oszlanyi and A. Suto, Acta Crystallogr. A **60** 134 (2004).

[13] S. Marchesini *et al.*, Phys. Rev. B **68** 140101 (2003).

[14] G. J. Williams *et al.*, Phys. Rev. Lett **97** 025506 (2006).

[15] S. Eisebitt *et al.*, Nature **432** 885 (2004).

[16] M. Germann, T. Latychevskaia, C. Escher and H.-W. Fink, Phys. Rev. Lett. **104** 095501 (2010).

[17] T. Latychevskaia, F. Gehri and H.-W. Fink, Novel Fourier-domain constraint for fast phase retrieval in coherent diffraction imaging, to be published.

[18] E. Steinwand, J.-N. Longchamp and H.-W. Fink, Ultramicroscopy **110** 1148 (2010).

[19] E. Steinwand, J.-N. Longchamp and H.-W. Fink, Ultramicroscopy **111** 282 (2011).

16 Physical Systems Biology and non-equilibrium Soft Matter

C.M. Aegerter, D. Assmann, G. Ghielmetti, U. Nienhaus, M. Schindlberger (Master Student), T. Schluck

in collaboration with: Institute of Molecular Life Sciences (K. Basler, T. Aegerter-Wilmsen, C. Lehner, S. Luschnig), ETH Zürich (E. Hafen, I. Sbalzarini, P. Koumoutsakos), EPF Lausanne (P. Renaud, D. Floreano), University of Lausanne (S. Bergmann), Biozentrum Basel (M. Affolter), University of Strasbourg (N. Rivier), University of Konstanz (G. Maret, W. Bührer, T. Sperling, N. Isert), New York University (C.C. Maass), Deutsches Luft- und Raumfahrtzentrum (M. Sperl), University of Twente (A. Mosk), Bulgarian Academy of Sciences (V. Petrov), Universite Joseph Fourier Grenoble (S. Skipetrov, F. Graner), Technion Haifa (E. Akkermans), University of Exeter (P. Vukusic), Yale University (A. Monteiro).

Work in the group of physical systems biology and non-equilibrium soft-matter is concerned with the study of developmental biology using physical techniques. In this, we are developing novel imaging techniques for the study of the influence of mechanical stresses on developmental processes. Moreover, the group works on the study of inherent non-equilibrium systems that can be tracked physically, such as driven granular gases. In the last year, we have made considerable progress in these two areas, where we have determined the elastic properties of developing wing disc tissues of the fruit fly Drosophila, as well as a description of the velocity distributions of granular gases in terms of kinetic theory, which is able to describe not only the driven steady state, but also the cooling state. These two projects will be described in detail below.

16.1 Photoelastic properties of Drosophila wing imaginal discs

In the study of developing tissues, we and others have put forward the idea that mechanical feedback can work as a regulatory mechanism in tissue growth [1–3]. In order to study this proposal experimentally, we have determined the photo-elastic properties of the wing disc tissue after the application of controlled forces while simultaneously determining its birefringence [4]. Unforced discs show a compression in the centre of the disc, as shown in Fig. 16.1, which increases with the age of the discs as they develop [5].

A schematic of the setup used to exert controlled forces onto the tissues is drawn in Fig. 16.2. The wing imaginal discs were attached to two separate cover slips using poly-lysine solution. This leads to an electrostatic attraction of the tissue with the cover slip and thus an efficient fixation. While one of these cover slips is fixed, the other is attached to a sheet of spring steel at a right angle. Due to the geometric measures and the bending stiffness of the spring sheet, a calibrated force can be exerted on the cover slip and hence the wing disc by bending the spring sheet. For this purpose we have used a translation stage capable of resolving movements down to a micron over a range of several mm.

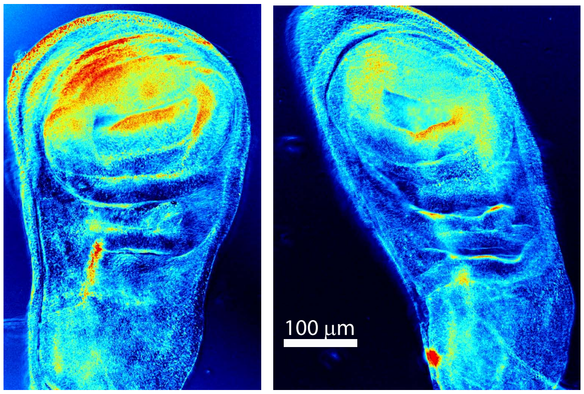

Fig. 16.1 – The retardance map of a wild type wing disc before (left) and after (right) uncontrolled stretching. The results are similar to those found previously on longer time scales and using a different setup. The colormap indicates retardance varying between 0 nm (black) and 10 nm (red) [6]. For a determination of photo-elastic properties, the stretching needs to be performed in a quantitative manner.

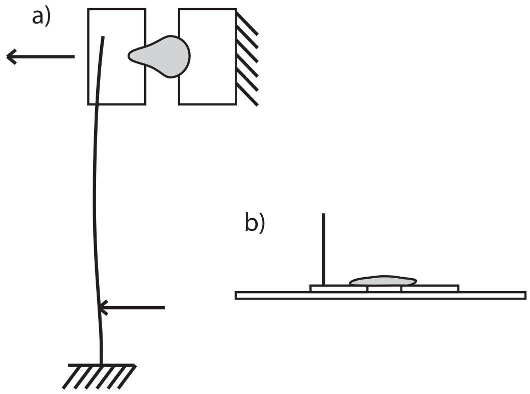

Fig. 16.2 – Top (a) and side (b) view of the mechanical forcing setup. The wing disc (grey) is attached to two glass cover slides, one of which is attached to a surface. The other cover slide is fixed to a spring sheet, which is forced by a translation stage at a given distance. This gives a controllable force ranging from 1μN to 1 mN, which is ideally suited to study epithelial tissues.

Given the point of contact of the translation stage with the spring sheet, we can easily calculate the force exerted on the wing disc from classical elasticity [8]:

$$F = \frac{6EI}{w^2(L-w)}d.$$

Here, $E = 2\times10^{11}$ Pa is the Young's modulus of the spring sheet, $I = a^3b/12$ is the area moment of inertia of the sheet with a thickness of $a = 50\mu$m and a width of $b = 1.1$cm. Furthermore, $L = 12$cm is the total length of the sheet and $w = 4$cm is the point of contact with the translation stage. Finally, d is the distance traveled by the translation stage. Taking these data on the spring sheet together yields a bending spring constant of 1.0 N/m, such that the setup is capable of exerting forces between 1μN and 1 mN.

Using the pulling setup described above, we have compressed and stretched wing discs with a controlled force exerted by the spring sheet. Typical results for different mechanical forcing are shown in Fig. 16.3. Here, the retardance map is somewhat different from the unattached discs, which could be due to the fact that the attachment with poly-lysine also exerts mechanical stresses locally. In the figure, three different stages of the experiment can be seen, corresponding to a compression of the wing disc with a force of 30 μN (top), a slight stretching (10 μN - middle) and strong stretching at 50 μN (bottom). We have averaged the retardance over the central area of the pulled disc tissue and find values of 2.9 nm in the compressed case, 2.5 nm in the marginally stretched case and 2.1 nm in the fully stretched case. In some of our experiments, the force of attachment on the cover slide was comparable to the force exerted by the spring sheet. This led to a detachment of the wing disc after having been subject to a stretching force for several minutes to half an hour. As can be seen from Fig. 16.4, such detached wing discs revert to their original size, which takes place over the course of 2-3 seconds. The slight difference in appearance visible in Fig. 16.4 is due to the fact that the unattached side of the disc can move in the z-direction bringing it

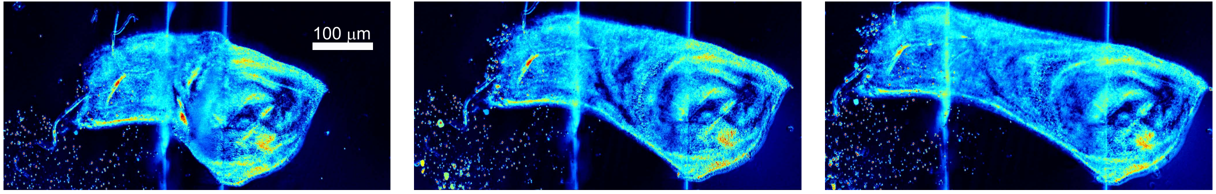

Fig. 16.3 – The retardance map of a wing disc at different levels of stretching in the y-direction. The colormap indicates retardance, changing from 0 nm (black) to 10 nm (red). In the left picture, the disc is compressed with a force of 30 μN, while in the middle the disc is roughly in its initial state with a stretching force of about 10 μN. The right picture shows a stretched wing disc at a force of 50 μN. Note that for an accurate determination of the changes in retardance, proper averages over the stretched tissues need to be taken. The resulting differences are of the order of 0.5 nm, with an increase in retardance for compressional stress and a decrease for tensional stress.

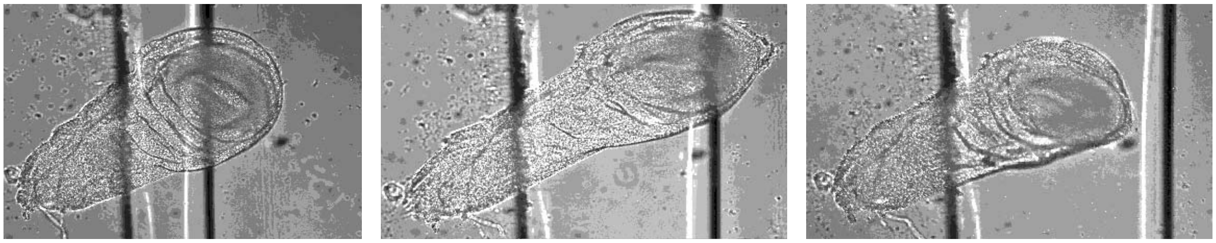

Fig. 16.4 – A stretched wing disc that has been detached from the cover slide (right). The disc reverted to its original shape and size before stretching (left) in spite of having been stretched substantially, (middle). The discrepancy in shape is explained by the fact that the unattached part of the disc is free to move in the z-direction thus losing the focus. This indicates that on the corresponding time scale of half an hour and for strains as big as 1, the disc behaves elastically.

out of focus and thus changing the form somewhat. This implies that on the time-scale of half an hour, the tissue does act elastically. In fact, a force extension curve of a typical wing disc is rather linear, as can be seen in Fig. 16.5, with an effective spring constant of 0.5(1)N/m. This directly corresponds to a Young's modulus of the order of 10^4 Pa.

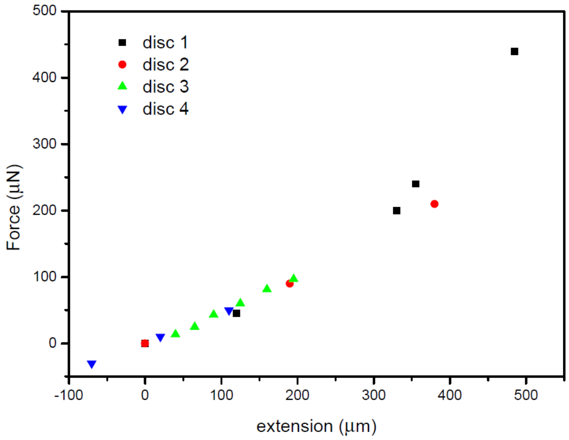

Fig. 16.5 – Force extension curves for four different wing imaginal discs. The extension is taken starting from the relaxed state. For a large range of extensions, the force needed is linear and only increases at strains in excess of 2. The initial slope of the curve implies a high spring constant of wing disc tissue as compared to embryonic samples [7; 9; 10].

In other developing tissues, which have been studied experimentally [7; 9; 10], spring constants of the order of 10^{-3} N/m were found. Thus it seems that the wing discs behave more stiff and elastic than other tissues. It should be noted, however, that these investigations were done on embryonic tissues, which is not the case for wing imaginal discs.

For instance, the mechanical stresses in the larva when feeding and moving are much higher than in the embryo thus invoking stronger tissues. This is corroborated by moduli of adult tissues, such as blood vessels, skin or muscle, which range between 10^5 and 10^6 Pa [12; 13].

[1] T. Aegerter-Wilmsen, C.M. Aegerter, E. Hafen, and K. Basler, Mech. Develop. **124**, 318 (2007).

[2] B.I. Shraiman, Proc. Natl. Acad. Sci. USA. **102**, 3318 (2005).

[3] L. Hufnagel, A.A. Teleman, H. Rouault, S.M. Cohen, and B.I. Shraiman, Proc. Natl. Acad. Sci. USA. **104**, 3835 (2007).

[4] T. Schluck and C.M. Aegerter, Europ. Phys. J. **33**, 111 (2010).

[5] U. Nienhaus, T. Aegerter-Wilmsen, and C.M. Aegerter, Mech. Dev. **127**, 942 (2009).

[6] M. Shribak and R. Oldenbourg, App. Optics **42**, 3009 (2003); R.J. Wijngaarden, M.S. Welling, C.M. Aegerter, and K. Heek. NATO Science Series II: **142**, 61 (2004).

[7] R.A. Foty, C.M. Pfleger, G. Forgacs, and M.S. Steinberg, Development **122**, 1611 (1996).

[8] L.D. Landau and E.M. Lifshitz, Oxford (1960).

[9] E.M. Schötz, R.D. Burdine, F. Jülicher, M.S.

Steinberg, C.P. Heisenberg, and R.A. Foty, HFSP Journal **2**, 42 (2008).

[10] C. Wiebe and G.W. Brodland, J. of Biomechanics **38**, 2087 (2005).

[11] T. Aegerter-Wilmsen, A. Christen, E. Hafen, C.M. Aegerter, and K. Basler, Development **137**, 499 (2010).

[12] J.Zhou and Y.C. Fung, Proc. Nat. Ac. Sci. USA **94**, 14255 (1997).

[13] M.R. Neidert, E.S. Lee, T.R. Oegema, and R.T. Tranquillo, Biomaterials **23**, 3717 (2002).

16.2 Velocity distributions in levitated granular media

In collaboration with the University of Konstanz, we are studying the behaviour of granular gases using diamagnetic levitation [1]. Due to the levitation of the particles, it is possible to study the behaviour of the grains as a function of time when the excitation is switched off. Under normal circumstances, this behaviour is completely masked by the gravitational effect of grains falling to the bottom of the container. Due to the inelasticity of collisions between grains, the particles continually loose energy, which is a fundamental ingredient in the theoretical description of granular gases using kinetic theory [2]. This has led to a description of the freely cooling granular gas by Haff more than 25 years ago [3], which is used as a ground state in the description of excited granular gases [4].

Using a collection of monodisperse Bismuth shots, we have created a granular gas in the bore of a strong superconducting solenoid [5]. At an applied field of 13.5 T, the field gradient at the edge of the solenoid is strong enough such that the diamagnetic susceptibility of Bismuth leads to a repulsive force that equals gravity. Exciting the granular gas using an alternating component of the levitating field, a homogeneously driven granular gas can be created. This is different from usual granular gases, which are typically driven by mechanical shaking from the outside, which implies an inhomogeneous input of energy, which is difficult to calculate theoretically. For these differently excited granular gases, we can then determine the velocity distributions using particle identification and tracking given snapshots as those shown in Fig. 16.6. Here, deviations from the Maxwellian distribution are expected due to the non-equilibrium nature of the gas. This description will typically take place in the framework of kinetic theory, which in its simplest form will take the homogeneously cooling state as its starting point, which will be a scaling solution also for the steady state [6].

For a simple model, we will resort to the description of the homogeneous cooling state given in [5]. This implies that we will normalise the speeds by their mean, $c = v/\langle|v|\rangle$. For small speeds, it is then possible to calculate the velocity distribution

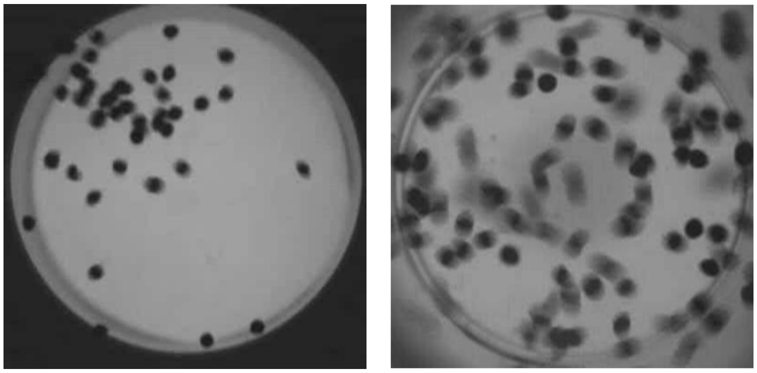

Fig. 16.6 – Snapshots of the distribution of particles during excitation using a magnet coil (left) and mechanically via a loudspeaker (right). In the first case the driving force is homogeneously distributed over the whole sample, whereas in the second case energy transfer takes place only at the boundary which results in a different distribution.

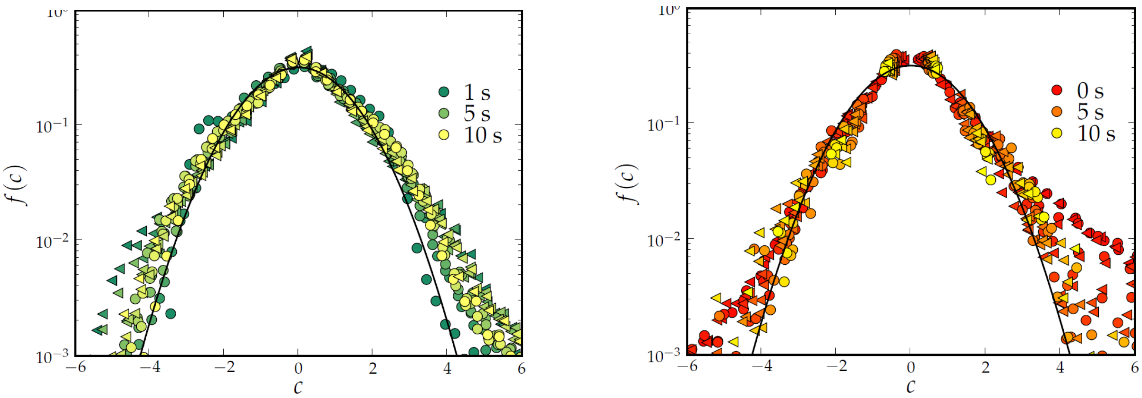

Fig. 16.7 – Velocity distributions for the different cases of driving (left: coil; right: speaker). The distributions are given for different time periods after which the driving has been switched off. This means that the cooling process is studied. In case kinetic theory can be used to describe the process, the distributions should only scale via their width, which decreases according to Haff's law. As can be seen, this is not the case for the driving with a speaker. Here the distribution at late times approaches that of the homogeneously driven case, which does scale with cooling time.

starting from the equilibrium case of a Gaussian distribution given by:

$$G(c) = \frac{1}{\pi} exp(-c^2/\pi).$$

The distribution $p(c)$ can then be treated by $\Delta(c) = p(c)/G(c) - 1$, corresponding to the first Sonine polynomial, assuming a normalised distribution with a mean speed of unity. For a full characterisation, we will finally have to determine $\langle c^2 \rangle$, which in the simplest description of the homogeneously cooling granular gas, can be achieved using the collisional dynamics of an average particle. With the loss of kinetic energy due to collisions one obtains:

$$\begin{aligned} 2\ell \frac{d\langle |v| \rangle}{dt} &= (1-\rho^2)\langle |v| \rangle^2 \\ &= \langle v^2 - \langle |v| \rangle^2 - \rho^2(\langle |v| \rangle - v)^2 \rangle \end{aligned}$$

for the rate of change in the speed of an average particle, where the first term corresponds to the dynamics implied by Haff's law. Here, ℓ is the mean free path of a particle between collisions and $(1-\rho^2)$ is the average coefficient of restitution. Solving this equation by taking into account that $\langle v \rangle = 0$, one obtains $\langle v^2 \rangle = 2\langle |v| \rangle^2$ or alternatively $\langle c^2 \rangle = 2$, independent of the coefficient of restitution. This implies for the velocity distribution:

$$p(c) = G(c)(\frac{2}{\pi})^3(\pi^2/2 - 5\pi/2c^2 + c^4).$$

We have now determined the velocity distributions during the cooling process in order to assess whether this state can be used as a ground state onto which the steady state properties scale. The different distributions for different excitations are shown in Fig. 16.7.

The velocity distribution at different times in the cooling process do scale with the temperature of the gas in the homogeneously excited case, as is predicted by kinetic theory. This however is not the case for a mechanically shaken gas, where the energy input is from a boundary. Interestingly, the coefficient of restitution does not seem to play a role in the description of the velocity distributions at small speeds, as the Sonine expansion we find is independent of the coefficient of restitution. This is corroborated from our data of particles at different $\rho = 0.35$ and $\rho = 0.7$, as well as the data of Reis *et al.* [7] with still higher $\rho = 0.95$. In addition, the data show conclusively that the deviations from near equilibrium distributions in most experiments [2] are mainly due to boundary effects implied by the excitation of the particles in these studies.

[1] W. Braunbek, Z. Phys. **121**, 764 (1939).

[2] J.S. Olafsen, and J.S. Urbach, Phys. Rev. Lett. **81**, 4369 (1998); Phys. Rev. E **60**, R2468 (1999); D.L. Blair, and A. Kudrolli, Phys. Rev. E **67**, 041301 (2003).

[3] P.K. Haff, J. Fluid. Mech. **134**, 401 (1983).

[4] X. Nie, E. Ben-Naim, and S. Chen, Phys. Rev. Lett. **89**, 204301 (2002).

[5] C.C. Maass, N. Isert, G. Maret, and C.M. Aegerter, Phys. Rev. Lett. **100**, 248001 (2008).

[6] J.M. Montanero and A. Santos, Gran. Mat. **2**, 53 (2000).

[7] P. Reis, R.A. Ingale and M.D. Shattuck, Phys. Rev. E **75**, 051311 (2007).

17 Mechanical Workshop

K. Bösiger, B. Lussi, R. Maier, M. Schaffner, S. Scherr, D. Dürst (apprentice), T. Naterop (apprentice)

Many interesting and demanding projects were realized for the research groups at the institute in the reporting period. In addition the mechanical workshop again supported other departments of the University and outside companies. The service provided by the central metal and technical material store maintained by the mechanical workshop could be further extended. [6] The large demand for the store services was demonstrated by a highly succesfull information meeting that we organized in November 2010 (Fig. 17.1) and by the over thirty institutes that used the supply of raw material, semi-finished products and components.

Fig. 17.1 – Visitors of the information meeting for the central store customers.

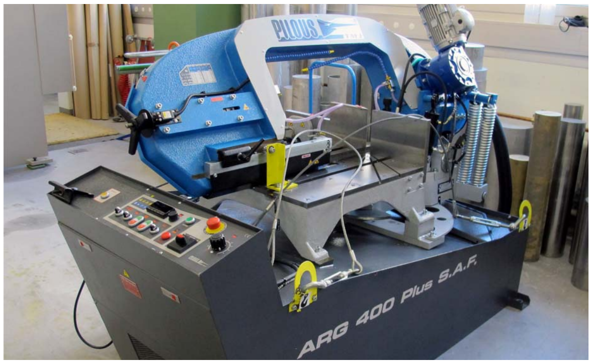

Fig. 17.2 – The new band saw in the material store.

The income from production of components for outside firms was again used to supplement and extend the central store. Also new tooling and the continuing education of the workshop staff and the apprentices could be financed this way. Various investments and acquisitions were made. In the material store we replaced a metal cutting bow saw with a powerful band saw (Fig. 17.2). The new semi-automatic machine allows to precisely cut raw materials with diameters up to 400 mm. The whole cutting process is automated which substantially increases the productivity, especially for solid materials. The integrated saw band speed control improves the cut quality and the saw band life time.

With the network license for the SolidWorks 3D design software, owned by the workshop and made available for the institute staff, the quality and the reliability of the technical drawings prepared by the research groups improved noticeably.

In August 2010 we started with the procurement of a new CNC-lathe. It is planned, that the new computer controlled machine, which replaces a 20 years old tool, will be installed in autumn 2011.

During two months we conducted the basic mechanical workshop courses for bachelor students. There were twelve courses with a work load of 35 hours each. In October 2010 and January 2011 we provided again one-week introductory mechanical workshop courses for the research staff of our institute and other institutes of the University.

Besides maintenance and repair work and support of various Bachelor- and Master-thesis projects we like to mention the following activities:

- **LHCb silicon tracking detector (Sec. 10)**
  Spare parts were manufactured for the LHCb silicon tracking detector. For this purpose we also produced new work holding devices and other auxiliary components.

---

[6] For a catalog see http://www.physik.unizh.ch/groups/werkstatt/dienstleistung.html

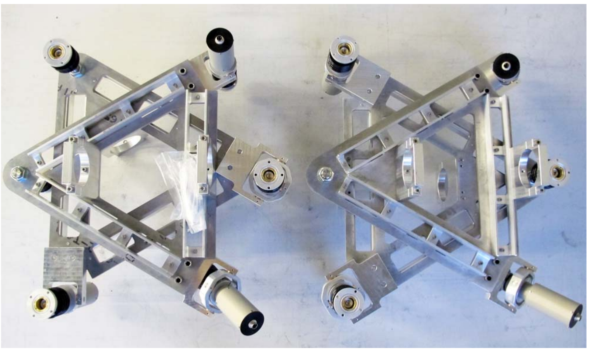

Fig. 17.3 – Complete mirror support structures for the CTA prototype telescope.

- **CTA Cherenkov Telescope Array (Sec. 6)**
  Test setups were assembled and a mirror support structure for the CTA prototype telescope was built (Fig. 17.3).

- **Surface Physics (Sec. 14)**
  We produced components for the upgrade of the Synergia project. On our five-axes milling machine very complex vacuum flanges were machined. Series of various molybdenum and stainless steel parts were fabricated (Fig. 17.4).

- **GERDA (Secs. 3)**
  A new calibration system for the GERDA experiment was designed in collaboration with the research group and the electronics workshop (Fig. 17.5). Three systems were manufactured.

- **Physics of Biological Systems (Sec. 15)**
  The custom-built vapour deposition device with six coating stations had to be modified. The water cooling system was improved. We manufactured ceramic mounts with contacts to hold silicon wafers and performed maintenance and repair work (Fig. 17.6).

Fig. 17.4 – Molybdenum parts.

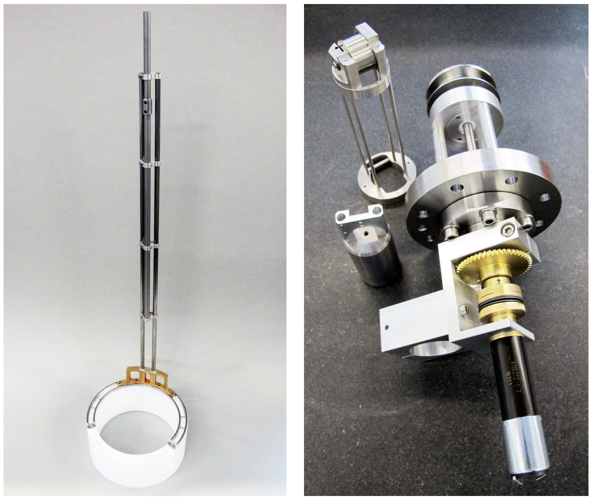

Fig. 17.5 – Left: teflon cooling component for the XENON experiment. Right: parts for one complete calibration system for the GERDA experiment.

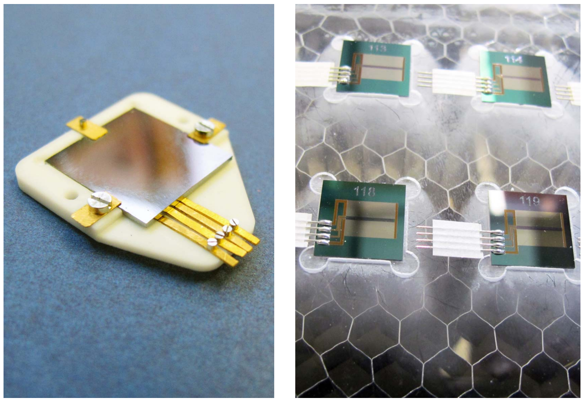

Fig. 17.6 – Left: custom-built silicon wafer holder. Right: labeling of printed circuit boards on the laser engraving system.

- **Solid State Physics (Sec. 12)**
  The high temperature superconductor demonstration experiment with a model magnetic levitation train built in previous years attracted broad interest. The frequent operation resulted in lot of maintenance work. We also built motor driven probe manipulators, evaporation masks and high pressure containers made of high-tensile materials (Fig. 17.7).

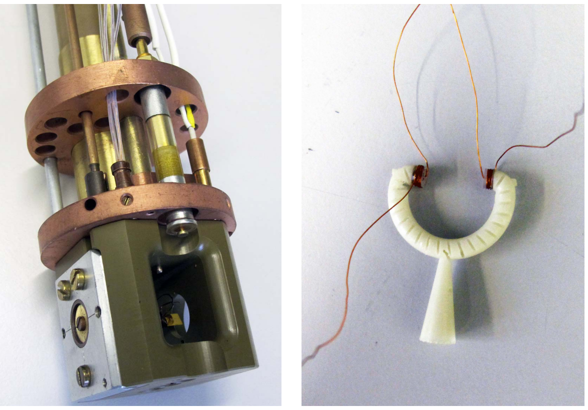

Fig. 17.7 – Left: probe manipulator. Right: special molded coil carrier.

- **Fusion Neutron source**
  In summer 2010 the neutron generator vessel was finally filled with paraffin in the assembly hall of the workshop. The system was then installed and brought into operation in the custom-built shielding compartment in the basement (Fig. 17.8).

Fig. 17.8 – Neutron generator installed in the shielding compartment. The fusion neutron source is mounted in the vessel to the right.

- **Demonstration and laboratory experiments**
  Several instruments and devices used in the demonstration experiments for the physics courses were improved and refurbished. We produced the mechanical components for a new demonstration experiment (a Wilson chamber, see Fig. 17.9) which will also be shown at expositions.

Fig. 17.9 – Housing of the Wilson chamber during machining on the mill.

- **Continuing education of the workshop staff**
  The main focus was again on welding seminars and software courses. Higher level tutorials for the CAM software packages “hyperMill” and “Mastercam” used in the mechanical workshop were attended.

- **Education of the apprentices**
  In April 2010 and January 2011 we organized again trial apprenticeship for candidates interested in getting a grade as poly-technician. Besides the mandatory Swissmechanic courses the apprentices attended again advanced courses in computer controlled machine (CNC) programming, pneumatics and electronics. Also introductary seminars on graphical and office software were attended. By the end of February 2011 preparations for the intermediate and final apprenticeship examinations started.

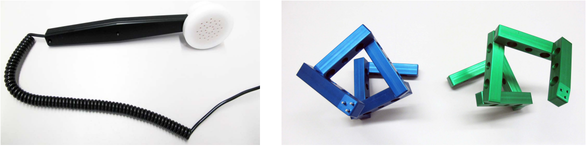

Fig. 17.10 – Left: headphone for the museum of zoology. Right: Two construction sets visualizing right- and left-turning DNA structures.

Fig. 17.11 – Sealed greenhouse with integrated control adaptors to study CO_2 metabolism.

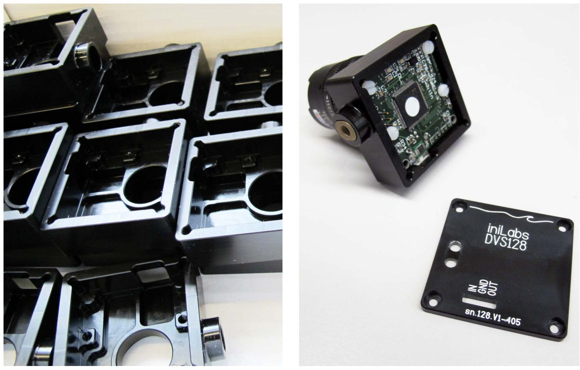

Fig. 17.12 – Left: plastic camera housings. Right: complete opened camera.

Activities for other departments and outside companies:

- For the museum of zoology we designed and produced head phones (Fig. 17.10 left).
- We manufactured construction sets which are presently used to demonstrate DNA molecules in the exhibition “Astrophysics and Biology” (Fig. 17.10 right).
- For a research group at the department of geography we designed and built two hermetically sealed greenhouse boxes with integrated control adaptors to study the CO_2 metabolism (Fig. 17.11).
- Micro drives with sensor holders used at universities in New York and custom designed camera packages made out of plastic (POM) were manufactured for the institute of neuroinformatics (Fig. 17.12).
- For the institute of medical virology special filter cartridges were fabricated.
- A series of custom-built portable cases with embedded x-y linear stages supporting a movable probe carrier were designed and assembled for the institute of pathology (Fig. 17.13). Up to 96 DNA probes can be filled computer controlled into the probe holder.
- For outside companies we built prototypes and produced limited-lot series. We also manufactured special LED-lamp housings for a company which is selling illuminating systems.

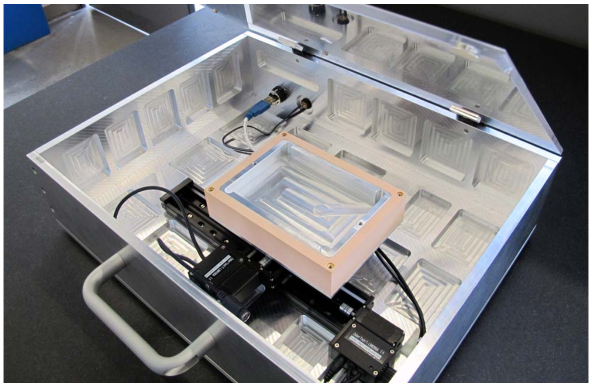

Fig. 17.13 – Custom-built portable case with x-y linear stages supporting a movable probe carrier.

18 Electronics Workshop

D. Florin, P. Soland, and A. Vollhardt

During the reporting period the electronics workshop again supported the research groups by maintaining and repairing their equipment. For various experiments at the institute electronic circuits were designed and test setups assembled. In collaboration with Hp. Koch and L. Pauli who are responsible for the preparation of the demonstration experiments for the undergraduate lectures we renewed and improved again some devices and setups.

Below we list some major activities:

- **Electronics for the Cherenkov Telescope Array (CTA) experiment (Sec. 6)**
  A decentralized master clock scheme is under study. To maintain a fixed phase relation between independent clock sources, a GPS-disciplined crystal oscillator unit was developed. As high-resolution phase measurements are required for characterizing the relative stability of two clocks, a time-to-digital converter with a noise floor of 60 ps was designed (Fig. 18.1). The phase data is transmitted to a host computer for further analysis. Two prototypes of the GPS-disciplined oscillator have been built and are currently being optimized (Fig. 18.2). Recent tests suggest a relative frequency instability below $2{\cdot}10^{-11}$ for a time period of 100 seconds. This result is probably limited by the quality of the reference oscillator. For a more accurate analysis, a comparison to the METAS atomic time standard is planned.

  In addition, 200 controllers for the Active Mirror Control (AMC) electronics were procured and commissioned. Mounting on the full-size prototype dish structure is planned for summer 2011. To assist these tests, a small AMC Master Controller (Fig. 18.3) connecting to a host's USB interface was designed. Depending on the chosen

Fig. 18.1 – Time-to-digital converter.

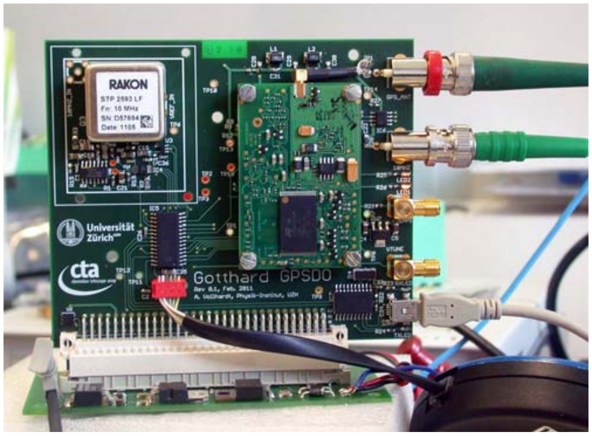

Fig. 18.2 – GPS-disciplined oscillator.

Fig. 18.3 – AMC master controller unit.

concept the bandwidth required to transfer the CTA FlashCam trigger data reaches up to 480 Gb/s. For test purposes we designed and built an interface board (Fig. 18.4).

Using a Xilinx evaluation-board and with the appropriately programmed FPGA we performed measurements with transfer rates up to 2.5 Gb/s. We also tested different types of interfaces (Low Voltage Differential Signaling (LVDS), Current Mode Logic (CML)). Among other topics we also studied the alternative to use standard and cheap RJ-45 network cables for the data transmission.

- **X-ray tube control unit (Sec. 13)**
  For the recently acquired X-ray tube, a custom made control panel was constructed (Fig. 18.5) which allows control and monitoring of anode voltage and current. In case of an open radiation shield or missing water cooling, an interlock circuit automatically shuts down the tube's anode voltage providing safe conditions for both the operator and the hardware.

- **Solid State Physics (Sec. 12)**
  We designed and built a manually controlled constant current source to power a spectrometer magnet. A microwave spectrometer used in the ESR-laboratory and other spectrometers had to be repaired. Because a part of the faulty components had to be replaced by alternative devices we had to redesign and rebuild a complete device.

- **Surface Physics (Sec. 14)**
  For the sensitive light readout of a Mott spectrometer we designed a galvanically isolated interface with different amplifiers for avalanche photo diodes (APD). A final assembly was then realized on a printed circuit board (Fig. 18.6).

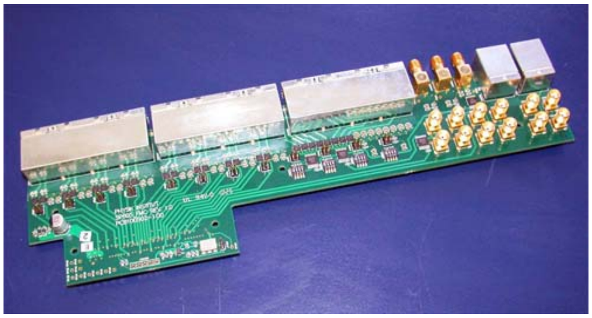

Fig. 18.4 – Interface board.

Fig. 18.5 – X-ray tube control unit.

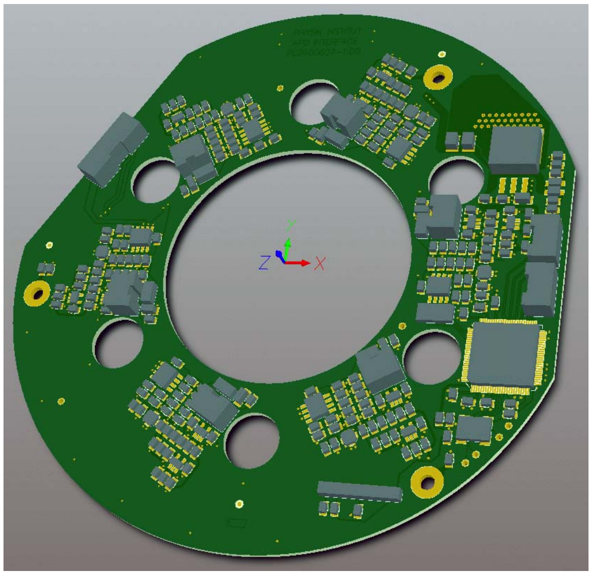

Fig. 18.6 – Printed circuit board design of the APD-interface.

The output signals of 6 APD-amplifiers are digitised with fast anolog comparators with adjustable thresholds. With a Complex Programmable Logic Device (CPLD) on the printed circuit board the width of the output pulses can be adjusted to a preselected value. We also assisted an engineer student in designing and assembling a custom-built heater control unit.

- **Demonstration and laboratory experiments**
  A new control interface for the student experiment determining the gravitational constant was built (Fig. 18.7). The interface allows both manual control and computer control of the position of the fieldmass while limiting the drive range via end switches.

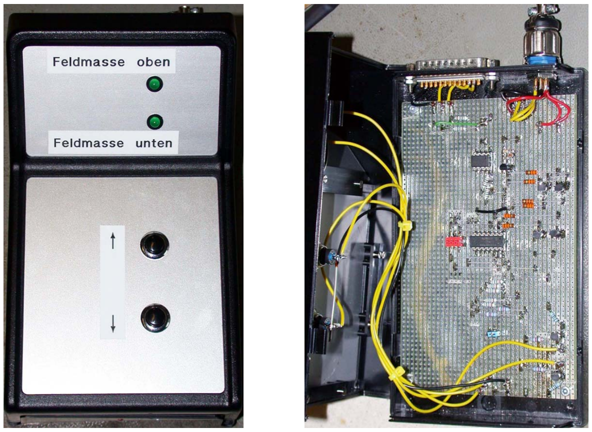

Fig. 18.7 – Left: control panel of the interface. Right: interface electronics.

- **LHCb experiment**
  During the LHC winter break 2010/11, malfunctioning readout boards of the LHCb Silicon Tracker were replaced. In addition the electronics workshop provided assistance during testing and installation of replacement silicon detector modules.

19 Publications

19.1 Elementary particles and their interactions

19.1.1 ArDM

Articles

- **First results on the light readout from the 1-ton ArDM liquid argon detector for dark matter searches**
  C. Amsler *et al.*, Journal of Instrumentation **5** (2010) P11003.

- **Development and test in liquid argon of the light readout system for the ArDM experiment**
  V. Boccone, AIP Conf. Proc. Volume **1182** (2009) 280.
- **The ArDM, a ton-scale liquid argon experiment for direct Dark Matter Detection**
  P. Otyugova, AIP Conf. Proc., Volume **1241** (2010) 435.
- **The ArDM-a ton-scale liquid argon experiment for direct Dark Matter Detection**
  P. Otyugova, Proc. 5th Patras Workshop on Axions, WIMPs and WISPs, Durham, UK, DESY-PROC-2009-05.
- **The Argon Dark Matter Experiment**
  C. Regenfus, Proceedings of the TAUP 2009 Conference, Rome, J. Phys. Conf. Ser. **203** (2010) 012024.

Articles in press

- **ArDM: a ton-scale LAr detector for direct Dark Matter searches**
  A. Marchionni *et al.* (ArDM Collaboration), Proc. 1st Int. Workshop towards the Giant Liquid Argon Charge Imaging Exp. (GLA2010), Tsukuba, Japan, arXiv:1012.5967v1 [physics.ins-det].

Lectures

- C. Amsler: **Search for WIMPS in liquid argon**
  WINÍ1– 23rd Int. Workshop on Weak Interactions and Neutrinos, Cape Town, South Africa, 31 January 2011.
- C. Regenfus: **ArDM a ton scale LAr WIMP detector prototype**
  6th Patras Workshop on Axions, WIMPs and WISPs, Zurich, 7 July 2010.
- W. Creus: **Light yield from nuclear recoils in liquid argon**
  Annual meeting of the Swiss Physical Society, Basel, Switzerland, 22 June 2010.

PhD thesis

- **Light Readout for a 1 ton Liquid Argon Dark Matter Detector**
  V. Boccone, Inaugural Dissertation, Universität Zürich, 2010.

19.1.2 ATHENA, AEgIS

Lectures

- C. Regenfus: **Relevant input and experience with Si-detectors from ATHENA**
  Workshop on Antimatter Physics, Bergen, Norway, 23 February 2011.

- Y. Allkofer: **Central Detector: boundary conditions**
  Workshop on Antimatter Physics, Bergen, Norway, 22 February 2011.

- C. Amsler: **A hybrid detector for antigravity measurements**
  Workshop on Antimatter Physics, Bergen, Norway, 22 February 2011.

- J. Storey: **Central detector: possible technologies**
  Workshop on Antimatter Physics, Bergen, Norway, 22 February 2011.

- J. Storey: **The AEgIS Inner Detector**
  the University of Bern, 12 January 2011.

19.1.3 CDMS

Articles

- **Results from a Low-Energy Analysis of the CDMS II Germanium Data**
  Z. Ahmed, D. S. Akerib, S. Arrenberg, C. N. Bailey, D. Balakishiyeva, L. Baudis, *et al.* (CDMS Collaboration), Phys. Rev. Lett. **106**, 131302 (2011).

- **Low-threshold analysis of CDMS shallow-site data**
  D.S. Akerib, M.J. Attisha, L. Baudis, D.A. Bauer, A.I. Bolozdynya, *et al.* (CDMS Collaboration), Phys. Rev. D **82**, 122004 (2010).

PhD thesis

- **A Search for Weakly Interacting Particles with the Cryogenic Dark Matter Search Experiment**
  Tobias Bruch, PhD Thesis, Physik-Institut, Universität Zürich, 2010.

Lectures

- S. Arrenberg: **Search for Inelastic Dark Matter with the CDMS experiment**
  Seminar, LPNHE, Paris, February 10th, 2011.

- S. Arrenberg: **Search for Dark Matter with the CDMS experiment**
  Darkness Visible, Cambridge, August 3rd, 2010.

- S. Arrenberg: **Search for Inelastic Dark Matter with the CDMS experiment**
  IDM2010, Montpellier, July 26th, 2010.

19.1.4 DARWIN

Articles

- **DARWIN: dark matter WIMP search with noble liquids**
  Laura Baudis (DARWIN Consortium), Proceedings of Science, PoS(IDM2010)122 (2010).
- **Complementarity of Dark Matter Direct Detection Targets**
  Miguel Pato, Laura Baudis, Gianfranco Bertone, Roberto Ruiz de Austri, Louis E. Strigari and Roberto Trotta, Phys. Rev. D **83**, 083505 (2011).

Lecture

- L. Baudis: **DARWIN: DARk matter WImp search with Noble liquids**
  Identification of Dark Matter, University of Montpellier, July 23, 2010.

19.1.5 GERDA

Article

- **Procurement, production and testing of BEGe detectors depleted in ^{76}Ge**
  M. Agostini, L. Baudis, E. Belotti *et al.*, Nuclear Physics B, Proceedings Supplements (2011).

Lecture

- F. Froborg: **GERDA / EXO**
  CHIPP Meeting, Gersau, August 23rd, 2010.

19.1.6 XENON

Articles

- **A study of the electromagnetic background in the XENON100 experiment**
  E. Aprile, K. Arisaka, F. Arneodo, A. Askin, L. Baudis, *et al.* (XENON100 Collaboration), Phys. Rev. D. 082001 (2011).
- **First Dark Matter Results from the XENON100 Experiment**
  E. Aprile, K. Arisaka, F. Arneodo, A. Askin, L. Baudis, *et al.* (XENON100 Collaboration), Phys. Rev. Lett. **105**, 131302 (2010).
- **Design and Performance of the XENON10 Dark Matter Experiment**
  E. Aprile, J. Angle, F. Arneodo, L. Baudis, A. Bernstein, *et al.* (XENON10 Collaboration), Astroparticle Physics **34** (2011), 679-698.
- **Spatially uniform calibration of a liquid xenon detector at low energies using 83m-Kr**
  A. Manalaysay, T. Marrodan Undagoitia, A. Askin, L. Baudis, A. Behrens, A. Kish, O. Lebeda, D.

Venos, Review of Scientific Instruments **81**, 073303 (2010).

Article in press

- **Background measurements in the Gran Sasso Underground Laboratory**
  M. Haffke, L. Baudis, T. Bruch, A.D. Ferella, T. Marrodan Undagoitia, M. Schumann, Y.-F. Te, A. van der Schaaf, Nucl. Instr. Meth. Phys. Res. Sect. A.

PhD thesis

- **Studien des externen Untergrunds eines XENON Detektors auf Tonnenskala zum Nachweis von Dunkler Materie**
  Marijke Haffke, PhD Thesis, Physik-Institut, Universität Zürich, 2010.

Lectures

- L. Baudis: **Status report on XENON100, XENON1T and DARWIN**
  ApPEC SAC Meeting, DESY Zeuthen, November 22, 2010.

- L. Baudis: **Dark Matter Searches with XENON100, XENON1T and DARWIN**
  Dark Matter: Its Origin, Nature and Prospects for Detection, GGI Arcetri, Florence, June 17, 2010.

- L. Baudis: **XENON, ZEPLIN and DARWIN**
  Aspera SAC meeting, LPNHE, Paris, April 13, 2010.

- T. Marrodan Undagoitia: **The XENON100 experiment: status and results**
  DPG, Karlsruhe, March 30th, 2011.

- T. Marrodan Undagoitia: **Status of XENON100**
  E15 seminar, Munich, October 30th, 2010.

- T. Marrodan Undagoitia: **Status of the XENON100 experiment**
  Darkness Visible, Cambridge, August 3rd, 2010.

- T. Marrodan Undagoitia: **Dark matter search with the XENON100 experiment**
  Joint Astroparticle physics seminar, Dortmund, May 11, 2010.

- T. Marrodan Undagoitia: **Dark matter search with the XENON100 experiment**
  Joint EP PP seminar, CERN, Geneva, April 19, 2010.

- M. Schumann: **The Search for Dark Matter with XENON**
  Seminar, Universität Erlangen, January 19th, 2011.

- M. Schumann: **XENON: Results and Prospects**
  TPC Symposium 2010, Paris, December 15th, 2010.

- M. Schumann: **Dark Matter and the XENON Experiment**
  Lunch Seminar, Weizmann Institute, Israel, November 4th, 2010.

- M. Schumann: **DARWIN**
  ASPERA Technology Meeting, Munich, October 22nd, 2010.

- M. Schumann: **XENON and DARWIN**
  CHIPP Meeting, Gersau, August 23rd, 2010.
- M. Schumann: **XENON100**
  IDM2010, Montpellier, July 26th, 2010.
- M. Schumann: **Dark Matter and the XENON100 Experiment**
  CP3 seminar, Université catholique Louvain, June 24th, 2010.
- M. Schumann: **Dark Matter and the XENON100 Experiment**
  Particle Physics Seminar, University of Geneva, Geneva, April 14, 2010.
- A. Kish: **The XENON100 Detector for Dark Matter Searches**
  CHIPP Meeting, Gersau, August 23rd, 2010.
- A. Behrens: **Calibration of the XENON100 PMTs**
  SPS meeting 2010, Basel, June 22th, 2010.

19.1.7 H1

Articles

- **Measurement of Leading Neutron Production in Deep-Inelastic Scattering at HERA**
  F.D. Aaron *et al.* (H1-Collaboration), European Physical Journal **C68** (2010), 381.
- **Inelastic Production of J/Ψ Mesons in Photoproduction and Deep Inelastic Scatteringat HERA**
  F.D. Aaron *et al.* (H1-Collaboration), European Physical Journal **C68** (2010), 401.
- **Diffractive Dijet Photoproduction in ep Collisions at HERA**
  F.D. Aaron *et al.* (H1-Collaboration), European Physical Journal **C70** (2010), 15.
- **Measurement of Charm and Beauty Jets in Deep Inelastic Scattering at HERA**
  F.D. Aaron *et al.* (H1-Collaboration), European Physical Journal **C71** (2011), 1509.
- **Measurement of the Diffractive Deep-Inelastic Scattering Cross Section with a Leading Proton at HERA**
  F.D. Aaron *et al.* (H1-Collaboration), European Physical Journal **C71** (2011), 1578.
- **Search for Squarks in R-Parity Violating Supersymmetry in ep Collisions at HERA**
  F.D. Aaron *et al.* (H1-Collaboration), European Physical Journal **C71** (2011), 1572.

Articles in print

- **Measurement of the Inclusive $e^{\pm}p$ Cross Section at High Inelasticity y and of the Structure Function F_L**
  F.D. Aaron *et al.* (H1-Collaboration),
  DESY 10 – 228, arXiv:1012.4355 [hep-ex], European Physical Journal **C** (2011).
- **Search for Lepton Flavour Violation at HERA**
  F.D. Aaron *et al.* (H1-Collaboration),
  DESY 11 – 044, arXiv:1103.4938 [hep-ex], Physics Letters **B** (2011).

Invited conference contributions

- Katharina Müller: **Photon Structure in Photoproduction**
  Photon 2009: 18th International Workshop on Photon-Photon Collisions,
  Hamburg, Germany, Jan 2010, DESY-PROC-2009-03, p. 181-189.

- Katharina Müller, on behalf of the H1 and ZEUS collaborations: **Precision measurements with jets and particles at HERA**
  QCD 2010, 15th International QCD-conference,
  Montpellier, France, June 2010, Nucl. Phys. Proc. Suppl. **207-208** (2010), 17-20.

19.1.8 LHCb

Articles

- **First observation of $B_s \to D_{s2}^{*+} X \mu\nu$ decays**
  LHCb-Collaboration, R. Aaij *et al.*, Phys. Lett. **B698** (2011) 14.

- **Measurement of $\sigma(\mathrm{pp} \to \mathrm{b\bar{b}}X)$ at $\sqrt{s}$=7 TeV in the forward region**
  LHCb-Collaboration, R. Aaij *et al.*, Phys. Lett. **B694** (2010) 209.

- **Prompt $\mathrm{K_s}$ production in pp collisions at $\sqrt{s}$=0.9 TeV**
  LHCb-Collaboration, R. Aaij *et al.*, Phys. Lett. **B693** (2010) 69.

- **Search for the rare decays $B_s^0 \to \mu^+\mu^-$ and $B^0 \to \mu^+\mu^-$**
  LHCb-Collaboration, R. Aaij *et al.*, Phys. Lett. **B699** (2011) 330.

Submitted Articles

- **First observation of $B_s^0 \to J/\psi f_0(980)$ decays**
  LHCb-Collaboration, R. Aaij, Phys. Lett. B, arXiv:1102.0206 [hep-ex].

- **Measurement of J/ψ production in pp collisions at $\sqrt{s}$=7 TeV**
  LHCb-Collaboration, R. Aaij, Eur. Phys. J. C, arXiv:1103.0423 [hep-ex].

LHCb notes and reports

- **Measurements of muon identification efficiencies for $Z \to \mu\mu$ and $W \to \mu\nu$ decays**
  J. Anderson and J. Keaveney, CERN-LHCb-INT-2011-001.

- **W and Z cross-section results**
  T. Shears *et al.* CERN-LHCb-ANA-2011-032.

- **Search for the rare decays $B_s^0 \to \mu^+\mu^-$ with the LHCb experiment**
  C. Adrover *et al.* CERN-LHCb-ANA-2011-007.

- **Measurement of the trigger efficiency for $Z \rightarrow \mu\mu$ and $W \rightarrow \mu\nu$ events in Reco06-Stripping10 data at LHCb**
  A. Bursche, J. Anderson, K. Müller, CERN-LHCb-INT-2010-057.

- **A Measurement of the Tracking Efficiency for High-pT Tracks in Reco06-Stripping10 Collision Data**
  M. De Cian, CERN-LHCb-INT-2010-058.

- **Revision of Adding TT Hits to Long Tracks**
  M. De Cian, CERN-LHCb-INT-2010-020.

Conference contributions

- Katharina Müller: **Electroweak physics: results and prospects**
  Physics at LHCb, 479 WE-Heraeus Seminar, 26th-29th April 2011, Bad Honnef, Germany.

- Michel De Cian: **First Mass Measurements at LHCb**
  XIX International Workshop on Deep-Inelastic Scattering and Related Subjects (DIS 2011), Newport News, Virginia, United States Of America, 11 - 15 Apr 2011.

- Christian Elsasser: **Rare B decays at LHC**
  SM@LHC, Workshop, IPPP Durham, 11. - 14. April 2011, London, Great Britain.

- Nicola Chiapolini: **Understanding Cryptography: From Caesar to Public-Key**
  iCSC (inverted Cern School of Computing) 2011, 3 - 4. March 2011, CERN, Geneva, Switzerland.

- Jonathan Anderson: **Prospects for indirect luminosity measurements at LHCb**
  Workshop LHC Lumi Days, 13th-14th January 2011, CERN, Geneva, Switzerland.

- Katharina Müller: **W and Z production in forward region at LHCb**
  EPIPHANY 2011 conference, 10th - 12th January 2011, Cracow, Poland.

- Angela Büchler: **Search for New Physics with Rare Heavy Flavour Decays at LHCb**
  SILAFAE conference, 6th - 12th December 2011, Valparaíso, Chile.

- Olaf Steinkamp: **LHCb Status, First Physics and Discovery Potential**
  Workshop on Discovery Physics at the LHC, 5.-10. Dec 2010, Mpumalanga, South Africa.

- Mark Tobin: **Performance of the LHCb Silicon Tracker in pp Collisions at the LHC**
  IEEE Nuclear Science Symposium, 30th October to 6th November 2010, Knoxville, Tennessee, U.S.A.

- Jonathan Anderson: **Constraints on low x PDFs from Drell Yan processes, and first studies of exclusive dimuon production with the LHCb experiment**
  XL International Symposium on Multiparticle Dynamics (ISMD10), 21st - 25th September 2010, Antwerp, Belgium.

- Mark Tobin: **Early experience with running the TT in LHCb and first results on electroweak physics studies**
  CHIPP workshop on the High-Energy Frontier, Universität Zürich, 1st September 2010, Zürich.

- Michel De Cian: **Grid Computing in LHCb. Or: How I learned to stop worrying and love distributed analysis**
  CHIPP workshop on the high-energy frontier, Universität Zürich, 1st September 2010, Zürich.

- Jeroen van Tilburg: **LHCb: Preparation for LHC beam**
  CHIPP annual meeting 2010, 23.-24.August 2010, Appenberg.

- Juan P. Palacios: **LHCb: first results and prospects for the 2010-11 run**
  16th International Symposium on Particles, Strings and Cosmology (PASCOS 2010)
  19–23 July 2010, Valencia, Spain.

- Michel De Cian: **A Tale of Two Ts: The Performance of the Tracker Turicensis at LHCb**
  Annual meeting of the Swiss Physical Society, 22. June 2010, Basel.

- Jeroen van Tilburg: **Search for New Physics in Heavy Quark Decays at LHCb**
  prepared for 9th International Conference on Hyperons, Charm and Beauty Hadrons (BEACH),
  Perugia, Italy, 21 - 26 June 2010.

- Jonathan Anderson: **First performance results for the LHCb Silicon Tracker**
  Proceedings 12th Topical Seminar on Innovative Particle and Radiation Detectors (IPRD10)
  7–10 June 2010, Siena, Italy, LHCb-PROC-2010-029.

- Jonathan Anderson: **Electroweak physics at LHCb**
  Seminar at the School of Physics and Astronomy, University of Manchester, May 26, 2010.

19.1.9 CMS

Articles

- **Study of the Bs meson with forthcoming LHC data at CMS**
  B. Millán Mejías, VIII Latin American Symposium on Nuclear Physics and Applications,
  AIP Conf. Proc. Volume **1265** (2010) 264.

- **Beam Background Effects in the CMS Pixel Detector**
  H. Snoek, Proc. of Science (Vertex 2010 - 013).

- **First measurements of beauty quark production at $\sqrt{s} = 7$ TeV with the CMS experiment**
  V. Chiochia, Nuclear Physics **A 855** (2011) 436.

- **Search for Quark Compositeness with the Dijet Centrality Ratio in pp Collisions at $\sqrt{s} = 7$ TeV**
  CMS Collaboration, Phys. Rev. Lett. **105** (2010) 262001.

- **Search for Dijet Resonances in 7 TeV pp Collisions at CMS**
  CMS Collaboration, Phys. Rev. Lett. **105** (2010) 211801.

- **Observation of Long-Range Near-Side Angular Correlations in Proton-Proton Collisions at the LHC**
  CMS Collaboration, J. High Energy Physics **1009** (2010) 091.

- **CMS Tracking Performance Results from early LHC Operation**
  CMS Collaboration, Eur. Phys. J. **C 70** (2010) 1165.

- **First Measurement of the Underlying Event Activity at the LHC with $\sqrt{s} = 0.9$ TeV**
  CMS Collaboration, Eur. Phys. J. **C 70** (2010) 555.

- **Measurement of the charge ratio of atmospheric muons with the CMS detector**
  CMS Collaboration, Phys. Lett. **B 692** (2010) 83.

- **Transverse-momentum and pseudorapidity distributions of charged hadrons in pp collisions at $\sqrt{s} = 7$ TeV**
  CMS Collaboration, Phys. Rev. Lett. **105** (2010) 022002.

- **First Measurement of Bose-Einstein Correlations in proton-proton Collisions at $\sqrt{s}$ = 0.9 and 2.36 TeV at the LHC**
  CMS Collaboration, Phys. Rev. Lett. **105** (2010) 032001.

- **Transverse momentum and pseudorapidity distributions of charged hadrons in pp collisions at $\sqrt{s}$ = 0.9 and 2.36 TeV**
  CMS Collaboration, J. High Energy Physics **1002** (2010) 041.

- **Measurement of the muon stopping power in lead tungstate**
  CMS Collaboration, J. Instrumentation **5** (2010) P03007.

- **Measurement of $B\bar{B}$ Angular Correlations based on Secondary Vertex Reconstruction at $\sqrt{s} = 7$ TeV**
  CMS Collaboration, J. High Energy Physics **1103** (2011) 136.

- **Dijet Azimuthal Decorrelations in pp Collisions at $\sqrt{s} = 7$ TeV**
  CMS Collaboration, Phys. Rev. Lett. **106** (2011) 122003.

- **Search for Supersymmetry in pp Collisions at 7 TeV in Events with Jets and Missing Transverse Energy**
  CMS Collaboration, Phys. Lett. **B 698** (2011) 196.

- **Measurement of the B^+ Production Cross Section in pp Collisions at $\sqrt{s} = 7$ TeV**
  CMS Collaboration, Phys. Rev. Lett. **106** (2011) 112001.

- **Search for a heavy gauge boson W' in the final state with an electron and large missing transverse energy in pp collisions at $\sqrt{s} = 7$ TeV**
  CMS Collaboration, Phys. Lett. **B 698** (2011) 21.

- **Search for Microscopic Black Hole Signatures at the Large Hadron Collider**
  CMS Collaboration, Phys. Lett. **B 697** (2011) 434.

- **Measurements of Inclusive W and Z Cross Sections in pp Collisions at $\sqrt{s} = 7$ TeV**
  CMS Collaboration, J. High Energy Physics **1101** (2011) 080.

- **Measurement of the Isolated Prompt Photon Production Cross Section in pp Collisions at $\sqrt{s} = 7$ TeV**
  CMS Collaboration, Phys. Rev. Lett. **106** (2011) 082001.

- **Search for Stopped Gluinos in pp collisions at $\sqrt{s} = 7$ TeV**
  CMS Collaboration, Phys. Rev. Lett. **106** (2011) 011801.

- **Charged particle multiplicities in pp interactions at $\sqrt{s}$ = 0.9, 2.36, and 7 TeV**
  CMS Collaboration, J. High Energy Physics **1101** (2011) 079.

- **First Measurement of the Cross Section for Top-Quark Pair Production in Proton-Proton Collisions at $\sqrt{s} = 7$ TeV**
  CMS Collaboration, Phys. Lett. **B 695** (2011) 424.

- **Inclusive b-hadron production cross section with muons in pp collisions at $\sqrt{s} = 7$ TeV**
  CMS Collaboration, J. High Energy Physics **1103** (2011) 090.

- **Search for Heavy Stable Charged Particles in pp collisions at $\sqrt{s} = 7$ TeV**
  CMS Collaboration, J. High Energy Physics **1103** (2011) 024.

- **Prompt and non-prompt J/psi production in pp collisions at $\sqrt{s} = 7$ TeV**
  CMS Collaboration, Eur. Phys. J. **C 71** (2011) 1575.

Article in press

- **Search for Large Extra Dimensions in the Diphoton Final State at the Large Hadron Collider**
  CMS Collaboration, J. High Energy Phys. [arXiv:1103.4279].

- **Measurement of the lepton charge asymmetry in inclusive W production in pp collisions at $\sqrt{s} = 7$ TeV**
  CMS Collaboration, J. High Energy Phys. [arXiv:1103.3470].

- **Search for Physics Beyond the Standard Model in Opposite-Sign Dilepton Events at $\sqrt{s} = 7$ TeV**
  CMS Collaboration, J. High Energy Phys. [arXiv:1103.1348].

- **Search for Resonances in the Dilepton Mass Distribution in pp Collisions at $\sqrt{s} = 7$ TeV**
  CMS Collaboration, J. High Energy Phys. [arXiv:1103.0981].

- **Search for Supersymmetry in pp Collisions at $\sqrt{s} = 7$ TeV in Events with Two Photons and Missing Transverse Energy**
  CMS Collaboration, [arXiv:1103.0953].

- **Search for a W' boson decaying to a muon and a neutrino in pp collisions at $\sqrt{s} = 7$ TeV**
  CMS Collaboration, [arXiv:1103.0030].

- **Study of Z boson production in PbPb collisions at $\sqrt{s_{NN}}$= 2.76 TeV**
  CMS Collaboration, Phys. Rev. Lett. [arXiv:1102.5435].

- **Measurement of W^+W^- Production and Search for the Higgs Boson in pp Collisions at $\sqrt{s} = 7$ TeV**
  CMS Collaboration, Phys. Lett. B [arXiv:1102.5429].

- **Search for a Heavy Bottom-like Quark in pp Collisions at $\sqrt{s} = 7$ TeV**
  CMS Collaboration, [arXiv:1102.4746].

- **Strange Particle Production in pp Collisions at $\sqrt{s} = 0.9$ and 7 TeV**
  CMS Collaboration, [arXiv:1102.4282].

- **Measurement of Dijet Angular Distributions and Search for Quark Compositeness in pp Collisions at $\sqrt{s} = 7$ TeV**
  CMS Collaboration, Phys. Rev. Lett. [arXiv:1102.2020].

- **Observation and studies of jet quenching in PbPb collisions at nucleon-nucleon center-of-mass energy = 2.76 TeV**
  CMS Collaboration, [arXiv:1102.1957].

- **First Measurement of Hadronic Event Shapes in pp Collisions at $\sqrt{s} = 7$ TeV**
  CMS Collaboration, Phys. Lett. B [arXiv:1102.0068].

- **Measurement of Bose-Einstein Correlations in pp Collisions at $\sqrt{s} = 0.9$ and 7 TeV**
  CMS Collaboration, J. High Energy Phys. [arXiv:1101.3518].

- **A new CMS pixel detector for the LHC luminosity upgrade**
  C. Favaro, Nucl. Instr. Meth. A, [arXiv:1104.1288].

- **Measurement of the Inclusive Upsilon production cross section in pp collisions at $\sqrt{s} = 7$ TeV**
  CMS Collaboration, Phys. Rev. D [arXiv:1012.5545].

- **Search for Pair Production of Second-Generation Scalar Leptoquarks in pp Collisions at $\sqrt{s} = 7$ TeV**
  CMS Collaboration, Phys. Rev. Lett. [arXiv:1012.4033].

- **Search for Pair Production of First-Generation Scalar Leptoquarks in pp Collisions at $\sqrt{s} = 7$ TeV**
  CMS Collaboration, Phys. Rev. Lett. [arXiv:1012.4033].

Invited Lectures

- E. Aguiló: **The alignment of the CMS Silicon Tracker**
  12th Topical Seminar on Innovative Particle and Radiation Detectors, Siena, Italy, 8 June 2010.

- V. Chiochia: **Beauty quark production with the CMS experiment**
  Workshop on Heavy Particles at the LHC, ETH Zurich, 6 January 2011.

- V. Chiochia: **Beauty and charm production with the CMS experiment**
  CERN Physics Days: Charm and Bottom Quark Production at the LHC, CERN, 3 December 2010.

- V. Chiochia: **Measurement of the inclusive beauty production with the CMS experiment**
  4th Int. Conf. on Hard and Electromagnetic Probes of High-Energy Nucl. Coll., Eilat, Israel, 10 October 2010.

- V. Chiochia: **Tracker for b-cross section measurements**
  CMS Tracker Week, La Biodola, Isola d'Elba, Italy, 25 May 2010.

- S. de Visscher: **First results from the CMS experiment**
  Annual meeting of the Swiss Physical Society, Basel, Switzerland, 21 June 2010.

- S. de Visscher: **Evaluation of the CMS pixel detector data from the first LHC collisions**
  12th Topical Seminar on Innovative Particle and Radiation Detectors, Siena, Italy, 8 June 2010.

- C. Favaro: **The upgrade of the CMS Pixel Detector**
  8th Int. Conf. on Rad. Effects on Semiconductor Materials Detectors and Devices, Florence, 12 October 2010.

- C. Favaro: **Hit resolution measurement with the CMS pixel detector**
  Annual meeting of the Swiss Physical Society, Basel, Switzerland, 21 June 2010.

- A. Jaeger: **Data comparison with Monte-Carlo**
  CMS Tracker Week, La Biodola, Isola d'Elba, Italy, 4 May 2010.

- A. Jaeger : **Performance of the CMS silicon pixel detector: results from the first data**
  Annual meeting of the Swiss Physical Society, Basel, Switzerland, 22 June 2010.

- M. Ivova Rikova: **Measurement of the Lorentz angle in the CMS barrel pixel detector**
  Annual meeting of the Swiss Physical Society, Basel, Switzerland, 21 June 2010.

- B. Millán Mejías: **Study of the B_s-meson with forthcoming data at the CMS detector**
  Annual meeting of the Swiss Physical Society, Basel, Switzerland, 22 June 2010.

- P. Otyugova: **First CMS physics results**
  CHIPP Workshop on the High Energy Frontier, Zurich, 1 September 2010.

- T. Rommerskirchen: **Supersymmetry at CMS with multijet events: an experimental strategy**
  Annual meeting of the Swiss Physical Society, Basel, Switzerland, 21 June 2010.

- A. Schmidt: **Performance of Track and Vertex Reconstruction and B-Tagging Studies with CMS in pp Collisions at $\sqrt{s}$ =7 TeV**
  Kruger 2010: Workshop on Discovery Physics at the LHC, Kruger National Park (South Africa), 5 December 2010.

- A. Schmidt: **b-quarks in the CMS experiment: from detector design to physics results**
  Seminar at the University of Freiburg i.B., Germany, 15 February 2011.

- H. Snoek: **Beam backgrounds in the CMS pixel detector**
  19th Int. Workshop on Vertex Detectors, Loch Lomond, Scotland, 6 June 2010.

- H. Snoek: **The CMS pixel detector: commissioning and performance**
  6th Trento Workshop on Advanced Silicon Radiation Detectors, FBK–IRST, Trento, 3 March 2011.

PhD thesis

- **Supersymmetry with Multijet Events at CMS: an Experimental Strategy**
  T. Rommerskirchen, Inaugural Dissertation, Universität Zürich, 2010.

19.1.10 Miscellaneous

Articles

- **Review of Particle Physics**
  Particle Data Group (C. Amsler), Journal of Physics **G 37** (2010) 075021.

- **Particle Physics Booklet**
  Particle Data Group (C. Amsler), IOP Publishing, 2010.

- **Note on scalar mesons**
  C. Amsler, T. Gutsche, S. Spanier and N.A. Törnqvist,
  Journal of Physics G: Nucl. and Part. Phys. **37** (2010) 075021-680.

- **The $\eta(1405)$, $\eta(1475)$, $f_1(1420)$, and $f_1(1510)$**
  C. Amsler and A. Masoni, Journal of Physics G: Nucl. and Part. Phys. **37** (2010) 075021-630.

- **Quark Model**
  C. Amsler, T. DeGrand and B. Krusche,
  Journal of Physics G: Nucl. and Part. Phys. **37** (2010) 075021-184.

Errata

- **A New Measurement of K^+_{e4} Decay and the $s-$Wave $\pi\pi$ Scattering Length**
  E865-Collaboration, S. Pislak *et al.*, Erratum: Phys. Rev. Lett. **105** (2010), 019901.

- **High Statistics Measurement of K_{e4} Decay Properties**
  E865-Collaboration, S. Pislak *et al.*, Erratum: Phys. Rev. **D81** (2010), 119903 (E).

Lectures

- L. Baudis: **Dark matter searches with CDMS and XENON**
  Particle Physics Seminar, Tel Aviv University, February 24, 2011.

- L. Baudis: **Direct searches for dark matter in the Milky Way**
  Physics Colloquium, Weizmann Institute of Science, Rehovot, February 17, 2011.

- L. Baudis: **Direct searches for dark matter in the Milky Way**
  Physics Colloquium, TU Dresden, February 1, 2011.

- L. Baudis: **Direct searches for dark matter in the Milky Way**
  Munich Physics Colloquium, TUM, Munich, January 17, 2011.

- L. Baudis: **Highlights from the astroparticle physics session**
  Summary talk, TEXAS2010, Heidelberg, December 10, 2010.

- L. Baudis: **Direct searches for dark matter in the Milky Way**
  Physics Colloquium, University of Heidelberg, November 26, 2010.

- L. Baudis: **Recent results on direct WIMP searches from the CDMS-II and XENON100 experiments**
  Physics Seminar, INFN Roma La Sapienza, October 11, 2010.

- L. Baudis: **Direct searches for dark matter**
  Physics Colloquium, Stony Brook University, New York, September 7, 2010.

- L. Baudis: **Direct dark matter searches: an overview**
  SUSY 2010, Physikalisches Institut, Bonn, August 26, 2010.

- L. Baudis: **Direct dark matter searches**
  Physics at the LHC, DESY, Hamburg, June 12, 2010.

- L. Baudis: **Direct searches for dark matter**
  Physics Colloquium, Mainz University, May 11, 2010.

- T. Marrodan Undagoitia: **Direct dark matter search using liquid noble gases**
  TeVPA, Paris, July 19th, 2010.

- T. Marrodan Undagoitia: **Direct dark matter search using liquid noble gases**
  TEXAS workshop, Heidelberg, December 9th, 2010.
- T. Marrodan Undagoitia: **Neutrino astrophysics and particle physics in LAGUNA**
  Seminars on Astroparticle physics, DESY, Hamburg, May 03, 2010.
- A. Manalaysay: **Dark matter detection with noble liquids**
  Rencontres de Moriond, Eletroweak Interactions and Unified Theories, La Thuile, Italy, March 18th, 2011.

Outreach

Lectures

- C. Amsler: **La Recherche au CERN**
  Café Scientifique, University of Fribourg, Switzerland, 17 February 2011.
- L. Baudis: **Die unerträgliche Leichtigkeit der Neutrinos**
  Montagsforum, Dornbirn, Austria, May 17, 2010.

19.2 Condensed matter

19.2.1 Superconductivity and Magnetism

Articles

- **Identification of magnetic properties of few nm sized FePt crystalline particles by characterizing the intrinsic atom order using aberration corrected S/TEM**
  J. Biskupek, J. R. Jinschek, U. Wiedwald, M. Bendele, L. Han, P. Ziemann, and U. Kaiser, Ultramicroscopy **110**, 820-825 (2010).
- **Microwave-Hydrothermal Synthesis of Nanostructured Zinc-Copper Gallates**
  F. Conrad, Y. Zhou, M. Yulikov, K. Hametner, S. Weyeneth, G. Jeschke, D. Günther, J.-D. Grunwaldt, and G. R. Patzke, Eur. J. Inorg. Chem. **13**, 2036-2043 (2010).
- **Direct measurement of the London penetration depth in $YBa_2Cu_3O_{6.92}$ using low-energy μSR**
  R. F. Kiefl, M. D. Hossain, B. M. Wojek, S. R. Dunsiger, G. D. Morris, T. Prokscha, Z. Salman, J. Baglo, D. A. Bonn, R. Liang, W. N. Hardy, A. Suter, and E. Morenzoni, Phys. Rev. B **81**, 180502-1-4 (2010).
- **Quasiparticle relaxation dynamics in spin-density-wave and superconducting $SmFeAsO_{1-x}F_x$ single crystals**
  T. Mertelj, P. Kusar, V. V. Kabanov, L. Stojchevska, N. D. Zhigadlo, S. Katrych, Z. Bukowski, J. Karpinski, S. Weyeneth, and D. Mihailovic, Phys. Rev. B **81**, 224504-1-9 (2010).
- **Anisotropic superconducting properties of single-crystalline $FeSe_{0.5}Te_{0.5}$**
  M. Bendele, S. Weyeneth, R. Puzniak, A. Maisuradze, E. Pomjakushina, K. Conder, V. Pomjakushin, H. Luetkens, S. Katrych, A. Wisniewski, R. Khasanov, and H. Keller, Phys. Rev. B **81**, 224520-1-10 (2010).

- **Comment on "Muon-spin-rotation study of the superconducting properties of Mo_3Sb_7"**
  R. Khasanov, A. Shengelaya, I. M. Savić, C. Baines, and H. Keller,
  Phys. Rev. B **82**, 016501-1-3 (2010).

- **Iron isotope effect on the superconducting transition temperature and the crystal structure of $FeSe_{1-x}$**
  R. Khasanov, M. Bendele, K. Conder, H. Keller, E. Pomjakushina, and V. Pomjakushin,
  New J. Phys. **12**, 073024-1-8 (2010).

- **Suppression of the antinodal coherence of superconducting $(Bi,Pb)_2(Sr,La)_2CuO_{6+\delta}$ as revealed by muon spin rotation and angle-resolved photoemission**
  R. Khasanov, T. Kondo, M. Bendele, Y. Hamaya, A. Kaminski, S. L. Lee, S. J. Ray, and T. Takeuchi,
  Phys. Rev. B **82**, 020511(R)-1-4 (2010).

- **Th-substituted SmFeAsO: Structural details and superconductivity with T_c above 50 K**
  N. D. Zhigadlo, S. Katrych, S. Weyeneth, R. Puzniak, P. J. W. Moll, Z. Bukowski, J. Karpinski, H. Keller, and B. Batlogg, Phys. Rev. B **82**, 064517-1-11 (2010).

- **Field Dependent Superfluid Density in Optimally Doped $SmFeAsO_{1-x}F_y$**
  S. Weyeneth, M. Bendele, R. Puzniak, F. Muranyi, A. Bussmann-Holder, N. D. Zhigadlo, S. Katrych, Z. Bukowski, J. Karpinski, A. Shengelaya, R. Khasanov, and H. Keller,
  Europhys. Lett. **91**, 47005-1-6 (2010).

- **Electron spin dynamics and electron spin resonance in graphene**
  B. Dóra, F. Murányi, and F. Simon, Europhys. Lett. **92**, 17002-1-5 (2010).

- **Magnetic anisotropy and ferromagnetic correlations above the Curie temperature in Eu_2CuSi_3 single crystals**
  C. D. Cao, R. Klingeler, H. Vinzelberg, N. Leps, W. Löser, G. Behr, F. Muranyi, V. Kataev, and B. Büchner, Phys. Rev. B **82**, 134446 (2010).

- **Microscopic Study of the Superconducting State of the Iron Pnictide $RbFe_2As_2$ via muon spin rotation**
  Z. Shermadini, J. Kanter, C. Baines, M. Bendele, Z. Bukowski, R. Khasanov, H.-H. Klauss, H. Luetkens, H. Maeter, G. Pascua, B. Batlogg, and A. Amato, Phys. Rev. B **82**, 144527-1-5 (2010).

- **Bulk superconductivity at 2.6 K in undoped $RbFe_2As_2$**
  Z. Bukowski, S. Weyeneth, R. Puzniak, J. Karpinski, and B. Batlogg,
  Physica C **470**, S328-S329 (2010).

- **Tuning the superconducting and magnetic properties of $Fe_ySe_{0.25}Te_{0.75}$ by varying the iron content**
  M. Bendele, P. Babkevich, S. Katrych, S. N. Gasaliya, E. Pomjakushina, K. Conder, B. Roessli, A. T. Boothroyd, R. Khasanov, and H. Keller, Phys. Rev. B **82**, 212504-1-4 (2010).

- **Intrinsic and structural isotope effects in iron-based superconductors**
  R. Khasanov, M. Bendele, A. Bussmann-Holder, and H. Keller, Phys. Rev. B **82**, 212505-1-4 (2010).

- **Comment on "Isotope Effect in Multi-Band and Multi-Channel Attractive Systems and Inverse Isotope Effect in Iron-Based Superconductors"**
  A. Bussmann-Holder and H. Keller, J. Phys. Soc. Jpn. **79**, 126001-1-6 (2010).

- **Anomalies in the Fermi Surface and Band Dispersion of Quasi-One-Dimensional CuO Chains in the High-Temperature Superconductor $YBa_2Cu_4O_8$**
  T. Kondo, R. Khasanov, J. Karpinski, S.M. Kazakov, N.D. Zhigadlo, Z. Bukowski, M. Shi, A. Bendounan, Y. Sassa, J. Chang, S. Pailhés, J. Mesot, J. Schmalian, H. Keller, and A. Kaminski,
  Phys. Rev. Lett. **105**, 267003-1-4 (2010).

- **Structural dependence of the efficiency of functionalization of silica-coated FeO_x magnetic nanoparticles studied by ATR-IR**
  A. Vargas, I. Shnitko, A. Teleki, S. Weyeneth, S. E. Pratsinis, and A. Baiker,
  App. Surf. Sci. **257**, 2861-2869 (2011).

- **Synthesis and crystal growth of $Cs_{0.8}(FeSe_{0.98})_2$: a new iron-based superconductor with $T_c = 27$ K**
  A. Krzton-Maziopa, Z. Shermadini, E. Pomjakushina, V. Pomjakushin, M. Bendele, A. Amato, R. Khasanov, H. Luetkens, and K. Conder, J. Phys.: Condens. Matter **23**, 052203-1-4 (2011).

- **Absence of Orbital Currents in Superconducting $YBa_2Cu_4O_8$ Using a Zeeman-Perturbed Nuclear-Quadrupole-Resonance Technique**
  S. Strässle, B. Graneli, M. Mali, J. Roos, and H. Keller, Phys. Rev. Lett. **106**, 097003-1-4 (2011).

- **Coexistence of Magnetism and Superconductivity in the Iron-based Compound $Cs_{0.8}(FeSe_{0.98})_2$**
  Z. Shermadini, A. Krzton-Maziopa, M. Bendele, R. Khasanov, H. Luetkens, K. Conder, E. Pomjakushina, S. Weyeneth, V. Pomjakushin, O. Bossen, and A. Amato,
  Phys. Rev. Lett. **106**, 117602-1-4 (2011).

- **Pressure Effects in the Isoelectronic $REFe_{0.85}Ir_{0.15}AsO$ System**
  B. Maroni, D. Di Castro, M. Hanfland, J. Boby, C. Vercesi, M. C. Mozzati, S. Weyeneth, H. Keller, R. Khasanov, C. Drathen, P. Dore, P. Postorino, and L. Malavasi,
  J. Am. Chem. Soc. **133**, 3252-3255 (2011).

- **Anisotropic phase diagram and superconducting fluctuations of single-crystalline $SmFeAsO_{0.85}F_{0.15}$**
  U. Welp, C. Chaparro, A. E. Koshelev, W. K. Kwok, A. Rydh, N. D. Zhigadlo, J. Karpinski, and S. Weyeneth, Phys. Rev. B **83**, 100513(R) (2011).

Bachelor and Master theses

- **Sauerstoffisotopeneffekt des Pseudo-Gap-Phänomens im Kuprat-Hochtemperatursupraleiter $Y_{0.6}Pr_{0.4}Ba_2Cu_3O_7$**
  E. Eisenring, Bachelor thesis, Universität Zürich.

- **Lanthan-139 NQR Messungen im HTC-Supraleiter $LaBa_2Cu_3O_7$**
  L. Maag, Bachelor thesis, Universität Zürich.

- **Magnetic and Superconducting properties of $FeSe_{1-x}$, dependency on sample preparation**
  A. Ichsanov, Master thesis, Universität Zürich.

- **Measurements of Longitudinal Nuclear Magnetism with NMR Probes**
  S. Gross, Master thesis, Universität Zürich.

Articles in press

- **Identifying the Pairing Mechanism in Feï¿ŘAs Based Superconductors: Gaps and Isotope Effects**
  A. Bussmann-Holder, A. Simon, H. Keller, and A. R. Bishop, J. Supercond. Nov. Magn.

- **Strong coupling between the Eu^{2+} spins and the Fe$_2$As$_2$ layers in EuFe$_{1.9}$Co$_{0.1}$As$_2$ observed with NMR**
  Z. Guguchia, J. Roos, A. Shengelaya, S. Katrych, Z. Bukowski, S. Weyeneth, F. Murányi, S. Strässle, A. Maisuradze, J. Karpinski, and H. Keller, Phys. Rev. B.

- **Rearrangement of the antiferromagnetic ordering at high magnetic fields in SmFeAsO and SmFeAsO$_{0.9}$F$_{0.1}$ single crystals**
  S. Weyeneth, P. J. W. Moll, R. Puzniak, K. Ninios, F. F. Balakirev, R. D. McDonald, H. B. Chan, N. D. Zhigadlo, S. Katrych, Z. Bukowski, J. Karpinski, H. Keller, B. Batlogg, and L. Balicas, Phys. Rev. B

- **Diamagnetism, Nernst signal, and finite-size effects in superconductors above the transition temperature T_c**
  T. Schneider and S. Weyeneth, Phys. Rev. B.

- **Oxygen Isotope Effect in Cuprates Results from Polaron-Induced Superconductivity**
  S. Weyeneth and K. A. Müller, J. Supercond. Nov. Magn.

Conference reports

- **Anisotropic properties of superconducting single crystals of La$_{2-x}$Sr$_x$CuO$_4$**
  S. Bosma, S. Weyeneth, G. Deng, E. Pomjakushina, K. Conder and H. Keller,
  Annual meeting of the Swiss Physical Society, Basel, June 21-22, 2010.

- **Anisotropic superconducting properties of single-crystalline FeSe$_{0.5}$Te$_{0.5}$**
  M. Bendele, S. Weyeneth, R. Puzniak, A. Maisuradze, E. Pomjakushina, K. Conder, V. Pomjakushin, H. Luetkens, S. Katrych, A. Wisniewski, R. Khasanov, and H. Keller,
  Annual meeting of the Swiss Physical Society, Basel, June 21-22, 2010.

- **NMR Search for orbital-current Effects in under-doped YBCO**
  B. Graneli, S. StréČŋsle, J. Roos, M. Mali, H. Keller, and J. Karpinski,
  Annual meeting of the Swiss Physical Society, Basel, June 21-22, 2010.

- **Electron Paramagnetic Resonance (EPR) investigation of EuFe$_{2-x}$Co$_x$As$_2$ ($x = 0$, 0.1, 0.2) single crystals**
  Z. Guguchia, A. Shengelaya, F. Murányi, A. Maisuradze, S. Weyeneth, S. Katrych, Z. Bukowski, J. Karpinski, and H. Keller, Annual meeting of the Swiss Physical Society, Basel, June 21-22, 2010.

- **Muon spin rotation study of the CaC$_6$ superconductor at low temperatures**
  F. Murányi, M. Bendele, R. Khasanov, S. Weyeneth, C. Baines, and H. Keller,
  Annual meeting of the Swiss Physical Society, Basel, June 21-22, 2010.

- **Anisotropic properties and multi-gap superconductivity in SmFeAsO$_{1-x}$F$_y$**
  S. Weyeneth, R. Puzniak, N. D. Zhigadlo, S. Katrych, Z. Bukowski, J. Karpinski, M. Bendele, F. Murányi, A. Bussmann-Holder, A. Shengelaya, R. Khasanov, and H. Keller,
  Annual meeting of the Swiss Physical Society, Basel, June 21-22, 2010.

- **Low energy muon spin rotation study of the Meissner effect in $La_{2-x}Sr_xCuO_4$ heterostructures**
  B. M. Wojek, E. Morenzoni, A. Suter, T. Prokscha, Z. Salman, G. Logvenov, A. Gozar, I. Bozovic, and H. Keller, Annual meeting of the Swiss Physical Society, Basel, June 21-22, 2010.

- **Electron Paramagnetic Resonance (EPR) investigation of $EuFe_{2-x}Co_xAs_2$ ($x = 0$, 0.1, 0.2) single crystals**
  Z. Guguchia, A. Shengelaya, F. Murányi, A. Maisuradze, S. Weyeneth, S. Katrych, Z. Bukowski, J. Karpinski, and H. Keller,
  9th PSI Summer School on condensed matter research, Zuoz, Switzerland, August 7-13, 2010.

- **Anisotropic properties and multi-gap superconductivity in iron-pnictide superconductors**
  S. Weyeneth, R. Puzniak, N. D. Zhigadlo, S. Katrych, Z. Bukowski, J. Karpinski, M. Bendele, F. Murányi, A. Bussmann-Holder, A. Shengelaya, R. Khasanov, and H. Keller,
  23rd General Conference of the Condensed Matter Division of the European Physical Society, CDM23, Warsaw, Poland, August 30 - September 3, 2010.

- **Iron isotope effect on the superconducting transition temperature and the crystal structure of $FeSe_{1-x}$**
  M. Bendele, R. Khasanov, K. Conder, E. Pomjakushina, V. Pomjakushin, A. Bussmann-Holder, and H. Keller, March Meeting of the American Physical Society, Dallas, USA, March 21-25, 2011.

- **Generics of the diamagnetism, Nernst signal, and finite size effects in superconductors above the transition temperature**
  S. Weyeneth and T. Schneider,
  March Meeting of the American Physical Society, Dallas, USA, March 21-25, 2011.

Invited lectures

- H. Keller: **Isotope effects and multi-band superconductivity in layered high-temperature superconductors**
  International Conference on Superconductivity and Magnetism,
  ICSM 2010, Antalya, Turkey, April 25-30, 2010.

- H. Keller: **Isotope effects and multi-band superconductivity in layered high-temperature superconductors**
  6th International Conference Science and Engineering of Novel Superconductors,
  CIMTEC 2010, Montecatini Terme, Italy, June 13-18, 2010.

- H. Keller: **Isotope effects and multi-band superconductivity in layered high-temperature superconductors**
  3rd International Symposium on Structure-Property Relationships in Solid State Materials,
  Max Planck Institute for Solid State Research, Stuttgart, Germany, June 27 - July 2, 2010.

- H. Keller: **Isotope effects and multi-band superconductivity in layered high-temperature superconductors**
  International Conference on Quantum Phenomena in Complex Matter, Stripes 2010, Ettore Majorana Foundation and Centre for Scientific Culture Erice, Erice, Italy, July 19-25, 2010.

- H. Keller: **Isotope effects and multi-band superconductivity in layered high-temperature superconductors**

23rd General Conference of the Condensed Matter Division of the European Physical Society, CDM23, Warsaw, Poland, August 30 - September 3, 2010.

- M. Bendele: **Muon Spin Rotation and Relaxation (μSR) studies on Fe-based superconductors**
  Festkörperphysikseminar, Universität Ulm, Germany, February 27, 2011.

- H. Keller: **From cuprate to iron-based superconductors - what are the key elements of high-temperature superconductivity?**
  High Pressure Science Society of America, Study of Matter at Extreme Conditions,
  SMEC2011, Miami, U.S.A., March 27 - April 2, 2011

19.2.2 Phase transitions and superconducting photon detectors

Articles

- **Nanoscale fabrication by intrinsic suppression of proximity-electron exposures and general considerations for easy and effective top-down fabrication**
  H. Bartolf, K. Inderbitzin, L. B. Gómez, A. Engel, A. Schilling,
  J. of Micromech. and Microeng. **20** (2010) 125015.

- **Influence of thickness, width and temperature on critical current density of Nb thin film structures**
  K. Il'in, D. Rall, M. Siegel, A. Engel, A. Schilling, A. Semenov, H.-W. Huebers,
  Phys. C, **470** (2010) 953-956.

Articles in press

- **Dynamic stability of organic conducting polymers and its replications in electrical conduction and degradation mechanics**
  E. F. C. Chimamkpam, T. Schweizer, A. Schilling, J. M. F. Ferreira, Advanced Functional Materials.

Contributed Conference Presentations

- A. Engel: **Superconducting Single-Photon Detectors from meV to keV**
  The 6th Patras Workshop on Axions, WIMPs and WISPs, University of Zurich, Switzerland,
  5.-9.7.2010.

- H. Bartolf: **Dissipative Fluctuation Mechanisms in BCS-Superconductors**
  Kryoelektronische Bauelemente Kryo 2010, Zeuthen (Berlin), Germany, 3.-5.10.2010.

Invited Lectures

- A. Schilling: **Bose-Einstein condensates in magnetic insulators from a traditional perspective**
  Spintronics Days at UPV-EHU, Bilbao, Spain, 28.7.2010.

- H. Bartolf: **Research on Nanoscaled Superconducting Highspeed Single-Photon Detectors Enabled by Easy and Effective Top-Down Fabrication**
  ABB Switzerland, 9.9.2010.

- A. Engel: **Superconducting Nanostructures and Detectors**
  University of San Andrés, La Paz, Bolivia, 17.12.2010.

19.2.3 Surface Physics

Articles

- **Structure determination of the coincidence phase of graphene on Ru(0001)**
  W. Moritz, B. Wang, M.-L. Bocquet, T. Brugger, T. Greber, J. Wintterlin, S. Günther,
  Phys. Rev. Lett. 104, 136102:1-4 (2010).

- **Graphene on Ru(0001): a corrugated and chiral structure**
  D. Martoccia, M. Björk, C. M. Schlepütz, T. Brugger, S. A. Pauli, B. D. Patterson, T. Greber, P. R. Willmott, New J. Phys. 12, 043028:1-12 (2010).
- **Robust spin polarization and spin textures on stepped Au(111) surfaces**
  J. Lobo-Checa, F. Meier, J. H. Dil, T. Okuda, M. Corso, V. N. Petrov, M. Hengsberger, L. Patthey, J. Osterwalder, Phys. Rev. Lett. 104, 187602:1-4 (2010).
- **Graphene and hexagonal boron nitride layers: nanostructures with three bond hierarchy levels**
  T. Greber, e-J. Surf. Sci. Nanotechnol. 8, 62-64 (2010).
- **Graphene based quantum dots**
  H. G. Zhang, H. Hu, Y. Pan, J. H. Mao, M. Gao, H. M. Guo, S. X. Du, T. Greber, H.-J. Gao, J. Phys.: Condens. Matter 22, 302001:1-4 (2010).
- **Rare-earth surface alloying: a new phase for GdAu2**
  M. Corso, M. J. Verstraete, F. Schiller, M. Ormaza, L. Fernandez, T. Greber, M. Torrent, A. Rubio, J. E. Ortega, Phys. Rev. Lett. 105, 016101:1-4 (2010).
- **Negative-electron-affinity diamondoid monolayers as high-brilliance source for ultrashort electron pulses**
  S. Roth, D. Leuenberger, J. Osterwalder, J. E. Dahl, R. M. K. Carlson, B. A. Tkachenko, A. A. Fokin, P. R. Schreiner, M. Hengsberger, Chem. Phys. Lett. 495, 102-108 (2010).
- **Nanotexture switching of single-layer hexagonal boron nitride on rhodium by intercalation of hydrogen atoms**
  T. Brugger, H. Ma, M. Iannuzzi, S. Berner, A. Winkler, J. Hutter, J. Osterwalder, T. Greber, Angew. Chem. Int. Ed. 49, 6120-6124 (2010).
- **Corrugated single layer templates for molecules: from h-BN nanomesh to graphene based quantum dot arrays**
  H. Ma, M. Thomann, J. Schmidlin, S. Roth, M. Morscher, T. Greber,
  Front. Phys. China, 5, 387-392 (2010).
- **Structural influence on the Rashba-type spin splitting in surface alloys**
  I. Gierz, B. Stadtmüller, J. Vuorinen, M. Lindroos, F. Meier, J. H. Dil, K. Kern, C. R. Ast,
  Phys. Rev. B 81, 145430:1-7 (2010).
- **Comment on "Potential energy landscape for hot electrons in periodically nanostructured graphene"**
  H. G. Zhang, T. Greber, Phys. Rev. Lett. 105, 219701 (2010).

- **Strong 3p-T1u hybridization in Ar@C60**
  M. Morscher, A. Seitsonen, S. Ito, H. Takagi, N. Dragoe, T. Greber,
  Phys. Rev. A 82, 051201(R):1-4 (2010).

- **Direct observation of spin-polarized surface states in the parent compound of a topological insulator using spin- and angle-resolved photoemission spectroscopy in a Mott-polarimetry mode**
  D. Hsieh, L. Wray, D. Qian, Y. Xia, J. H. Dil, F. Meier, L. Patthey, J. Osterwalder, G. Bihlmayer, Y. S. Hor, R. J. Cava, M. Z. Hasan, New J. Phys. 12, 125001:1-9 (2010).

- **Interference of spin states in photoemission from Sb/Ag(111)**
  F. Meier, V. Petrov, H. Mirhosseini, L. Patthey, J. Henk, J. Osterwalder, J. H. Dil,
  J. Phys.: Condens. Matter 23, 072207:1-6 (2011).

- **Controlling the effective mass of quantum well states in Pb/Si(111) by interface engineering**
  B. Slomski, F. Meier, J. Osterwalder, J. H. Dil, Phys. Rev. B 83, 035409:1-7 (2011).

- **Real-space multiple scattering method for angle-resolved photoemission and valence-band photoelectron diffraction and its application to Cu(111)**
  P. Krüger, F. Da Pieve, J. Osterwalder, Phys. Rev. B 83, 115437:1-8 (2011).

- **Topological phase transition and texture inversion in a tunable topological insulator**
  Su-Yang Xu, Y. Xia, L. A. Wray, S. Jia, F. Meier, J. H. Dil, J. Osterwalder, B. Slomski, A. Bansil, H. Lin, R. J. Cava, M. Z. Hasan, Science 332, 560-564 (2011).

Articles in press

- **Strongly enhanced electron-phonon coupling in the Rashba-split state of the Bi/Ag(111) surface alloy**
  D. Guan, M. Bianchi, S. Bao, E. Perkins, F. Meier, J. H. Dil, J. Osterwalder, Ph. Hofmann,
  Phys. Rev. B.

- **Time-resolved photoelectron spectroscopy to probe ultrafast charge transfer and electron dynamics in solid surface systems and at metal-molecule interfaces**
  L. Castiglioni, M. Greif, D. Leuenberger, S. Roth, J. Osterwalder, M. Hengsberger, Chimia.

- **Synthesis of graphene on rhodium from 3-pentanone**
  S. Roth, J. Osterwalder, T. Greber, Surf. Sci..

- **Tuning the spin texture in binary and ternary surface alloys on Ag(111)**
  I. Gierz, F. Meier, J. H. Dil, K. Kern, C. R. Ast, Phys. Rev. B.

Articles for the general public

- **Modengekoppelte Laser: (Im-)Pulse für die Forschung**
  M. Hengsberger, D. Leuenberger, S. Roth, Bulletin VSE/SEV Electrosuisse, 06/2010, S. 48-52.

- **Materialien für die Computer von morgen: Topologische Isolatoren - die neueste Entdeckung der Festkörperphysik**
  J. Osterwalder, Neue Zürcher Zeitung, 7. Juli 2010, S. 57.

PhD theses

- **Rashba-type spin-orbit coupling in the surface alloys on Ag(111) probed by spin- and angle-resolved photoemission spectroscopy**
  Fabian Meier, PhD Thesis, Physik-Institut, Universität Zürich, 2010.
- **Tools for investigating molecular magnetism: a new Mott detector and resonant photoelectron diffraction with circular dichroism**
  Martin Morscher, PhD Thesis, Physik-Institut, Universität Zürich, 2010.

Master theses

- **COPHEE and SMOKE: in-situ surface magneto-optic Kerr effect setup for the spin- and angle-resolved photoemission experiment COPHEE**
  Gabriel Landolt, Master Thesis, Physik-Institut, Universität Zürich, 2010.

Contributed conference presentations including posters

- H. Cun: **Multiple roles of carbon chains in quinacridone monolayers**
  Swiss Physical Society Meeting, Basel, 22.06.10.
- M. Hengsberger: **Electron emission dynamics from negative-electron-affinity diamondoid monolayers**
  1st International Conference on Ultrafast Structural Dynamics (ICUSD), Lausanne, 10.06.10.
- H. Yanagisawa: **Optical control of field emission sites by femtosecond laser pulses**
  2nd International Workshop on Ultrafast Nanooptics, Bad Türkheim, Germany, 28.06.10.
- J. H. Dil: **Spin- and angle-resolved photoemission on model systems for spintronics**
  Low-Energy Electrodynamics in Solids 2010, Les Diablerets, 09.07.10.
- B. Slomski: **Rashba-type spin-orbit splitting in PbBiSi (Poster)**
  PSI Summer School on Magnetic Phenomena, Zuoz, 07.-13.08.10.
- J. H. Dil: **Interference of spin states in photoemission from Sb/Ag(111)**
  European Conference on Surface Science (ECOSS-27), Groningen, The Netherlands, 02.09.10.
- B. Slomski: **Interface mediated spin effects in Pb quantum well states**
  European Conference on Surface Science (ECOSS-27), Groningen, The Netherlands, 02.09.10.
- H. Cun: **Water and xenon self-assembly on h-BN nanomesh (Poster)**
  Graphene International School, Cargese, France, 11.-23.10.10.
- S. Roth: **CVD growth of graphene on rhodium (Poster)**
  Graphene International School, Cargese, France, 11.-23.10.10.
- J. H. Dil: **Manipulation of spin structures in quantum well states and topological insulators**
  Gerhard Ertl Young Investigator Award, DPG Frühjahrsmeeting, Dresden, Germany, 17.03.11.

Invited lectures

- T. Greber: **Looking inside endofullerenes with photoemission**
  IFW-Seminar, Leibniz Institute for Solid State and Materials Research, Dresden, Germany, 03.05.2010.
- J. H. Dil: **Spin- and angle-resolved photoemission of low-dimensional Rashba systems**
  IAP-Seminar, Technische Universität Wien, Austria, 04.05.10.
- J. H. Dil: **Spin-resolved ARPES on low-dimensional systems with strong spin-orbit interaction**
  Solid State Physics Seminar, MIT, Boston, 17.05.10.
- J. H. Dil: **Spin- and angle-resolved photoemission: a direct probe for spintronics and topological insulators**
  Molecular Physics Seminar, Fritz-Haber-Institut, Berlin, 28.05.10.
- F. Meier: **Spin- and angle-resolved photoemission spectroscopy on topological insulators**
  Electronic, Transport, and Optical Properties of Low-Dimensional Systems (WS10-ETOLDS) Workshop, Valencia, Spain, 01.06.10.
- T. Greber: **Templates for molecules: from h-BN nanomesh to graphene based quantum dots**
  Poelsema Group Seminar, Universiteit Twente, The Netherlands, 03.06.10.
- H. Cun: **Multiple roles of carbon chains in quinacridone monolayers**
  5th Swiss Molecules on Surfaces (MolCH) Meeting, Bern, 10.06.10.
- J. H. Dil: **Spin-resolved ARPES on low-dimensional systems with strong spin-orbit interaction**
  Albert Fert Group Seminar, Unité Mixte de Physique CNRS/Thales, Orsay, France 10.06.10.
- J. H. Dil: **SARPES: a direct probe for spintronics and topological insulators**
  Seminar, Nanoscale Science Department, MPI Stuttgart, Germany, 23.06.10.
- H. Yanagisawa: **Optical control of field emission sites**
  6th Workshop on Numerical Methods for Optical Nanostructures, ETH Zürich, 05.07.19.
- J. Osterwalder: **Surface states as a bonanza for spin-polarized electrons**
  37th International Conference on Vacuum Ultraviolet and X-Ray Physics, Vancouver, Canada, 13.07.10.
- J. H. Dil: **The timely and the unexpected: spin-resolved ARPES on systems with strong spin-orbit interaction**
  Seminar, Donostia International Physics Center, San Sebastian, Spain, 19.08.10.
- H. Yanagisawa: **Optical control of field-emission sites**
  Seminar, Institute of Solid State Physics, University of Tokyo, Japan, 21.09.20.
- H. Yanagisawa: **Optical control of field-emission sites**
  Oshima Group Seminar, Waseda University, Tokyo, Japan, 30.09.10.
- J. Osterwalder: **Measuring spin polarization vectors of surface states**
  Workshop on Spin-Resolved Photoemission, Advanced Light Source Users Meeting, LBL Berkeley, California, USA, 14.10.10.
- J. H. Dil: **The timely and the unexpected: spin-resolved ARPES on systems with strong spin-orbit interaction**
  PSI-IOP (Beijing) Joint Workshop, Bad Zurzach, 15.10.10.

- J. Osterwalder: **Topological insulators: new physics with old materials**
  Kolloquium, EMPA Dübendorf, 02.11.10.

- J. Osterwalder: **Hexagonal boron nitride monolayer systems and nanomeshes**
  Materials Research Society Fall Meeting, Boston, Massachusetts, USA, 30.11.10.

- J. H. Dil: **From model systems to topological insulators; spectroscopy on systems with strong spin-orbit interaction**
  Seminar, Laboratorium für Festkörperphysik, ETHZ, 09.12.10.

- M. Hengsberger: **(Time-resolved) photoelectron spectroscopy (Tutorial)**
  NCCR MUST Assembly Meeting, Lenk, 12.01.11.

- T. Greber: **Resonant photoelectron diffraction (RXPD) for the determination of magnetic and atomic structure**
  Symposium on Surface and Nanoscience (SSNS'11), Shizukuishi, Japan, 20.01.11.

- T. Greber: **Resonant photoelectron diffraction (RXPD)**
  Seminar, Physics Department, Hiroshima University, Japan, 24.01.11.

- T. Greber: **Resonant photoelectron diffraction ... and how photons turn the electrons**
  26th Workshop on Novel Materials and Superconductors, Planneralm, Austria, 17.02.11.

- J. H. Dil: **A photoemission experimentalist's view on topological insulators**
  Edgar Lüscher Seminar, Klosters, 16.01.11.

- J. Osterwalder: **An introduction to topological insulators**
  Zürich Physics Colloquium, Uni/ETH Zürich, 16.03.11.

19.2.4 Physics of Biological Systems

Articles

- **Fabrication and characterization of low aberration micrometer-sized electron lenses**
  E. Steinwand, J.-N. Longchamp and H.-W. Fink, Ultramicroscopy 110(9) (2010) 1148-1153.

- **Depth-resolved holographic reconstructions by three-dimensional deconvolution**
  T. Latychevskaia, F. Gehri and H.-W. Fink, Optics Express 18(21) (2010) 22527-22544.

- **Graphene as a transparent conductive support for studying biological molecules by transmission electron microscopy**
  R. R. P. Blake *et al.*, Appl. Phys. Lett. 97(15): 153102 (2010).

- **Highly collimated electron beams from double-gate field emitter arrays with large collimation gate apertures**
  P. Helfenstein, E. Kirk, K. Jefimovs, T. Vogel, C. Escher, H.-W. Fink, S. Tsujino,
  Appl. Phys. Lett. 98(6) (2011) 061502.

- **Coherent low-energy electron diffraction on individual nanometer sized objects**
  E. Steinwand, J.-N. Longchamp and H.-W. Fink, Ultramicroscopy 111(4) (2011) 282-284.

Articles in press

- **Field-emission characteristics of molded molybdenum nano-tip arrays with stacked collimation gate electrodes**
  S. Tsujino, P. Helfenstein, E. Kirk, T. Vogel, C. Escher, and H.-W. Fink,
  IEEE Electron Device Letters.

- **Novel Fourier-domain constraint for fast phase retrieval in coherent diffraction imaging**
  T. Latychevskaia, J.-N. Longchamp and H.-W. Fink, arXiv:1102.3838v1.

Talks

- T. Latychevskaia: **Coherent diffraction imaging**
  seminar at the Institute of Genetics and Molecular and Cellular Biology, Strasbourg, France,
  3 December 2010.

- T. Latychevskaia: **Coherent imaging of individual molecules with low-energy electrons**
  seminar at the Physics Department EPFL Lausanne, Switzerland, 27 April 2010.

- T. Latychevskaia: **Imaging of individual molecules with coherent low-energy electrons**
  Gordon Research Conference *Diffraction Methods In Structural Biology*, Bates College Lewiston, USA.
  July 2010.

- T. Latychevskaia: **Numerical reconstruction of low-energy electron holograms**
  Gordon Research Conference *Three Dimensional Electron Microscopy*, Lucca Barga, Italy, June 2010.

- P. Helfenstein: **Highly collimated electron beams from double-gate field-emitter arrays**
  EMPA PhD Symposium, EMPA Dübendorf, 7.10.2010.

- P. Helfenstein: **Beam collimation properties of molded molybdenum field emitters**
  IVNC, Palo Alto, California, USA, 27.7.2010.

- P. Helfenstein: **Electron beam properties of molybdenum field emitter arrays with stacked gates**
  SPG Jahrestagung 2010, Basel, 22.6.2010.

- E. Steinwand: **Coherent diffraction imaging with low-energy electrons**
  From Physics to Life Sciences, Dubrovnik, Croatia, June 2010.

PhD thesis

- **Coherent Diffraction Imaging with Low-Energy Electrons**
  Elvira Steinwand, PhD Thesis, Physik-Institut, Universität Zürich, November 2010.

Bachelor theses

- **Kohärente Beugung niederenergetischer Elektronen: Beamstop und Probenpräparation**
  Flavio Wicki, Bachelor thesis, Universität Zürich, Mai 2010.

- **Holographische Untersuchung an Graphitflakes**
  Roland Stania, Bachelor thesis, Universität Zürich, January 2011.

19.2.5 Physical Systems Biology and non-equilibrium Soft Matter

Articles

- **Scattering based fluorescence microscopy: imaging through turbid media**
  I.M. Vellekoop and C.M. Aegerter, Optics Letters **35**, 1245 (2010).

- **Photo-elastic properties of the wing imaginal disc of Drosophila**
  T. Schluck and C.M. Aegerter, Europ. Phys. J. E **33**,111 (2010).

- **Exploiting disorder for perfect focusing**
  I.M. Vellekoop, A. Lagendijk, and A. P. Mosk, Nature Photonics **4**, 320 (2010).

- **Turbidity suppression from the ballistic to the diffusive regime in biological tissues using optical phase conjugation**
  E.J. McDowell, M. Cui, I.M. Vellekoop, V. Senekerimyan, Z. Yaqoob, and C. Yang,
  J. Biomed. Optics **15**, 025004 (2010).

Articles in press

- **Integrating Mechanical Control Theory into Models of Biological Development**
  V. Petrov, and C.M. Aegerter, Journal of Mechanics in Medicine and Biology (2011).

- **Velocity distributions of uniformly heated three dimensional granular gases**
  C.C. Maass, G. Maret, and C.M. Aegerter.

- **Integrating force sensing and signalling pathways in a model for the regulation of size in the wing imaginal disc of Drosophila**
  T. Aegerter-Wilmsen, M.B. Heimlicher, A.C. Smith, C.M. Aegerter, and K. Basler

Conference reports including posters

- **In-vivo imaging**
  U. Nienhaus and C.M. Aegerter, WingX retreat, Olivone, Switzerland (June 30th - July 2nd 2010).

- **Imaging through turbid media**
  G. Ghielmetti, I.M. Vellekoop, and C.M. Aegerter,
  WingX retreat, Olivone, Switzerland (June 30th - July 2nd 2010).

- **Photo-elastic properties of the wing imaginal disc of Drosophila**
  T. Schluck, A. Smith, and C.M. Aegerter,
  WingX retreat, Olivone, Switzerland (June 30th - July 2nd 2010).

- **Mechanical growth regulation of Drosophila wing discs**
  U. Nienhaus, T. Aegerter-Wilmsen, T. Schluck and C.M. Aegerter,
  Workshop 'New trends on growth and form', Agay, France (June 20-25, 2010).

- **Imaging through turbid layers (poster)**
  G. Ghielmetti, I.M. Vellekoop, and C.M. Aegerter,
  Summer School "Mesoscopic Physics in Complex Media", Cargese, France (July 12-16, 2010).
- **Nonlinear effects in Anderson localization of light (poster)**
  W. Bührer, S. Fiebig, T. Sperling, G. Maret, and C.M. Aegerter,
  Summer School "Mesoscopic Physics in Complex Media", Cargese, France (July 12-16, 2010).
- **2D transmission profile of light through highly scattering media (poster)**
  T. Sperling, W. Bührer, C.M. Aegerter , and G. Maret,
  Summer School "Mesoscopic Physics in Complex Media", Cargese, France (July 12-16, 2010).
- **Effects of growth regulation by mechanical stress on epithelial tissues (poster)**
  T. Aegerter-Wilmsen, A. Christen, A. Smith, C.M. Aegerter, E. Hafen, and K. Basler,
  Systemsbiology of Development, Monte Verita, Switzerland (August 16th - 19th 2010).
- **Birefringent properties of developing trachea (poster)**
  D. Assmann, T. Schluck, and C.M. Aegerter,
  Systemsbiology of Development, Monte Verita, Switzerland (August 16th - 19th 2010).
- **Photo-elastic properties of the wing imaginal disc of Drosophila (poster)**
  T. Schluck, D. Assmann, A. Smith, and C.M. Aegerter, Systemsbiology of Development, Monte Verita, Switzerland (August 16th - 19th 2010).
- **Mechanical growth control of Drosophila wing imaginal discs**
  U. Nienhaus, T. Aegerter-Wilmsen, T. Schluck and C.M. Aegerter, Workshop 'Nonlinear response of soft matter',
  Konstanz, Germany (February 28th - March 2nd, 2011).
- **Levitated granular gases**
  C.C. Maass, N. Isert, G. Maret, and C.M. Aegerter., Workshop 'Nonlinear response of soft matter',
  Konstanz, Germany (February 28th - March 2nd, 2011).

Invited lectures

- C.M. Aegerter: **Teaching Physics by using biological examples**
  Symposium "Bringing modern biology to school", Zürich, Switzerland (14.6.2010).
- C.M. Aegerter: **Imaging through turbid layers**
  International Conference on Systems Biology of Development, Monte Verita, Switzerland (17.8.2010).
- C.M. Aegerter: **Elastic properties of the wing imaginal disc of Drosophila**
  Developmental Biology Seminar, Université de Geneve, Switzerland (13.10.2010).
- C.M. Aegerter: **Interferenz und Streuung - von der Physik zur Biologie**
  Inaugural lecture, Universität Zürich, Switzerland (27.11.2010).
- C.M. Aegerter: **Interference and Scattering - from Physics to Biology**
  Physics Colloqium, University of Fribourg, Switzerland (24.01.2011).
- C.M. Aegerter: **Elastic properties of the wing imaginal disc of Drosophila**
  Colloqium in Plant Sciences, Universität Bern, Switzerland (21.03.2011).

- C.M. Aegerter: **Was hat Physik mit Systembiologie zu tun?**
  Physikalische Gesellschaft Zürich, ETHZ, Switzerland (24.03.2011).